Protein complexes of the excitatory and inhibitory synapse

van der Spek, Sophie Jeanne Frederika

2022

document version
Publisher's PDF, also known as Version of record

citation for published version (APA)
van der Spek, S. J. F. (2022). *Protein complexes of the excitatory and inhibitory synapse*.

Protein complexes of the excitatory and inhibitory synapse

Sophie J. F. van der Spek

promotor:	prof.dr. A.B. Smit
copromotor:	dr. K.W. Li
promotiecommissie:	dr. N.J. Pandya prof.dr. C.R. Jimenez prof.dr. H.W.H.G. Kessels prof.dr. R.J. Harvey prof.dr. R.E. van Kesteren

Cover by Sophie J.F. van der Spek

Printing: Ridderprint, www.ridderprint.nl

VRIJE UNIVERSITEIT

PROTEIN COMPLEXES OF THE EXCITATORY AND INHIBITORY SYNAPSE

ACADEMISCH PROEFSCHRIFT

ter verkrijging van de graad Doctor aan
de Vrije Universiteit Amsterdam,
op gezag van de rector magnificus
prof.dr. J.J.G. Geurts,
in het openbaar te verdedigen
ten overstaan van de promotiecommissie
van de Faculteit der Bètawetenschappen
op woensdag 18 mei 2022 om 9.45 uur
in een bijeenkomst van de universiteit,
De Boelelaan 1105

door

Sophie Jeanne Frederika van der Spek

geboren te Alkmaar

Table of contents

Appendices

Chapter 1: General introduction

The brain is one of the most complex organs of the human body. An organ that without, we could not think, feel or move. The brain contains billions of interconnected communicating neurons surrounded by glia, that enable physiological and mental processes. Failure of nerve cells to properly communicate underlies a plethora of brain disorders, including common neurodegenerative disorders like Alzheimer's disease (AD)[1,2]. For many brain disorders, the exact cause is unknown, and likely involves a complex interplay between environmental factors, genes and different cell (sub)types (i.e. excitatory and inhibitory neurons, astrocytes and microglia) of the brain[2,3] .

Synaptic neurotransmission

Neurons are specialized in intercellular communication via electro-chemical signaling. Active signal transmission between neurons takes place at synapses. The most common are chemical synapses that convert axonal electric activity at the presynaptic terminal into a chemical message that subsequently activates receptors on the receiving post-synapse. Upon stimulation, pre-synaptic vesicles fuse with the synaptic membrane, releasing neurotransmitters into synaptic cleft[4]. Binding of neurotransmitters (in)directly results in opening or closing of ion channels, the activation or inhibition of intracellular signaling cascades, and modification of the electrical properties of the receiving cells[5,6].

The downstream effect of presynaptic signal transduction on the post-synapse, depends on many factors including the molecular composition of the synapse, the timing of stimulation and the state of the synapse prior to receiving input. Importantly, the efficacy of synaptic transmission can be altered in an activity dependent manner also known as synaptic plasticity. Synaptic plasticity is regulated by many pre- and postsynaptic mechanisms, influenced by glial cells and can last from milliseconds to days and possibly even longer[7]. Multiple forms of short- and long-term synaptic plasticity exist and are thought to form the molecular basis of higher order processes such as learning and memory[7].

Neurotransmission involves a diverse set of synaptic proteins that act as part of protein complexes together forming an intricate molecular network[8]**.** Dysfunction of the molecular machineries regulating elementary synaptic processes are causal to many brain disorders, such as Autism[9], Schizophrenia[10] and Alzheimer's disease[1]. These synaptic dysfunctions are, also called synaptopathies[11,12]. Therefore, research into the organization of synaptic proteins and their relation to synaptic plasticity forms an important branch of molecular neuroscience.

Synaptic structure

The vast diversity of proteins present in the synapse (recently catalogued in the SynGO knowledgebase[13]), their differential expression across the brain and high number of isoforms underpins the complexity and diversity of the synaptic organelle[13,14]. Synapses can be subdivided based on the inhibitory or excitatory effect they elicit, and the type of neurotransmitter they release, including glutamate (excitatory) and glycine (inhibitory)[14]. All chemical synapses contain a presynaptic element opposing the post-synapse, which are connected through transsynaptic adhesion proteins that ensures the exact alignment of the transmitter release and signal-receiving protein components[15].

Excitatory synapses are asymmetric in shape and form on dendritic spines (Figure 1a,b). Most inhibitory synapses are symmetrical and are formed directly on the dendritic shaft or cell soma (Figure 1a)[16]. The presynaptic structure of inhibitory and excitatory synapses are molecularly different, such as the enzymes and transporters involved in neurotransmitter production and vesicle loading[17]. In contrast, the excitatory post-synapse is characterized by a post-synaptic density (PSD) with variable thickness (20-50nm), whereas the post-synaptic scaffold of inhibitory synapses are much thinner (~12nm) and more uniform (Figure 1c)[17].

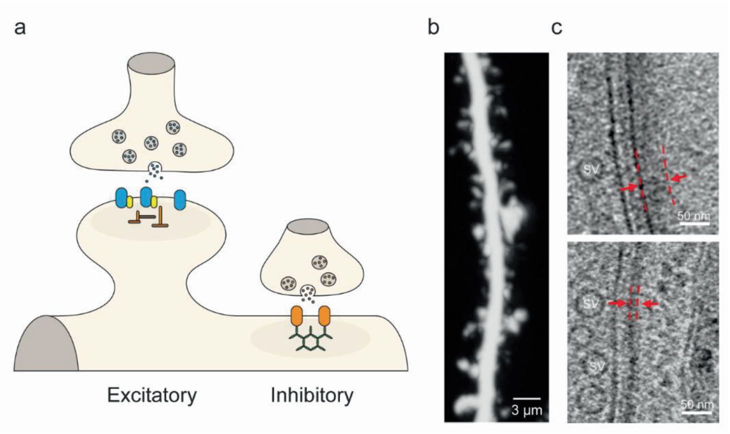

Figure 1. Morphological features of excitatory and inhibitory synapses. (**a**) Cartoon showing the morphological difference between the excitatory and inhibitory synapse. Where excitatory synapses often occur at spines on dendrites, inhibitory synapses are most abundant on aspiny dendrites and cell soma. (**b**) Confocal image of a dendrite covered with dendritic spines. Taken from Basu *et al.* 2018. (**c**) EM images of excitatory synapse (upper panel) and inhibitory synapse (lower panel). SV: synaptic vesicle. Arrows and lines in red highlight the thickness of the post-synaptic density. Taken from Tao *et al.* 2018.

The presynapse

The pre-synaptic structure can be recognized by the presence of small (~40 nm diameter) clear core vesicles, waiting to be released[17]. These spherical membrane organelles are covered by dozens of integral membrane and associated proteins involved in vesicle release and recycling processes[18]. Only a subset of vesicles is docked and primed for fusion at the presynaptic active zone, an electron-dense interphase (0.2-0.5 µm in diameter) between the presynaptic terminal and synaptic cleft[19].

Docking, priming and fusion involves a complex interplay between proteins of the release machinery[20]. The main components are proteins of the SNARE complex: the vesicular SNARE Synaptobrevin-2, and Syntaxin-1 and SNAP25 located in at the presynaptic membrane [20]. Essentially, during the process of priming and fusion Synaptobrevin, Syntaxin-1 and SNAP25 bind through their coiled-coils, forming a tight “zipped” macromolecular complex[20,21]. This brings the vesicle and synaptic membrane in close proximity and drives membrane fusion[20]. This reaction is controlled by accessory proteins that bind SNARE components, including vesicular Synaptotagmin-1 that is able to bind both SNARE proteins and phospholipids[20]. Upon electrical stimulation, a strong local influx of Ca^{2+} activates synaptotagmin-1 enabling membrane fusion[20].

After fusion, vesicles are recycled via clathrin-dependent and independent pathways (e.g. through kiss-and-run fusion, bulk or ultra-fast endocytosis), through endosomal intermediates or directly, ensuring a continuous supply of vesicles prepared to be released[22]. The reliability of vesicle release is highly variable across presynaptic terminals, even when originating of the same axon[23]. This is in part determined by the identity and feedback of the postsynaptic cell, and can be modulated by activity which allows for multiple forms of short- and long-term presynaptic mechanisms of plasticity[23].

The postsynapse

A typical mature post-synapse can be recognized as a dendritic membrane protrusion (of 0.5-2 µm in length) with a spine neck (of ~0.2 µm thickness) and a mushroom shaped spine head[24,25]. These types of synapses are mostly excitatory in nature, whereas inhibitory synapses are in general aspiny in shape[26,27]. The shape and size of the post-synapse is controlled by a dynamic network of globular and filamentous actin that regulates structural plasticity[28]. Synapse size shows a positive correlation with synaptic strength[29]. Larger synapses would therefore form stronger connections, although these correlations may not hold true for all synapses[30]. Besides the actin network, the postsynaptic structure contains an endocytic zone, endosomes, ER for local protein synthesis, mitochondria, and most importantly the PSD formed by a set of proteins directly involved in synaptic transmission[25].

The post-synaptic density

The PSD forms a characteristic post-synaptic structural platform that anchors receptor proteins. These post-synaptic receptors are crucial for synaptic transmission, as they allow for neurotransmitters to alter functional properties of the receiving neuron by (in)direct opening or closing of ion channels and modulation of intracellular signaling cascades. A framework of PSD scaffold proteins facilitates the functional organization of post-synaptic receptors, and other signaling and adhesion molecules[25,31].

During the last two decades, synaptic receptors were shown to be highly dynamic regarding their localization[32]. Multiple types of evidence revealed that receptors are exchanged between subsynaptic domains and intrasynaptic compartments through lateral diffusion and membrane recycling respectively[32]. Changes in receptor traffic rates lead to alterations in receptor type and number at the PSD, which form important post-synaptic mechanisms of plasticity[32]. Data obtained on activity dependent modulation of α-amino-3-hydroxy-5-methyl-4-isoxazolepropionic acid receptor (AMPAR) trafficking at the excitatory synapse resulted in a multi-step model of synaptic plasticity (see figure 2)[32,33]. During long-term potentiation (LTP), receptors are first inserted into the membrane[34]. This exchange occurs at a distance from the PSD[35]. Second, in the membrane, receptors diffuse through Brownian motion between synaptic and exta-synaptic sites [36,37]. As a last step, these receptors are reversibly trapped at the PSD through diffusion trapping[36,37]. Conversely, in this model during long-term depression (LTD), receptors that diffuse out of the synapse are endocytosed[32,33]. Functionally relevant receptors are trapped in so-called nanodomains at the PSD that when aligned with the presynaptic release machinery together are called nanocolumns[38–40], likely depending on transsynaptic adhesion molecules[15]. The same mechanisms of receptor trafficking and clustering in nanodomains have been observed at the inhibitory synapse[41–43], and seems to be a common way for regulating synaptic efficacy across synapse types[32].

Regulation of receptor trafficking and their biophysical properties largely depend on post-translational modifications and interacting proteins[44,45]. Indeed, proteins including synaptic receptors are commonly assembled with interactors into multiprotein complexes[46–48]. Importantly, as many receptor interactors show brain region or cell-type specific expression and involvement in specific circuitries, interactors are increasingly recognized as promising therapeutic targets[49]. The characterization of receptor complexes forms, for the main part, the focus of my studies in this thesis. In particular I focus on the AMPAR, the Glycine receptor (GlyR) and its major interactor Gephyrin, which are therefore introduced in the following sections.

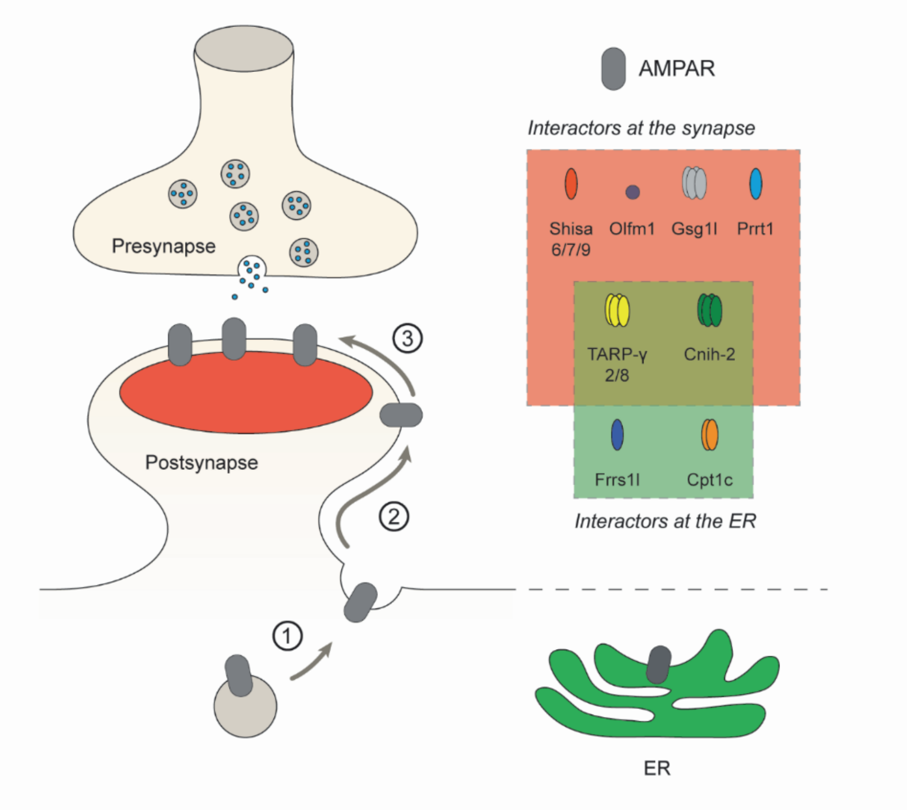

Figure 2. A multi-step model of AMPAR trafficking during synaptic plasticity. AMPARs are inserted into the plasma membrane (**1**), followed by lateral diffusion (**2**) and diffusion trapping at the post-synaptic density (**3**), leading to enhanced neurotransmission. Conversely, receptor diffusion out of the synapse followed by endocytosis results in reduced transmission (steps not depicted). Subsets of known AMPAR auxiliary subunits were shown to work at the synapse (in red) or ER (in green).

The AMPA-receptor

The AMPAR is responsible for most of the fast-excitatory neurotransmission in the brain[50]. This ion channel directly binds glutamate, and when open, facilitates the flux of Na^+, K^+ and in some cases Ca^{2+} ions across the synaptic membrane[50]. Four different homologous AMPAR subunits exist (GluA1-4), that can assemble in distinct compositions and form the functional ion channel inner core[51,52]. The predominant forms of AMPARs are heterotetramers containing GluA1/2 subunits or GluA2/3 subunits[53]. Both subtypes contain two GluA2 subunits, that due to RNA editing of glutamine 607 to arginine in the channel pore region are impermeable for calcium[54]. In early development and specific populations of cells (e.g. parvalbumin neurons[55]), calcium permeable AMPARs have been observed as well[44].

The AMPAR has been widely implicated in several forms of synaptic plasticity[44,56]. Especially GluA1/2 receptors are important for changes in synaptic transmission[53,57], and show enhanced gating after phosphorylation[58] and fast incorporation into the synapse upon induction of LTP[59]. GluA2/3 receptors cycle constitutively in and out of the synapse in absence of activity, and replace newly incorporated GluA1/2 receptors over time[59,60]. GluA2/3 receptors also show differences in biophysical properties, such as faster decay kinetics and lower probability of opening, which can be enhanced in the presence of cAMP[57,61]. The exact roles of distinct AMPAR subtypes in synaptic transmission and plasticity remains to be fully understood.

AMPA-receptor interacting proteins

AMPARs are decorated by interacting proteins[44,46]. Early yeast-two hybrid studies have implicated a number of cytosolic proteins in organizing AMPAR insertion and removal from the synapse[62]. For example, GRIP1 and PICK1, that directly interact with the C-terminal domain of GluA2[63,64]. Studies showed that phosphorylation of the GluA2 Ser880 residue by PKCα results in detachment of GRIP1, enhanced binding of PICK1, increased endocytosis and long-term depression (LTD)[65]. Interestingly, these and additional classical AMPAR interactors (e.g. Protein 4.1 and NSF) are only sporadically detected using interaction proteomics, possibly due to the instable or transient nature of their interaction[46,66,67].

More recent efforts using immuno-purifications and mass spectrometry (IP-MS), have resulted in the identification of around 30 transmembrane and secreted AMPAR interactors[46,66,68]. Most of the identified auxiliary proteins have been functionally characterized (see Table 1). In particular, proteins of the Transmembrane AMPAR Regulatory Protein (TARP) and Cornichon homolog (CNIH) families. These proteins decorate the majority of AMPARs and are considered core proteins of the AMPAR complex[46,69]. TARP-γ2 (Stargazin) was the first discovered AMPAR auxiliary subunit[70]. Disruption of the TARP-γ2 gene in Stargazer mice causes an epileptic and ataxic phenotype[71] and loss of functional AMPARs in granule cells of the cerebellum[70]. Whereas TARP-γ2 shows clear functional importance and high expression in the cerebellum, TARP-γ8 is widely expressed in the hippocampus[72]. Both proteins interact with the scaffold protein PSD95 through their C-terminal, affecting lateral diffusion of the receptor in the plasma membrane[73,74]. In addition, both TARP proteins, CNIH2 and 3 are implicated in ER-exit, and slow AMPAR deactivation and desensitization[68,72,75–78]. Unlike TARPs, CNIH2 and CNIH3 do not contain a PDZ-binding domain, however, they do remain present with the AMPAR at the PSD[68].

The sheer number of AMPAR interactors, and their distinct subcellular expression profiles[79], suggests these proteins assemble into distinct subcomplexes with different or overlapping protein compositions. In fact, previous studies revealed several interactors group in distinct AMPAR assemblies with different properties[77,80] (Figure 2). FRRS1L together with CPT1C were reported to form a subassembly in the endoplasmic reticulum where they regulate AMPAR biogenesis[77,80]. This complex is distinct from synaptic complexes containing, among others,TARP-γ8[77,80]. Both TARP-γ8 and FRRS1L compete for the same binding site on the AMPAR[8], and are therefore part of at least two separate AMPAR populations[80]. In addition, several AMPAR interactors revealed preferred association with distinct AMPAR subunits[46,81]. For instance, GRIP and PICK that interact with the AMPAR through a sequence (-SKVI) shared by GluA2 and GluA3, and lacking on GluA1 and GluA4[63,64]. Also several more recently identified AMPAR interactors revealed stronger binding with specific AMPAR subunits[46]. For example, PRRT1 associates preferentially with GluA1[46,82], and GSG1L with GluA2[46]. The identification of receptor subcomplex compositions, and their functional implications remains a field of active research, and may prove diverse among brain regions, cell types and developmental stages[69,83,84].

Table 1. Functional implications of AMPA-receptor interactors that were discovered by proteomics analyses.

Protein symbol	Alias	AMPAR modulation	Reference
TARP-γ2	CACNG2, Stargazin	Regulates surface expression, ER exit, gating properties and lateral diffusion by interacting with PSD95.	Cheng et al., 2001; Tomita et al., 2005; Kessels et al., 2009
TARP-γ8	CACNG8	Regulates surface expression, gating properties and synaptic localization by interacting with PSD95.	Rouach et al., 2005; Sumioka et al., 2011; Zheng et al., 2005
CNIH2		Regulates AMPAR export from ER and gating properties (activation, deactivation and desensitization).	Schwenk et al., 2009; Herring et al., 2013; Boudkkazi et al., 2014
SHISA6	CKAMP52	Regulates lateral mobility and prolongs desensitization.	Klaassen et al., 2016
SHISA9	CKAMP44	Regulates surface expression and recovery from desensitization.	von Engelhardt et al., 2010; Karataeva et al., 2014
GSG1L		Regulates AMPAR trafficking, surface expression and gating properties.	Shanks et al., 2012; McGee et al., 2015
CPT1C	CPT-1	Modulates AMPAR surface levels and assembly in the ER.	Gratacos-Batlle et al., 2015; Fado et al., 2015; Brechet et al., 2017
FRRS1L	C9ORF4, CG6	Modulates AMPAR surface levels and assembly in the ER.	Brechet et al., 2017
SAC1	PIP-PP SAC1, SACM1L	Modulates AMPAR secretory trafficking and surface levels.	Yang et al., 2013
ABHD6/12		Regulates AMPAR biogenesis in ER and surface delivery.	Wei et al., 2016; Schwenk et al., 2019
PRRT1	NG5, Syndig4	Regulates surface expression and gating properties.	Matt et al., 2018
OLFM1	Noelin1, Pancortin	Regulates AMPAR lateral diffusion and synaptic localization.	Pandya et al., 2018
NRN1	CPG15	Recruitment of AMPAR and PSD95 to the postsynapse.	Cantallops et al., 2000; Subramanian et al., 2019
LRRTM4	LRRT-4	Regulates activity-dependent AMPAR trafficking.	Siddiqui et al., 2013
RAP2B		Modulates AMPAR surface trafficking (removal and reallocation).	Fu et al., 2007; Kielland et al., 2009
PORCN		Regulates early formation of AMPAR in ER.	Erlenhardt et al., 2016

The Glycine-receptor

Ionotropic receptors on inhibitory synapses of the central nervous system mostly include $GABA_A$-receptors, and in the brainstem and spinal cord GlyRs are more abundant[85]. The GlyR enables fast inhibitory neurotransmission through conduction of chloride, and is involved in generating rhythmic motor behaviors such as locomotion and respiration[86,87], and nociception[88]..

The GlyR has five different subunits (α1-4 and β) that can form distinct pentameric compositions[85,89]. The α-subunits are ligand-binding and are targeted for modulation of GlyR functioning[90]. For instance, phosphorylation of the α3 subunit reduces glycinergic synaptic transmission in the spinal cord[88]. The β-subunit binds the scaffold protein Gephyrin, which is essential for clustering of GlyRs at the PSD[91], although also different α-subunits were shown to affect the level of synaptic GlyR clustering[89]. Unlike the β-subunit, all α-subunits can form homomers in heterologous expression systems[85]. Also in vivo, α2 homomers are detected, however, their expression is restricted to embryonic neurons and decreases sharply after birth[85]. The majority of GlyRs in the spinal cord and brain stem are heteromers containing α1 and β subunits, and were recently determined to be expressed in a 4:1 stoichiometry[92]. This GlyR subtype is the main mediator of glycinergic transmission in the adult brain[85,93]. Mutations in the α1 subunit of the GlyR are causative for hyperplexia, also known as human startle disease[94,95]. Additional GlyRs heteromers exist, containing α2, α3, or α4 in combination with the GlyR β subunit, with roles in: (α2) cortical neuron migration[96] and autism spectrum disorder (ASD)[97]; (α3) pain sensation caused by chronic inflammation[88] and rhythmic breathing[98]; and (α4) early embryonic development[99].

Compared to the GABA-receptor system, the glycinergic synapse has a low variety of presynaptic neurotransmitter synthesizing enzyme isoforms and GlyR subunit compositions[100]. Due to this relative molecular simplicity, glycinergic synapses are thought to have a limited number of mechanisms underlying plasticity[100].

The Glycine-receptor interactome

In line with the relative molecular simplicity of the GlyR, the number of reported GlyR interactors remains limited. The first and most well-established interactor of the GlyR is Gephyrin[101]. Additional interactions have been reported between the GlyR and PACN1, also known as Pacin1 (PACN1)[102,103], VPS35[104], Neurobeachin (NBEA)[104], the Leptin receptor[105], Karyopherin α3 and α4 (KPNA3 and KPNA4)[106]. Both GlyR β and GlyR α1 were shown to interact directly with PACN1[102,103] Because removal of PACN1 in spinal cord neurons resulted in a reduction in size and number of GlyR clusters, PACN1 was proposed to play a role in GlyR trafficking and/or cytoskeletal anchoring[102]. GlyR β was revealed to interact with VPS35[104] and NBEA[104]. Both proteins are involved in endosomal dynamics and surface expression of glutamate receptors[107,108], and may likewise regulate GlyR trafficking. The functional implications of the GlyR interactions with VPS35 and NBEA have not been investigated further.

All reported GlyR interactors have been identified with similar in vitro assays, using the large intracellular loop of the GlyR α1, α3 or β subunit as bait. For several interactors, colocalization experiments were performed in neuronal cells in support of their interaction with the receptor. Overlapping stainings with the GlyR were observed for PACN1[102] and VPS35[104]. However, minor to no colocalization was reported with the Leptin receptor[105], KPNA3 and KPNA4[106]. As suggested by the authors, this may point to non-stable interactions *in vivo*[106]*.* To date, the exact nature of their interaction or functional involvement in GlyR regulation remains unknown.

Gephyrin, its interactors and isoforms

Gephyrin is the major scaffolding protein of the inhibitory PSD[109]. A single Gephyrin protein comprises three structural domains (G, C and E) (Figure 3a). Multiple Gephyrin proteins can self-aggregate through the N-terminal G- and C-terminal E-domains, which led to a model of Gephyrin forming a hexagonal lattice shaped framework (Figure 3b)[110,111]. In addition, the G and E domains are similar as the MogA and MoeA proteins, respectively, that are responsible for molybdenum cofactor (Moco) production in bacteria[112]. Also Gephyrin catalyzes the last step in Moco production, and is therefore a multifunctional protein[112].

The Gephyrin scaffold is necessary for receptor clustering at the inhibitory PSD, and conversely receptor binding stabilizes Gephyrin below the membrane[100]. Both the GlyR and $GABA_A$-receptor bind the same receptor binding site at the E-domain of Gephyrin[113]. Their interaction strength determines their relative accumulation in the synapse, and can be modified by post-translational modifications[109,114,115]. GlyRs and $GABA_A$-receptors can anchor together in “mixed” synapses, or in synapses exclusively containing one of both receptors[116,117]. The dynamic (dis-)assembly of Gephyrin and subsequent receptor accumulations allows for fast adaptations of synaptic strength[118–120].

As a scaffold, Gephyrin interacts with many proteins itself, that belong to various functional classes (for an overview of all interactors see[109]). For instance, Gephyrin was shown to bind the adhesion molecule Neuroligin-2 (NLGN2), which is important for synapse formation. NLGN2 is thought to drive the formation of Gephyrin-GABA_A-receptor clusters at the PSD[121]. A more recently identified Gephyrin interactor is IQSEC3, a brefeldin A-resistant ARF guanine nucleotide exchange factor (GEF)[122]. This protein has been implicated in maintenance of Gephyrin cluster size, and the correct apposition of GABA_A-receptor-containing post-synapses with presynaptic terminals, in an Arf6 signaling dependent manner during synapse development[123]. Gephyrin also interacts with cytoskeletal (binding) proteins, like tubulin and Profilin1/2, and transport proteins including Kinesin heavy chain 5 (KIF5) and Dynein light chain 1 and 2 (DLC1 and DLC2). Gephyrin has been observed in intracellular GlyR-containing vesicles, where it interacts with motor protein complexes[120,124,125]. The preassembled Gephyrin-GlyR complexes were shown to comigrate with KIF5 and Dynein through neurites over time, suggesting Gephyrin to act as motor-cargo adaptor protein enabling intracellular GlyR transport [120,125].

Interestingly, several isoforms of Gephyrin are created through alternative splicing[126], and show biochemical differences in affinity for the GlyR[127,128], folding[128], aggregation[129], phosphorylation[128] and subcellular localization[128]. These splice-isoforms can therefore control important aspects of inhibitory synapse function. For example, in some neurons GlyRs are excluded from the synapse along the course of development, which has been proposed to be regulated by the expression of the Gephyrin G2 (also called C5 or C5'[130]) isoform[100,131]. To understand the importance of Gephyrin isoforms and their regulation further research is required.

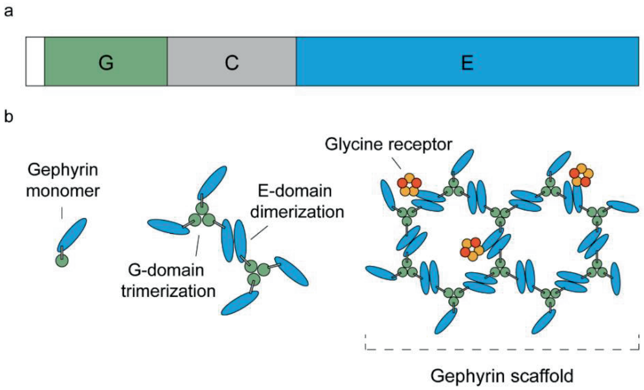

Figure 3. Gephyrin structure and self-aggregation model. (**a**) The Gephyrin protein containing an N-terminal G domain and C-terminal E domain connected by a C-linker region. (**b**) Gephyrin monomers can trimerize through its G-domain and dimerize through its E-domain, forming a hexagonal lattice. Binding of the Glycine receptor to the E-domain of Gephyrin stabilizes the oligomer[100].

The molecular composition of the synapse in Alzheimer's disease

Aberrant functioning of the synapse has been implicated in several brain disorders[11,12], including AD[1]. Reduced synapse density strongly correlates with cognitive decline in AD[132]. In addition, Amyloid-beta (Aβ), a cleavage product of APP and one of the pathological hallmarks of AD, appears to play an important role in synapse toxicity[2]. As part of my research on synaptic proteins, I therefore explored the synapse proteome alterations induced by overexpression of Aβ using the APP/PS1 mouse model of AD.

AD is a progressive neurodegenerative disorder and the most common cause of dementia[3,133]. In the initial stages, AD can be recognized by the inability to store new memories and, as the disease progresses, previously stored memories get lost and essential cognitive functions are affected. The majority of patients suffers from sporadic AD, that mostly occurs starting at the age of 65[3]. With age being its highest risk factor, and an increasing worldwide life expectancy, the number of AD cases is expected to increase further in the coming decades[3,133]. Currently, there is no cure for AD, and available treatments provide only temporary symptomatic relief. Major efforts are made to search for (preventive) therapies and understanding of AD etiology, which have resulted in big advances[134–137]. However, to date, the causal mechanisms underlying AD pathology remain unknown.

The accumulation of Aβ is believed to play an important role in AD pathogenesis[138,139]. Aβ peptides are products of the transmembrane Amyloid Precursor Protein (APP) that is cleaved by Presenelin 1 and 2 (PSEN1 and PSEN2) containing γ-secretases (see Figure 4). Mutations in the APP and PSEN1/2 genes are disease-causative for cases of familial AD, and form the genetic basis of the APP/PS1 mouse model[140,141]. In addition to accumulations of Aβ in extracellular plaques, the brains of AD patients are characterized by neurofibrillary tangles (intraneuronal aggregates of hyperphosphorylated tau), synapse loss, astro- and microgliosis and neuronal death[2].

Synapse dysfunction and loss is the strongest correlate to cognitive decline in AD patients [142,143]. Already in early stages of AD a large reduction in synaptic protein expression is observed in both humans and mouse models of AD[144,145]. In APP transgenic mice synapse dysfunction and loss is observed before the onset of plaque formation, and correlates well with the increase of soluble oligomeric Aβ[145]. Indeed, multiple animal studies have shown that oligomeric Aβ reduces synaptic strength, impairs synaptic plasticity and causes synapse loss and cognitive deficits[145,146,]. Several studies suggest oligomeric Aβ can induce the formation of tau tangles[147]. In addition, removal of phospho-tau can prevent synapto-toxic effects of oligomeric Aβ, demonstrating a close link between the two pathological hallmarks and synapto-toxicity[148,149]. Exactly how oligomeric Aβ causes the synaptic defects, and its relation with tau and AD etiology is unclear, as this peptide comes in many oligomeric forms, and binds a plethora of receptors triggering different pathways[150]. In addition, distinct types of synapses and neurons may be affected differentially[151].

Reactive glia in the AD brain are increasingly considered as key players in disease pathogenesis, and not only treated as a consequence of pathology[136,152]. Astrocytes and microglia are the major cell types responsible for the inflammatory response in the brain, and are observed in activated state around Aβ plaques in the AD mouse and in human AD[152]. Several genetic risk factors for AD are highly expressed by astrocytes and microglia (e.g. Apolipoprotein E (APOE), Clusterin (CLU) and Triggering receptor expression on myeloid cells 2 (TREM2)), suggesting a causal role for these cell types in AD pathology[136]. In addition, microglia and the complement system were shown to be involved in early synaptic loss in AD mice[153]. The exact mechanisms involving astrocytes and microglia in AD, and whether they are harmful or protective are not fully understood.

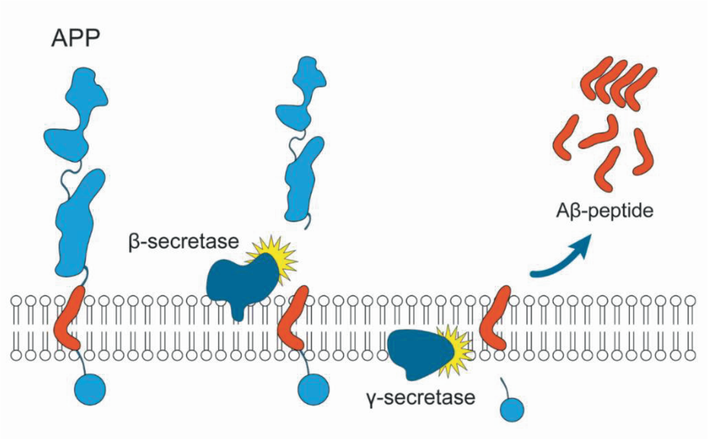

Figure 4. Amyloidogenic pathway of processing the Amyloid Precursor Protein (APP). The transmembrane protein APP undergoes proteolytic cleavage by secretases. Cleavage of APP by β- and α-secretase, results in the production of Aβ that can accumulate into oligomers and eventually aggregate into plaques. Known AD associated mutations in the APP gene, and genes coding for PSEN1 and PSEN2 (part of the γ-secretase complex) causes enhanced production of Aβ.

Aim and outline of this thesis

The primary aim of this thesis was to determine protein complex compositions of major synaptic proteins of the excitatory and inhibitory synapse, using a combination of several proteomics approaches. More precisely, we aimed to push for further specification of the GlyR, Gephyrin and AMPAR interactomes, by focusing on their subcomplex compositions and the differential protein assemblies of AMPAR subtypes and Gephyrin isoforms. The specification of GlyR, Gephyrin and AMPAR protein assemblies is intended to add to the understanding of their functional regulation, in health and disease.

In **chapter 2** the GlyR interactome in the brainstem was determined using an immunopurification (IP)- mass spectrometry strategy with multiple antibodies against the GlyR and Gephyrin. The excitatory synapse protein IQSEC2, and IQSEC3 known as Gephyrin interactor in $GABA_A$-receptor containing synapses, were shown to be part of GlyR containing complexes. Additional separation of GlyR complexes with an IP-Blue Native/Mass spectrometry approach, demonstrated that this novel GlyR-Gephyrin-IQSEC2/3 assembly forms a small and distinct high molecular weight population of GlyRs**.**

The scaffolding protein Gephyrin has multiple splice isoforms with different biochemical properties. In **chapter 3** we designed specific antibodies against the major Gephyrin-C3 and C4A splice isoforms, and validated their specificity. With these novel antibodies, we determined Gephyrin-C3 and -C4A cellular expression, their interaction profiles with overlapping and specific interactors and subcomplex compositions. The neuronally expressed Gephyrin-C4A revealed strong binding to the GlyR, IQSEC3 and Nitric oxide synthase 1 (NOS1), whereas Gephyrin-C3 revealed high expression in astrocytes, reduced binding to the GlyR and specific interaction with NLGN2.

In **chapter 4** I moved to the excitatory synapse and analyzed the complex compositions of the two most abundant AMPAR subtypes in the hippocampus. We performed quantitative and interaction proteomics on wildtype and GluA1- and GluA3 gene deleted mice. Whereas GluA1/2 co-purified TARP-γ8, PRRT1 and CNIH2 with highest abundances, GluA2/3 receptors revealed strongest co-purification of CNIH2, TARP-γ2, and OLFM1. Additional IP-MS, IP-BN-PAGE/MS and microscopy analysis revealed a direct interaction between TARP-γ8 and PRRT1 and their co-assembly into an AMPAR subcomplex especially near the synapse.

Alzheimer’s disease, one of the most well-known disorders of the brain, is characterized by early hippocampal memory deficits and dysfunctional synapses. **In chapter 5** I study the proteome of a synapse enriched fraction obtained from the hippocampus of the APP/PS1 mouse model of AD at 6 and 12 months of age using data independent acquisition (DIA) mass spectrometry. We first assessed the usefulness of a recently improved directDIA analysis workflow as an alternative to conventional DIA analysis using a project specific library. We subsequently applied this workflow to our datasets, and revealed most regulation at 12-months. In particular proteins involved in Aβ homeostasis and microglial-dependent processes.

In **chapter 6** the results of the proteomics analyses on the GlyR, Gephyrin isoforms, AMPAR protein assemblies and the APP/PS1 proteome are summarized, and their implications are discussed. In addition, the challenges and future perspectives for the study of synaptic proteins complexes and (interaction) proteomics are highlighted.

Chapter 2: Glycine receptor complex analysis using immunoprecipitation-blue native gel electrophoresis-mass spectrometry

Sophie J. F. van der Spek, Frank Koopmans, Iryna Paliukhovich, Sarah L. Ramsden, Kirsten Harvey, Robert J. Harvey, August B. Smit and Ka Wan Li

Proteomics 2020, 20, 1900403

Abstract

The pentameric glycine receptor (GlyR), comprising the α1 and β subunits, is a major inhibitory ionotropic receptor in brainstem and spinal cord. GlyRs interact with Gephyrin (GPHN), a scaffold protein that anchors the GlyR in the plasma membrane and enables it to form clusters in glycinergic postsynapses. Using an interaction proteomics approach, we provides evidence of the ArfGEFs IQ motif and Sec7 domain 3 (IQSEC3) and IQ motif and Sec7 domain 2 (IQSEC2) as two novel synaptic proteins interacting with GlyR complexes. When the affinity-isolated GlyR complexes were fractionated by blue native gel electrophoresis and characterized by mass spectrometry, GlyR α1β-GPHN appeared as the most abundant complex with a molecular weight of approximately 1 MDa, and GlyR α1β-GPHN-IQSEC3 as a minor protein complex of approximately 1.2 MDa. A third GlyR α1β-GPHN-IQSEC2 complex existed at the lowest amount with a mass similar to the IQSEC3-containing complex. Using yeast two-hybrid we demonstrate that IQSEC3 interacts with the GlyR complex by binding to the GPHN G domain at the N-terminal of the IQSEC3 IQ-like domain. Our data provide direct evidence of the interaction of IQSEC3 with GlyR-GPHN complexes, underscoring a potential role of these ArfGEFs in the function of glycinergic synapses.

Introduction

The glycine receptor (GlyR) is an anion-selective ligand-gated ion channel expressed mainly in the brain stem and spinal cord. GlyRs mediate fast inhibitory neurotransmission, and are involved in the regulation of locomotion, respiration and nociceptive processes[154]; e.g., malfunction of the major adult α1β subunit containing GlyR is known to cause startle disease/hyperekplexia[95]. The glycinergic synapse has a relatively simple postsynaptic density at the ultra-structural level[100]. It consists of multiple GlyRs, each composed of a pentamer of α1 and β subunits clustered by the synaptic scaffolding protein Gephyrin (GPHN), and is thought to have limited ability for plastic change[100]. Recent interaction proteomics studies on ligand-gated ion channels and membrane receptors, such as $GABA_A$ and glutamate receptors, have revealed the presence of many protein interactors[46,47,84,155,156]. However, the relatively simple composition known of the GlyR complex (GlyR α1β-GPHN) may in part be explained by the low sensitive biochemical methods used in the previous studies, leaving additional interactors undetected. While some potential GlyR interactors have been characterised, including karyopherin 3 and 4[106], Vacuolar Protein Sorting 35 and Neurobeachin[104], and syndapin I[102], a detailed proteomics analysis of synaptic GlyRs is currently lacking. In this study, we used immuno-precipitation (IP)-based interaction proteomics to characterize GlyR associated proteins from a brain stem extract. Using the AMPAR interactome as background to identify candidates[84], we identified two ArfGEFs: IQ motif and Sec7 domain 3 (IQSEC3, also known as BRAG3/SynArfGEF) and, to a lesser extent, IQ motif and Sec7 domain 2 (IQSEC2, also known as BRAG1/IQ-ArfGEF) as new GlyR interactors. The IQSEC3 and IQSEC2 interaction with GlyR complexes was validated by using a multi-dimensional IP-Blue native gel electrophoresis (BN)-mass spectrometry (MS) approach. IP-captured protein complexes were size-fractionated by BN and analysed by quantitative proteomics. Correlation profiling of protein migration patterns on the BN gel distinguished several GlyR complexes, of which the main pool consisted of GlyR α1β-GPHN. At the higher molecular weight range IQSEC2 and IQSEC3 were also detected, corresponding to the complexes GlyR α1β-GPHN-IQSEC3 and GlyR α1β-GPHN-IQSEC2. Using yeast two-hybrid, we demonstrated that IQSEC3 interacts with the GlyR complex through the binding of the GPHN G domain with a unique motif (amino acids 160-210) N-terminal of the IQSEC3 IQ-like domain.

Results

In this study we examined the interactome of the major adult GlyR (α1β) subtype by immunoprecipitating the GlyR subunits GlyR α1, β and GPHN and identifying interacting proteins by mass spectrometry. For this we used a commercially available GlyRα1 antibody obtained from Genscript (anti-GlyR α1a) and three custom-made antibodies raised against GlyRα1 (anti-GlyR α1b), GlyRβ and GPHN, which recognised the bait proteins specifically (Supplementary Fig. 1A, see also Supplementary Materials and Methods). In addition, to distinguish the bulk of proteins binding in the IPs from GlyR-specific interactors [156,157], two custom-made antibodies raised against the AMPA-receptor subunits GluA2/3 and GluA4 (Supplementary Fig. 1A) were used as background to identify candidates.

In the first instance, we examined the effect of different detergents on integrity of the GlyR protein complex. Brain stem proteins were extracted in 1% DDM, NP-40 and Triton X-100, and run on a blue-native gel and stained for GlyR β. Clear immuno-reactivity for the GlyR was observed around 1 MDa for all three extraction conditions, and a lack of signal around 50 kDa, i.e., the molecular weight of single GlyR subunits. Triton X-100 and NP-40 conditions showed immuno-reactivity around 700 kDa, which may implicate mild breakdown of the protein complex during extraction (Supplementary Fig.1B). In addition, DDM was previously found as preferred detergent for maintaining the integrity of the AMPA receptor protein complex[84]. We therefore used 1% DDM for subsequent experiments.

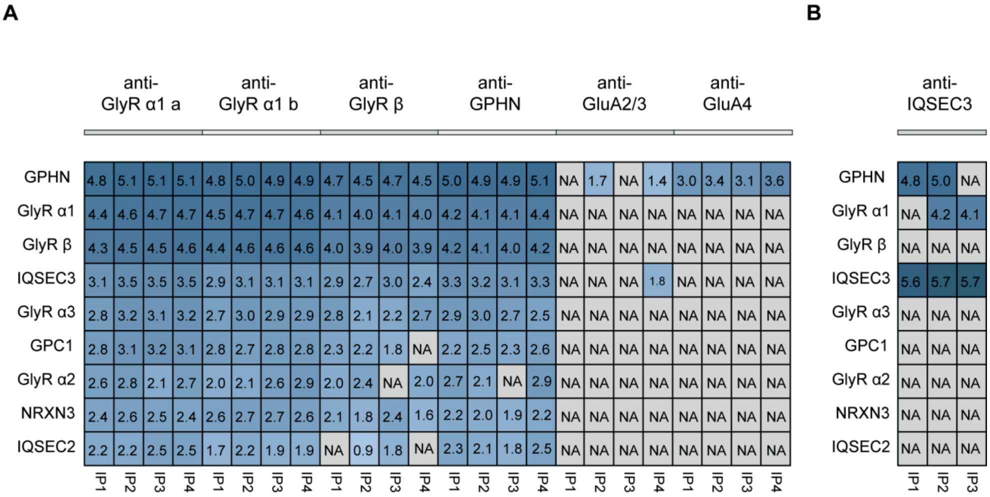

A

	anti-GlyR α1 a				anti-GlyR α1 b				anti-GlyR β				anti-GPHN				anti-GluA2/3				anti-GluA4			
	IP1	IP2	IP3	IP4	IP1	IP2	IP3	IP4	IP1	IP2	IP3	IP4	IP1	IP2	IP3	IP4	IP1	IP2	IP3	IP4	IP1	IP2	IP3	IP4
GPHN	4.8	5.1	5.1	5.1	4.8	5.0	4.9	4.9	4.7	4.5	4.7	4.5	5.0	4.9	4.9	5.1	NA	1.7	NA	1.4	3.0	3.4	3.1	3.6
GlyR α1	4.4	4.6	4.7	4.7	4.5	4.7	4.7	4.6	4.1	4.0	4.1	4.0	4.2	4.1	4.1	4.4	NA	NA	NA	NA	NA	NA	NA	NA
GlyR β	4.3	4.5	4.5	4.6	4.4	4.6	4.6	4.6	4.0	3.9	4.0	3.9	4.2	4.1	4.0	4.2	NA	NA	NA	NA	NA	NA	NA	NA
IQSEC3	3.1	3.5	3.5	3.5	2.9	3.1	3.1	3.1	2.9	2.7	3.0	2.4	3.3	3.2	3.1	3.3	NA	NA	NA	1.8	NA	NA	NA	NA
GlyR α3	2.8	3.2	3.1	3.2	2.7	3.0	2.9	2.9	2.8	2.1	2.2	2.7	2.9	3.0	2.7	2.5	NA	NA	NA	NA	NA	NA	NA	NA
GPC1	2.8	3.1	3.2	3.1	2.8	2.7	2.8	2.8	2.3	2.2	1.8	NA	2.2	2.5	2.3	2.6	NA	NA	NA	NA	NA	NA	NA	NA
GlyR α2	2.6	2.8	2.1	2.7	2.0	2.1	2.6	2.9	2.0	2.4	NA	2.0	2.7	2.1	NA	2.9	NA	NA	NA	NA	NA	NA	NA	NA
NRXN3	2.4	2.6	2.5	2.4	2.6	2.7	2.7	2.6	2.1	1.8	2.4	1.6	2.2	2.0	1.9	2.2	NA	NA	NA	NA	NA	NA	NA	NA
IQSEC2	2.2	2.2	2.5	2.5	1.7	2.2	1.9	1.9	NA	0.9	1.8	NA	2.3	2.1	1.8	2.5	NA	NA	NA	NA	NA	NA	NA	NA

B

	anti-IQSEC3		
	IP1	IP2	IP3
GPHN	4.8	5.0	NA
GlyR α1	NA	4.2	4.1
GlyR β	NA	NA	NA
IQSEC3	5.6	5.7	5.7
GlyR α3	NA	NA	NA
GPC1	NA	NA	NA
GlyR α2	NA	NA	NA
NRXN3	NA	NA	NA
IQSEC2	NA	NA	NA

Figure 1. Putative GlyR interactors in brainstem extract. (A) Proteins identified by interaction proteomics that were present in > 75% of the GlyR/GPHN IPs with an iBAQ enrichment of ≥10 folds compared to the mean iBAQ intensity observed in GluA2/3 and GluA4 IPs. (B) Reverse IP with an antibody against IQSEC3 showed the presence of GlyR α1 and GPHN. iBAQ intensity values are shown as a log10 value.

To obtain high consistency in our IP-MS/MS experiment, volumes, protein concentrations and amount of antibody used, were kept constant. In addition, four biological replicates for all GlyR/GPHN and AMPAR antibodies were performed in a single batch. The IP samples were run on SDS-PAGE gel, cut into three fractions, trypsin digested and analysed by LC-MS/MS. This classic approach is more labour intensive and time consuming than the recently developed FASP and SP3 methods[156,158]. However, the advantages are that it allows for quality control of the IP experiments by staining the proteins on the SDS-PAGE gel (Supplementary Fig. 2), while the fractionation and separate LC-MS/MS of each fraction increases the depth of the proteomics analysis. The control GluA IPs in brainstem and hippocampus consistently purified the previously reported AMPA receptor interactors[46,84], which were not present in the GlyR and GPHN IP sets, indicating the reliability and high sensitivity of the approach (Supplementary Fig. 3). For enrichment analysis, only brainstem GluA-IPs were used to filter out background proteins. Figure 1A shows the iBAQ intensity values of proteins present in >75% of the GlyR/GPHN IP experiments (i.e. > 12 out of the 16 IP experiments) with an iBAQ enrichment of ≥10 fold compared to the GluA2/3 and GluA4 IPs. The complete list of proteins detected in each individual IP of all antibodies used in this analysis is given in supplementary Table 1. Overviews of the IP data per antibody, highlighting the fold change ranking of the interactors are provided in Supplementary figure 4.

The core proteins GlyR α1, GlyR β and GPHN, were recovered from the GlyR α1 and GlyR β IPs, in here GPHN was detected as the most abundant protein. Similar results were obtained from GPHN IPs. GlyR α2 and α3 were detected as well, albeit at a considerable lower amount. Interestingly, we detected two ArfGEFs, IQSEC3 and IQSEC2, which were purified at 10 to 100 fold lower levels, respectively, than the GlyR and GPHN. Two additional potential interactors were present at similar low detection level, NRXN3 and GPC1.

Among the several novel potential GlyR interactors, IQSEC3 is detected at the highest level that is nevertheless about 10 fold lower than GlyR and GPHN. To validate the GlyR-IQSEC3 interaction, we performed reverse IPs on IQSEC3 (Fig. 1B, supplementary Table 2). GPHN was recovered at a 5x lower level than IQSEC3, and GlyR α1 at a 20x lower level. This suggests a primary interaction between IQSEC3 and GPHN, with the GlyR as secondary interaction via GPHN. IQSEC2 was not recovered from the IQSEC3 IPs, suggesting that IQSEC2 and IQSEC3 are contained in distinct complexes.

To discern different protein complexes, we extended the IP approach with mass separation of native protein complexes by blue-native gel electrophoresis followed by their proteomics analysis (IP-BN Proteomics; Fig. 2A), focussing on the core proteins GlyR α1 and GlyR β. As a protein contained in a complex likely will spread out across multiple BN gel fractions resulting in a lower protein amount in individual BN gel fractions, the IP experiments were scaled-up ten-fold to compensate for the dilution across gel fractions. To reveal the validity of the BN-MS approach, we first tracked unique tryptic peptides derived from a single protein as these should provide the same migration pattern on the BN gel. A representative example is provided by the three tryptic peptides of GlyR α1 on the GlyR β IP-BN (Figure 2B). We observed pronounced intensity differences between the peptides. When the intensities are normalized to 100% at their maximum, their highly correlated migration patterns become apparent (Pearson’s correlation ≥ 0.99) (Fig. 2C).

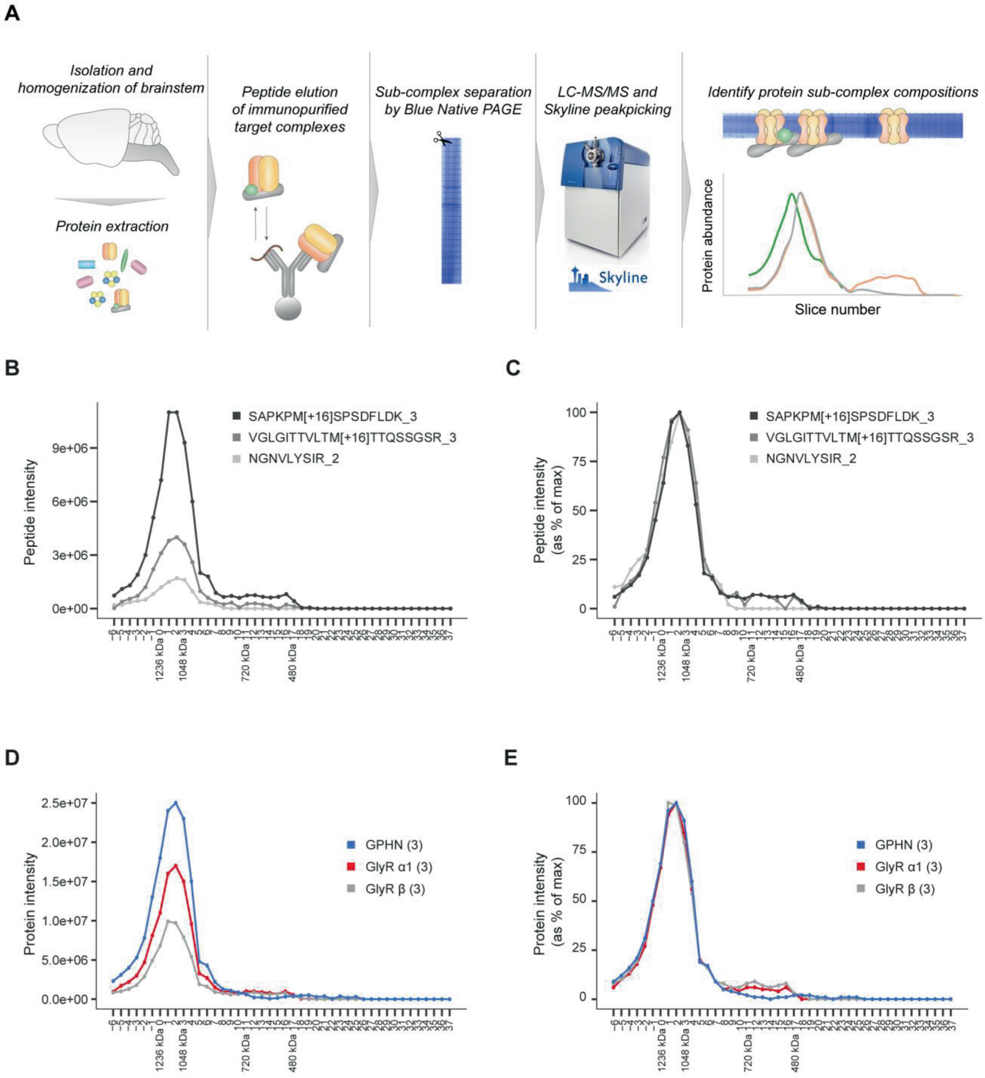

Figure 2. Analysis of the GlyR protein complex by IP-BN proteomics. (**A**) Workflow of the IP-BN proteomics. Bait protein was immunoprecipitated from tissue extract, and then competed off from the antibody with a synthetic peptide corresponding to the epitope of the antibody. The eluted complexes were size-fractionated by blue native gel electrophoresis. The gel was cut into multiple slices, and analysed by conventional proteomics approach. (**B-E**) IP-BN mass spectrometry of GlyR β shows identical migration profiles on the BN gel for GlyR α1, GlyR β and GPHN. (**B**) Three unique GlyR α1 peptides curated in Skyline show similar migration profiles but pronounced differences in intensity values. (**C**) Normalization of peptide peak intensities to their maximum intensity value reveal the high

degree of correlation among the different peptides derived from the same protein (Pearson correlation ≥0.99). (**D**) GlyR α1, GlyR β and GPHN co-migrate in a molecular weight range peaking at approximately 1 MDa. (**E**) The normalized data reveals more clearly the high degree of correlation among the different proteins (Pearson correlation ≥0.99) and the presence of a small population of GlyR α1β complex without GPHN that migrated at a mass between 480-720 kDa. Four marker proteins were included in each IP-BN run as reference for molecular weight, which are depicted on the x-axis. The number of peptides used for peak-picking are shown in brackets.

To achieve the most accurate migration profiling of the proteins across the gel, the summed intensities from individually peak-picked peptides in Skyline were plotted (Fig. 2D). Peptides chosen for curation in Skyline included those that are unique for the protein of interest, preferably unmodified and most abundant. Highly correlated migration profiles of GlyR α1, GlyR β and GPHN (Pearson's correlation ≥ 0.99) were observed, implying that they are part of the same complex (Fig. 2E). Of note, four marker proteins were included as reference for molecular weight. The main GlyR-GPHN complex peaked at approximately 1 MDa. In addition, a small fraction of the GlyR subunits were detected in a lower mass range between 480 and 720 kDa without GPHN. IQSEC2 and IQSEC3 were recovered at a ten to hundred-fold lower level than the GlyR and GPHN from IP experiments (Fig. 1). Both proteins were also recovered from the IP-BN experiments. When plotted against the subunits of the GlyR, IQSEC3 has a lower intensity (Fig. 3A) and peaked at the high mass range of the GlyR complex in the BN at approximately 1.2 MDa (Fig. 3B). Thus, the GlyR-GPHN-IQSEC3 protein complex presents as a minor component with a larger MW than the average of the GlyR-GPHN complex (Fig. 3A-B). IQSEC2 showed a similar migration pattern on the BN gel. It was present also at slightly lower MW than IQSEC3 and with substantially lower intensity.

The initial IP-MS analysis (Fig. 1) showed the presence of several additional putative GlyR interactors at low intensities. In the IP-BN proteomics experiments, NRXN3 and GPC1 both migrated at a low MW range of <420 kDa that do not overlap with the detection of the GlyR subunits (Fig. 3 C-D). To conclude, the majority of the GlyR protein complex represents the GlyR receptor and GPHN, and a small population of the GlyR complex contains IQSEC2 or IQSEC3.

To reveal the reproducibility of this approach, we isolated the GlyR complexes using two different anti-GlyR α1 antibodies, and examined their migration pattern on the BN gel (Fig. 3E-H). Similar to the results of the GlyR β IP-BN-MS experiment, GlyR α1-β-GPHN show highly correlated migration profiles and peaked at approximately 1 MDa. IQSEC2 and IQSEC3 again appeared in the higher mass range of the GlyR complex with substantially lower intensities than the GlyR core proteins. Low MW complexes were also present including one that peaked at approximately 480 kDa that contained GlyR α1 and β subunits but not GPHN.

To unequivocally identify the binding partner of IQSEC3 in the GlyR α1β-GPHN complex, we utilised the GAL4 yeast two-hybrid system. While we were unable to detect interactions between IQSEC3 with GlyR α1 or β subunit baits (data not shown), robust interactions between IQSEC3 and GPHN were detected. To map the reciprocal binding sites for the GPHN-IQSEC3 interactions, we assessed interactions with IQSEC3 and GPHN G, C and E domains, using GPHN G domain trimerisation, and GlyR β-GPHN E domain interactions as positive controls. The GPHN E-domain interacted with GlyR β (Fig. 4A). Interestingly, this analysis revealed that full-length IQSEC3 and the N-terminus of IQSEC3 (amino acids 1-649) interacted with the GPHN G domain, but not the C or E domains (Fig. 4A). Furthermore, we screened 8 overlapping IQSEC3 baits against GPHN G domain to reveal the specific binding site of IQSEC3 to GPHN. A single bait (amino acids 160 and 210 of IQSEC3) yielded strong signal, situated upstream of the regulatory IQ-like domain (at amino acids 316-326, Fig. 4B). Taken together, we validated the IQSEC3-GPHN interaction and located to a core GPHN G domain binding motif on IQSEC3.

Discussion

Our interaction proteomics study suggests that the major adult GlyR α1β subtype contains mainly GlyR α1, GlyR β and GPHN. This organization was initially demonstrated three decades ago by the affinity isolation of the GlyR on an aminostrychnine-agarose column which showed the presence of three main protein bands after separation of the receptor complex on the SDS-PAGE gel[159]. We now provided evidence that the ArfGEF IQSEC3 is an additional partner in GlyR complexes, via an interaction between the IQSEC3 N-terminus and the GPHN G domain. Existence of additional more labile interactors, and interactors shared by the GlyR and AMPAR cannot be excluded.

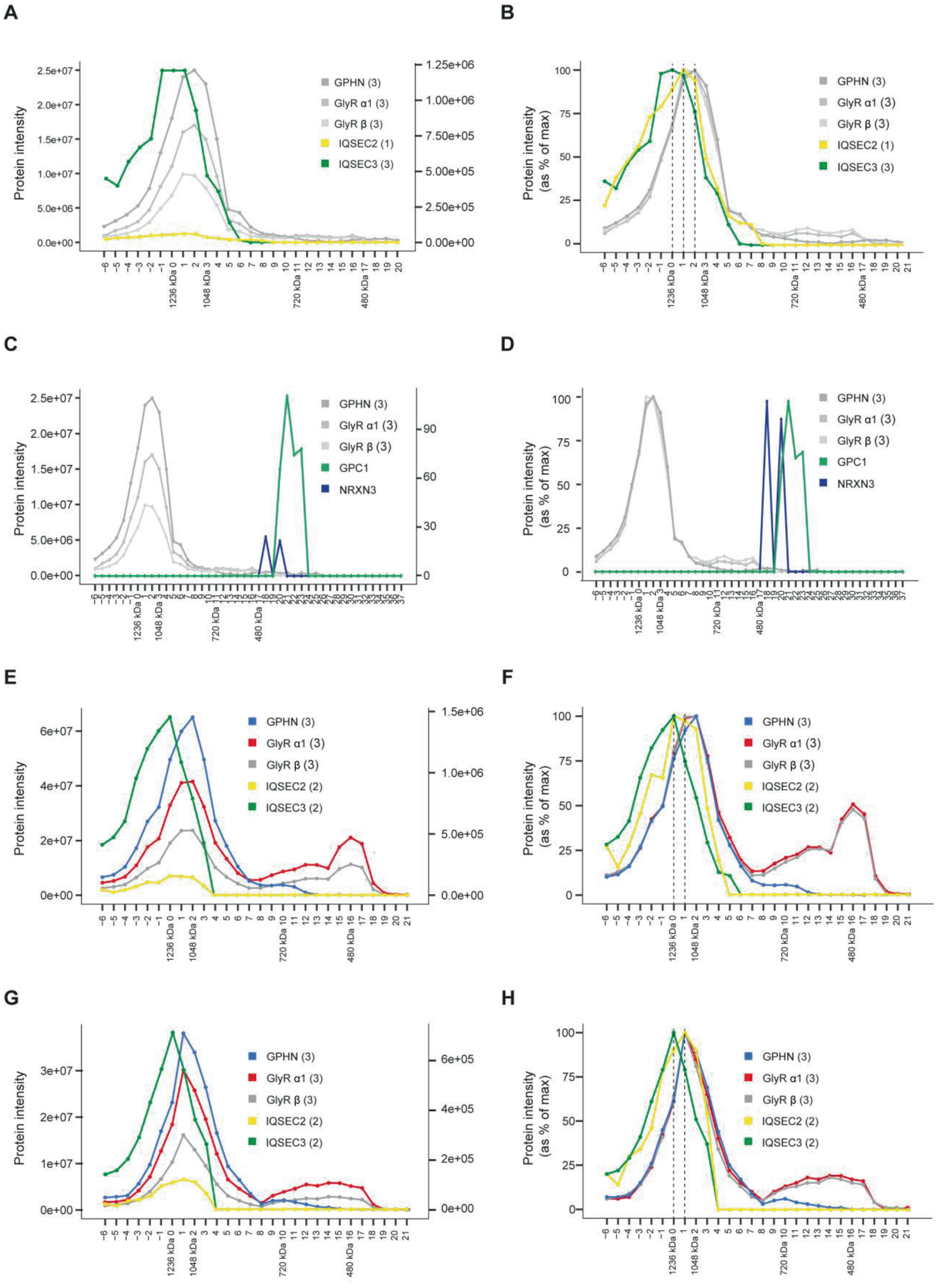
A
Protein intensity
2.5e+07
2.0e+07
1.5e+07
1.0e+07
5.0e+06
0.0e+00
1.25e+06
1.00e+06
7.50e+05
5.00e+05
2.50e+05
0.00e+00
GPHN (3)
GlyR α1 (3)
GlyR β (3)
IQSEC2 (1)
IQSEC3 (3)
1236 kDa
1048 kDa
720 kDa
480 kDa
B
Protein intensity
(as % of max)
100
75
50
25
0
GPHN (3)
GlyR α1 (3)
GlyR β (3)
IQSEC2 (1)
IQSEC3 (3)
C
Protein intensity
GPHN (3)
GlyR α1 (3)
GlyR β (3)
GPC1
NRXN3
90
60
30
0
D
Protein intensity
(as % of max)
GPHN (3)
GlyR α1 (3)
GlyR β (3)
GPC1
NRXN3
E
Protein intensity
6e+07
4e+07
2e+07
0e+00
1.5e+06
1.0e+06
5.0e+05
0.0e+00
GPHN (3)
GlyR α1 (3)
GlyR β (3)
IQSEC2 (2)
IQSEC3 (2)
F
Protein intensity
(as % of max)
GPHN (3)
GlyR α1 (3)
GlyR β (3)
IQSEC2 (2)
IQSEC3 (2)
G
Protein intensity
3e+07
2e+07
1e+07
0e+00
6e+05
4e+05
2e+05
0e+00
GPHN (3)
GlyR α1 (3)
GlyR β (3)
IQSEC2 (2)
IQSEC3 (2)
H
Protein intensity
(as % of max)
GPHN (3)
GlyR α1 (3)
GlyR β (3)
IQSEC2 (2)
IQSEC3 (2)

Figure 3. Analysis of GlyR sub-complexes. (A-D) IP-BN mass spectrometry of GlyR β. (A) IQSEC2 and IQSEC3 migrated at the highest molecular weight range of the GlyR. Both IQSEC2 and IQSEC3 show low intensity values (right scale) compared to the GlyR subunits and GPHN (left scale). (B) Normalization of protein peak intensities to their maximum intensity shows that IQSEC2 and IQSEC3 are both present at a high molecular weight (Pearson correlation of IQSEC3 with the GlyR subunits and GPHN is between 0.54-0.56, and of IQSEC2 0.73-0.76). (C) Additional potential GlyR interactors NRXN3 and GPC1 were detected with low intensities (right scale) compared to the GlyR subunits and GPHN (left scale). (D) Normalized data shows a clear detection of NRXN3 and GPC1on the BN gel outside the range of the major GlyR peak (Pearson correlation between -.15 and -0.1), currently excluding these proteins as true interactors. (E-H) Two anti-GlyR α1 IP-BN mass spectrometry (E-F and G-H for two different antibodies, respectively) recapitulate the results obtained for the anti-GlyR β IP-BN. (E and G) The GlyR subunits and GPHN show high intensities (left scale), and IQSEC2 and IQSEC3 were detected with low intensities (right scale) in the GlyR α1 IP-BN experiment. (F and H) Normalized data reveals a tight co-migration of the GlyR subunits and GPHN (Pearson correlation ≥0.87 for F; ≥ 0.97 for H), a small GlyR population without GPHN in the low molecular weight range and IQSEC2 and IQSEC3 at a high molecular weight (F: Pearson correlation IQSEC3 with the GlyR subunits and GPHN is between 0.40-0.44, and of IQSEC2 between 0.84-0.86. H: IQSEC3 with the GlyR subunits and GPHN is between 0.60-0.65, and of IQSEC2 0.91-0.93).

Immuno-precipitation of a protein using an antibody followed by proteomics analysis is a well-established technique to reveal the individual components of protein complexes[158]. In addition to the quality of the antibody, the ability to filter contaminants is equally critical to the success of the experiment. Often, hundreds of proteins are identified in a single IP, most of them are false positives bound non-specifically to the antibody or beads causing random noise. Furthermore, antibodies may show cross-reactivity, recognizing additional proteins with their specific sites yielding false positives, or target the bait protein at the site of protein-protein interaction giving rise to false negatives. Multiple strategies can be used to reveal false positives, including the use of gene knockout tissue[66,156], peptide-blocking the antibody specific site using the antigen peptide[157], or including multiple antibodies against other non-related target proteins.

In the present study, we used a comparative analysis of four antibodies against GlyR α1, GlyR β and GPHN, and two antibodies against the excitatory AMPAR. Using the criterion of abundance difference, resulting in a high percentage of true positives for the AMPAR, we were able to select potential GlyR-specific protein interactors. Subsequent BN-PAGE MS/MS revealed the interaction of IQSEC 2 and 3 to GlyR forming sub-complexes with higher masses (>1 MDa).

A

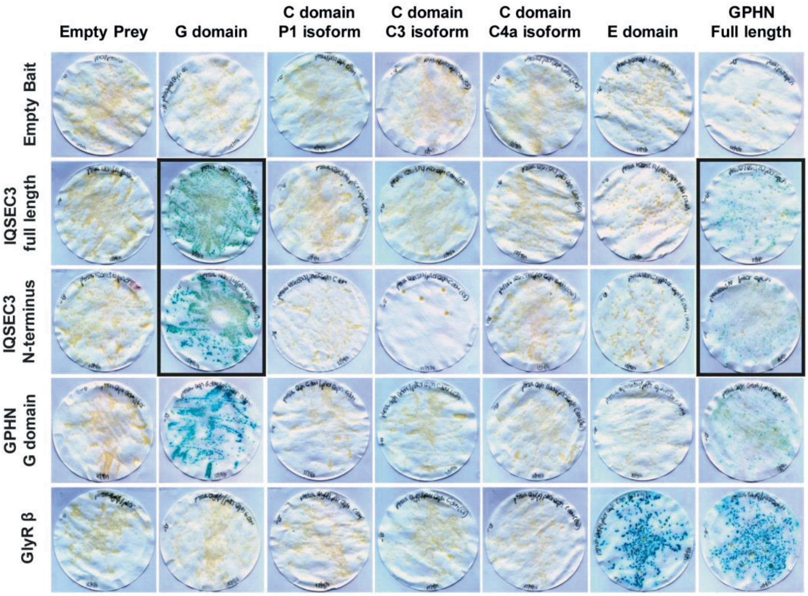

B

MESLLENPVRAVLYLKELTAIVQNQQSLIHTQRERIDELERRLDELSAEN 50

RSLWEHQQLLQAQPPPGLVPPSSAPLPAAPATAPAAAARAQEPLQDQGQR 100

SAAAPHPAPDRPPRQHHGQLLEQPQRGPGSRAHTPQSPHKHLGTQGAVTD 150

GPHN

KEKERPPSC**CAAAGALLQHKSPSALGKGVLSRRPENETVLHQFCCPAADA** 200

CSDLASQSDGSCTQAGGGMEDSVVAAAAVAAGRPSAHAPKAQAQELQEEE 250

ERPGAGAASPRAGPQHKASPGRQQPALATALCPHAPAASDYELSLDLKNK 300

QIEMLEHKYGGHLVS**RRAACTIQTAFRQYQLSKNFE**KIRNSLLESRLPRR 310

IQ like-domain

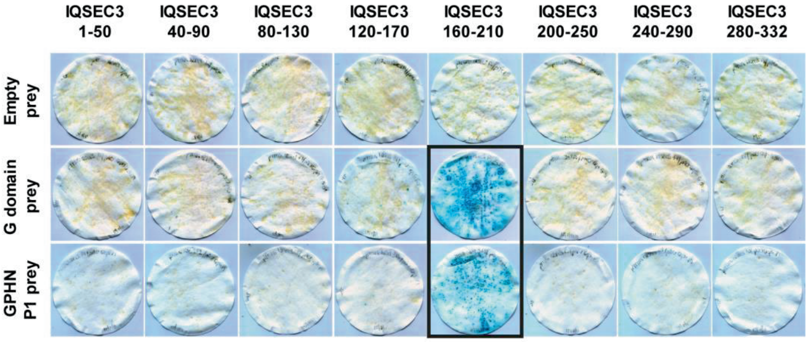

Figure 4. Validation of protein-protein interaction by yeast two-hybrid assay. (A) The GAL4BD-IQSEC3 N-terminal fragment (amino acids 1-649) and full-length IQSEC3 interact with GPHN G domain (amino acids 1-173) and full-length GPHN (1-736), but not the GPHN C domain (173-323) or E domain (323-736). G domain:G domain, and GlyR β subunit:E domain interactions utilised as controls, demonstrating that all GPHN preys were correctly expressed. (B)The amino acid sequence of the rat IQSEC3 N-terminus (1-310) depicting the GPHN binding region and IQ-like domain. (c) Assays for overlapping 50-amino acid IQSEC3 baits with GAL4AD (Empty prey), the GPHN G domain, or full-length GPHN, where only fragment IQSEC3 160-210 mediated a robust interaction with the GPHN G domain and full-length GPHN.

With our IPs we were able to identify both IQSEC3 and IQSEC2 as part of GlyR complexes, and we confirmed that IQSEC3 is an interactor of the GPHN G domain. The observation that IQSEC3 and IQSEC2 exist in the GlyR IPs at lower amount than GlyR-GPHN, suggests that they are found in sub-complexes of the α1β GlyRs. To improve insight into these GlyR sub-complexes, we used a combination of immunoprecipitation and BN for their separation and identification.

Stable constituents of a protein complex should co-migrate in a biochemical separation medium in which the migration pattern of the complex is defined by the overall physico-chemical properties of the protein constituents. Various native separation methods have been used to fractionate intact protein complexes, which include ion-exchange chromatography, sucrose gradient centrifugation, size exclusion chromatography and BN[160]. The commercially available BN gel enables the reproducible separation of protein complexes that span between 200-1400 kDa. We combined IP with BN to size separate and then characterize the distinct protein sub-complexes of the GlyR. The highest intensities were observed for the three core GlyR proteins. The ~3 times higher mean intensity of GPHN compared to GlyR α1 and GlyR β, and the high apparent molecular weight of the GPHN containing complex(es) is in line with the clustering ability and scaffolding function of GPHN. The two terminal domains of GPHN (G and E) can trimerize and dimerize, respectively, and oligomerize into hexagonal scaffolds. These lattices can be stabilized by GlyR binding and are thought to exist in different packing densities[100]. Pearson correlation of IQSEC3 migration pattern to that of GlyR-GPHN is around 0.4-0.6, which is substantially lower than the ~0.9 among GlyR subunits and GPHN. IQSEC3 co-migrated with a subfraction of the GlyR-GPHN complex at the high mass end of 1.2 MDa. The lower intensity of IQSEC3 may indicate the interaction of this protein to the protein lattice containing multiple copies of GlyR-GPHN.

By using a yeast two-hybrid approach, we validated the IQSEC3-GPHN interaction and identified the binding site in a previously uncharacterized region of IQSEC3 (between amino acids 160 and 210), upstream the IQ-like domain. Interestingly, IQSEC3 was found interacting with the G domain of GPHN, whereas GlyR β-subunit bound to the E domain. This suggests that IQSEC3, GPHN and GlyR can coexist within the same protein complex, in agreement with our previous experiments. IQSEC3 may influence the trimerization of GPHN by interacting with the G domain, leading to the regulation of GPHN clustering and inhibitory synapse formation[122].

Previous studies have also revealed the co-localization of IQSEC3 with GPHN, $GABA_A$Rs and GlyRs at inhibitory synapses in mouse retina[161] and biochemical interactions with GPHN[122,123]. Labelling with iBioID using Bira-GPHN demonstrated the presence of IQSEC3 in the vicinity of GPHN within GABAergic synapses[162]. Thus, previous studies have indicated evidence that IQSEC3 may be part of inhibitory $GABA_A$R complexes. In the pHluorin/Myc-tagged $GABA_A$R pulldown experiment that identified 149 putative $GABA_A$R interactors, IQSEC3 ranked in the middle of the protein list in terms of peptide count[163]. However, IQSEC3 was not identified in a recent $GABA_A$R γ2-subunit pull down study[155]. Nonetheless, IQSEC3 is clearly involved in the organisation of GABAergic synapses, in particular the correct alignment of the GABAergic pre- and postsynaptic compartments[123]. Curiously, we also identified IQSEC2, a known constituent of excitatory post-synaptic densities[164], in GlyR α1β complexes. While this may appear unusual, IQSEC2 was also recently shown by others to interact with GPHN in an *in vitro* system[122], and was clearly identified in our GlyR and GPHN IPs. Taken together, our findings suggest that both IQSEC2 and IQSEC3 interact with GPHN and may play roles in inhibitory glycinergic synaptic transmission, extending the role of IQSEC2 beyond excitatory synaptic transmission.

Another two putative interactors, the presynaptic NRXN3 and the extracellular matrix component GPC1, were detected at a lower molecular weight than the GlyR in the IP-BN experiment. This includes the possibility that both NRXN3 and GPC1 are false positive interactors. Alternatively, the affinity of NRXN3 and GPC1 to GlyR might be labile causing their dissociation from the GlyR complex during the long process of antibody elution/protein complex concentrating and the BN gel electrophoresis. Future studies using, for example, a crosslinking agent to stabilize the interaction may be used to validate their interaction.

Finally, previous studies have reported several interactors of the GlyR that were not identified in our IPs[106]. For example, karyopherin 3 and 4 were identified as GlyR interacting partners using Y2H and GST-pulldown with the TM3-4 loop of GlyR α3 and GlyR α1, respectively. However, the authors found only minimal colocalization between the GlyR and karyopherins using subsequent confocal immunocytochemistry and suggested there might be no strong static interaction between the proteins *in vivo.* The recovery of these types of interactors may also benefit from stabilization of the interaction prior to the IP-MS procedures in future studies.

Materials and Methods

Immuno-precipitation / SDS-PAGE fractionation**.** One mouse brainstem was used per IP experiment. Brainstem tissue was homogenized in 1% *n*-dodecyl β-d-maltoside buffer containing 25 mM HEPES, 150 mM NaCl (pH 7.4) and proteinase inhibitor (Roche), and incubated for 1h at 4ºC. After centrifugation at 20,000 x *g*, 10 μg of antibody was added to the supernatant, and incubated overnight at 4ºC. The antibody was captured by 0.1 mL protein A/G plus agarose beads (Santa Cruz). After washing four times with 0.1% Triton-X buffer containing 25 mM HEPES and 150 mM NaCl (pH 7.4), the beads were mixed with SDS sample buffer and heated to 98°C for 5 min. Proteins were separated on a 10% SDS polyacrylamide gel and stained with Coomassie Blue. Each sample lane was cut into three fractions, each fraction was further cut into small gel pieces and transferred to a 96 well plate (0.45 μm filter; MultiScreen-HV 96 well filter-plate from Millipore). The proteins were destained, digested with trypsin overnight at 37°C and dried in a speedvac as described previously[165].

The IPs of GluA2/3 and GluA4 have also been performed on the hippocampal extract, with one mouse hippocampus per IP experiment, as a control for sensitivity of our IP-MS approach.

A commercially available GlyR α1 antibody (A01636-100; labelled as GlyR α1a), and custom-made antibodies against GlyR α1 (NTTNPPPAPSKSPE; labelled as GlyR α1b), GlyR β *(*NGLGKPQAKNKKPP*)*, GPHN *(*PTPKQIRRPDESKG), GluA2/3 (QNFATYKEGYNVYGIESVKI) and GluA4 (RQSSGLAVIASDLP) obtained from Genscript were used for IP-analysis. The IQSEC3 antibody (sc-324895) was obtained from Santa Cruz.

Immuno-precipitation / peptide elution / BN*.* The protein input, antibody, and beads used for IPs followed by peptide elution experiments were scaled up 10 times. To elute protein complexes from the antibody, synthetic peptide (0.5 mg/mL) corresponding to the antibody epitope was dissolved in wash buffer, added to the beads after IP and washing, and incubated for 45 min at room temperature. Protein complex elution was performed twice and the supernatant was pooled. Using a 30 kDa cut-off centrifuge filter (Vivaspin 500 from Sartorius), supernatant was concentrated to about 30 μL as input material for BN, while the synthetic peptide was largely removed. The peptide eluted sample was mixed with 5 μL 8× BN loading buffer, 0.5 μL of molecular weight marker and 1 μL 5% G-250 Coomassie blue and loaded on a pre-cast Invitrogen NativePAGE 4-16% Bis-Tris Gel (ThermoFisher). The gel was run at 4°C, 150 V for 1.5h, followed by 250 V for 1h. The gel was fixed overnight, washed 3× in water, and cut with a grid cutter (The Gel Company) into 48 equal sized pieces. Each piece was transferred individually to a well in a 96-well filter plate (0.45 μm filter; MultiScreen-HV 96 well filter-plate from Millipore) for destaining and trypsin digestion.

Trypsin digestion. The gel pieces in the well of a 96-well filter plate were destained with sequential application and centrifugation removal of 50 mM NH_3HCO_3/50% acetonitrile and 100% acetonitrile with incubation times of 20 min and 5 min, respectively, and NH_3HCO_3/50% acetonitrile incubation overnight. After dehydration in 100% acetonitrile, the gel pieces were incubated with MS grade endo lysC/Trypsin (Promega) at 37 ºC overnight. The resulting peptides were extracted with 0.1% TFA in 50% and 80% acetonitrile, 20 min each, dried in the SpeedVac and subjected to MS analysis.

HPLC-ESI MS/MS and data analysis. The TripleTOF 5600+ MS was coupled to an Ultimate 3000 LC system (Dionex, Thermo Scientific).

For IP-BN samples, the MS was run in nano-mode. Peptides were re-dissolved in 7 μL of 2% acetonitrile with 0.1% formic acid, loaded onto a 5 mm Pepmap 100 C18 column, and then fractionated on a 200 mm Alltima C18 homemade column (100 μm i.d., 3 μm particle size) using 0.1% formic acid with a linear gradient of increasing acetonitrile concentration from 5% to 30% in 35 min, to 40% at 37 min and to 90% for 10 min at a flow rate of 500 nL/min. Peptides were electro-sprayed into the MS using an ion spray voltage of 2500 V, ion source gas at 2 p.s.i., curtain gas at 35 p.s.i and an interface heater temperature of 150°C.

For IP samples, the MS was run in micro-mode. Peptides were fractionated on a 200 mm Alltima C18 column (300 μm i.d., 3 μm particle size) at a flow rate of 5 μl/min, with the same gradient as the nano-mode. The eluted peptides were electro-sprayed with a micro-spray needle voltage of 5500 V.

The MS survey scan range was *m/z* 350–1250 acquired for 250 ms. The top 20 precursor ions were selected for 90 ms per MS/MS acquisition, with a threshold of 90 counts. Dynamic exclusion was 10 s. Rolling CID function was activated, with an energy spread of 5 eV. The MS/MS spectra were searched against the Mouse database (UP000000589_10090) using MaxQuant software[166] (version 1.6.3.4). For IP-BN data, unique high-quality peptides were manually curated in Skyline[167] for further analysis.

IQSEC3 IPs were processed with FASP and analysed using a LTQ-Orbitrap[156] (see supplementary material and methods).

Yeast two-hybrid assays. Yeast two-hybrid assays and *LacZ* freeze fracture assays were carried out as previously described, using the yeast strain Y190 and GAL4 vectors pYTH16 and pACT[168]. GPHN constructs encoded the rat GPHN G domain (amino acids 1-173), C domain (173-323), E domain (323-736) or full-length GPHN (1-736), while those for rat IQSEC3 encoded amino acids 1-649 (N-terminus), 1-1182 (full length) or 50 amino acid overlapping N-terminal fragments (1-50, 40-90, 80-130, 120-170, 160-210, 200-250, 240-290, etc). Control baits for the rat GPHN G domain (1-173) and GlyR β subunit intracellular loop were as previously described[168]. Co-transformed yeast were plated on selective dropout media lacking leucine and tryptophan (Takara) and incubated at 30°C for 3-6 days to allow prototropic colonies to emerge.

Conflict of interest

The authors declare that they have no conflict of interest.

Acknowledgements

We thank Miguel A. Gonzalez-Lozano for critically reading of the manuscript.

Supplementary Figures

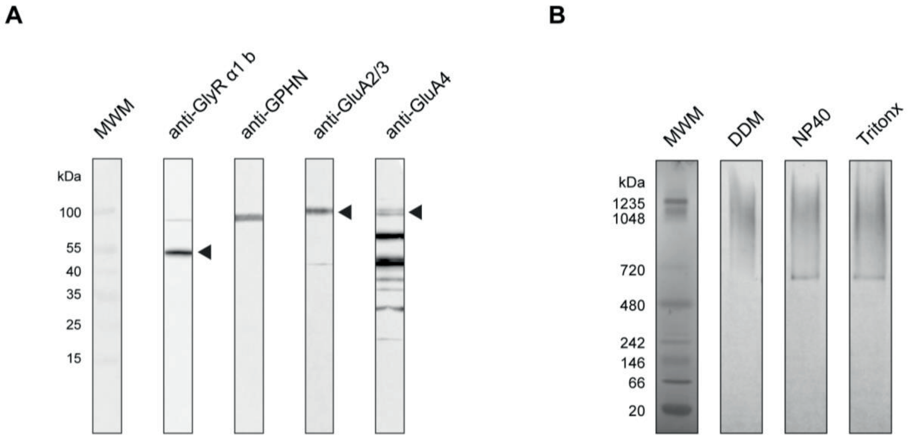

Supplementary figure 1. Antibody and detergent testing. (**A**) Custom made GlyR/GPHN and AMPAR antibodies tested on brainstem homogenate for bait recognition and crossreactivity. Anti-GlyR α1 b, anti-GPHN and anti-GluA2/3 stain proteins with the molecular weight of their respective bait proteins of GlyR α1 around 53kDa, GPHN at 93kDa and GluA2 and 3 at 100kDa. Anti-GluA4 recognizes multiple proteins outside GluA4 at 100 kDa. (**B**) Brain stem protein extracts were run on a BN-gel and immunoblotted for GlyR β. For all three detergents, GlyR β is present around 1-1.2 MDa. In the conditions of NP40 and Triton-X, a second band is observed around 720 kDa. No staining is seen around 56 kDa, the size of single GlyR β subunits.

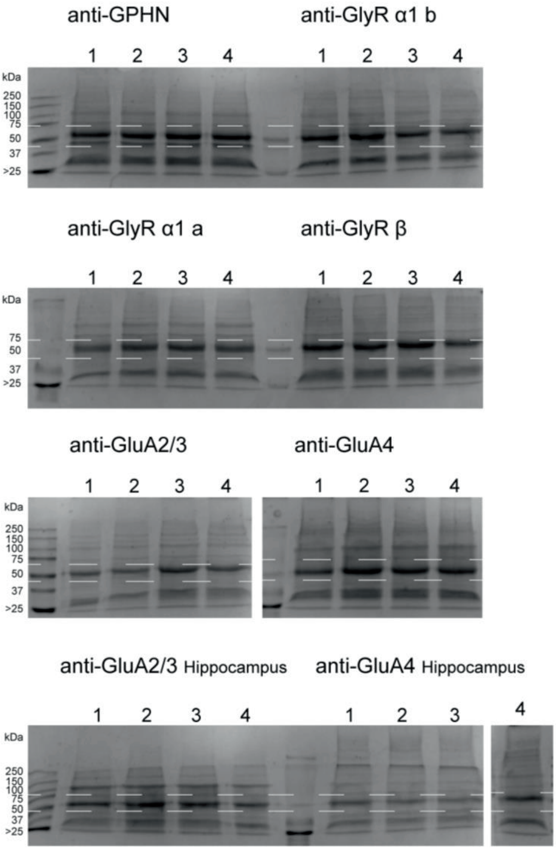

Supplementary figure 2. SDS-PAGE gels of the IP experiments. All GlyR/GPHN and AMPAR IPs performed on brainstem or hippocampus homogenate were run on gel, and fractioned in three sections before trypsin-digestion and LC-MS/MS analysis.

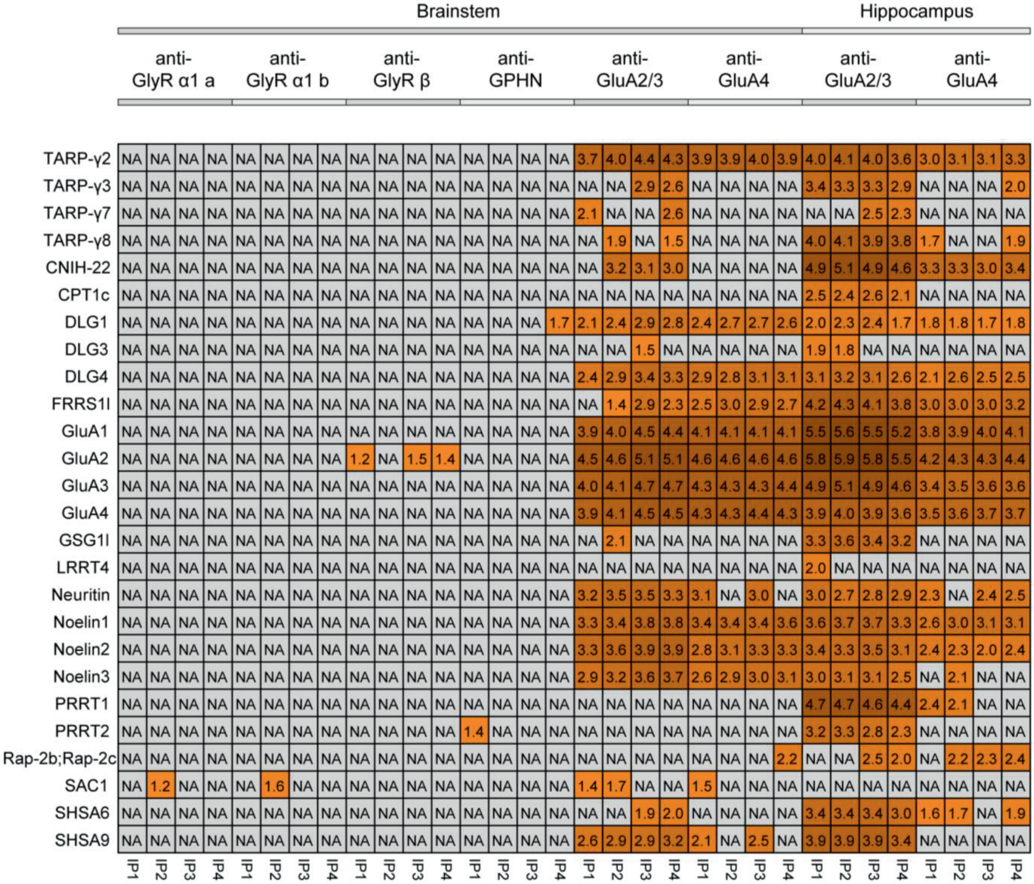

	Brainstem																								Hippocampus							
	anti-GlyR α1 a				anti-GlyR α1 b				anti-GlyR β				anti-GPHN				anti-GluA2/3				anti-GluA4				anti-GluA2/3				anti-GluA4			
	IP1	IP2	IP3	IP4	IP1	IP2	IP3	IP4	IP1	IP2	IP3	IP4	IP1	IP2	IP3	IP4	IP1	IP2	IP3	IP4	IP1	IP2	IP3	IP4	IP1	IP2	IP3	IP4	IP1	IP2	IP3	IP4
TARP-γ2	NA	NA	NA	NA	NA	NA	NA	NA	NA	NA	NA	NA	NA	NA	NA	NA	3.7	4.0	4.4	4.3	3.9	3.9	4.0	3.9	4.0	4.1	4.0	3.6	3.0	3.1	3.1	3.3
TARP-γ3	NA	NA	NA	NA	NA	NA	NA	NA	NA	NA	NA	NA	NA	NA	NA	NA	NA	NA	2.9	2.6	NA	NA	NA	NA	3.4	3.3	3.3	2.9	NA	NA	NA	2.0
TARP-γ7	NA	NA	NA	NA	NA	NA	NA	NA	NA	NA	NA	NA	NA	NA	NA	NA	2.1	NA	NA	2.6	NA	NA	NA	NA	NA	NA	2.5	2.3	NA	NA	NA	NA
TARP-γ8	NA	NA	NA	NA	NA	NA	NA	NA	NA	NA	NA	NA	NA	NA	NA	NA	NA	1.9	NA	1.5	NA	NA	NA	NA	4.0	4.1	3.9	3.8	1.7	NA	NA	1.9
CNIH-22	NA	NA	NA	NA	NA	NA	NA	NA	NA	NA	NA	NA	NA	NA	NA	NA	NA	3.2	3.1	3.0	NA	NA	NA	NA	4.9	5.1	4.9	4.6	3.3	3.3	3.0	3.4
CPT1c	NA	NA	NA	NA	NA	NA	NA	NA	NA	NA	NA	NA	NA	NA	NA	NA	NA	NA	NA	NA	NA	NA	NA	NA	2.5	2.4	2.6	2.1	NA	NA	NA	NA
DLG1	NA	NA	NA	NA	NA	NA	NA	NA	NA	NA	NA	NA	NA	NA	NA	1.7	2.1	2.4	2.9	2.8	2.4	2.7	2.7	2.6	2.0	2.3	2.4	1.7	1.8	1.8	1.7	1.8
DLG3	NA	NA	NA	NA	NA	NA	NA	NA	NA	NA	NA	NA	NA	NA	NA	NA	NA	NA	1.5	NA	NA	NA	NA	NA	1.9	1.8	NA	NA	NA	NA	NA	NA
DLG4	NA	NA	NA	NA	NA	NA	NA	NA	NA	NA	NA	NA	NA	NA	NA	NA	2.4	2.9	3.4	3.3	2.9	2.8	3.1	3.1	3.1	3.2	3.1	2.6	2.1	2.6	2.5	2.5
FRRS1l	NA	NA	NA	NA	NA	NA	NA	NA	NA	NA	NA	NA	NA	NA	NA	NA	NA	1.4	2.9	2.3	2.5	3.0	2.9	2.7	4.2	4.3	4.1	3.8	3.0	3.0	3.0	3.2
GluA1	NA	NA	NA	NA	NA	NA	NA	NA	NA	NA	NA	NA	NA	NA	NA	NA	3.9	4.0	4.5	4.4	4.1	4.1	4.1	4.1	5.5	5.6	5.5	5.2	3.8	3.9	4.0	4.1
GluA2	NA	NA	NA	NA	NA	NA	NA	NA	1.2	NA	1.5	1.4	NA	NA	NA	NA	4.5	4.6	5.1	5.1	4.6	4.6	4.6	4.6	5.8	5.9	5.8	5.5	4.2	4.3	4.3	4.4
GluA3	NA	NA	NA	NA	NA	NA	NA	NA	NA	NA	NA	NA	NA	NA	NA	NA	4.0	4.1	4.7	4.7	4.3	4.3	4.3	4.4	4.9	5.1	4.9	4.6	3.4	3.5	3.6	3.6
GluA4	NA	NA	NA	NA	NA	NA	NA	NA	NA	NA	NA	NA	NA	NA	NA	NA	3.9	4.1	4.5	4.5	4.3	4.3	4.4	4.3	3.9	4.0	3.9	3.6	3.5	3.6	3.7	3.7
GSG1l	NA	NA	NA	NA	NA	NA	NA	NA	NA	NA	NA	NA	NA	NA	NA	NA	NA	2.1	NA	NA	NA	NA	NA	NA	3.3	3.6	3.4	3.2	NA	NA	NA	NA
LRRT4	NA	NA	NA	NA	NA	NA	NA	NA	NA	NA	NA	NA	NA	NA	NA	NA	NA	NA	NA	NA	NA	NA	NA	NA	2.0	NA	NA	NA	NA	NA	NA	NA
Neuritin	NA	NA	NA	NA	NA	NA	NA	NA	NA	NA	NA	NA	NA	NA	NA	NA	3.2	3.5	3.5	3.3	3.1	NA	3.0	NA	3.0	2.7	2.8	2.9	2.3	NA	2.4	2.5
Noelin1	NA	NA	NA	NA	NA	NA	NA	NA	NA	NA	NA	NA	NA	NA	NA	NA	3.3	3.4	3.8	3.8	3.4	3.4	3.4	3.6	3.6	3.7	3.7	3.3	2.6	3.0	3.1	3.1
Noelin2	NA	NA	NA	NA	NA	NA	NA	NA	NA	NA	NA	NA	NA	NA	NA	NA	3.3	3.6	3.9	3.9	2.8	3.1	3.3	3.3	3.4	3.3	3.5	3.1	2.4	2.3	2.0	2.4
Noelin3	NA	NA	NA	NA	NA	NA	NA	NA	NA	NA	NA	NA	NA	NA	NA	NA	2.9	3.2	3.6	3.7	2.6	2.9	3.0	3.1	3.0	3.1	3.1	2.5	NA	2.1	NA	NA
PRRT1	NA	NA	NA	NA	NA	NA	NA	NA	NA	NA	NA	NA	NA	NA	NA	NA	NA	NA	NA	NA	NA	NA	NA	NA	4.7	4.7	4.6	4.4	2.4	2.1	NA	NA
PRRT2	NA	NA	NA	NA	NA	NA	NA	NA	NA	NA	NA	NA	1.4	NA	NA	NA	NA	NA	NA	NA	NA	NA	NA	NA	3.2	3.3	2.8	2.3	NA	NA	NA	NA
Rap-2b;Rap-2c	NA	NA	NA	NA	NA	NA	NA	NA	NA	NA	NA	NA	NA	NA	NA	NA	NA	NA	NA	NA	NA	NA	NA	2.2	NA	NA	2.5	2.0	NA	2.2	2.3	2.4
SAC1	NA	1.2	NA	NA	NA	1.6	NA	NA	NA	NA	NA	NA	NA	NA	NA	NA	1.4	1.7	NA	NA	1.5	NA	NA	NA	NA	NA	NA	NA	NA	NA	NA	NA
SHSA6	NA	NA	NA	NA	NA	NA	NA	NA	NA	NA	NA	NA	NA	NA	NA	NA	NA	NA	1.9	2.0	NA	NA	NA	NA	3.4	3.4	3.4	3.0	1.6	1.7	NA	1.9
SHSA9	NA	NA	NA	NA	NA	NA	NA	NA	NA	NA	NA	NA	NA	NA	NA	NA	2.6	2.9	2.9	3.2	2.1	NA	2.5	NA	3.9	3.9	3.9	3.4	NA	NA	NA	NA

Supplementary figure 3. IP-MS detection of known AMPAR interactors. A high recovery of known AMPAR interactors is observed in GluA2-4 IPs performed on both hippocampus and brainstem, serving as a control for sensitivity of the IP-MS approach used. Only GluA2, SAC1 and PRRT2 were observed in GlyR/GPHN IPs, sporadically and with low iBAQ values. iBAQ intensities are shown as a log10 value.

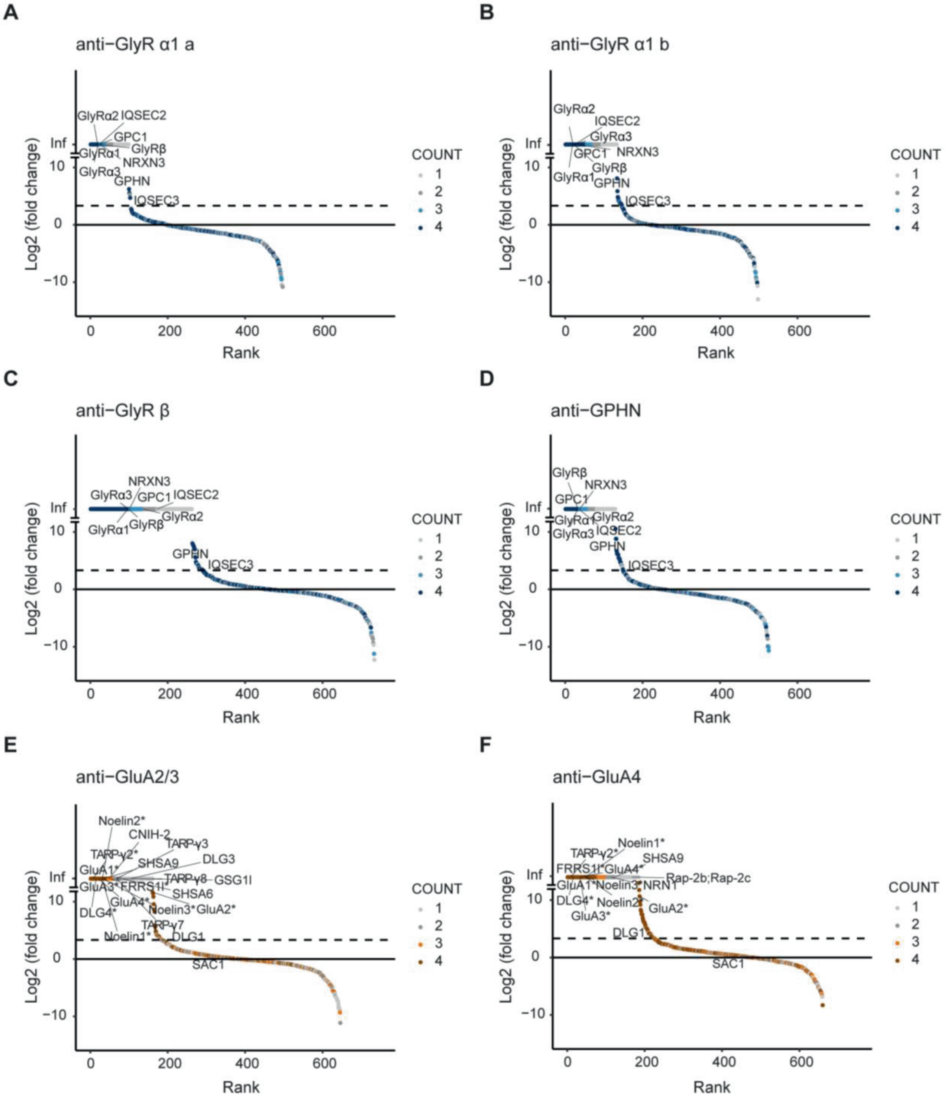

Supplementary figure 4. Overview of IP-MS analysis shown per antibody. (A-D) Proteins are ranked on log2 fold change, as the mean iBAQ intensity observed/ the mean iBAQ intensity of all brainstem GluA2-4 IPs taken together for (A) anti-GlyR α1a (B) anti-GlyR α1b (C) ant-GlyR β and (D) anti-GPHN. Proteins that meet the criteria of being enriched ≥10 fold in >75% of all GlyR/GPHN IPs are labeled in each plot. (E-F) Proteins are ranked on log2 fold change, as the mean iBAQ intensity observed/the mean iBAQ intensity of all GlyR/GPHN IPs taken together for (E) anti-GluA2/3 and (F) anti-GluA4. All known AMPAR interactors are labeled in each plot. The number of times a protein is observed with an antibody is shown as count.

Supplementary data

Supplementray Table 1. All raw IP data associated with Figure 1A
(PMID: 31984645; DOI:10.1002/pmic.201900403).

Supplementary Table 2. The raw data from IQSEC3 IPs
(PMID: 31984645; DOI:10.1002/pmic.201900403)

Supplementary Material and Methods

Protein extraction/ immunoblot analysis. Brainstem tissue was first homogenized in buffer containing 5mM HEPES/NaOH (pH 7.4), 0.32M sucrose and proteinase inhibitor (Roche), and protein concentration was determined using a Bradford protein assay (Biorad).

For antibody testing, samples were mixed with SDS-loading buffer, boiled at 98 ºC for 5 min. and run on a 10% home-made polyacrylamide gel. Next, proteins were transferred to a PVDF membrane (Biorad) at at 4°C, 40V, blocked in 5% non-fat milk for 1 h at room temperature, and incubated with primary antibody overnight at 4ºC in 3% non-fat milk. After 1h incubation with HRP-conjugated secondary antibody at room temperature, the proteins were visualized with ECL substrate (Pierce), using the Odyssey FC Western Blot Detection System (LI-COR).

For testing detergents on GlyR protein complex integrity, sample was diluted with extraction buffer (1:1) to an end concentration of 1% DDM, NP-40 or Triton X-100, 25 mM HEPES and 150 mM NaCl (pH 7.4). After 1h incubation at 4ºC, the samples were centrifuged at 20,000 x *g* for 20 min. Around 50ug of supernatant per condition was mixed with 5 µL 8× BN loading buffer and 1 µL 5% G-250 Coomassie blue and loaded on a pre-cast Invitrogen NativePAGE 4-16% Bis-Tris Gel (ThermoFisher). The gel was run at 4°C, 150 V for 45 min using the dark blue cathode buffer, followed by 150 V for 45 min and 250 V for 20 min using the light blue cathode buffer. Next, the gel was incubated in transfer buffer for 15 min, and transferred to a PVDF membrane (Bio-Rad) overnight at 4°C, 40V. The PVDF membrane was subsequently destained in 100% MeOH for 10 sec. while shaking, and immuno-stained as described above, using anti-GlyR β.

Immunoprecipitation and HPLC-ESI MS/MS of IQSEC3. IP-MS analysis of IQSEC3 followed the IP protocol described in the main text. After the IP, the beads were incubated with 2% SDS, and the proteins subjected to a filter-aided sample preparation, as described previously[156]. The samples were analysed using a LTQ-Orbitrap Discovery. Peptides were re-dissolved in 10 µL 0.1% acetic acid, and trapped on a 5 mm Pepmap 100 C18 (Dionex) trapping column (300 µm ID, 5 µm particle size). Peptides were fractionated on a 200 mm Alltima C18 homemade column (75 µm ID, 3 µm particle size), starting with 5% acetonitrile and 0.5% acetic acid). Acetonitrile concentration was increased linearly from 5% to 32% in 80 min, and to 72% in 10 min, at a flow rate of 400 nL/min. Peptides were electrosprayed into the mass spectrometer in a data dependent manner with one MS survey scan ranging from m/z 350-2000. The MS scan followed by MS/MS on the five most abundant ions, with an exclusion window of 20 sec.

Chapter 3: Protein complexes of Gephyrin-C3 and -C4A isoforms: an analysis by interaction proteomics

Sophie J.F. van der Spek, Nila van Overbeek, Miao Chen, Iryna Paliukhovich,
August B. Smit and Ka Wan Li

Abstract

Gephyrin is the major scaffolding protein of the inhibitory synapse. At the post-synaptic membrane, Gephyrin dynamically clusters the Glycine receptor (GlyR) and GABA$_A$-receptor (GABA$_A$R), and is therefore a crucial regulator of inhibitory neurotransmission. Interestingly, several Gephyrin isoforms can be generated through alternative splicing. Previous in vitro studies revealed isoform differences in folding, aggregation and binding affinities to the GlyR. However, characterization of the major Gephyrin isoforms in the mammalian brain is lacking. In the current study we created Gephyrin-C3 and -C4A isoform specific antibodies that were used for a first characterization of these isoforms in mice. We revealed Gephyrin-C3 and -C4A protein expression in the brain and cell types expressing these isoforms, and their differential interacting partners. Whereas Gephyrin-C4A binds the GlyR, IQ motif and Sec7 domain 3 (IQSEC3) and Nitric oxide synthase 1 (NOS1) and is expressed in neurons, Gephyrin-C3 reveals highest expression in astrocytes and specifically binds to the GlyR and Neuroligin-2 (NLGN2). This first dissection of Gephyrin isoform assemblies provides a framework for future molecular and functional studies.

Introduction

Gephyrin is the most abundant scaffold protein of the inhibitory synapse and core component of the inhibitory synaptic scaffold[169]. This scaffolding protein contains three structural domains, an N-terminal G-domain, a C-terminal E-domain, and a linker C-domain in between. This protein can trimerize and dimerize through its G- and E-domains, respectively, which has led to a model where Gephyrin forms a hexagonal lattice onto which the Glycine receptor (GlyR) and $GABA_A$ receptor ($GABA_AR$) are anchored[111,170,171]. Dynamic alterations in Gephyrin aggregation and receptor clustering at the inhibitory post-synaptic membrane allows for fast adaptations of synaptic strength[118–120]. In addition, Gephyrin catalyzes Molybdenum Cofactor (MoCo) synthesis like its G- and E-domain homolog proteins in bacteria[172], and reveals high expression in the liver[129]. In the brain Gephyrin produces MoCo in glia cells specifically[129].

Gephyrin interacts with a variety of proteins including cytoskeletal, vesicle-associated, signaling and adhesion proteins, that mediate transport and clustering of GlyRs and $GABA_ARs$[109]. For instance, Gephyrin binds the adhesion molecule Neuroligin-2 (NLGN2), which is important for synapse formation, and drives the formation of Gephyrin-$GABA_A$-R clusters at the synaptic scaffold[121]. A more recent identified Gephyrin interactor is IQ motif and Sec7 domain 3 (IQSEC3), a brefeldin A-resistant ARF guanine nucleotide exchange factor (GEF)[122]. This protein is involved in the maintenance of Gephyrin cluster size and the correct apposition of $GABA_{A-}$R containing post-synapses with presynaptic terminals during synapse development[123]. Gephyrin binding to dynein light chain 1 and 2 (DYL1 and DYL2) has been associated with intracellular trafficking of GlyRs[120,125].

Several Gephyrin isoforms are generated through alternative splicing, which contain a canonical backbone and presence of additional exons, or cassettes[126,130]. The main isoforms previously studied contain a C3, C4A-D or G2 (sometimes called C5 or C5'[130]) cassette and show biochemical differences in their affinity to the GlyR[127,128], folding[128] and aggregation[127,129]. For instance, heterologous overexpressed Gephyrin containing the C3 cassette (Gephyrin-C3) or C4C cassette both form hexagonal oligomers of ~600 kDa[128], whereas an additional high-oligomeric form of ~900 kDa is exclusively formed by Gephyrin containingthe C4C cassette[128]. The C-linker domain was proposed to control domain movement required for Gephyrin oligomerization, and is altered by insertion of the different cassettes[128]. In addition, insertion of a G2 cassette prevents GlyR binding[127], and insertion of C3 lowers the GlyR binding affinity [128]. C3 cassette insertion in the C-domain reduces stability of the E-domain[128], which contains the binding site for the β-subunit of the GlyR[111,173] likely causing this reduction in affinity[174]. Alternatively spliced cassettes influence important Gephyrin properties, which may affect additional interactions beyond the GlyR.

The C3 and C4A cassette are consistently identified cassettes in previous reports on rodent and human brain tissue [130], which were therefore chosen as target for the current study. Here we created antibodies against the C3 and -C4A cassette sequences and revealed their expression in the brain, the cell types expressing the Gephyrin-C3 and -C4A isoforms and their differential interacting partners in mouse cortex and brainstem. Gephyrin-C4A revealed neuronal expression, and binding to the GlyR, IQSEC3 and NOS1. In contrast, Gephyrin-C3 revealed highest expression in astrocytes, and specific binding to the GlyR and NLGN2. Together these data provides a first description of the differential Gephyrin isoform assemblies, a framework supporting future molecular and functional studies.

Results

As no antibodies are available that are specific for Gephyrin splice isoforms, we designed and custom-made antibodies against the specific sequences of Gephyrin-C3 (anti-C3) and Gephyrin-C4A (anti-C4A) splice cassettes, and a sequence that overlaps with C4A and the shared backbone of Gephyrin (anti-C4A+) (Figure 1a). We tested the antibodies on specificity for the Gephyrin isoforms, by overexpressing Gephyrin isoforms in HEK cells, separately, followed by their immuno-purification (IP) (Figure 1b). Because Gephyrin is endogenously expressed by HEK cells, we made use of Flag-tagged Gephyrin isoform-specific expression constructs. Gephyrin-C3 and -C4A revealed equal levels of overexpression, however, IP using anti-C3 exclusively purified Gephyrin-C3 (Figure 1b). Likewise, anti-C4A only isolated Gephyrin-C4A, demonstrating these antibodies specifically recognize their target isoform (Figure 1b). Not surprisingly, anti-C4A+ purified both Gephyrin-C3 and -C4A, albeit with a large preference towards C4A (Figure 1b).

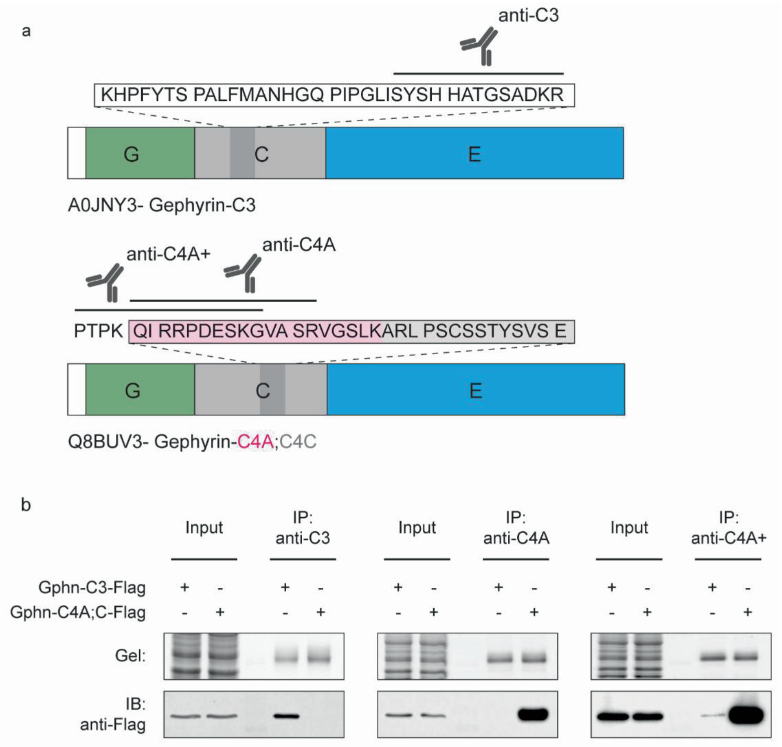

Figure 1. Specificity of Gephyrin-C3 and -C4A isoform antibodies. (**a**) Antibodies against Gephyrin-C3 and -C4A were raised against isoform specific sequences. An additional antibody was raised against a sequence overlapping with the canonical backbone of Gephyrin and Gephyrin-C4A. (**b**) Gephyrin isoform specificity tested by immuno-purification of overexpressed Gephyrin-C3 and -C4A;4C in HEK cells. IP: immuno-purification; IB: immunoblot.

Next, these antibodies were used to determine the relative expression levels of Gephyrin isoforms in different brain areas, and their enrichment in a membrane enriched fraction (Figure 2). Gephyrin-C3 revealed highest expression in cortex and brainstem, followed by hippocampus and cerebellum (Figure 2). Enrichment in the membrane enriched fraction was observed in brainstem only (Figure 2). Similar expression was observed for Gephyrin-C4A (Figure 2). This suggest that the majority of Gephyrin-C3 and -C4A in brainstem has a membrane, potentially synaptic, localization, whereas in other brain regions the synaptic localization may be limited. Cortex and brainstem were used for further experiments.

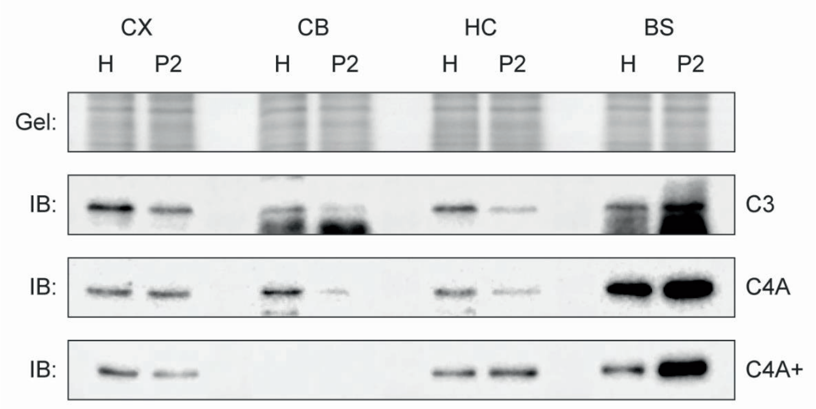

Figure 2. Gephyrin isoform expression in different brain areas. Immunoblots of Gephyrin isoforms using the isoforms specific and canonical antibodies. H: homogenate; P2: crude membrane fraction; CX: Cortex; CB: Cerebellum; HC: Hippocampus; BS: Brainstem; IB: immunoblot.

A previous report revealed Gephyrin-C3 transcripts in glial cells and Gephyrin-C4A in neurons[129]. In the current study, we detected the Gephyrin isoforms in cortical neurons and astrocytes by immunoblotting with our antibodies (Figure 3a). Gephyrin-C3 revealed expression in cultures of both cell types, albeit with a 3.8-fold increased expression level in astrocytes (Figure 3a). In contrast, Gephyrin-C4A revealed exclusive expression in neurons (Figure 3a). In line with these observations, immunohistochemistry of Gephyrin-C3 in mouse cortex revealed staining of cells reminiscent of astrocytes stained for glial fibrillary acidic protein (GFAP)[175] in deeper layers of the cortex and corpus callosum (Figure 3b). Gephyrin-C3 stained cells that lack colocalization with the neuronal nuclear marker (NeuN) (Figure 3d). In addition, staining of Gephyrin-C3 revealed puncta, with limited apposition towards vesicular GABA transporter (vGat) positive synapses (Figure 3d). In contrast, anti-C4A revealed a homogenous distribution throughout the cortex (Figure 3c) and a punctate staining (Figure 3e) matching a neuronal dendrite and synapse expression. Together these data reveals Gephyrin-C3 expression in astrocytes, and possible expression in neurons, whereas Gephyrin-C4A expression is limited to neurons. Minor presence of astrocytes in neuronal cultures and antibody cross-reactivity towards proteins other than Gephyrin (e.g. GFAP) in immunolabeling of slices cannot be excluded.

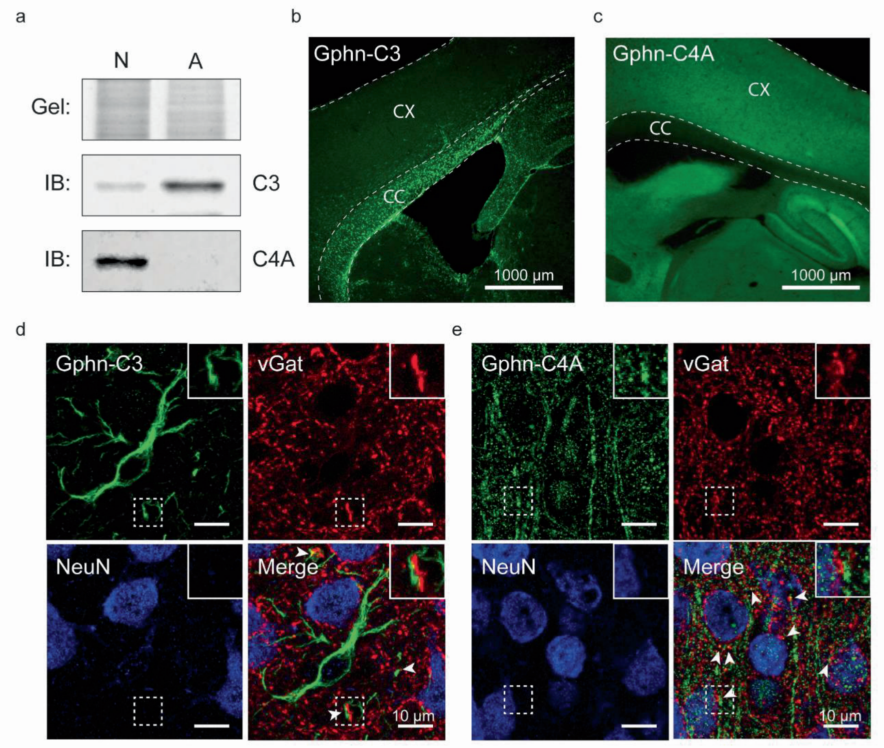

Figure 3. Differential expression of Gephyrin-C3 and -C4A in neurons and astrocytes. (**a**) Expression of Gephyrin-C3 and -C4A in cultured neurons and astrocytes. (**b**) Gephyrin-C3 and (**c**) Gephyrin-C4A distribution in cortex and corpus callosum revealed in sagittal sections of the mouse brain. (**d**) Higher magnification images of cortical Gephyrin-C3, and (**e**) Gephyrin-C4A, stained together with the inhibitory presynaptic marker vGat and neuronal nuclear marker NeuN. Scale bar 10 µm. Arrowheads point out Gephyrin-C3 or C4A puncta opposing the presynaptic marker vGat. Inset shows zoom in of the marked area (dotted square). N: Neurons; A: Astrocytes; IB: immunoblot; CX: Cortex; CC: Corpus Callosum.

To characterize differential associations of the two Gephyrin isoforms with known Gephyrin interactors (taken from Tyagarajan *et. al.* 2014[109] and Um *et. al.* 2016[122]) we performed IPs on cortex and brainstem homogenate with our isoform specific antibodies followed by mass spectrometry analysis (IP-MS) (Figure 4). To exclude non-specifically bound proteins from the analysis, we used antibodies raised against the α-amino-3-hydroxy-5-methyl-4-isoxazolepropionic acid receptor (AMPAR) subunits GluA1 and GluA3 as negative control (Supplemental Table 1 and 2). Gephyrin was purified with highest abundance in all IPs (Figure 4). In brainstem, anti-C4A and -C4A+ revealed clear copurification of the Glycine receptor alpha 1 (GlyR α1) and Glycine receptor beta (GlyR β) subunits of the GlyR (Figure 4a). Anti-

C3 copurified both proteins with a ≥ 8-fold lower abundance, in agreement with a lower affinity of the Gephyrin-C3 for the GlyR (Figure 4a). Of interest, peptides that could originate from both NLGN2 or NLGN1 (NLGN2;1) and peptides from NLGN3 were isolated by anti-C3 exclusively, whereas IQSEC3, Nitric oxide synthase 1 (NOS1) and Protein phosphatase 1 catalytic subunit alpha (PP1A) were copurified by anti-C4A and/or anti-C4A+ (Figure 4a).

In cortex, GlyR β, the direct binding partner of Gephyrin, was retained in IP-MS using anti-C4A and anti-C4A+ only (Figure 4b). Relative to Gephyrin, GlyR β was co-purified with lower abundance than observed in brainstem (Figure 4a,b). The lower abundance values of GlyR β in cortex IP-MS, and the absence of GlyR α1, are in agreement with a reduced expression of the GlyR in this brain area as documented at the transcript level in the Allen Brain Atlas. Also in cortex, only anti-C3 co-isolated NLGN2;1 and 3, whereas IQSEC3 and NOS1 were copurified by anti-C4A and/or anti-C4A+ (Figure 4b).

PP1A was detected using anti-C4A (Figure 4b). Anti-C3 and anti-C4A+ also isolated PP1A (Figure 4b), however, with similar abundance values as observed in the negative controls (Supplemental Table 2). In addition, Heat shock cognate 71 kDa protein (HSP7C) was detected in Gephyrin IPs at similar levels as the negative controls in both brain regions (Supplemental Table 1 and 2). SLIT-ROBO Rho GTPase Activating Protein 3 (SRGAP3) and DYL2 were only detected in cortex, also at similar levels as the negative controls (Supplemental Table 2). As only part or none of the HSPC7, SRGAP3 and DYL2 signal may come from association with Gephyrin, IP-MS data on these proteins was not further interpreted (Figure 4). Together these data revealed consistent association between Neuroligins and Gephyrin-C3, and subunits of the GlyR, IQSEC3, NOS1 and PP1A with Gephyrin-C4A, in both cortex and brainstem.

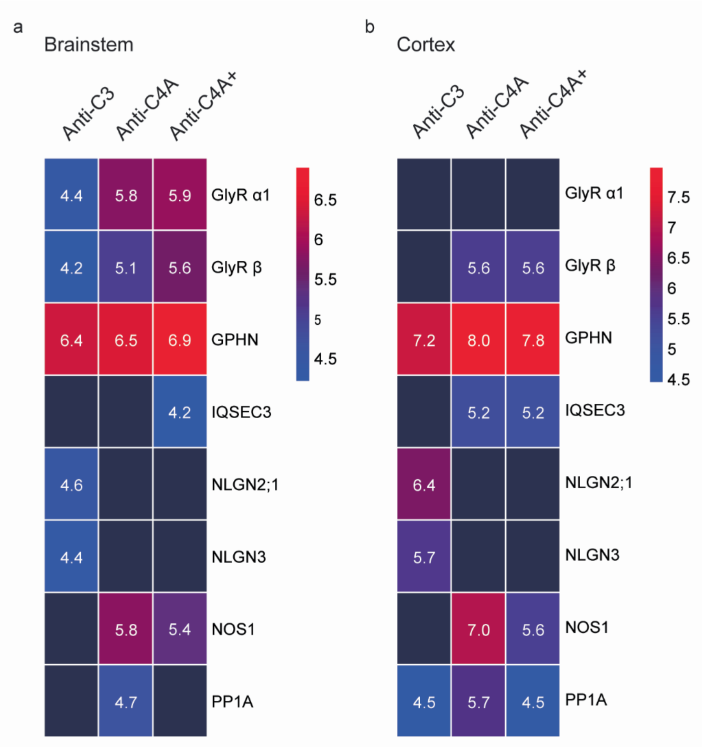

Figure 4. Characterization of Gephyrin-C3 and -C4A interactions and sub-complexes. (**a**) IP-MS of Gephyrin-C3 and -C4A in brainstem and (**b**) cortex. Protein abundances of Gephyrin and known interactors are shown as mean $\log_{10}$ iBAQ intensity values, and color coded from high abundance (red) to low abundance (blue).

We then continued to reveal potential Gephyrin sub-complexes by IP/blue-native-PAGE/mass spectrometry (IP-BN-MS), as previously described[176]. Native Gephyrin complexes were isolated by IP followed by elution using an epitope mimicking peptide, and subsequently size separated on a Blue Native Polyacrylamide Gel Electrophoresis (BN-PAGE) gel. The blue native gel was cut into 50 slices, and each slice was subjected to trypsin digestion and analyzed by MS individually. Proteins that form part of the same complex are expected to co-migrate to the same location on the gel.

All IP-BN-PAGE/MS experiments revealed similar abundance values of Gephyrin across the gel, and a two-to-300-fold lower abundance for the known interactors (Supplemental Figure 1-4). For further analysis we normalized protein abundances to their maximal intensity detected across the gel (Figures 5-8). In brainstem, Gephyrin-C4A(+) revealed migration across a wide range of molecular weights, and highest abundance at ~720 kDa and ~1 MDa, whereas Gephyrin-C3 revealed one abundance peak at ~720 kDa, consistent with previous observations (Figure 5a)[128]. In addition, low level of Gephyrin was observed just below the 480 kDa marker (peak abundance at slices 18-20) in all experiments (Figure 5a).

In agreement with IP-MS, GlyR α1 and GlyR β were identified with anti-C4A(+) with high abundances compared to anti-C3 (Supplemental Figure 1b). These two GlyR subunits co-migrated at ~1 MDa (Figure 5b). IQSEC3 was exclusively detected when Gephyrin-C4A was purified, and revealed co-migration with Gephyrin and GlyR subunits, at the highest molecular weight range of ~1.2 MDa (Figure 5b), as observed in previous GlyR IP-BN-PAGE/MS experiments[176]. Also, NOS1 was detected specifically in experiments containing Gephyrin-C4A, and revealed highest abundance between the 720 and 480 kDa markers (Figure 5c). NLGN2 was detected exclusively with anti-C3 and co-migrated with Gephyrin-C3 towards the lower molecular weight complex of ~720 kDa (Figure 5c).

In IP-MS additional known Gephyrin interactor HSP70C was detected with similar abundances as the negative controls (Supplemental Table 1). In IP-BN, HSP7C revealed relative high abundances migrating separate from Gephyrin-C3 and -C4A in all three IP-BN experiments, likely resulting from non-specific binding (Figure 6b, Supplemental Figure 2b). Of interest, HSP7C revealed a second co-migration peak with both Gephyrin isoforms at ~1.2 MDa (Figure 6b).

In cortex, peak abundance of Gephyrin at ~1 MDa was strongly reduced in all IP-BN-PAGE/MS experiments (Figure 7a). Both Gephyrin isoforms revealed highest abundance towards the 720 kDa marker and low abundance just below 480 kDa (Figure 7a). Reduced abundance of GlyR β was observed in Gephyrin-C4A and -C4A+ IP-BN-PAGE/MS (Supplemental Figure 3b), and revealed the same migration profile as observed in brainstem (Figure 7b). IQSEC3 and NOS1 were detected with Gephyrin-C4A exclusively (Figure 7b-c), while NLGN2 was detected with Gephyrin-C3 (Figure 7c). These proteins revealed similar migration profiles as observed in brainstem (Figure 7b-c), albeit with lower abundances and more sporadic detection (Supplemental Figure 3).

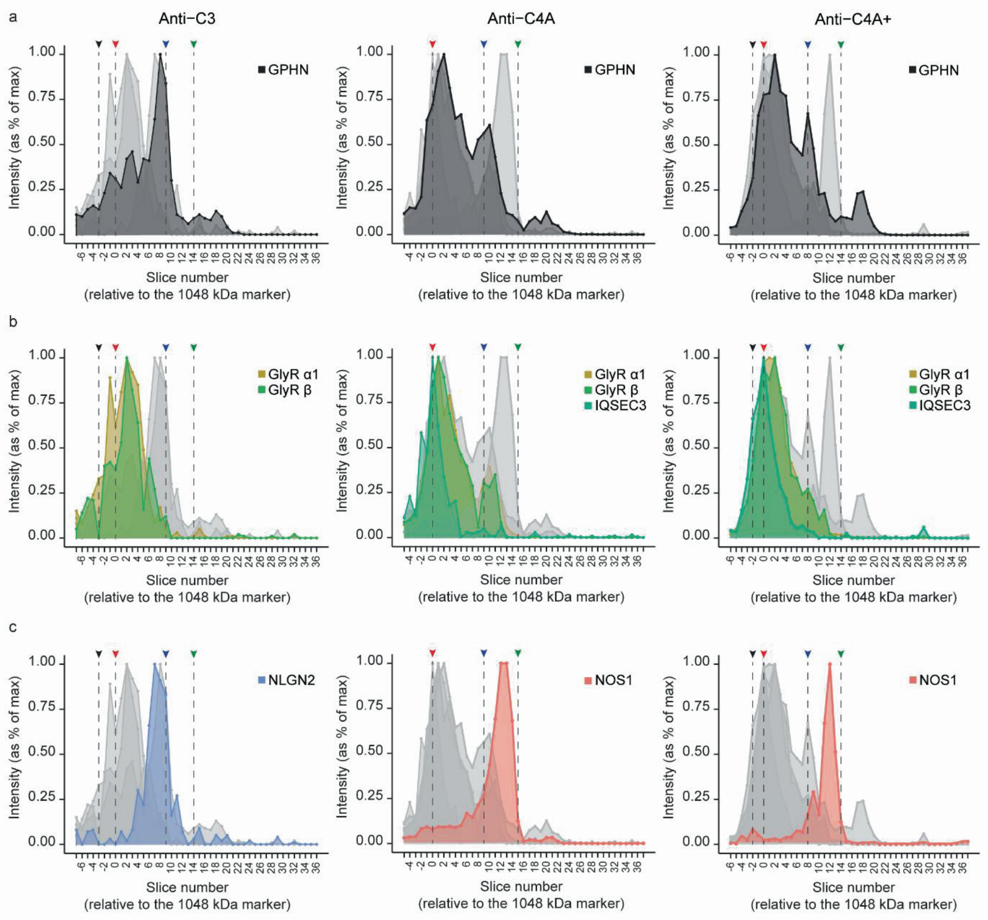

Figure 5. Subcomplex analysis of Gephyrin-C3 and -C4A in brainstem by IP-BN-PAGE/MS. (**a**) Migration profile of Gephyrin-C3 and -C4A native protein complexes in brainstem on a blue native gel. (**b**) Subset of Gephyrin interactors that revealed co-migration with the high molecular weight complex of Gephyrin-C3 and -C4A. (**c**) Gephyrin interactors that co-migrated with the low molecular weight complex of Gephyrin-C3 and -C4A. Protein abundances were normalized to the maximum intensity across the gel. On the x-axis slice numbers are shown, relative to the 1048 kDa spiked-in marker protein. Arrowheads point to the location of molecular weight markers on the gel: 1236 (black), 1048 (red), 720 (blue) and 480 (green).

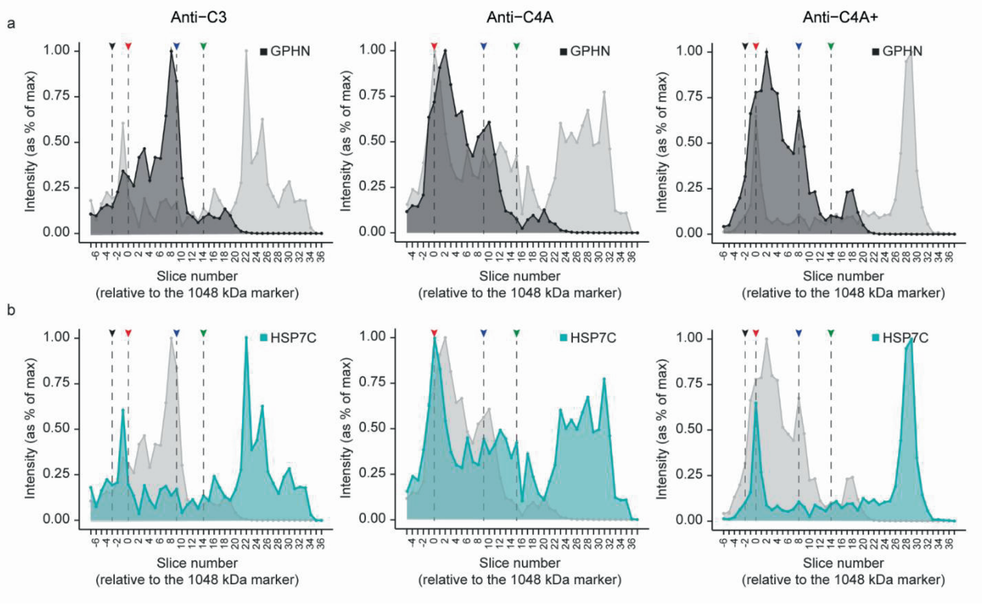

Figure 6. Migration profile of HSP7C obtained by IP-BN-PAGE/MS of Gephyrin-C3 and Gephyrin-C4A in brainstem. Protein abundances normalized to the maximum intensity across the gel, revealing the migration profiles of (**a**) Gephyrin and (**b**) HSP7C in brainstem. On the x-axis slice numbers are shown, relative to the 1048 kDa spiked-in marker protein. Arrowheads point to the location of molecular weight markers on the gel: 1236 (black), 1048 (red), 720 (blue) and 480 (green).

In IP-MS on cortex, HSP7C, SRGAP3 and DYL2 were detected at similar abundances as the negative controls (Supplemental Table 2). In IP-BN, SRGAP3 was not detected. HSP7C and DYL2 both revealed relatively high abundances migrating separate from Gephyrin-C3 and -C4A (Figure 8b,c). The second HSP7C co-migration peak at ~1.2 MDa was also detected with both Gephyrin isoforms in cortex albeit with reduced abundance compared to brainstem (Figure 8b). DYL2 revealed a clear second co-migration peak with Gephyrin-C3 and -C4A at 720 kDa (Figure 8c). In both brain regions, NLGN1 and 3 and PP1A only revealed extreme low abundance and sporadic detection and were not further analyzed (Supplemental Figure 1 and 3).

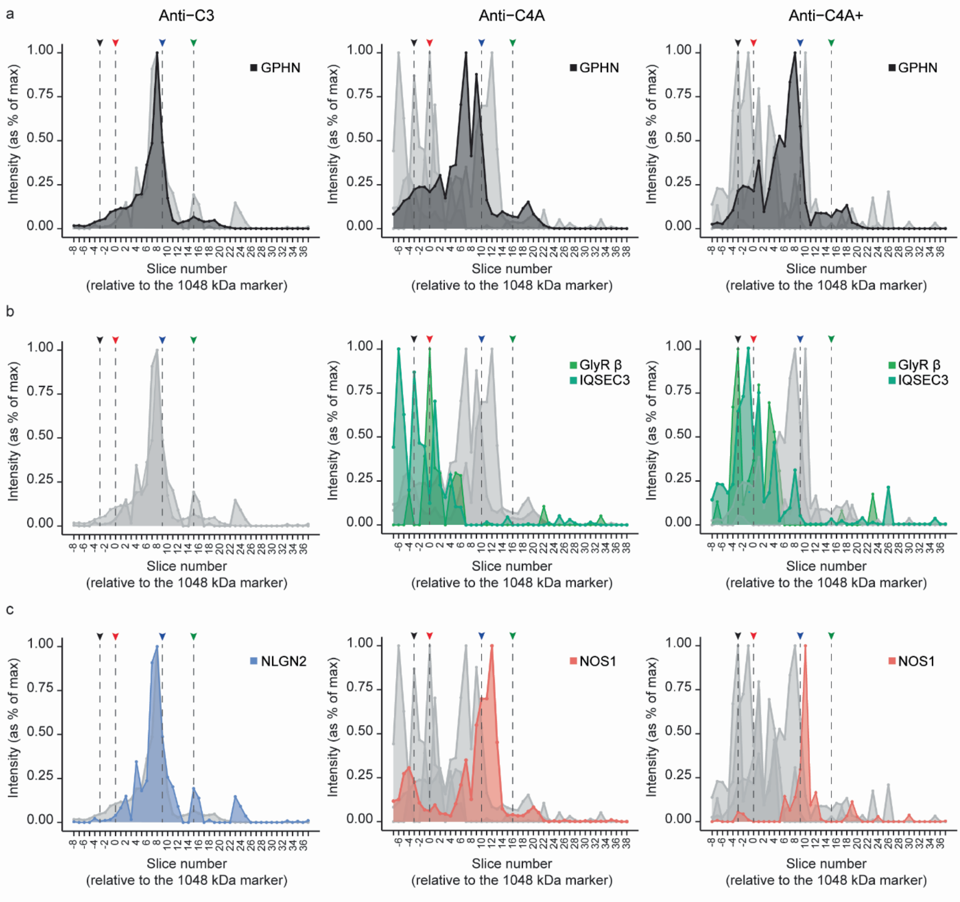

Figure 7. Subcomplex analysis of Gephyrin-C3 and -C4A in cortex by IP-BN-PAGE/MS. (**a**) Migration profile of Gephyrin-C3 and -C4A native protein complexes in cortex on a blue native gel. (**b**) Subset of Gephyrin interactors that revealed co-migration with the high molecular weight complex of Gephyrin-C3 and -C4A. (**c**) Gephyrin interactors that co-migrated with the low molecular weight complex of Gephyrin-C3 and -C4A. Protein abundances were normalized to the maximum intensity across the gel. On the x-axis slice numbers are shown, relative to the 1048 kDa spiked-in marker protein. Arrowheads point at the location of molecular weight markers on the gel: 1236 (black), 1048 (red), 720 (blue) and 480 (green).

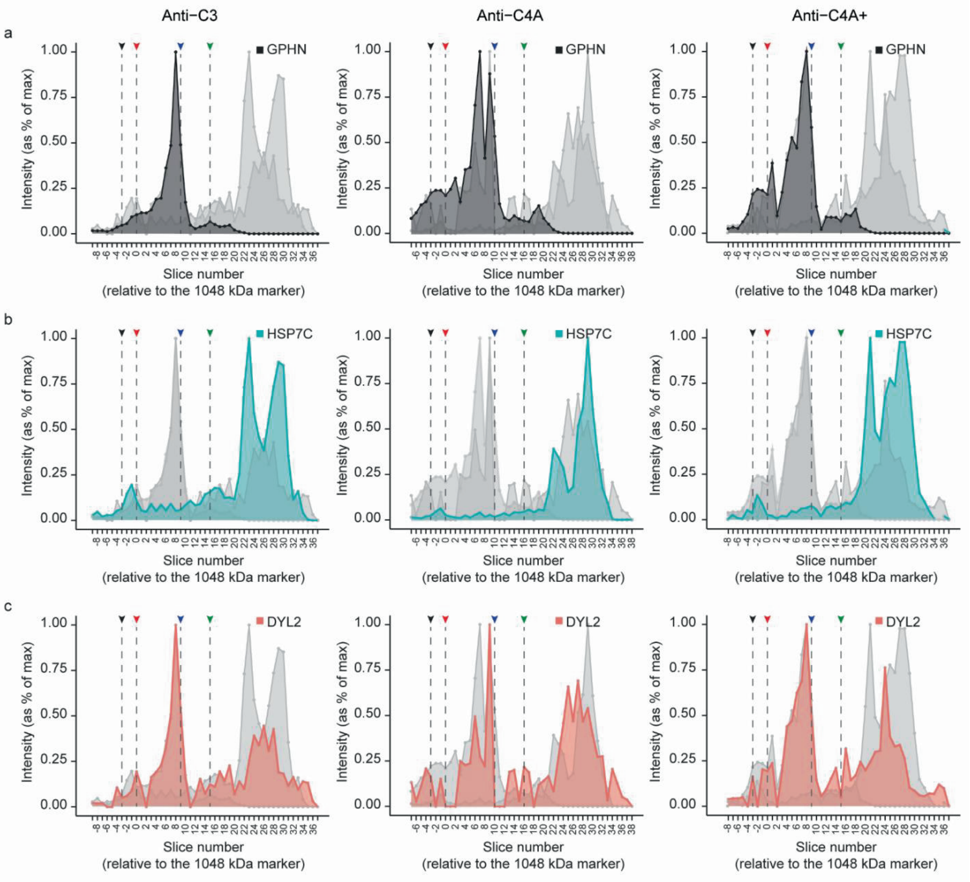

Figure 8. Migration profiles of HSP7C and DYL2 obtained by IP-BN-PAGE/MS of Gephyrin-C3 and Gephyrin-C4A in cortex. Protein abundances normalized to the maximum intensity across the gel, revealing the migration profiles of (**a**) Gephyrin, (**b**) HSP7C and (**c**) DYL2 in cortex. On the x-axis slice numbers are shown, relative to the 1048 kDa spiked-in marker protein. Arrowheads point at the location of molecular weight markers on the gel: 1236 (black), 1048 (red), 720 (blue) and 480 (green).

Together these data revealed a high molecular weight complex (~1 MDa) that contains the GlyR, IQSEC3 and HSP7C, and is most abundantly present in brainstem and -C4A containing Gephyrin. In addition, both Gephyrin isoforms revealed a low molecular weight complex (~720 kDa) containing DYL2. Whereas the low molecular weight complex of Gephyrin-C4A in part contains NOS1, this complex of Gephyrin-C3 is decorated by NLGN2.

Discussion

Our proteomics analysis revealed differences in Gephyrin-C3 and -C4A complexes. In addition, we confirmed a neuronal expression of Gephyrin-C4A, whereas Gephyrin-C3 has a strong astrocytic expression.

Our current BN-PAGE results on native Gephyrin obtained from brain lysates revealed two major migration peaks, one at ~720 kDa and one at ~1MDa. Previous research revealed migration of heterologous overexpressed Gephyrin on BN-PAGE to an apparent mass of ~640 kDa, which is roughly the size of a Gephyrin hexagon[171]. This suggests the 720 kDa peak we observed is a Gephyrin hexagon with little added molecular weight by interactors. The ~1 MDa complex was only abundant in presence of high GlyR α1 expression and affinity for the GlyR (Gephyrin-C4A(+) in brainstem). In addition, co-migration of the GlyR subunits was observed at this high molecular weight of ~1 MDa, which is roughly the size of one GlyR (~250 kDa) and a Gephyrin hexagon (~640 kDa)[171].

IQSEC3 co-migrated at the high end of the large molecular weight complex (~1.2 MDa), in agreement with IP-BN-PAGE/MS of the GlyR[176]. And revealed specific binding to Gephyrin-C4A that contains higher affinity for the GlyR than Gephyrin-C3. This tight relation between IQSEC3 and the GlyR suggests these proteins are also functionally related. HSP7C additionally co-migrated with the high molecular weight complex of Gephyrin. Both IQSEC3[122] and HSP7C[177] were previously implicated in induction/maintenance or reduction/prevention of Gephyrin clustering, respectively. Further investigation is required to determine the exact roles and interplay between IQSEC3, HSP7C and the GlyR in relation to Gephyrin.

Immunoblot analysis revealed enrichment of Gephyrin in the membrane enriched fraction of brainstem. This observation coincided with increased presence of the GlyR containing high molecular weight complex in this brain region. Conversely, in cortex, Gephyrin did not reveal enrichment in the membrane fraction, which coincided with a severely reduced level of the GlyR containing high molecular weight complex. Instead, in cortex the majority of Gephyrin is of 720 kDa. Of interest, this smaller molecular weight complex co-migrated with DYL2. Previous research revealed binding of Gephyrin to DYL1/2[178], forming a motor-cargo adaptor protein for intracellular GlyR trafficking[120,125]. Association of DYL2 with this small molecular weight complex, suggests this Gephyrin assembly at least in part is not synaptic. In Gephyrin-C3 IP-BN, this complex tightly co-migrated with NLGN2, and in Gephyrin-C4A IP-BN in part with NOS1. Further research is required to determine the relation between DYL2, NLGN2 and NOS1 and the different Gephyrin isoforms.

Whereas Gephyrin-C4A revealed exclusive expression in neurons, Gephyrin-C3 expression was largely observed in astrocytes at the corpus callosum. A previous report revealed Gephyrin-C3 in glial cells as the main, if not exclusive, source of Moco synthesis in the brain[129]. In addition, Gephyrin-C3 has been observed with high expression levels in the liver[179], suggesting a strictly enzymatic function of this isoform. However, binding of Gephyrin-C3 to the GlyR, DYL2 and NLGN2 as revealed in the current study, suggests this isoform additionally mediates a transport and scaffolding function.

GlyRs[90] and Neuroligins[180] are typically considered neuronal proteins, and therefore seem unlikely binding partners for astrocytic Gephyrin-C3. However, expression of the GlyR[181] and Neuroligins[180] by astrocytes has been reported recently. In addition, despite Gephyrin-C3 RNA repression in neurons by NOVA proteins, low levels of Gephyrin-C3 expression in neurons cannot be excluded[182]. The (sub)cellular location of the GlyR, DYL2 and NLGN2 interactions with Gephyrin-C3 remains unknown, and will be important for interpreting non-enzymatic functionalities of Gephyrin-C3 in future studies.

The data we obtained in the current study is a first exploration of Gephyrin-C3 and -C4A protein complexes. The differential interaction data reveals high consistency throughout the IP-MS and IP-BN-PAGE/MS experiments, which recapitulates several observations from literature in addition to providing novel insights. However, the detection of differential interactions as a result from antibody selection bias or antibody induced protein complex disruption cannot be excluded. Differential binding between Gephyrin-C3 and -C4A with IQSEC3, NOS1 and NLGN2 may be validated using total Gephyrin IP-MS in wildtype and Gephyrin- isoform specific knock-outs, inclusion of additional Gephyrin-C3 and -C4A specific antibodies and/or colocalization studies in mouse brain. For these validations, and further exploration of Gephyrin isoform interactions and functionalities, Gephyrin knock-out mice will be useful. Additionally, we did not identify GABA_ARs in the current IP-MS data, likely due to their low affinity for the Gephyrin protein[113]. Stabilizing the interaction with a cross-linking chemical agent prior to IP-MS may be an interesting strategy to dissect its binding to Gephyrin-C3 and/or -C4A isoforms.

Materials and methods

Animals- The use of mice in this study was approved by the animal ethical care committee of the Vrije Universiteit Amsterdam.

Antibodies- All primary antibodies used in the current study are listed in Table 1. Secondary antibodies used for immunoblotting included goat-anti-mouse (Dako Agilent, Santa Clara, CA, USA, P0447), goat-anti-rabbit (Dako Agilent, Santa Clara, CA, USA, P0448) and rabbit-anti-goat HRP (Dako Agilent, Santa Clara, CA, USA, P0449) HRP conjugated antibodies, and were all used at 1:10.000. Secondary antibodies used for immunohistochemistry included anti-rabbit Alexa 488 (Invitrogen, Waltham, MA, USA, A-11008) and anti-mouse Alexa 568 (Invitrogen, Waltham, MA, USA, A11011) and were both used at 1:400.

Table 1. Primary antibodies used in the current study. IP: immuno-purification, IHC: immuno histochemistry; IB: immunoblot; Conc.: concentration in μg/μL

Antibody	Company	Catalogue #	Epitope sequence	Experiment	IB conc.	IHC conc.
Anti-C3	Genscript	Custom	CSYSHHATGSADKRI	IB; IP; IHC	1:250	1:500
Anti-C4A	Genscript	Custom	QIRRPDESKGVASRC	IB; IP; IHC	1:250	1:500
Anti-C4A+	Genscript	Custom	CPTPKQIRRPDESKG	IB; IP; IHC	1:1000	1:500
Anti-GluA1	Genscript	Custom	RTSDSRDHTRVDWKRC	IP	-	-
Anti-GluA3	Genscript	Custom	NFKPAPATNTQNYC	IP	-	-
Anti-FLAG	Sigma	F1804	DYKDDDDK	IB	1:1000	-
Anti-vGat	SySy	131 011	a.a. 75-87 rat vGat	IHC	-	1:1000

Immuno-purifications- Immuno-purifications (IPs) were done as described in[176]. In short, cortex or brainstem were homogenized in a 1% n-Dodecyl β-D-maltoside (DDM) (Thermo Fisher, Waltham, MA, USA) buffer containing 25 mM HEPES, 150 mM NaCl, pH 7.4 and protease inhibitor (Roche, Basel, Switzerland). After protein extraction for 1 hour at 4 °C, samples were centrifuged two times at 20,000 x g for 20 min at 4 °C. Following incubation overnight with 10 μg of antibody, samples were incubated with 80 μL of protein A/G PLUS-Agarose beads (Santacruz, Dallas, TX, USA) for 1 h at 4 °C. Samples were then centrifuged at 1000 x g for 1 minute and washed four times with 1 mL of a 0.1% DDM buffer containing 25 mM HEPES, 150 mM NaCl, pH 7.4. 1x Laemmli buffer was added to the final pellet, boiled at 98 °C and run on a home-made 10% SDS polyacrylamide gel.

in-gel digestion-MS- Samples were digested as described in[176]. In short, gels were fixed in 50% ethanol 3% phosphoric acid, washed and stained with colloidal Coomassie blue. Samples were then cut in 3 slices, which were cut in smaller pieces, transferred to a Multiscreen HV filter Plate (Sigma-Aldrich, St. Louis, MO, USA), washed and destained with a mix of 50 mM ammonium bicarbonate (Sigma-Aldrich, St. Louis, MO, USA) in acetonitrile (VWR, Radnor, PA, USA). After drying of the gel pieces in acetonitrile, samples were incubated with trypsin (Mass Spec Grade, Promega, Madison, WI, USA) overnight at 37 °C dissolved in 50 mM ammonium bicarbonate. Peptides were extracted with 0.1 % Trifluoroacetic acid (Protein sequence grade; Applied Biosystems, Warrington, UK) in 50% acetonitrile twice, and in 0.1% trifluoracetic acid in 80% acetonitrile once. Samples were then dried in a speed vac (Savant, Thermo Fisher, Waltham, MA, USA) and stored at -20 °C until mass spectrometry analysis.

Peptides were analyzed on an LTQ-Orbitrap discovery (Thermo Fisher, Waltham, MA, USA) mass spectrometer, coupled to a High-Performance Liquid Chromatography (HPLC) and electro-spray system (Eksigent, Sciex, Framingham, MA, USA). Peptides were re-dissolved in 20 µL 0.1% acetic acid (VWR, Radnor, PA, USA), and loaded on a 5 mm Pepmap 100 C18 (Dionex, Thermo Fisher, Waltham, MA, USA) column (300 µm ID, 5 µm particle size). Separation of peptides was done on a 200 mm Alltima C18 homemade column (100 µm ID, 3 µm particle size) with a linear gradient of increasing acetonitrile (VWR, Radnor, PA, USA) concentration from 5% to 35% in 45 min, and to 90% in 5 min, and a flow rate of 400 nL/min. The mass spectrometer was operated in a data dependent manner with one MS (m/z range from 330 to 2000) followed by MS/MS on five most abundant ions, and an exclusion window of 25 sec. Obtained MS/MS spectra were searched against the Mouse database (UP000000589_10090, 2017_04) with the MaxQuant software (version 1.5.2.8). The search parameters were set to digestion with trypsin, and activated match-between-runs set at 2 min.

IP-BN-PAGE/MS- IPs were done using to the protocol described above, using 100 µg antibody and 1000 µL of beads. After pull-down and washing, samples were incubated twice with 500 µg antigen peptide dissolved in 1 mL 0.1 % Triton-X buffer containing 25 mM HEPES, 150 mM NaCl, pH 7.4 for 1 h. Samples were concentrated on a 30 kDa Vivaspin 500 filter (Sartorius Stedim Biotech, Göttingen, Germany) for 30 min at 14,000 x *g*, mixed with blue-native-PAGE loading buffer (Invitrogen, Waltham, MA, USA), 0.5 µL Molecular weight marker (Invitrogen, Waltham, MA, USA) and 1 µL Coomassie G-250 mix (Invitrogen, Waltham, MA, USA). Samples were run on a 3-12% blue native PAGE gel (Invitrogen, Waltham, MA, USA), at 150 V for 1.5 h followed by 250 V for 1 h at 4ºC. Gels were fixed overnight in 50% ethanol, 3% phosphoric acid, washed and stained with Colloidal Coomassie Blue. Each sample was cut into 48 slices using a grid cutter (Gel Company, San Francisco, CA, USA), and transferred to a Multiscreen HV filter Plate. Slices were then incubated with 1 mM TCEP in 50 mM ammonium bicarbonate for 30 minutes at 37ºC, and 4 mM MMTS in 50 mM ammonium bicarbonate for 15 minutes at room temperature. Next, samples were prepared and stored following the in-gel digestion protocol described above.

Each slice was analyzed separately on the Triple TOF 5600 Sciex, Framingham, MA, USA) in DDA mode as described previously[176]. The MS/MS spectra were searched against the Mouse database (UP000000589_10090, 2017_04) using MaxQuant software (version 1.5.2.8). The search parameters were set to digestion with trypsin and MMTS (C), and match-between-run activated. Protein abundances were normalized to their maximum intensity over all slices as shown in the figures.

Overexpression in HEK cells- HEK293 cells were plated in 10 cm dishes at 37 °C and 95 % air and 5 % CO2, in Dulbecco’s modified Eagle’s medium (DMEM, Gibco, Life Technologies, Carlsbad, CA, USA) supplemented with 10 % fetal bovine serum (Invitrogen, Waltham, MA, USA) and 1 % penicillin-streptomycin (Gibco, Life Technologies, Carlsbad, CA, USA). Cells were transfected using polyethylenimine (PEI) at ~70% confluency, with 5 µg plasmid cDNA for Gephyrin-C3 (pcDNA3.1+/C-(K)-DYK_Gphn NM_145965.2) and Gephyrin-C4A;C (pcDNA3.1+/C-(K)-DYK_Gphn NM_172952.3).

After 48h incubation, cells were washed two times with dPBS (37 °C) and resuspended in 1 mL extraction buffer containing 25mM HEPES/NaOH, pH 7.4, 150 mM NaCl, 1 % DDM and protease inhibitor (Roche, Basel, Switzerland). Proteins were extracted for 1 h on a rotator at 4°C. Afterwards, the samples were centrifuged at 20,000 x g for 10 min at 4°C, and 4 µg antibody was added. After incubation overnight at 4°C in the rotator, 40 µg beads were added, incubated for an additional hour, and washed 3 times with extraction buffer containing 0.1% n-Dodecyl ß-D-maltoside. Proteins were eluted with 50 µl 1 x SDS Laemmli buffer, boiled at 98°C and used for immunoblotting.

Neuronal and astrocyte culture- Primary cultures of cortical neurons from E18 wildtype C57Bl/6 mouse embryos were prepared as previously described[183]. Cortices were incubated in Hanks balanced salt solution (Gibco, Amarillo, TX, USA), with 1% HEPES buffer solution and 10% trypsin (Gibco, Amarillo, TX, USA) at 37 °C for 20 min. Following three washes, Neurobasal medium (Gibco, Amarillo, TX, USA) completed with 2% B27 (Gibco, Amarillo, TX, USA) 2% HEPES, 0.25% glutamine (200 mm; Gibco, Amarillo, TX, USA) and 0.1% Pen/Strep (Gibco, Amarillo, TX, USA) was added. Tissue was then triturated with a Pasteur pipette, counted and plated at 150k/well density in 24-well plates.

Astrocytes were cultured from postnatal day 1 (P1) mice. Brain tissue was incubated in Hanks Buffered Solution (HBSS; Sigma-Aldrich, St Louis, USA) with 7 mM HEPES (pH 7.4, Life Technologies, Carlsbad, CA, USA). The tissue was then digested with 0.25% trypsin for 20 min at 37°C, blocked in DMEM (Dulbecco's modified Eagle's medium) + Glutamax (Thermo Fisher, Waltham, USA) with non-essential amino acid solution (Sigma-Aldrich, St. Louis, USA), 1% penicillin-streptomycin (Life Technologies, Carlsbad, CA, USA) and 20% fetal bovine serum (FBS; Thermo Fisher, Waltham, USA). Cells were spun down at 1200 rpm, 10 min at room temperature and pellet was resuspended in DMEM + 10% FBS, 5 mM Glutamax and 0.1% penicillin-streptomycin. Cells were plated in a T25 flask (Greiner, Kremsmünster, Austria) and kept at 37 °C and 5% CO_2.

Immunoblot analysis- Samples containing SDS loading buffer were run on 10% homemade gels or 5–12% Criterion™ TGX Stain-Free™ precast gels (Bio-Rad, Hercules, CA, USA) and were transferred onto a PVDF membrane overnight. The membranes were then blocked using 5% non-fat milk in Tris-buffered saline (pH 7.4) with Tween-20 (TBST) followed by an overnight incubation with the primary antibody at 4 °C. The blots were washed three times in TBST after the primary antibody incubation followed by a 1 h incubation of HRP-conjugated secondary antibody in 3% non-fat milk. The blots were washed three times, incubated with SuperSignal West Femto Chemiluminescent Substrate (Thermo Fisher, Waltham, MA, USA) and scanned on an Odyssey® Fc scanner (Licor Biosciences, Lincoln, NE, USA).

Immunohistochemistry- Mice were perfused transcardially with phosphate-buffered saline (PBS) (pH7.4), followed by 4% paraformaldehyde (PFA) in PBS. Brains were then isolated, incubated overnight in 4% PFA and transferred to 30% sucrose in PBS with 0.01% NaN_3. After immersion in sucrose, brains were sliced in 35-μm sagittal sections using a cryostat. Slices were stored at in PBS with 0.02% NaN_3 and stored at 4°C until further use.

Slices were washed with PBS and incubated with primary antibody dissolved in 0.25% triton and 0.4% gelatin, overnight at 4°C. After three washes, slices were incubated with secondary antibodies in 0.25% triton and 0.4% gelatin at 4°C in the dark for 1.5 h. After two washed with PBS, slices were incubated with DAPI for 15 min, washed with PBS and mounted on glass slides with DABCO. Overview images were obtained on a wide-field fluorescent microscope, and zooms were taken on a confocal microscope.

Supplemental Table and Figures

sTable 1. Raw iBAQ intensity values of Gephyrin and known interactors observed in anti-C3, anti-C4A and anti-C4A+ IP-MS in brainstem homogenate. Antibodies against the GluA1 and GluA3 subunits of the AMPA-receptor involved in excitatory synaptic transmission were used as negative controls.

Gene name	Anti-C3	Anti-C3_2	Anti-C4A_1	Anti-C4A_2	Anti_C4A+_1	Anti_C4A+_2	GluA1_1	GluA1_2	GluA3_1	GluA3_3	MEAN_C3	MEAN_C4A	MEAN_C4A+	MEAN_GluA1	MEAN_GluA3
DYL2	NA	NA	NA	NA	NA	NA	NA	NA	NA	NA	NA	NA	NA	NA	NA
GEPH	2E+06	3E+06	2E+06	3E+06	6E+06	1E+07	2E+05	2E+05	2E+04	NA	2E+06	3E+06	8E+06	2E+05	2E+04
GlyR α1	NA	3E+04	6E+05	NA	6E+05	1E+06	NA	NA	NA	NA	3E+04	6E+05	8E+05	NA	NA
GlyR β	NA	2E+04	2E+05	2E+04	9E+04	8E+05	NA	NA	NA	NA	2E+04	1E+05	4E+05	NA	NA
HSP7C	1E+06	2E+06	1E+06	1E+06	2E+06	2E+06	2E+06	2E+06	4E+06	1E+06	2E+06	1E+06	2E+06	2E+06	3E+06
IQSEC3	NA	NA	NA	NA	NA	2E+04	NA	NA	NA	NA	NA	NA	2E+04	NA	NA
NLGN2;1	4E+04	NA	NA	NA	NA	NA	NA	NA	NA	NA	4E+04	NA	NA	NA	NA
NLGN3	NA	2E+04	NA	NA	NA	NA	NA	NA	NA	NA	2E+04	NA	NA	NA	NA
NOS1	NA	NA	7E+05	7E+05	1E+05	3E+05	NA	NA	NA	NA	NA	7E+05	2E+05	NA	NA
PP1A	NA	NA	5E+04	NA	NA	NA	NA	NA	NA	NA	NA	5E+04	NA	NA	NA
SRGAP3	NA	NA	NA	NA	NA	NA	NA	NA	NA	NA	NA	NA	NA	NA	NA

sTable 2. Raw iBAQ intensity values of Gephyrin and known interactors observed in anti-C3, anti-C4A and anti-C4A+ IP-MS in cortex homogenate. Antibodies against the GluA1 and GluA3 subunits of the AMPA-receptor involved in excitatory synaptic transmission were used as negative controls.

Gene name	Anti-C3_1	Anti-C3_2	Anti_C4A_1	Anti_C4A_2	Anti_C4A+_1	Anti_C4A+_2	Anti-GluA1_1	Anti-GluA1_2	Anti-GluA3_1	Anti-GluA3_2	MEAN_C3	MEAN_C4A	MEAN_C4A+	MEAN_GluA1	MEAN_GluA3
DYL2	NA	3E+06	NA	NA	3E+06	5E+06	2E+06	5E+05	NA	NA	3E+06	NA	4E+06	1E+06	NA
GEPH	2E+07	2E+07	1E+08	9E+07	7E+07	6E+07	1E+06	9E+05	5E+04	5E+04	2E+07	1E+08	7E+07	1E+06	5E+04
GlyR α1	NA	NA	NA	NA	NA	NA	NA	NA	NA	NA	NA	NA	NA	NA	NA
GlyR β	NA	NA	6E+05	3E+05	2E+05	6E+05	NA	NA	NA	NA	NA	4E+05	4E+05	NA	NA
HSP7C	7E+06	7E+06	1E+07	1E+07	3E+06	3E+06	1E+07	5E+06	1E+07	9E+06	7E+06	1E+07	3E+06	8E+06	1E+07
IQSEC3	NA	NA	2E+05	1E+05	2E+05	1E+05	NA	NA	NA	NA	NA	2E+05	1E+05	NA	NA
NLGN2;1	4E+06	2E+06	NA	NA	NA	NA	NA	NA	NA	NA	3E+06	NA	NA	NA	NA
NLGN3	6E+05	4E+05	NA	NA	NA	NA	NA	NA	NA	NA	5E+05	NA	NA	NA	NA
NOS1	NA	NA	1E+07	9E+06	3E+05	4E+05	NA	NA	2E+04	2E+04	NA	9E+06	4E+05	NA	2E+04
PP1A	3E+04	NA	5E+05	NA	5E+04	2E+04	NA	NA	NA	2E+04	3E+04	5E+05	3E+04	NA	2E+04
SRGAP3	NA	NA	3E+04	3E+04	NA	NA	3E+04	1E+04	3E+04	4E+04	NA	3E+04	NA	2E+04	3E+04

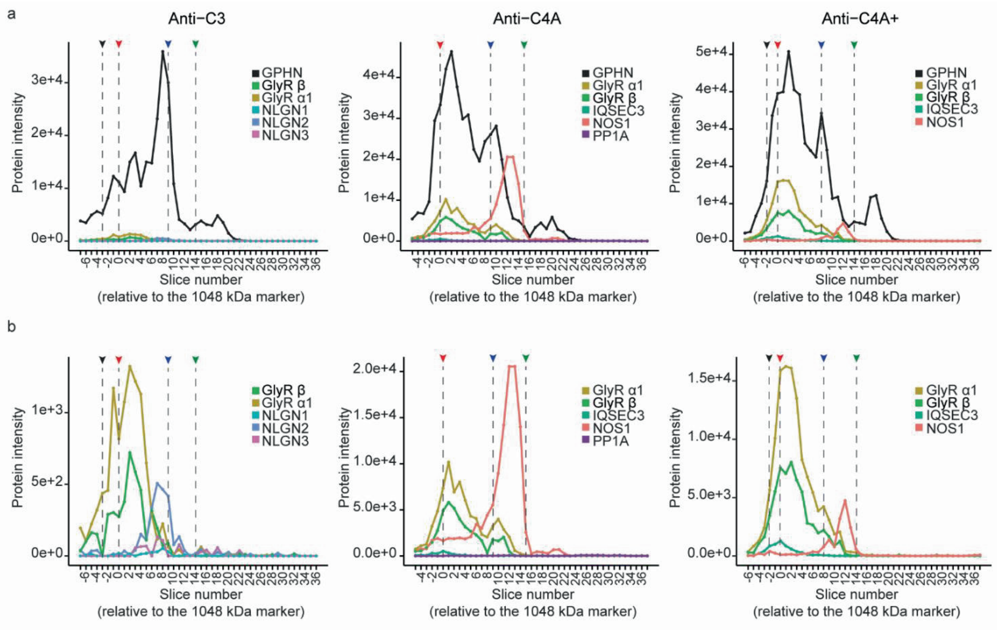

Supplemental Figure 1. Raw protein abundance values obtained by IP-BN-PAGE/MS of Gephyrin-C3 and Gephyrin-C4A in brainstem. (**a**) Raw protein iBAQ intensity values of Gephyrin and known Gephyrin interactors measured in each gel slice, per IP-BN-PAGE/MS experiment. (**b**) Focus on protein abundances of Gephyrin interactors. On the x-axis slice numbers are shown, relative to the 1048 kDa spiked-in marker protein. Arrowheads point to the location of molecular weight markers on the gel: 1236 (black), 1048 (red), 720 (blue) and 480 (green).

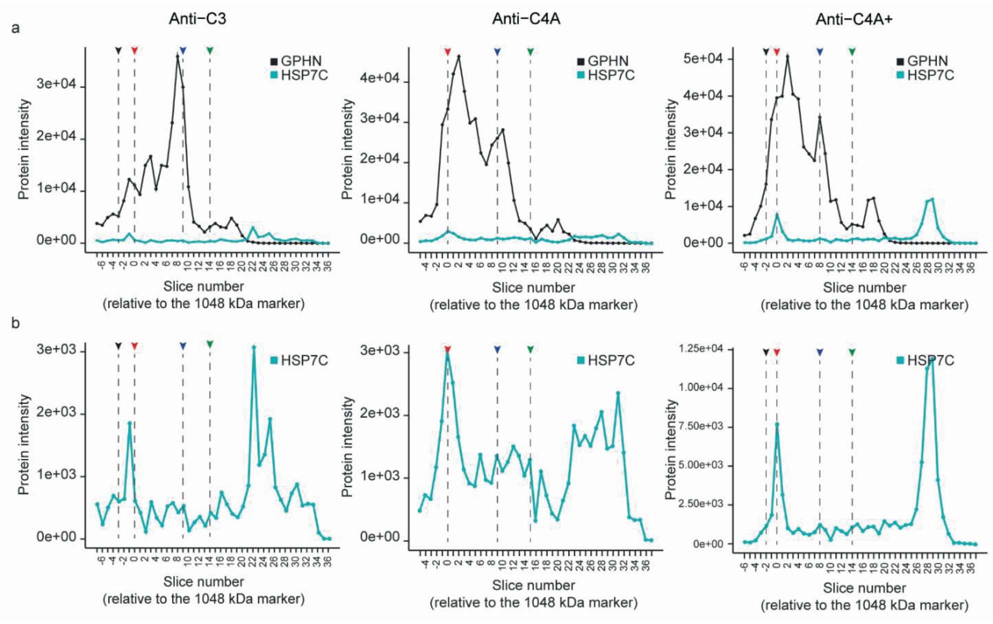

Supplemental Figure 2. Raw protein abundance values of Gephyrin, HSP7C and DYL2 obtained by IP-BN-PAGE/MS of Gephyrin-C3 and Gephyrin-C4A in brainstem. (**a**) Raw protein iBAQ intensity values of Gephyrin and HSP7C measured in each gel slice, per IP-BN-PAGE/MS experiment. (**b**) Focus on protein abundances of HSP7C. On the x-axis slice numbers are shown, relative to the 1048 kDa spiked-in marker protein. Arrowheads point at the location of molecular weight markers on the gel: 1236 (black), 1048 (red), 720 (blue) and 480 (green).

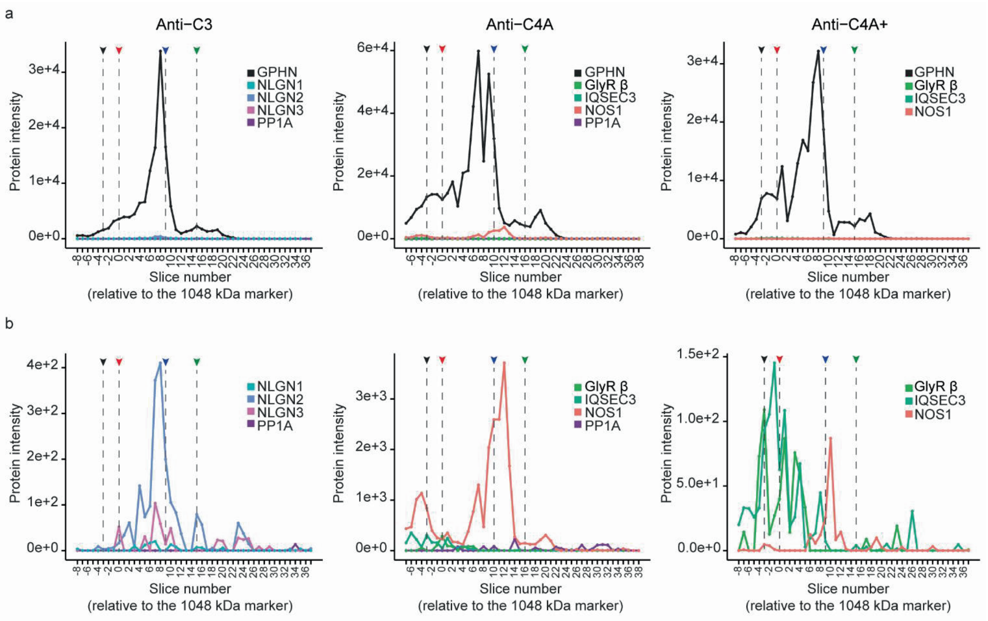

Supplemental Figure 3. Raw protein abundance values obtained by IP-BN-PAGE/MS of Gephyrin-C3 and Gephyrin-C4A in cortex. (**a**) Raw protein iBAQ intensity values of Gephyrin and known Gephyrin interactors measured in each gel slice, per IP-BN-PAGE/MS experiment. (**b**) Focus on protein abundances of Gephyrin interactors. On the x-axis slice numbers are shown, relative to the 1048 kDa spiked-in marker protein. Arrowheads point at the location of molecular weight markers on the gel: 1236 (black), 1048 (red), 720 (blue) and 480 (green).

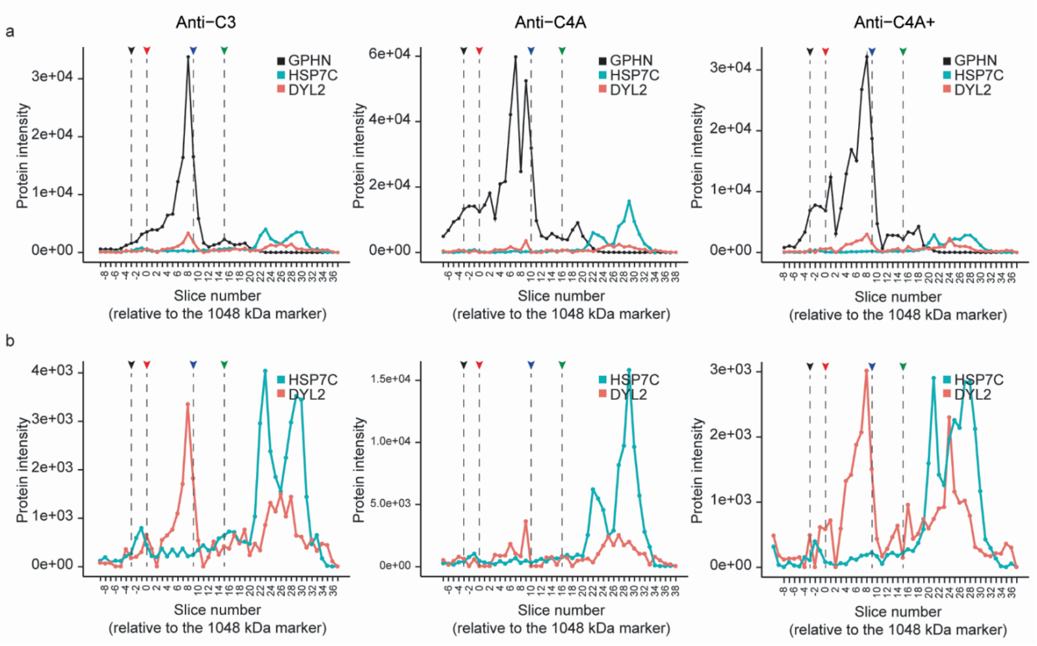

Supplemental Figure 4. Raw protein abundance values of Gephyrin, HSP7C and DYL2 obtained by IP-BN-PAGE/MS of Gephyrin-C3 and Gephyrin-C4A in cortex. (**a**) Raw protein iBAQ intensity values of Gephyrin, HSP7C and DYL2 measured in each gel slice, per IP-BN-PAGE/MS experiment. (**b**) Focus on protein abundances of HSP7C and DYL2. On the x-axis slice numbers are shown, relative to the 1048 kDa spiked-in marker protein. Arrowheads point at the location of molecular weight markers on the gel: 1236 (black), 1048 (red), 720 (blue) and 480 (green).

Chapter 4: Interactomes of GluA1 and GluA3 subunit containing AMPARs reveal distinct protein composition

Sophie J.F. van der Spek, Nikhil J. Pandya, Frank Koopmans, Iryna Paliukhovich,
Roel C. van der Schors, Mylene Otten, August B. Smit[$] and Ka Wan Li[$]

[$] These authors contributed equally to the work

Abstract

The AMPA glutamate receptor (AMPAR) is the major type of synaptic excitatory ionotropic receptor in the brain. The most abundant AMPAR subtypes in the hippocampus are GluA1/2 and GluA2/3 heterotetramers. Each subtype contributes differentially to mechanisms of synaptic plasticity, which may be in part caused by how these receptors are regulated by specific associated proteins. A broad range of AMPAR interacting proteins have been identified and several were shown to affect biogenesis, AMPAR trafficking, and channel properties, alone or in distinct assemblies, and several revealed preferred binding to specific AMPAR subunits. To date, a systematic separate interactome analysis of the major GluA1/2 and GluA2/3 AMPAR subtypes is lacking. To reveal interactors belonging to specific AMPAR sub-complexes, we performed both quantitative and interaction proteomics on hippocampi of wildtype and GluA1- or GluA3 knock-out mice. Whereas GluA1/2 receptors co-purified TARP-γ8, PRRT1 and CNIH2 with highest abundances, GluA2/3 receptors revealed strongest co-purification of CNIH2, TARP-γ2, and OLFM1. Further analysis revealed that TARP-γ8-PRRT1 can interact directly, and co-assemble into an AMPAR subcomplex especially near the synapse.

Introduction

AMPA receptors (AMPARs) are glutamate-gated cationic channels underlying the predominant component of fast excitatory synaptic transmission in the mammalian central nervous system. Functional synaptic AMPARs are localized primarily in nano-domains[39,184] residing at the postsynaptic density, in which they are aligned to the glutamate-release sites of the presynaptic active zone[62]. AMPAR subunit composition, phosphorylation state, numbers and biophysical properties are regulated in an activity-dependent manner, which is a major postsynaptic contribution to alteration of synaptic efficacy. AMPARs have four different subunits GluA1-4 (GRIA1-4), that form distinct combinations[51,52]. In hippocampus, the majority of AMPARs consists of GluA1/2 followed by GluA2/3 heterotetramers[53,185]. The distinct AMPAR subunits show differences in levels of expression[53,79,83], posttranslational modifications[44], subcellular distribution[57,79], trafficking behavior[59,186] and channel properties[57,61], and contribute differentially to mechanisms of synaptic plasticity[59,61]. For instance, GluA1/2 receptors are inserted into the synapse upon stimulation, whereas GluA2/3 receptor cycle constitutively under basal conditions[59]. These specific properties of AMPARs are generated by interactions with associated (auxiliary) proteins[44,46,187]. As such these proteins may cause different subunits to become differentially implicated in distinct phases of memory[188] and disease[189].

Currently more than 30 AMPAR associated proteins have been reported[46,190]. These interactors include multiple membrane proteins, that are considered auxiliary proteins due to their effects on both AMPAR gating properties as well as trafficking[68,46]. In particular, TARP-γ2 (Stargazin/CACNG2) and TARP-γ8 (CACNG8*)* are known to alter AMPAR surface expression[191]; to affect AMPAR post-synaptic density (PSD) mobility by the interaction with PSD-95 (DLG4)[73,192]; and to prolong AMPAR deactivation and desensitization[76]. Apart from TARPs, Cornichons (CNIH2/3) can regulate AMPAR channel properties[68,193]. The Shisa family of proteins (CKAMP44/SHISA9, CKAMP52/SHISA6) has also been implicated in affecting AMPAR membrane mobility[194] and channel conductance properties[66,187,194,195]*.*

Previous studies revealed several interactors gathering in distinct AMPAR assemblies[77,80]. For instance, FRRS1L together with CPT1C is located in the ER forming a subcomplex that regulates AMPAR biogenesis[80,77]. This complex is distinct from synaptic complexes containing, for example, the high abundant AMPAR interactor TARP-γ8[77,80]. Both TARP-γ8 and FRRS1L compete for the same binding site on the AMPAR[8], and are therefore part of at least two separate AMPAR populations[80]. In addition, several AMPAR interactors revealed preferred association with distinct AMPAR subunits[46,81]. For instance, the classical AMPAR interactor SAP97 (or DLG1) specifically binds GluA1[196,197]. Additionally, unlike GluA1, the GluA2 and GluA3 subunits contain a shared sequence (-SKVI) at their C-terminal end. Through this sequence GRIP1[63] and PICK1[64] interact with the AMPAR and regulate insertion and retainment[198,199] and removal[200] of the AMPAR from the synapse, respectively. Also several more recently identified AMPAR interactors revealed stronger binding with specific AMPAR subunits[46]. For instance, PRRT1 and GSG1L were reported to preferentially associate with GluA1 and GluA2, respectively[46,201].

The two major AMPAR subtypes GluA1/2 and GluA2/3 in hippocampus contribute differentially to synaptic plasticity[59,61], which may in part be brought about by that these receptors are regulated by distinct interactors. Several studies demonstrated that certain interacting proteins associate differentially to specific AMPAR subunits[46,196,197,201]. However, an interactome analysis of the GluA1/2 and GluA2/3 subtypes in isolation is lacking. In the current study, we set out to determine the GluA1/2 and GluA2/3 complex compositions separately. We used (interaction) proteomics, and super-resolution microscopy, in mouse brain hippocampus from wildtype and GluA1 or GluA3 knock-out (KO) mice. Immunopurification-mass spectrometry (IP-MS) revealed strongest copurification of TARP-γ8, PRRT1 and CNIH2 with the GluA1/2 receptor specifically. In contrast, GluA2/3 revealed most abundant association with TARP-γ2, CNIH2 and OLFM1. Further analysis revealed a direct interaction between TARP-γ8 and PRRT1, and their co-assembly into an AMPAR subcomplex, especially near the synapse.

Results

Immunopurification-Mass Spectrometry (IP-MS) using GluA1 or GluA3 specific antibodies

In hippocampus, GluA1/2 and GluA2/3 are the major AMPAR subtypes[53]. We performed immunopurifications (IPs) on a synapse enriched biochemical fraction (P2+M), using anti-GluA1 and -GluA3 subunit specific antibodies (sFigure1) to delineate interactors that may be associated preferentially with either AMPAR subtype (Figure 1). As a common reference, a well characterized antibody recognizing both GluA2 and GluA3 (sFigure1) was included[84,202]. The isolated protein complexes were trypsin digested, and measured by LC-MS/MS in data dependent acquisition mode for protein identification and quantification.

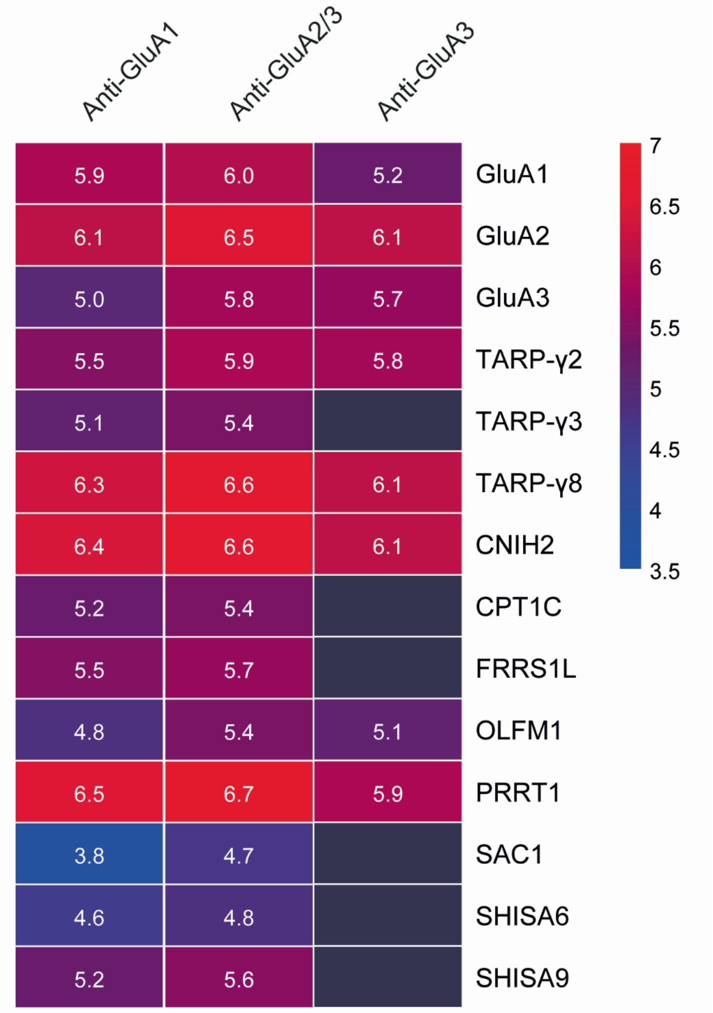

Figure 1. Immunopurification-Mass Spectrometry using GluA1, GluA-2/3 and GluA-3 antibodies in wildtype hippocampus. Protein abundances of AMPAR subunits and known interactors are shown as mean $\log_{10}$ iBAQ intensity values, and color coded from high abundance (red) to low abundance (blue).

IP-MS of anti-GluA1, GluA2/3 and GluA3 revealed co-purification of GluA1,-A2,-A3 in all experiments (Figure 1). GluA4 was not detected, in agreement with a low expression of GluA4 in hippocampus[79,83]. Out of the AMPAR-subunits, anti-GluA1 revealed highest enrichment of GluA2 and GluA1 followed by a 7-fold lower abundance of GluA3. Anti-GluA2/3 IP-MS also revealed highest enrichment for GluA2 followed by GluA1 and GluA3, respectively, which is in agreement with their expression levels in hippocampus[79,83]. Anti-GluA3 revealed strongest co-purification of GluA2 and GluA3 followed by a 3-fold lower abundance of GluA1. Together, this is in line with previous reports demonstrating the presence of two main types of AMPARs in hippocampus, i.e., GluA1/2 and GluA2/3. It further indicates the existence of a minor pool of GluA1/3 receptors[51–53].

The IP-MS experiments identified 11 AMPAR interactors (Figure1). IP-MS with GluA1 and GluA2/3 antibodies revealed strongest co-enrichment of TARP-γ8, CNIH2 and PRRT1. TARP-γ2/3, CPT1C, FRRS1L, OLFM1, SAC1 and SHISA6,-9 were observed at >10 times lower intensity. Anti-GluA3 also revealed highest co-enrichment of TARP-γ8, CNIH2 and PRRT1 with similar abundance as anti-GluA1 or anti-GluA2/3. However, anti-GluA3 in addition only co-purified TARP-γ2 and OLFM1, suggesting a less complex interactome of GluA3-containing AMPARs than GluA1-containing AMPARs in the P2+M fraction.

To reveal the selective interactome of GluA1/2 and GluA2/3 AMPAR subtypes, we used GluA1 or GluA3 knock-out (KO) mice. First, we performed quantitative proteomics on a hippocampal synapse enriched fraction obtained from GluA1 and GluA3 KO mice. Selective interactors of GluA1- and GluA3-containing receptors can be deduced based on the assumption that proteins contained in the same complex will be co-regulated in the KO mice.

Quantitative proteomics on GluA1- and GluA3 knock-out synapses reveals differential expression of known AMPAR interactors

Quantitative proteomics was performed on hippocampal synapse enriched fractions of both GluA1- and GluA3 KO mice and their wildtype controls (n=6/condition). Data was analyzed using the recently released Mass Spectrometry Downstream Analysis Pipeline (MS-DAP) for quality control and differential expression analysis (DEA) (available at https://github.com/ftwkoopmans/msdap). Quality control using MS-DAP showed a clear outlier in the GluA3 KO group, possibly due to the sample preparation prior to analysis on the mass spectrometer (sFigure 2). This sample was subsequently removed from further analysis.

Per dataset, DEA was performed using high-quality peptides detected in at least 75% of the samples in each experimental condition. In addition, peptides shared between different proteins were removed. Both GluA1- and GluA3-KO datasets revealed similar numbers of peptides and proteins and Coefficient of Variation (CoV) per sample group (sFigure 3). In the GluA1 KO dataset, filtering left 15,955 peptides that mapped to 3051 unique proteins with a CoV of 12.2% and 14.8% in wildtype and GluA1 KO samples, respectively (sFigure 3a). In the

GluA3-KO dataset, 15,867 peptides were retained that mapped to 3048 proteins, and revealed a CoV of 12.6% in wildtype and 12.2% GluA3 KO samples (sFigure 3b). In the GluA1 KO dataset, two unique GluA1 peptides were detected, albeit at a 97% lower expression compared to wildtype (sFigure 4). Both peptides originated from the N-terminal domain. This is in agreement with a previous report demonstrating low expression of a truncated GluA1 N-terminal fragment in this GluA1 KO line[203]. GluA3 KO mice revealed no expression of GluA3 unique peptides.

Differential testing at FDR-corrected $p<0,05$ revealed downregulation of five proteins in the hippocampal proteome of GluA1 KO mice (Figure 2a). These included known AMPAR subunits and interactors GluA1, GluA2, PRRT1 and TARP-γ8 (Figure 2a). The proteome of GluA3 KO mice did not reveal alterations (Figure 2a). Analysis of known AMPAR interactors revealed additional significant up-regulation of DLG4, SHISA6 and SHISA7 selectively in GluA1 KO mice, albeit at low fold-change (1.09, 1.15 and 1.16; non-FDR $p < 0.05$, respectively) (Figure 2b). GluA3 KO synapses showed selective up-regulation of AP2 subunit M1, MPP2, PRRT2 and RAP2B (with fold-changes of 1.09, 1.06, 1.24 and 1.16; non-FDR $p < 0.05$, respectively) (Figure 2b). An additional 19 interactors revealed no altered expression in either GluA1- or GluA3 KO mice (sFigure 5).

Subsequently, selective regulation of GluA1, PRRT1 and TARP-γ8 in GluA1 KOs was validated by immunoblotting (Figure 2c). Quantification also revealed selective upregulation SHISA6, albeit not significant (Figure 2d). Of interest, CNIH2 was detected with one peptide in wildtypes and GluA3 KO mice. In GluA1 KO mice, this peptide failed the quality criteria for quantitative analysis, suggestive of a down-regulation, which was corroborated by immunoblotting (Figure 2c, d).

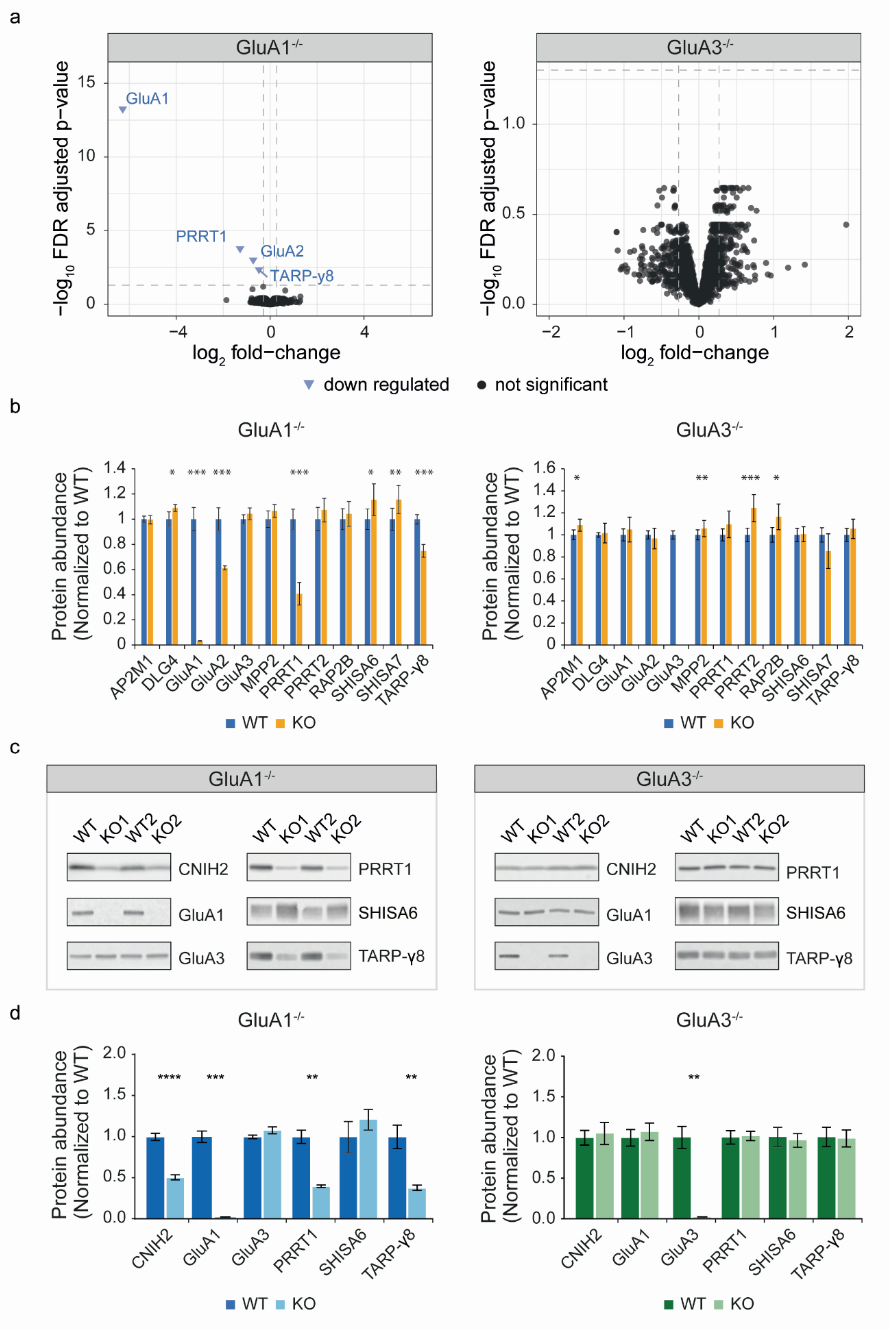
a
GluA1-/-
GluA3-/-
−log10 FDR adjusted p−value
log2 fold−change
GluA1
PRRT1
GluA2
TARP-γ8
15
10
5
0
−4
0
4
1.0
0.5
0.0
−2
−1
0
1
2
▼ down regulated
● not significant
b
GluA1-/-
GluA3-/-
Protein abundance (Normalized to WT)
1.4
1.2
1
0.8
0.6
0.4
0.2
0
1.6
*
***
**
AP2M1
DLG4
GluA1
GluA2
GluA3
MPP2
PRRT1
PRRT2
RAP2B
SHISA6
SHISA7
TARP-γ8
■ WT ■ KO
c
GluA1-/-
GluA3-/-
WT
KO1
WT2
KO2
CNIH2
GluA1
GluA3
PRRT1
SHISA6
TARP-γ8
d
GluA1-/-
GluA3-/-
Protein abundance (Normalized to WT)
2.0
1.5
1.0
0.5
0.0
****
***
**
CNIH2
GluA1
GluA3
PRRT1
SHISA6
TARP-γ8
■ WT ■ KO

Figure 2. Quantitative proteomics of GluA1 and GluA3 knock-out (KO) synapse enriched fractions. (**a**) Differential abundance analysis revealed 5 downregulated proteins in GluA1 KO mice (left) (eBayes, FDR-adjusted p-value cut-off < 0.05). No overall changes were observed in GluA3 KO animals (right). (**b**) Selective MS data analysis of known AMPAR interactors revealed specific differential regulation of interactors in GluA1 KO or GluA3 KO mice (eBayes, non-FDR-adjusted p-value cut-off < 0.05). (**c**) Immunoblot validation of mass spectrometry data. (**d**) Quantification of immunoblot validation. WT: wildtype; KO: knock-out.

IP-MS of GluA1/2 and GluA2/3 reveals preferential interaction with TARP-γ8 and Prrt1, and TARP-γ2 and Olfm1 respectively

As a next step, we performed AMPAR IPs on the GluA1- and GluA3 KO synapse enriched fraction (Figure 3a). IP-MS using anti-GluA2/3 in GluA1 KO mice revealed enrichment of GluA2 and GluA3 (Figure 3a). Strongest co-enrichment was observed for CNIH2, followed by TARP-γ2 and OLFM1 and at low abundance interactors TARP-γ3, TARP-γ8, FRRS1L, SHISA9, OLFM3, CPT1C and SHISA6 (Figure 3a). In GluA3 KO mice, IP-MS of anti-GluA2/3 revealed enrichment of GluA1 and GluA2 (Figure 3a). CNIH2 was co-enriched with highest abundance, followed by TARP-γ8 and PRRT1 and additional interactors FRRS1L, TARP-γ2, SHISA9, OLFM1, SHISA6, CPT1C and TARP-γ3 (Figure 3a). To reveal the level of receptor decoration with known interactors, we summed protein intensities of GluA-subunits and interactors and showed their relative abundance (Figure 3b). Comparison between GluA1- and GluA3 KO AMPARs revealed a lower level of receptor decoration of AMPARs lacking GluA1(Figure 3b).

To further validate the observations on preferential interactions, independently in wildtype animals, we performed AMPAR IPs on wildtype hippocampus after depletion of GluA1 containing receptors by IP, followed by immunoblotting (Figure 3c). Indeed, anti-GluA2/3 revealed a lack of GluA1 immunoreactivity after GluA1-depletion (Figure 3c). In addition, immunoreactivity of PRRT1 and TARP-γ8 were absent post depletion of GluA1, while immunoreactivity remained present for CNIH2 and TARP-γ2 (Figure 3c). This suggests that PRRT1 and TARP-γ8 are the major interactors of GluA1-containing receptors.

Next, we examined the degree of co-localization of PRRT1 and the AMPAR subtypes in wildtype neurons by super-resolution imaging. We 85mmune-labeled hippocampal neurons for GluA1 or GluA3 and combined with PRRT1, and revealed their level of colocalization by Stimulated Emission Depletion (STED) microscopy (Figure 3d-h). Both GluA1 and GluA3 colocalized with PRRT1, in agreement with the GluA1 and GluA3 IP-MS data obtained in wildtype animals (Figure 3d-h). Approximately 59% of GluA1 immunoreactivity also showed

PRRT1 immunoreactivity (Manders' coefficient: 0.59 ± 0.022), whereas only 44% of GluA3 labeling also showed immunoreactivity for PRRT1 (Manders' coefficient: 0.44 ± 0.011) ($\chi^2(1) = 9.09$, $p = 0.0026$) (Figure 3h). The higher overlap of GluA1 with PRRT1 compared to GluA3 with PRRT1, is in line with the AMPAR IP-MS data obtained in KO animals. Both GluA1 and GluA3 containing PRRT1 immunoreactivity overlapped largely with Homer positive confocal puncta (Manders' coefficient: 0.74 ± 0.02; 0.73 ± 0.01, respectively) (Figure 3i). Taken together, these data demonstrates GluA1/2 containing receptors have a preferred interaction with CNIH2, TARP-γ8 and PRRT1 whereas GluA2/3 containing receptors strongly interact with CNIH2, TARP-γ2 and OLFM1.

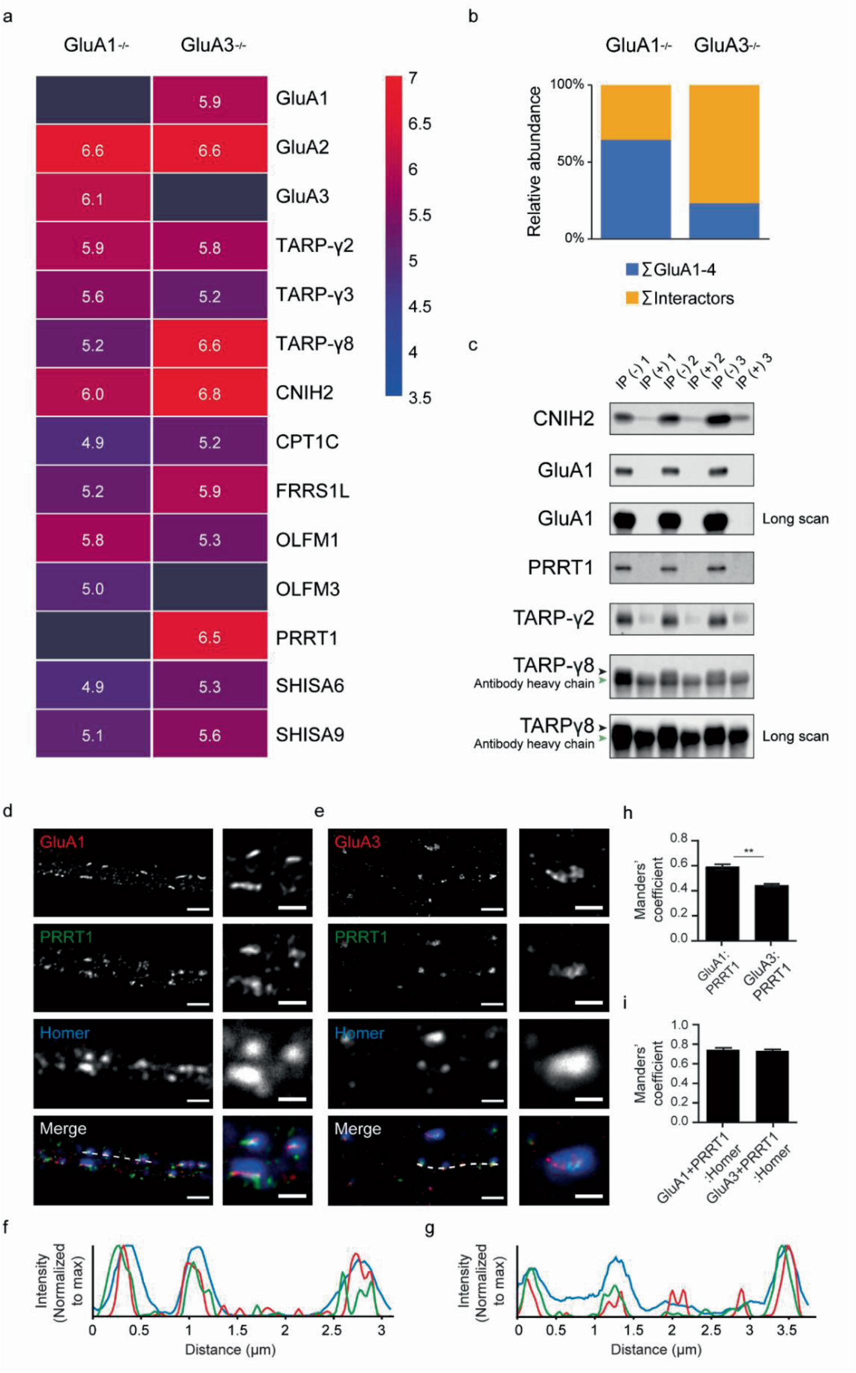
a
GluA1-/-
GluA3-/-
GluA1 5.9
GluA2 6.6 6.6
GluA3 6.1
TARP-γ2 5.9 5.8
TARP-γ3 5.6 5.2
TARP-γ8 5.2 6.6
CNIH2 6.0 6.8
CPT1C 4.9 5.2
FRRS1L 5.2 5.9
OLFM1 5.8 5.3
OLFM3 5.0
PRRT1 6.5
SHISA6 4.9 5.3
SHISA9 5.1 5.6
7
6.5
6
5.5
5
4.5
4
3.5
b
GluA1-/-
GluA3-/-
Relative abundance
100%
50%
0%
∑GluA1-4
∑Interactors
c
IP (-) 1
IP (+) 1
IP (-) 2
IP (+) 2
IP (-) 3
IP (+) 3
CNIH2
GluA1
GluA1
Long scan
PRRT1
TARP-γ2
TARP-γ8
Antibody heavy chain
TARPγ8
Antibody heavy chain
Long scan
d
GluA1
PRRT1
Homer
Merge
e
GluA3
PRRT1
Homer
Merge
h
Manders' coefficient
0.8
0.6
0.4
0.2
0.0
**
GluA1: PRRT1
GluA3: PRRT1
i
Manders' coefficient
1.0
0.8
0.6
0.4
0.2
0.0
GluA1+PRRT1 :Homer
GluA3+PRRT1 :Homer
f
Intensity (Normalized to max)
0
0.5
1
1.5
2
2.5
3
Distance (μm)
g
Intensity (Normalized to max)
0
0.5
1
1.5
2
2.5
3
3.5
Distance (μm)

Figure 3. Differential GluA1/2 and GluA2/3 AMPAR interactomes. (a) Immunopurification-Mass Spectrometry (IP-MS) using anti-GluA2/3 in GluA1- and GluA3 knock-out (KO) hippocampus. Protein abundances of AMPAR subunits and known interactors are shown as mean $\log_{10}$ iBAQ intensity values, and color coded from high abundance (red) to low abundance (blue). (**b**) Relative mean abundance of AMPAR subunits and interactors, obtained with IP-MS. Per IP the iBAQ intensity values for GluA1-3 were summed and averaged across sample replicates (n=3). The same was done for all identified AMPAR interactors. (**c**) Validation of GluA1 KO IP-MS, using anti-GluA2/3 on GluA1-depleted wildtype hippocampus followed by immunoblotting. Antibody heavy chain in the gel reveals equal sample loading. IP-: IP without prior depletion of GluA1; IP+: IP with prior depletion of GluA1. (**d**) Staining of GluA1 with PRRT1 on wildtype neurons to analyze colocalization. Dendrite images (left) with a zoom in on selected puncta (right) are shown (n=49 fields of view; N=3 cultures). (**e**) Staining of wildtype neurons with GluA3 and PRRT1 (left), and a zoom in on selected puncta (right) (n=83 fields of view; N=3 cultures). (**f**) Line graphs revealing the relative intensity of GluA1 and PRRT1 in consecutive GluA1 positive puncta, or (**g**) GluA3 and PRRT1 in consecutive GluA3-positive puncta. (**h**) Mander's overlap coefficients revealing the fraction of GluA1 or GluA3 colocalizing with PRRT1. (**i**) Mander's overlap coefficient revealing the fraction of colocalizing GluA1 or GluA3 with PRRT1 that overlap with Homer. Mean Manders' Coefficients are shown ± s.e.m.; ** $p < 0.01$. Image scale bar = 1 µm; Zoom-in scale bar = 0.5 µm.

PRRT1 and TARP-γ8 are direct binding partners forming an AMPAR subcomplex especially near the synapse

The AMPAR IP-MS data and quantitative proteomics in wildtype and GluA1- and GluA3 KO synaptic fractions revealed a strong co-occurrence of TARP-γ8 and PRRT1 with GluA1/2 (Figure 1-3). We therefore hypothesized that these AMPAR interactors are part of a shared AMPAR subcomplex. To test this, we first performed IP-MS using anti-TARP-γ2/(4)/8 and anti-PRRT1 antibodies (sFigure 6).

IP-MS using antibodies against TARP-γ2/(4)/8 copurified high amounts of GluA1, GluA2, GluA3, and revealed PRRT1 as one of the most abundant proteins in TARP-containing complexes (Figure 4a). Additionally, the cornichon proteins (CNIH2, -3) were enriched with high abundance (Figure 4a). Other interactors were only copurified with >10-fold lower intensity values (Figure 4a). Anti-PRRT1 co-purified GluA1/2, CNIH3, TARP-γ8, TARP-γ2 and RAP2B (Figure 4a), demonstrating the presence of a TARP-γ8-PRRT1 assembly by both approaches. In addition, we performed immunocytochemistry on hippocampal neurons with anti-TARP-γ8 and anti-PRRT1 to reveal their colocalization by super-resolution microscopy (Figure 4 b-d). Approximately 30% of TARP-γ8 immunoreactivity showed immunoreactivity for PRRT1 (Manders' coefficient: 0.30 ± 0.017), and 14% of PRRT1 immunoreactivity showed immunolabeling for TARP-γ8 (0.14 ± 0.009) (Figure 4c). A large fraction colocalizing TARP-γ8 and PRRT1 (59%) overlapped with Homer positive puncta, imaged at confocal resolution (Manders' coefficient: 0.59 ± 0.02) (Figure 4c). TARP-γ8-PRRT1 revealed especially strong signal at the edge of Homer positive puncta (Figure 4d), together revealing these proteins mostly associate near synapses.

Both TARP-γ8[204] and PRRT1[46] are known to directly bind AMPAR subunits. Similarly, AMPAR interactors FRRS1L and CPT1C bind the AMPAR directly, in addition to binding each other[80].To test if also TARP-γ8 and PRRT1 can bind in absence of AMPAR subunits, we purified overexpressed TARP-γ8-myc from HEK293 cells in the presence of PRRT1-HA (Figure 4e). Indeed, isolation of TARP-γ8-myc revealed co-assembly with PRRT1 demonstrating these proteins can directly interact (Figure 4e).

To further scrutinize this TARP-γ8-PRRT1 assembly as a subcomplex of the AMPAR in the hippocampus, we investigated the migration of TARP-γ8 and PRRT1 immunopurified native complexes on BN-PAGE followed by mass spectrometry (termed IP-BN-PAGE-MS), as described previously (Figure 4f)[176]. Following IP, native complexes were eluted with an epitope-mimicking peptide, mixed with marker proteins and separated by size on a BN-PAGE gel. The gel was cut in consecutive slices that were separately analyzed by mass spectrometry for protein identification and quantification (Figure 4f). Protein abundance values were normalized to their max intensity across the gel, and gel slices were numbered relative to the 720 kDa spiked-in marker protein.

In the gel, purified TARP-γ8 and PRRT1 were expected to co-migrate together with GluA1 in the migration range of the AMPAR at ~720 kDa and higher (sFigure 7). Indeed, IP-BN-PAGE-MS of anti-TARP-γ2/8 revealed highest abundance of TARP-γ8 between slice -14 till 1, peaking above the 720 kDa spiked in marker protein (slice -3) (Figure 4g). In the same range also PRRT1 and GluA1 co-migrated, peaking at slightly higher (slice -5) or lower (slice 1) molecular weight, respectively, with large overlapping migration profiles (Figure 4g). Similarly, IP-BN-PAGE-MS of PRRT1 revealed peak abundance of PRRT1 above the 720 kDa marker (slice -4), migration across a broad range of molecular weights, and large overlapping migration profiles of both TARP-γ8 (peaking at slice -6) and GluA1 (peaking at slice -4) (Figure 4h). Migration of TARP-γ8 and PRRT1 bait protein below the 720 kDa marker in their respective IP-BN-PAGE-MS experiments, may result from disassembly in the BN-gel or represent native AMPAR-independent complexes. Taken together, these data is in line with the presence of a TARP-γ8- PRRT1 containing AMPAR subcomplex.

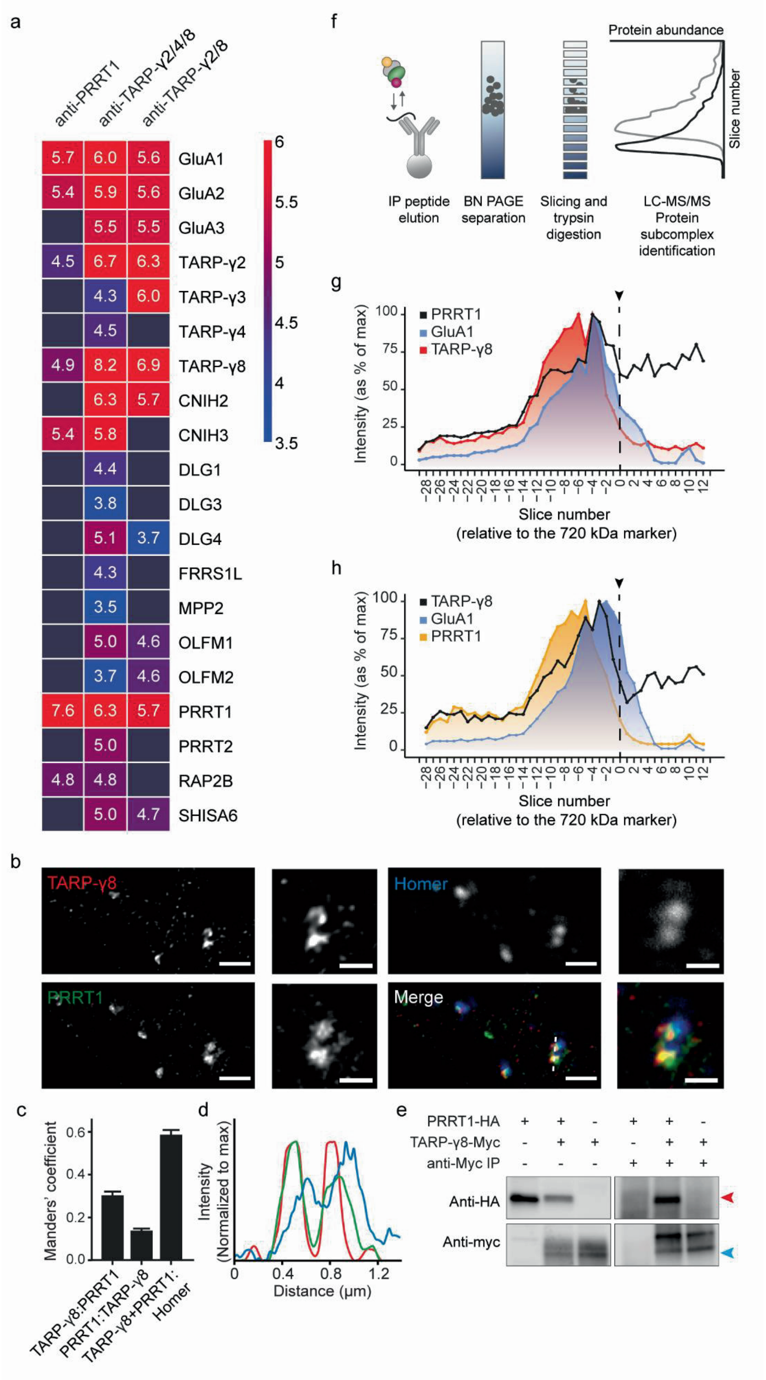

	anti-PRRT1	anti-TARP-γ2/4/8	anti-TARP-γ2/8
GluA1	5.7	6.0	5.6
GluA2	5.4	5.9	5.6
GluA3		5.5	5.5
TARP-γ2	4.5	6.7	6.3
TARP-γ3		4.3	6.0
TARP-γ4		4.5	
TARP-γ8	4.9	8.2	6.9
CNIH2		6.3	5.7
CNIH3	5.4	5.8	
DLG1		4.4	
DLG3		3.8	
DLG4		5.1	3.7
FRRS1L		4.3	
MPP2		3.5	
OLFM1		5.0	4.6
OLFM2		3.7	4.6
PRRT1	7.6	6.3	5.7
PRRT2		5.0	
RAP2B	4.8	4.8	
SHISA6		5.0	4.7

Figure 4. Identification of a TARP-γ8: PRRT1 containing AMPAR subcomplex. (a) Immunopurification-Mass Spectrometry (IP-MS) with antibodies against TARP-γ8 and PRRT1 in wildtype hippocampus. Protein abundances of AMPAR subunits and known interactors are shown as mean $\log_{10}$ iBAQ intensity values, and color coded from high abundance (red) to low abundance (blue). All values above the 0.75 quantile ($>10^6$) were capped to maximum (red) to prevent the bait protein(s) from dominating the scaling. (**b**) TARP-γ8 and PRRT1 colocalization analysis on wildtype hippocampal neurons by STED microscopy. Dendrites labeled for TARP-γ8 and PRRT1 with a zoom in on selected puncta (right) (n=55 fields of view; N=2 cultures). (**c**) Manders' overlap coefficients revealing the fraction of TARP-γ8 positive for PRRT1; fraction of PRRT1 positive for TARP-γ8, and the fraction of colocalizing TARP- γ8 and PRRT1 overlapping with Homer. (**d**) Line graph revealing the relative intensity of TARP-γ8 and PRRT1 in consecutive TARP-γ8 positive puncta near Homer positive puncta. Mean Manders' Coefficients are shown ± s.e.m. Image scale bar = 1 μm; Zoom-in scale bar = 0.5 μm. (**e**) TARP-γ8-myc (~50 kDa) can directly bind to PRRT1-HA (~37 kDa) as shown by co-purification from HEK293 cells, using a Myc antibody. Blue arrowhead points to the 50 kDa marker; red arrowhead points to the 37 kDa marker the sizes of TARP- γ8 and Prrt1 respectively. (**f**) IP-Blue Native Polyacrylamide Gel Electrophoreses BN-PAGE-MS explained: after IP, target proteins were eluted from the antibody using an epitope mimicking peptide. Native complexes were separated by size on a BN gel, cut in 70 consecutive slices which were separately analyzed by mass spectrometry (see M&M for further detail). (**g**) IP-BN-PAGE-MS of anti-PRRT1 proteins revealing the migration profile of PRRT1, GluA1 and TARP-γ8. (**h**) IP-BN-PAGE-MS of anti- TARP-γ8 proteins revealing the migration profile of TARP-γ8, GluA1 and PRRT1. Protein abundance values were normalized to their max intensity across the gel. On the x-axis, slices are numbered relative to the 720 kDa spiked-in marker protein.

Discussion

In the current study, we analyzed the separate interactomes of GluA1/2 and GluA2/3 receptors using wildtype and GluA1 KO or GluA3 KO hippocampi. Interaction proteomics revealed TARP-γ8, CNIH2 and PRRT1 as highest abundant interactors of the GluA1/2 subtype specifically, whereas GluA2/3 IP-MS revealed strongest co-purification of TARP-γ2, CNIH2 and OLFM1. Further co-expression analysis revealed that TARP-γ8-PRRT1 directly interact, and STED microscopy showed co-assembly into an AMPAR subcomplex especially near the synapse.

In the past decades, multiple AMPAR interactors have been identified[46,81]. Known AMPAR binding partners vary in their interaction strength and stability[46]. The IP-MS protocol used in the current study, favored the identification of a subset of established interactors. These included the more stable interacting transmembrane proteins, consistently identified by proteomics studies, and which are considered "core" interactors[46,193].

Previous IP-MS analysis on the total pool of hippocampal AMPARs revealed TARP-γ8 and CNIH2 as most abundant interactors[83]. In the current study, TARP-γ8, CNIH2 and PRRT1 were identified as highest abundant interactors of the GluA1/2 receptor subtype specifically. In contrast to the GluA1/2 receptor, IP-MS on GluA2/3 receptors revealed strongest interaction with TARP-γ2, CNIH2 and OLFM1. These latter proteins may therefore be of highest interest for functional studies on the GluA2/3 receptor subtype.

Of the GluA2/3 isolated interactors, CNIH2 was most strongly co-purified. This is in contrast with a previous report revealing lack of CNIH2 interaction with GluA2/3 receptors purified from GluA1 KO mice using immunoblotting as read out[205]. It was suggested that GluA1 is necessary for binding CNIH2 to native AMPARs[44,205]. Our IP-MS data reveals that GluA1 is not required for binding CNIH2.

In the current study, we observed an AMPAR subtype containing both GluA1 and 3 subunits in hippocampus. The GluA1/3 receptor subtype has been observed in previous studies[46,51,52], but is often overlooked. We validated its presence in mouse hippocampus by direct purification with GluA1 or GluA3 specific antibodies. In addition, we revealed PRRT1 as an interactor of this AMPAR subtype. Whereas GluA1 and PRRT1 co-purified with GluA3 in wildtype samples, they were both absent in GluA2/3 IP-MS performed on GluA1 KO mice. Further experiments are necessary to determine additional interactors of the GluA1/3 receptor subtype.

A previous interaction proteomics study revealed strong correlation between TARP-γ8 and PRRT1 across different brain regions[83]. As the authors pointed out, these correlations may arise from co-assembly in native subcomplexes, or co-expression in the same brain regions, cell types and/or subcellular compartments[83]. In the current study, we revealed co-assembly of TARP-γ8 and PRRT1 in an AMPAR subcomplex by TARP-γ8 and PRRT1 IP-MS and IP-BN-PAGE-MS, which at least in part, causes this correlation.

Both TARP-γ8 and PRRT1 revealed a similar expression profile across biochemical synaptic subfractions, including de-enrichment at the PSD[79]. Our microscopy analysis revealed colocalization of these proteins largely overlapping with Homer positive synaptic puncta, revealing this subcomplex exist mainly near synapses.

In a previous report a model was proposed in which the primary function of PRRT1 is to retain AMPARs extrasynaptically, which upon stimulation then may be released allowing other interactors to transport them into the synapse[201]. In the current study, we identified TARP-γ8-PRRT1 as part of an AMPAR co-assembly, and a direct interaction between TARP-γ8 and PRRT1. The identified interaction between these proteins may fulfill a role in this proposed switch. The exact mechanism of AMPAR regulation by PRRT1 and TARP-γ8, and the interplay between these two proteins remains to be established. Exact identification of the PRRT1 binding sites to the AMPAR and TARP-γ8 and posttranslational modifications in absence and presence of activity may prove informative.

IP-MS of TARP-γ8 revealed a > 5 times higher abundance ratio between TARP-γ8 (bait) and PRRT1 (interactor), than observed between PRRT1 (bait) and TARP-γ8 (interactor) in the PRRT1 IP-MS experiments. In agreement with this, TARP-γ8 revealed a higher level of colocalization with PRRT1, than PRRT1 with TARP-γ8. This indicates that a larger portion of TARP- γ8 protein is associated with AMPAR receptors decorated with PRRT1, than the other way around. Possibly a small portion of PRRT1 protein is associated with AMPAR-TARP-γ8, and is additionally part of other AMPAR-(in)dependent interactions.

Materials and methods

Animals- GluA1- and GluA3-KO mice were obtained from the Gria1tm3Rlh/J[203] and Gria3tm1Dgen/Mmnc (RRID:MMRRC_030969-UNC) (MMRRC, Davis, CA) mouse lines, respectively, crossed with C57BL6. All breedings were approved by The Netherlands central committee for animal experiments (CCD) and the animal ethical care committee (DEC) of the Vrije Universiteit Amsterdam.

Of note, GluA1 KO mice revealed strong reduction in the expression of α-synuclein (sFigure 8). Loss of SNCA expression has been observed previously in a sub population of C57BL/6J mice without alteration of additional genes or a noticeable phenotype[206]. As reduced SNCA in the current study is likely due to cross breeding with this C57BL/6J strain, we removed this protein from further analysis.

Antibodies- Detailed information on the antibodies used is shown in the Supplemental Materials and Methods.

Preparation of crude synaptosomal fractions- Biochemical fractions containing crude synaptosomes and microsomes (P2+M) were prepared as previously described[84] (Supplemental Materials and Methods).

Immuno-purifications/in-gel digestion/DDA analysis- Proteins were extracted from P2+M using n-Dodecyl β-D-maltoside (DDM) (Thermo Fisher, Waltham, MA, USA) dissolved in sample suspension buffer (25 mM, 150 mM NaCl and protease inhibitor cocktail (Roche, Basel, Switzerland), pH 7.4), at a 1% end-concentration, two times for 1 h at 4 °C. Following each extraction, samples were centrifuged at 20,000 x *g* for 20 min. Next, supernatant was incubated with 10 µg of antibody overnight at 4 °C, followed by incubation with 80 µL of protein A/G PLUS-Agarose beads (Santacruz, Dallas, TX, USA) for 1 h at 4 °C. Samples were centrifuged at 1000 x *g* for 1 minute, supernatant was discarded and beads were washed four times with 1 mL washing buffer containing 0.1% DDM, 150 mM NaCl (Sigma-Aldrich, St. Louis, MO, USA), 250 mM HEPES (Sigma-Aldrich, St. Louis, MO, USA), pH 7.4. SDS sample buffer was added to the final pellet, samples were heated at 98 °C and run on a home-made 10% SDS polyacrylamide gel.

Gels were fixed overnight in 50% ethanol and 3% phosphoric acid (Sigma-Aldrich, St. Louis, MO, USA), washed in MilliQ water and stained with Colloidal Coomassie Blue. Each sample lane was cut in 3-5 slices that were subsequently cut into smaller pieces. The gel pieces were transferred to a Multiscreen HV filter Plate (Sigma-Aldrich, St. Louis, MO, USA), washed and destained with a mixture of 50 mM ammonium bicarbonate (Sigma-Aldrich, St. Louis, MO, USA) in acetonitrile (VWR, Radnor, PA, USA). The gel pieces were dried with 100% acetonitrile, and incubated overnight at 37 °C with trypsin (Mass Spec Grade, Promega, Madison, WI, USA) dissolved in 50 mM ammoniumbicarbonate. Peptides were extracted twice in 0.1 % Trifluoroacetic acid (Protein sequence grade; Applied Biosystems, Warrington, UK) and 50% acetonitrile, followed by extraction in 0.1% Trifluoroacetic acid and 80% acetonitrile. Subsequently the samples were dried in a speed vac (Savant, Thermo Fisher, Waltham, MA, USA) and stored at -20 °C until mass spectrometry analysis.

Peptides were analyzed on an LTQ-Orbitrap discovery (Thermo Fisher, Waltham, MA, USA) mass spectrometer as previously described[84], with some modifications (Supplemental Materials and Methods).

Depletion immuno-purifications- Depletion IPs were performed using a similar protocol as described for the regular IPs, with some modifications (Supplemental Materials and Methods).

Immuno-purifications/BN-PAGE/DDA analysis- IPs were done using the protocol described above, now using 30mg P2+M, 100 µL antibody and 1000 µL of beads. After purification and washing of the samples, purified protein complexes were eluted twice using 500 µg peptide dissolved in 1 mL washing buffer for 1 h. The samples were then concentrated using a 30 kDa filter (Bio-Rad, Hercules, CA, USA) for 30 min, and mixed with BN-PAGE loading buffer (Thermo Fisher, Waltham, MA, USA), 0.5 µL Molecular weight marker (Thermo Fisher, Waltham, MA, USA), 1 µL Coomassie G-250 mix (Thermo Fisher, Waltham, MA, USA). Samples were run on a 3-12% polyacrylamide precast BN-PAGE gel (Thermo Fisher, Waltham, MA, USA), at 1 mA constant current for 1 h and 2 mA constant current for 16 h at 4ºC.

Gels were fixed overnight in 50% ethanol, 3% phosphoric acid, washed in MilliQ water and stained with Colloidal Coomassie Blue. Each sample was cut into 70 slices using a grid cutter (Gel Company, San Francisco, CA, USA), and transferred to a Multiscreen HV filter Plate. Cysteines were derivatized using 1 mM TCEP (Sigma-Aldrich, St. Louis, MO, USA) in 50 mM ammonium bicarbonate for 30 minutes at 37ºC, and incubated with 4 mM methyl methanethiosulfonate (MMTS) (Fluka, Honeywell, Charlotte, NC, USA) in 50 mM ammonium bicarbonate for 15 minutes at room temperature. Next, samples were washed, destained, dried and digested following the in-gel digestion protocol described above. The samples were dried in a speed vac and stored at -20 °C before analysis on the mass spectrometer.

Each slice was analyzed separately on the Triple TOF 5600 (Sciex, Framingham, MA, USA) in DDA mode as described previously[176], with some modifications (Supplemental Materials and Methods).

Co-purification from HEK293 cells- HEK293 cells were plated in 10 cm dishes in Dulbecco's modified Eagle's medium (DMEM, Gibco, Life Technologies, Carlsbad, CA, USA) supplemented with 10 % fetal bovine serum (Invitrogen, Waltham, MA, USA) and 1 % penicillin-streptomycin (Gibco, Life Technologies, Carlsbad, CA, USA) and kept at 37 °C, 95% air and 5% CO2... At ~70% confluency, cells were transfected using polyethylenimine (PEI) and 5 µg plasmid cDNA for TARP-γ8-Myc and PRRT1-HA.

After 48 h, the HEK293 cells were washed with PBS resuspended in extraction buffer (1% DDM, 25 mM HEPES, 150 mM NaCl, and protease inhibitor cocktail, pH 7.4), and incubated for 1 hour at 4ºC. After two consecutive centrifugation steps at 20,000 x g for 15 min. 4ºC, 4 ug of antibody was added to the supernatant, incubated O/N at 4ºC, followed by 1 hour incubation with beads, 4ºC. The samples were washed four times with wash buffer (0.1% DDM, 25 mM HEPES, and 150 mM NaCl) in between centrifugation at 1000 x g, 4ºC, and the purified proteins were eluted by with 2x SDS sample buffer. Input samples were prepared from the supernatant fraction by addition of SDS sample buffer to a 2x final concentration.

BN-PAGE/immunoblot analysis- BN-PAGE for immunoblot analysis was performed following the manufacturer's recommendations (Thermo Fisher, Waltham, MA, USA), with some modification (Supplemental Materials and Methods). Immunoblot analysis was done following the regular immunoblot protocol described in the Supplemental Materials and Methods.

Quantitative proteomics by in-gel digestion/SWATH- Wildtype, GluA1- and GluA3 KO P2+M samples were run on a home-made 10% SDS polyacrylamide gel. Each sample was cut in small pieces, 100 µL of 50 mM ammoniumbicarbonate and 5 mM TCEP was added and incubated for 30 min, 37°C. Next, 100 µL of 50 mM ammoniumbicarbonate and 2.5 mM MMTS was incubated for 15 min, room temperature. The proteins were digested using the in-gel digestion protocol described above.

Peptides were analyzed by micro-Liquid Chromatography–Tandem Mass Spectrometry (LC-MS/MS) using an Ultimate 3000 LC system (Dionex, Thermo Fisher, Waltham, MA, USA) coupled to the TripleTOF 5600 mass spectrometer (Sciex, Framingham, MA, USA). Analysis was done in DIA/SWATH mode, as described previously [183,207,208], with some modifications (Supplemental Materials and Methods).

Primary neuronal culture- Detailed information on the preparation of dissociated hippocampal neuronal cultures is shown in Supplemental Materials and Methods.

Immunocytochemistry- Detailed information on immunolabeling of hippocampal neurons is shown in Supplemental Materials and Methods.

STED microscopy and analysis- Images were acquired on a TCS SP8 gated STED 3X Microscope (Leica, Wetzlar, Germany). Fluorophores were excited with a pulsed white light laser at their excitation peak, and a pulsed 775nm STED laser was used for depletion in the 635nm (GluA1, GluA3 or TARP-γ8) and 580nm (PRRT1) channel obtaining a lateral resolution of ~80 nm. Images in the 488nm (Homer) channel were taken in confocal mode. Images were obtained with a 100x oil objective (NA= 1.4), a mechanical zoom of 5 and the pinhole set at 1 Airy Units (AU). Signals were detected with a gated hybrid detector (HyD) set in photon counting mode.

The images were deconvolved with Huygens Software (Scientific Volume Imaging B.V., Hilversum, The Netherlands) using the Good's Roughness Maximum Likelihood Estimation (GMLE) algorithm, and analyzed with ImageJ extended in the Fiji framework. Analysis was performed on the maximum projections of the z-stack, and a threshold determined by the default algorithm was applied on all channels. The Manders' coefficients were obtained in the coloc2 application. A linear mixed-effects model was used to test the difference in colocalization of PRRT1 with GluA1 or GluA3, controlling for batches of cultures, using the lme4 R package.

Acknowledgements

We would like to thank Prof. Dr. H. Kessels who provided both GluA1 and GluA3 KO mouse lines as a kind gift; and the Microscopy and Cytometry Core Facility at the Amsterdam UMC – Location Vumc for providing assistance in STED microscopy.

Conflict of interest

The authors declare that they have no conflict of interest

Supplemental Figures

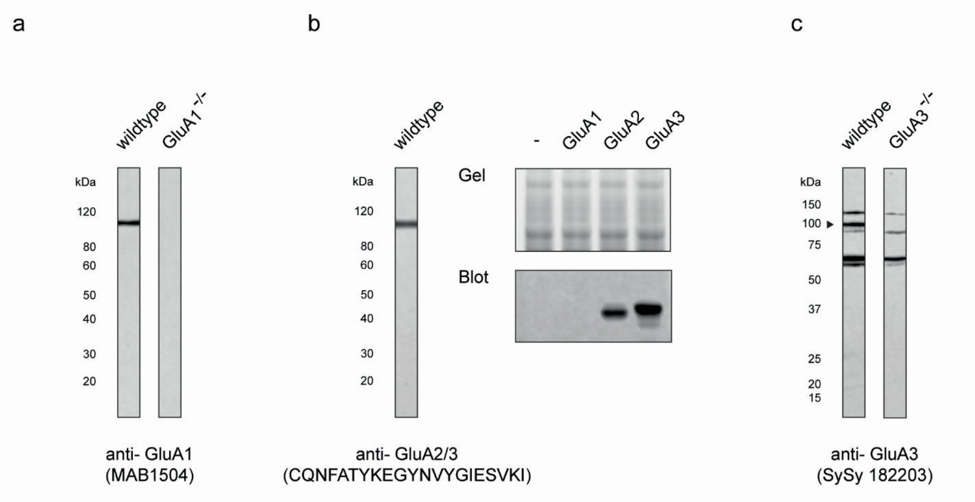

Supplemental Figure 1. Antibodies raised against distinct AMPAR-subunits tested for specificity by immunoblot. (a) Anti-GluA1 revealed a specific band around the molecular weight of GluA1 (~100kDa) in wildtype hippocampus (left). Immunoreactivity in hippocampus of GluA1-knock-out (KO) mice was absent (right). **(b)** Anti-GluA2/3 revealed immunoreactivity at the molecular weight of GluA2 and GluA3 (~100kDa) in wildtype hippocampus (left). Immunoreactivity was only observed in HEK-cell lysate of cells overexpressing GluA2 and -3, while absent in mock transfected cells (-) or overexpressing GluA1 (right). **(c)** Anti-GluA3 revealed immunoreactivity at the molecular weight of GluA3 (~100kDa) in wildtype hippocampus (right), that was absent in GluA3-KO hippocampus (left). Additional immunoreactive bands at different molecular weights were observed using anti-GluA3, that remained in GluA3 KO hippocampus (right), demonstrating cross-reactivity. The arrow indicates the correct molecular weight of GluA3.

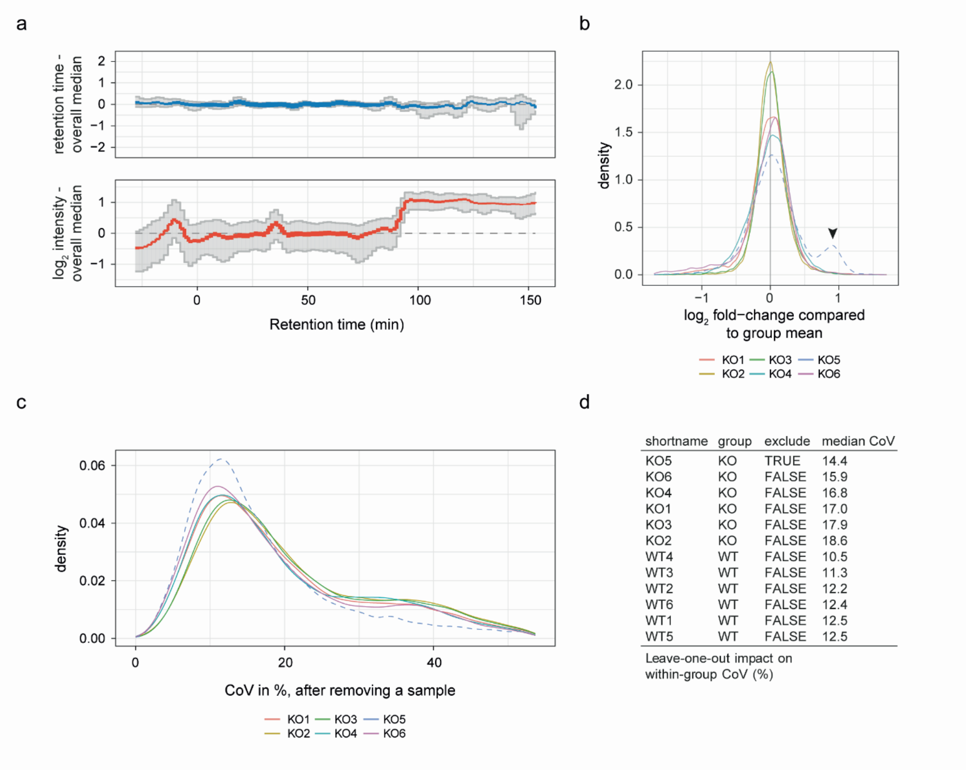

shortname	group	exclude	median CoV
KO5	KO	TRUE	14.4
KO6	KO	FALSE	15.9
KO4	KO	FALSE	16.8
KO1	KO	FALSE	17.0
KO3	KO	FALSE	17.9
KO2	KO	FALSE	18.6
WT4	WT	FALSE	10.5
WT3	WT	FALSE	11.3
WT2	WT	FALSE	12.2
WT6	WT	FALSE	12.4
WT1	WT	FALSE	12.5
WT5	WT	FALSE	12.5

Leave-one-out impact on within-group CoV (%)

Supplemental Figure 2. Outlier in the GluA3 knock-out (KO) proteomics dataset revealed by Mass Spectrometry – Downstream Analysis Pipeline (MS-DAP) quality control. (**a**) Towards the end of the High-Performance Liquid Chromatography (HPLC) run, GluA3 KO5 revealed a large deviation in peptide abundance compared to the group median. Peptide retention time showed normal compared to the overall group median, suggesting proper HPLC performance. Peptide retention time and $\log_2$ intensity values of GluA3 KO5 are shown as a blue or red line, respectively, and are normalized to the median over all samples. Line widths correspond to the number of eluted peptides at each particular timepoint, and the 5% and 95% quantiles are depicted in grey. (**b**) Increased abundance in a selective set of peptides (arrowhead) observed in GluA3 KO5 compared to the rest of the samples. (**c**) Removal of GluA3 KO5 results in a reduced median within-group Coefficient of Variation (CoV) (dashed line). Removal of other samples reveal limited effect on the CoV (solid lines). (**d**) Impact on within-group CoV upon removal of sample in question.

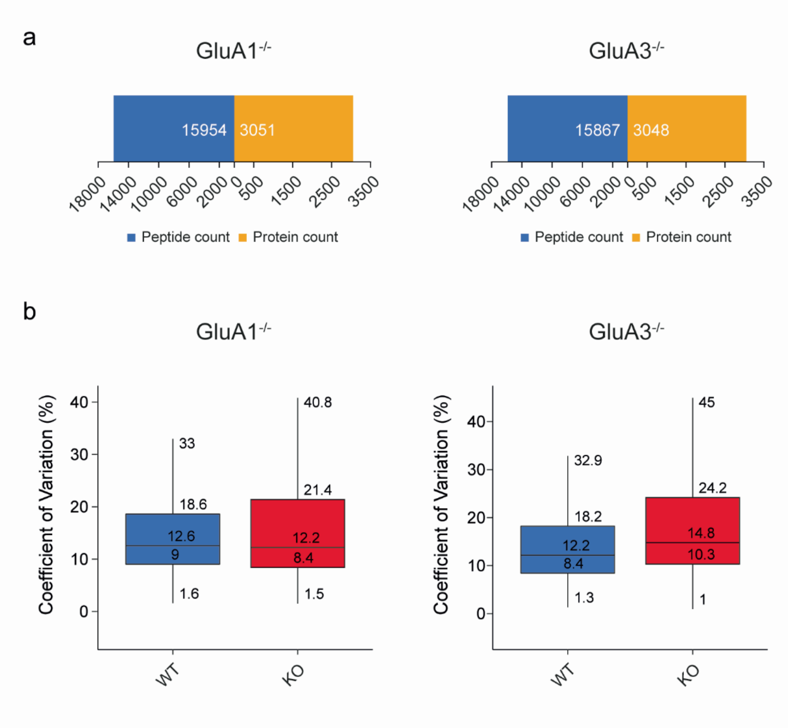

Supplemental Figure 3. Number of proteins and peptides used for differential expression analysis (DEA) in the Mass Spectrometry- Downstream Analysis Pipeline (MS-DAP) and variation among sample replicates in GluA knock-out (KO) proteomics. (**a**) Protein and peptide count after filtering for DEA in the GluA1 KO (left) and GluA3 KO (right) datasets. (**b**) Coefficient of variation of peptides observed in wildtype (WT) and KO samples of GluA1 KO (left) and GluA3 KO (right) mice.

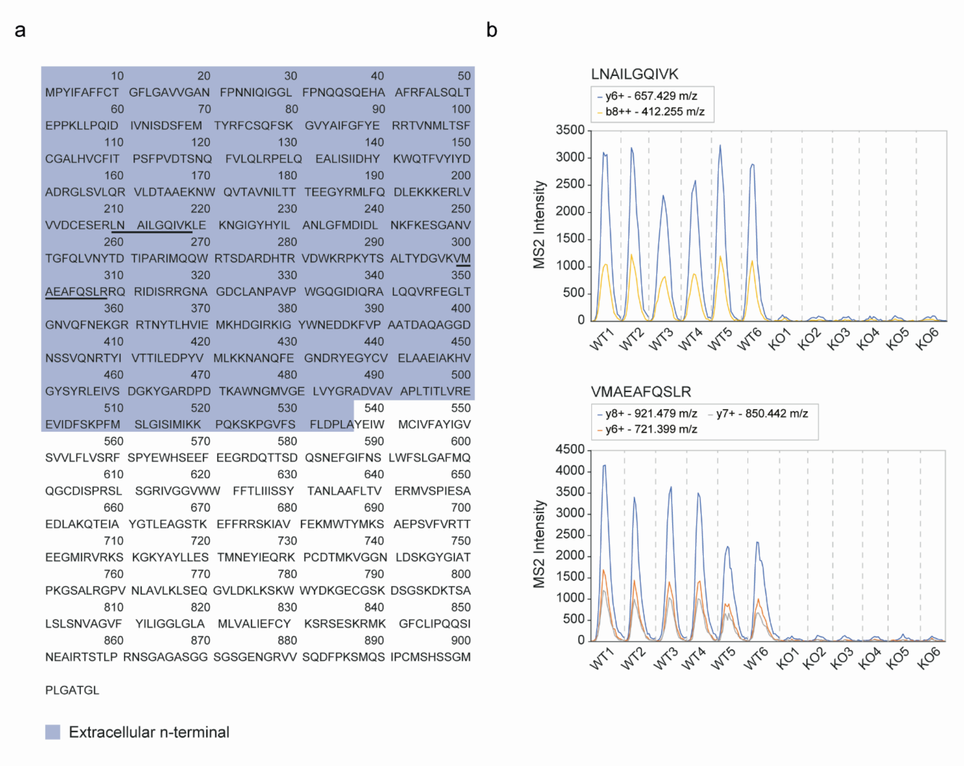

10 20 30 40 50
MPYIFAFFCT GFLGAVVGAN FPNNIQIGGL FPNQQSQEHA AFRFALSQLT
60 70 80 90 100
EPPKLLPQID IVNISDSFEM TYRFCSQFSK GVYAIFGFYE RRTVNMLTSF
110 120 130 140 150
CGALHVCFIT PSFPVDTSNQ FVLQLRPELQ EALISIIDHY KWQTFVYIYD
160 170 180 190 200
ADRGLSVLQR VLDTAAEKNW QVTAVNILTT TEEGYRMLFQ DLEKKKERLV
210 220 230 240 250
VVDCESERLN AILGQIVKLE KNGIGYHYIL ANLGFMDIDL NKFKESGANV
260 270 280 290 300
TGFQLVNYTD TIPARIMQQW RTSDARDHTR VDWKRPKYTS ALTYDGVKVM
310 320 330 340 350
AEAFQSLRRQ RIDISRRGNA GDCLANPAVP WGQGIDIQRA LQQVRFEGLT
360 370 380 390 400
GNVQFNEKGR RTNYTLHVIE MKHDGIRKIG YWNEDDKFVP AATDAQAGGD
410 420 430 440 450
NSSVQNRTYI VTTILEDPYV MLKKNANQFE GNDRYEGYCV ELAAEIAKHV
460 470 480 490 500
GYSYRLEIVS DGKYGARDPD TKAWNGMVGE LVYGRADVAV APLTITLVRE
510 520 530 540 550
EVIDFSKPFM SLGISIMIKK PQKSKPGVFS FLDPLAYEIW MCIVFAYIGV
560 570 580 590 600
SVVLFLVSRF SPYEWHSEEF EEGRDQTTSD QSNEFGIFNS LWFSLGAFMQ
610 620 630 640 650
QGCDISPRSL SGRIVGGVWW FFTLIIISSY TANLAAFLTV ERMVSPIESA
660 670 680 690 700
EDLAKQTEIA YGTLEAGSTK EFFRRSKIAV FEKMWTYMKS AEPSVFVRTT
710 720 730 740 750
EEGMIRVRKS KGKYAYLLES TMNEYIEQRK PCDTMKVGGN LDSKGYGIAT
760 770 780 790 800
PKGSALRGPV NLAVLKLSEQ GVLDKLKSKW WYDKGECGSK DSGSKDKTSA
810 820 830 840 850
LSLSNVAGVF YILIGGLGLA MLVALIEFCY KSRSESKRMK GFCLIPQQSI
860 870 880 890 900
NEAIRTSTLP RNSGAGASGG SGSGENGRVV SQDFPKSMQS IPCMSHSSGM

PLGATGL

▨ Extracellular n-terminal

Supplemental Figure 4. Two unique GluA1 peptides identified in GluA1 knock-out (KO) mice. (**a**) Uniprot sequence of GluA1 is depicted in which the sequences of the two GluA1 unique peptides identified in the GluA1 KO mice are underlined. The sequence of the N-terminal domain is highlighted in blue. (**b**) Raw MS2 peptide intensity peaks are shown in all samples for both GluA1-identified peptides.

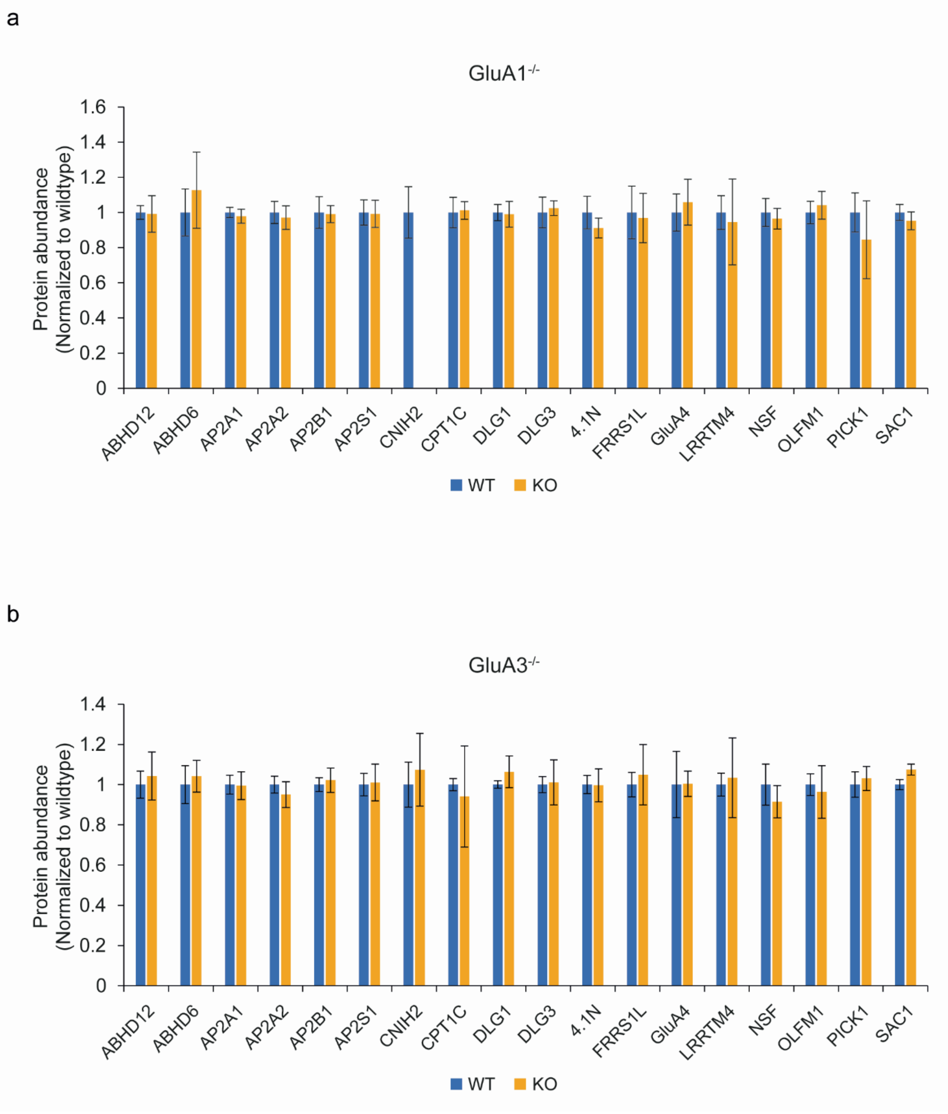

Supplemental Figure 5. Known AMPAR interactors quantified in wildtype and GluA1- or GluA3-knock-out (KO) mice. Protein abundances are shown for known AMPAR interactors, normalized to the wildtype controls. The peptides detected for CNIH2 and GluA3 in GluA1- and GluA3 KO mice, respectively, were not of high-quality in 75% of both wildtype and GluA KO conditions. These proteins were omitted from quantitative analysis.

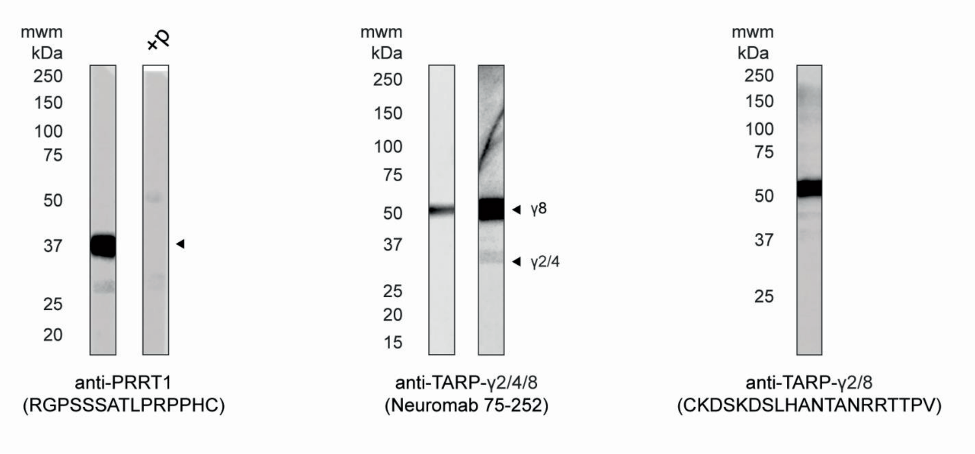

Supplemental Figure 6. Antibodies raised against PRRT1 and TARP proteins tested for specificity by immunoblot on wildtype hippocampus. Arrowheads indicate the correct molecular weight of the protein. +P indicates that the antibody was blocked with a peptide antigen prior to incubation with the blot.

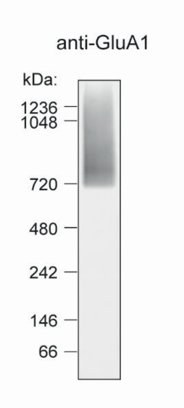

Supplemental Figure 7. Native GluA1 containing AMPAR separation by BN-PAGE. Protein extract from the P2+M fraction was run on a blue-native PAGE gel, and analyzed by immunoblot for GluA1. GluA1 revealed migration at ~720 kDa and higher.

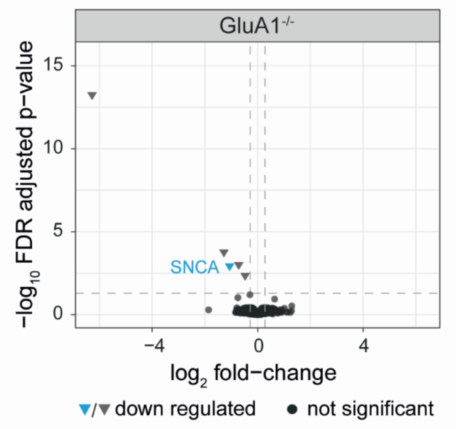

Supplemental Figure 8. Strong downregulation of SNCA in GluA1 KO mouse line revealed by mass spectrometry analysis (eBayes, FDR-adjusted p-value cut-off < 0.05).

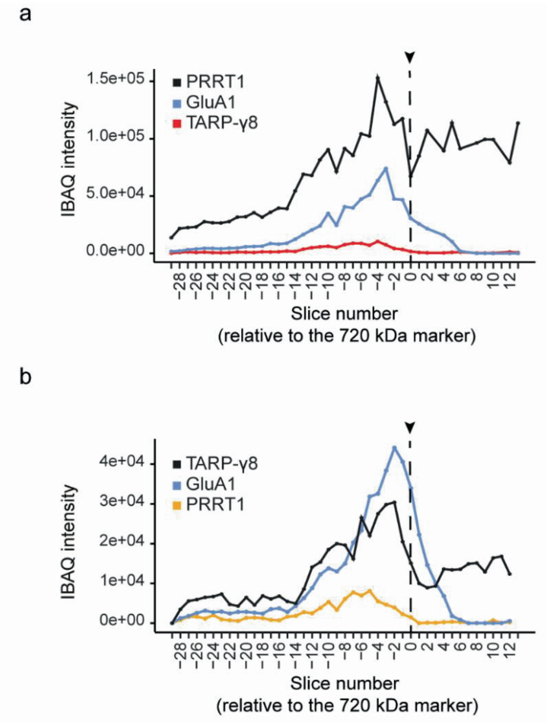

Supplemental Figure 9. Raw iBAQ intensity values of TARP-γ8, PRRT1 and GluA1 in anti-PRRT1 (a) and TARP- γ2/8 (b) IP-BN-PAGE-MS experiments.

Supplemental Materials and Methods

Antibodies- The following primary antibodies were used for indicated applications: Anti-CNIH2 (253 203, rabbit, SySy, Göttingen, Germany) has been used for immunoblot analysis (Figure 2;3) at 1:300. Anti-GluA1 (AB1504, rabbit, Millipore, Burlington, MA, USA) was applied to IP-MS (Figure 1) 1 µg, depletion-IP (Figure 3) 3 µg, immunoblot analysis (Figure 2;3) at 1:1000 and immunocytochemistry (Figure 3) at 1:30. Anti-GluA1 (custom, RTSDSRDHTRVDWKRC, rabbit, Genscript, Piscataway, NJ, USA) was applied for depletion-IP (Figure 3), 30 µg. Anti-GluA2/3 (custom, CQNFATYKEGYNVYGIESVKI, rabbit, Genscript) was used for IP-MS (Figure 1;3), 10 µg. Anti-GluA3 (182 203, rabbit, SySy) was used for IP-MS (Figure 1) and immunoblot analysis (Figure 2). Anti-PRRT1 (L102_45, mouse, Neuromab) was used for immunoblot analysis (Figure 2) at 1:1000 and immunocytochemistry (Figure 3;4) at 1:100. Anti-PRRT1 (custom, RGPSSSATLPRPPHC, rabbit, Genscript) was used for immunoblot analysis (Figure 3) at 1:500, IP-MS (Figure 4), 10 µg, IP-peptide elution (Figure 4), 100 µg. Anti-Shisa6 (custom, CDRYRMTKMHSHPSA, rabbit, Genscript) was used for immunoblot analysis (Figure 2) at 1:1000. Anti- TARP-γ2/4/8 (75-252, mouse, Neuromab) was used for IP-MS (Figure 4), 10 µg, and immunoblot analysis (Figure 2; 3) at 1:500. Anti-TARP-γ2/8 (custom, CKDSKDSLHANTANRRTTPV, rabbit, Genscript) was applied to IP-MS (Figure 4), 10ug, and IP-peptide elution (Figure 4), 100 µg. Anti-TARP-γ8 (AB_2572272, rabbit, Frontier Institute, Ishikari-shi, Japan) was used for immunocytochemistry (Figure 4) at 1:100.

The following secondary antibodies were used for indicated applications: Goat-anti-Rabbit (ST635p, Abberior, Göttingen, Germany) and Goat-anti-Mouse (ST580, Abberior) for immunocytochemistry (Figure 3;4) at 1:200. HRP-conjugated Goat-anti-Rabbit (P044801-2, Agilent Dako, Santa Clara, CA, USA) and HRP-conjugated Goat-anti-Mouse (P044701-2, Agilent Dako) for immunoblot analysis (Figure 2;3) at 1:10,000. Irdye 800CW Goat-anti-Rabbit (925-32211, Licor Biosciences, Lincoln, NE, USA) was applied for immunoblot analysis (Figure 3, PRRT1) at 1:2,500.

Preparation of crude synaptosomal fractions- Adult mice were sacrificed by cervical dislocation, hippocampi were dissected and stored at -80 °C until further use. Frozen hippocampus was homogenized in ice-cold homogenization buffer containing 0.32 M Sucrose (VWR, Radnor, PA, USA) and 5 mM HEPES (Sigma-Aldrich, St. Louis, MO, USA), pH 7.4 with protease inhibitor cocktail (Roche, Basel, Switzerland) in a homogenizer (Sartorius, Göttingen, Germany) at 900 rpm for 12 strokes. Homogenate was centrifuged at 1000 x *g* for 10 min, followed by centrifugation of the supernatant at 100,000 x *g* for 2 h at 4 °C. The resulting pellet containing crude synaptosomes and microsomes (P2+M) was resuspended in a sample suspension buffer (25 mM HEPES, 150 mM NaCl and protease inhibitor cocktail, pH 7.4) and stored at –80 °C until further use.

DDA analysis of immuno-purifications/in-gel digestion – Peptides were re-dissolved in 20 µL 0.1% acetic acid (VWR, Radnor, PA, USA), and loaded on a 5 mm Pepmap 100 C18 (Dionex, Thermo Fisher, Waltham, MA, USA) column (300 µm ID, 5 µm particle size). Peptides were separated on a 200 mm Alltima C18 homemade column (100 µm ID, 3 µm particle size) with High Performance Liquid Chromatography (HPLC) (Eksigent, Sciex, Framingham, MA, USA), using a linear gradient of increasing acetonitrile (VWR, Radnor, PA, USA) concentration from 5% to 35% in 45 min, and to 90% in 5 min. The flow rate was 400 nL/min. The eluted peptides were electro-sprayed into an LTQ-Orbitrap discovery (Thermo Fisher, Waltham, MA, USA). The mass spectrometer was operated in a data dependent manner with one MS (m/z range from 330 to 2000) followed by MS/MS on five most abundant ions. The exclusion window was 25 sec. Obtained MS/MS spectra were searched against the Mouse database (UP000000589_10090, 2021_02) with the MaxQuant software (version 1.6.17.0). The search parameters were set to unique peptides used for protein quantifications, digestion with trypsin and Propiomide (C) as fixed modification.

DDA analysis of Immuno-purifications/BN-PAGE -Peptides were redissolved in 2% acetonitrile with 0.1% formic acid (VWR, Radnor, PA, USA) and trapped on a 5 mm Pepmap 100 C18 column (300 µm i.d., 5 µm particle size). Samples were than fractionated on a 200 mm Alltima home-made C18 column (100 µm i.d., 3 µm particle size). In the mobile phase, the acetonitrile concentration was increased from 5 to 30% in 35 min, to 40% at 37 min, and to 90% for 10 min at a flow rate of 500 nL/min. Peptides were electro-sprayed into a Triple TOF 5600 (Sciex, Framingham, MA, USA) mass spectrometer using an ion spray voltage of 5500 V, ion source gas at 2 p.s.i., curtain gas at 35 p.s.i and an interface heater temperature of 150°C. The MS/MS spectra were searched against the Mouse database (UP000000589_10090, 2013_01_06) using MaxQuant software (version 1.3.0.5), with methyl methanethiosulfonate c, MMTS (C), set as fixed modification.

Low protein abundance per gel slice, resulted in irregular peak detection in MaxQuant (sFigure 9). Subsequently, per protein of interest, three unique high quality peptides were manually peak-picked with consistency in m/z and retention time across all slices in Skyline [167] for further analysis. Individual peptide abundances were normalized to their total intensity over all slices, and protein profiles were computed as the mean value at each slice. In the figures, protein abundances were shown relative to their max intensity.

SWATH analysis- Peptides were first trapped on a 5 mm Pepmap 100 C18 column (300 μm i.d., 5 μm particle size). A 200 mm Alltima home-made C18 column (100 μm i.d., 3 μm particle size) was used for fractionation. In the mobile phase, the acetonitrile concentration was increased from 5 to 18% in 88 min, to 25% at 98 min, 40% at 108 min and to 90% in 2 min, at a flow rate of 5 μL/min. Peptides were then electro-sprayed into a Triple TOF 5600 mass spectrometer with a micro-spray needle voltage of 5500 V. A parent ion scan of 150 ms was followed by a SWATH window of 8 Da with a scan time of 80 ms, that stepped through the mass range between 450 and 770 m/z. For each window, the collision energy was determined based on the energy required for a 2+ ion, centered upon the window with a 15eV spread.

Spectronaut 13.7 (Biognosys, Schlieren, Switzerland) was used for data analysis of the raw files. All SWATH runs were analyzed against a spectral library created with crude hippocampal synaptosomes published previously[208]. Samples of this library were analyzed with the Triple TOF 5600 in DDA mode. Library data was searched against the mouse proteome (the 2021_02 Uniprot release of UP000000589_10090.fasta) in Maxquant, with MMTS (C) as fixed modification. The Mass Spectrometry Downstream Analysis Pipeline (MS-DAP) (version beta 0.2.7.1) (available at https://github.com/ftwkoopmans/msdap) was used for quality control and differential testing. Peptide intensities without normalization in Spectronaut were taken for downstream analysis. The GluA1- and GluA3 knock-out (KO) datasets were analyzed separately. Peptides present in ≥ 75% of the sample replicates of both KO and wildtype condition were used for differential testing. In addition, peptides shared by proteins were removed. The Variation Within Mode Between (VWMB) and modebetween_protein algorithms were used for normalization. Statistical testing was done with the limma eBayes algorithm after rollup to proteins.

Depletion immuno-purifications **–** Proteins were extracted from hippocampal P2+M obtained from two wildtype mice per replicate, with 1% n-Dodecyl β-D-maltoside (DDM) (Thermo Fisher, Waltham, MA, USA) in 25 mM HEPES, 150 mM NaCl and protease inhibitor cocktail, pH 7.4. Samples were centrifuged twice for 20 min, 20,000 x *g* at 4ºC. Half of each sample extract was incubated with 30 μg anti-GluA1 (Genscript, Piscataway, NJ, USA) and 3 μg anti-GluA1 (Millipore, Burlington, MA, USA) overnight at 4 ºC. All samples were then incubated with 200 μl protein A/G PLUS-Agarose beads (Santacruz, Dallas, TX, USA) twice, for 1 h at 4ºC, and centrifuged at 20,000 x *g.* Supernatant was incubated with 10 μg anti-GluA2/3 for 2h at 4ºC. Next, 80 μl beads were incubated for 1 h at 4 ºC, centrifuged at 1,000 x *g* for 1 minute. Supernatant was discarded and beads were washed four times with 1 mL washing buffer (0.1% DDM, 150 mM NaCl, 250 mM HEPES, pH 7.4). SDS sample buffer was added to the final pellet, samples were heated at 98 °C and were used for immunoblot analysis.

BN-PAGE/immunoblot analysis- Proteins were extracted from wildtype hippocampal P2+M in a 1% DDM buffer, containing 25 mM, 150 mM NaCl and protease inhibitor cocktail, pH 7.4, for 1 h at 4ºC. Samples were centrifuged twice at 20,000 x *g,* for 20 min at 4ºC, and mixed with Blue Native Polyacrylamide Gel Electrophoresis (BN-PAGE) loading buffer (Thermo Fisher, Waltham, MA, USA) and Coomassie G-250 mix (Thermo Fisher, Waltham, MA, USA).On a 3-12% polyacrylamide precast BN-PAGE gel (Thermo Fisher, Waltham, MA, USA) 10 µg of protein was loaded. . The gel was then run at 150 V for 45 min. Following replacement of dark blue cathode buffer by light blue cathode buffer, the gel was run an additional 45 min at 150 V and 35 min at 250 V. The gel was incubated for 15 min in transfer buffer and proteins were transferred overnight at 40 V, at 4 ºC, unto a polyvinylidene fluoride (PVDF) membrane (Sigma-Aldrich, St. Louis, MO, USA). The PVDF membrane was incubated with 100% methanol for 10 sec. while shaking, and stained with the regular immunoblot protocol.

Immunoblot analysis- Samples containing SDS loading buffer were run on 5–12% Criterion™ TGX Stain-Free™ precast gels (Bio-Rad, Hercules, CA, USA) and were transferred onto a PVDF membrane overnight. The membranes were then blocked using 5% non-fat milk in Tris-buffered saline (pH 7.4) with Tween-20 (Sigma-Aldrich, St. Louis, MO, USA) (TBST) followed by an overnight incubation with the primary antibody at 4 °C. Then, the blots were washed three times in TBST followed by a 1 h incubation of horseradish peroxidase-conjugated secondary antibody in 3% non-fat milk. The blots were washed three times, incubated with SuperSignal West Femto Chemiluminescent Substrate (Thermo Fisher, Waltham, MA, USA) and scanned on an Odyssey® Fc scanner (Licor Biosciences, Lincoln, NE, USA).

Primary neuronal culture- Hippocampi were dissected from E18 wildtype mice, and incubated in Hank's balanced salts solution (HBSS)(Sigma-Aldrich, St. Louis, MO, USA) containing 7 mM HEPES, pH 7.4, and 0.25% trypsin (Thermo Fisher, Waltham, MA, USA) for 30 min. at 37 °C. After washing, neurons were triturated with fire-polished Pasteur pipettes (VWR, Radnor, PA, USA), counted, and plated in neurobasal medium supplemented with 2% B-27, 1.8% HEPES, 1% glutamax, 1% penicillin/streptomycin and 0.2% 14.3 mM β-mercapto-ethanol (Thermo Fisher, Waltham, MA, USA). Next, 95,000 cells were plated on coverslips that were coated in poly-d-lysine/laminin (Sigma-Aldrich, St. Louis, MO, USA) and treated with 5% heat-inactivated horse serum (Thermo Fisher, Waltham, MA, USA). Cells were kept at 37 °C/5% CO_2 until 17-21 days in vitro.

Immunocytochemistry- Neurons were fixed using methanol for 10 min at -20 °C, and washed twice with phosphate buffered saline (PBS) (Thermo Fisher, Waltham, MA, USA). Cells were permeabilized with 0.5% Triton-X (Sigma-Aldrich, St. Louis, MO, USA) for 10 min, and blocked with 5% normal goat serum (Sigma-Aldrich, St. Louis, MO, USA) in PBS for 1 h at room temperature followed by primary antibody incubation in 1% bovine serum albumin (BSA) (Sigma-Aldrich, St. Louis, MO, USA) and 0.1% Triton-X at 4 °C overnight. Cells were washed twice with PBS, and incubated with secondary antibodies in 1% BSA and 0.1% Triton-X at room temperature for 1.5 h in the dark. After washing in PBS, coverslips were mounted on glass slices using home-made dabco mowiol.

Chapter 5: Age-Dependent Hippocampal Proteomics in the APP/PS1 Alzheimer Mouse Model: A Comparative Analysis with Classical SWATH/DIA and directDIA Approaches

Sophie J. F. van der Spek, Miguel A. Gonzalez-Lozano, Frank Koopmans,
Suzanne S. M. Miedema, Iryna Paliukhovich, August B. Smit and Ka Wan Li

Cells 2021, 10, 1588

Abstract

Alzheimer's disease (AD) is the most common neurodegenerative disorder in the human population, for which there is currently no cure. The cause of AD is unknown; however, the toxic effects of amyloid-β (Aβ) are believed to play a role in its onset. To investigate this, we examined changes in global protein levels in a hippocampal synaptosome fraction of the APP swe/PS1dE9 (APP/PS1) mouse model of AD at 6 and 12 months of age (moa). Data independent acquisition (DIA), or Sequential Window Acquisition of all THeoretical fragment-ion (SWATH), was used for a quantitative label-free proteomics analysis. We first assessed the usefulness of a recently improved directDIA workflow as an alternative to conventional DIA data analysis using a project-specific spectral library. Subsequently, we applied directDIA to the 6- and 12-moa APP/PS1 datasets and applied the Mass Spectrometry Downstream Analysis Pipeline (MS-DAP) for differential expression analysis and candidate discovery. We observed most regulation at 12-moa, in particular of proteins involved in Aβ homeostasis and microglial-dependent processes, like synaptic pruning and the immune response, such as APOE, CLU and C1QA-C. All proteomics data are available via ProteomeXchange with identifier PXD025777.

Introduction

Alzheimer's disease (AD) is the most common age-related neurodegenerative disorder. There is currently no cure, and available medical treatments aim at alleviating symptoms. While the cause of AD is under investigation, accumulation of amyloid-β (Aβ) derived from the aberrant proteolytic cleavage of the amyloid precursor protein by γ- and β-secretases is believed to play an important role in its pathogenesis[138,139]. Deposition of Aβ progresses slowly throughout the brain, originating in basal cortical areas, spreading through the hippocampus and ultimately affecting all areas of the cortex[2]. Additional pathological changes in the brains of AD patients include the presence of neurofibrillary tau tangles, astro- and microgliosis, synapse loss and neuronal death[2].

APPswe/PSEN1dE9 transgenic mice[209] express two human pathologically mutated genes, the Amyloid Precursor Protein swe and Presenilin 1 dE9 (further mentioned as APP/PS1). The APP/PS1 mouse model is one of the most widely used to study AD[210] and specifically recapitulates the amyloid production aspect of the disease. For example, APP/PS1 mice show early elevated Aβ production and plaque formation in the hippocampus observed at 6 months of age (moa), which increases progressively with age[211]. In addition, these mice show synaptic dysfunction[189,212], presence of reactive astrocytes[213] and microglia[214], and multiple forms of memory impairments[189,215]. Studies have indicated synapse loss as early events in AD, which especially affect the hippocampus, and correlates with cognitive decline[2,132]. Aβ exists in multiple forms and appears to play an important role in synapse toxicity[2]. As synapse dysfunction and/or loss are believed to underlie the early pathology of AD, it is necessary to unravel the temporal changes in molecular and cellular processes encompassing the synapse in relation to the advancing Aβ challenge. To this end, we performed proteomics analysis on hippocampal synapse enriched fractions obtained from 6- and 12-moa APP/PS1 mice and their wildtype controls.

Alterations of molecular and cellular processes can be inferred from changes in protein expression levels. Proteomics technology, capable of quantifying thousands of proteins from a small sample size, is the method of choice to shed light on this. Data independent acquisition (DIA), also referred to as Sequential Window Acquisition of all THeoretical fragment-ion (SWATH)[216], is a quantitative proteomics methodology that offers quantification of a high number of proteins with low technical variation and number of missing values. Classical SWATH analysis requires a project-specific spectral library generated from separate data-dependent acquisition (DDA) runs for protein identification. A recently improved directDIA workflow now enables the creation of a spectral library directly from the SWATH samples, bypassing the need for additional mass spec run-time and sample fractionation[217,218].

In the present study, we used SWATH to examine differential protein expression levels in hippocampal synaptosomes of 6- and 12-moa APP/PS1 mice. First, we compared the use of directDIA versus a project-specific spectral library, and we revealed that directDIA preferentially identifies high-intensity peptides, consistently across all sample replicates, resulting in high data completeness. Importantly, using either method resulted in the detection of a largely overlapping group of significantly regulated proteins, which, together, validates the directDIA workflow as a good alternative to the use of a DDA library. Subsequently, we applied directDIA to both 6- and 12-moa datasets and used the Mass Spectrometry Downstream Analysis Pipeline (MS-DAP) for differential expression analysis and protein candidate discovery. We observed upregulation of multiple AD-associated proteins in the 12-moa APP/PS1 mice. At 6 months, these proteins revealed no regulation or lower levels of regulation. Proteins most differentially regulated between the two ages were those that are implicated in Aβ homeostasis and microglial-dependent synaptic pruning and/or immune activation such as APOE, CLU and C1QA-C.

Results

We first investigated the enrichment of synaptic proteins in the synaptosomal sample preparation and suitability of directDIA to reveal the effects of APP/PS1 Aβ expression on synaptic protein levels in animals at 6 and 12 moa. Synaptosomes were isolated using a standard protocol that in the past showed high reproducibility[79,194,219,220]. We performed GO-enrichment analysis on all proteins identified in the synaptosomal preparations under investigation in the current study. Using total brain genome as background, this revealed 'synapse' as strongest enriched term in both 6- and 12-moa datasets (Figure S1).

We continued investigating the suitability of directDIA for the analysis of our datasets. Label-free quantification mass spectrometry can be performed in DDA or DIA/SWATH mode. The classic approach of SWATH analysis uses a spectral library generated from extensive DDA analysis for protein identification. Recent developments in data analysis enable the construction of a library directly from the SWATH data in a workflow called directDIA[217,218]. Here we performed SWATH analysis and used the new software suite Spectronaut 14 containing the directDIA (2.0) workflow.

For comparison, we first searched the 12-moa APP/PS1 dataset (*n* = 6/condition) against our standard in-house hippocampal DDA-based spectral library in Spectronaut for peptide and protein identification and quantification, and we ran the data through MS-DAP, a recently released downstream analysis pipeline for quantitative proteomics (available at https://github.com/ftwkoopmans/msdap; version beta 0.2.5.1). This newly developed all-in-one analysis tool provided extensive quality control plots, allowed filtering and normalization of data, and revealed significantly changed proteins between experimental conditions by differential testing. The analysis resulted in the detection of 31,670 peptide precursors on average per sample. A sizeable fraction of peptides fell below the 0.01 confidence threshold and represents potential false positives (Figure 1a; Figure S2). Filtering out the low-quality precursors with a q-value > 0.01 removed, on average, 11,058 precursors (35%) per sample. On average, 20,612 (65%) precursors were retained per sample that were mapped to 19,413 target peptides and 3374 proteins (Figure S3a). A total of 15,306 peptides were quantified in all samples (Figure 1b).

To assess the performance of directDIA for analysis, we generated an internal spectral library with the same 12-moa dataset using the directDIA feature in Spectronaut 14. Using the library from directDIA, we detected on average 22,600 precursor peptides per sample. When the precursors were filtered on quality, per sample, an average of 4972 precursors (22%) with a q-value > 0.01 were removed, and 17,628 (78%) identifications were retained. These retained precursor identifications mapped to an average of 12,473 unique peptides and 2304 proteins per sample (Figure S3b). This is 36% and 32% fewer peptides and proteins than observed in the search against the project-specific spectral library. Against this apparent disadvantage of directDIA, the confidence score distributions clearly showed that the relative number of potential false-positive identifications, and loss of identifications after filtering for quality, was much lower using directDIA (Figure 1c; Figure S4). Of interest, the use of directDIA results in a high data completeness with nearly all identified peptides (98%) consistently observed across all sample replicates (Figure 1d).

Using directDIA a total of 12,517 peptides with a q-value ≤ 0.01 were identified in the entire 12-moa dataset, and 23,061 using the spectral library (Figure S5a). The large number of peptides uniquely identified using the spectral library (11,574) (Figure S5a) were of lower intensity (Figure S5b) and quality (Figure S5c) than the peptides identified in both the spectral library and directDIA (11,487). The intensities of peptides shared by both searches showed a high correlation (R^2 = 0.95) (Figure S5c), suggesting these peptides are based on the same peaks, and both workflows perform, to a large extent, equally.

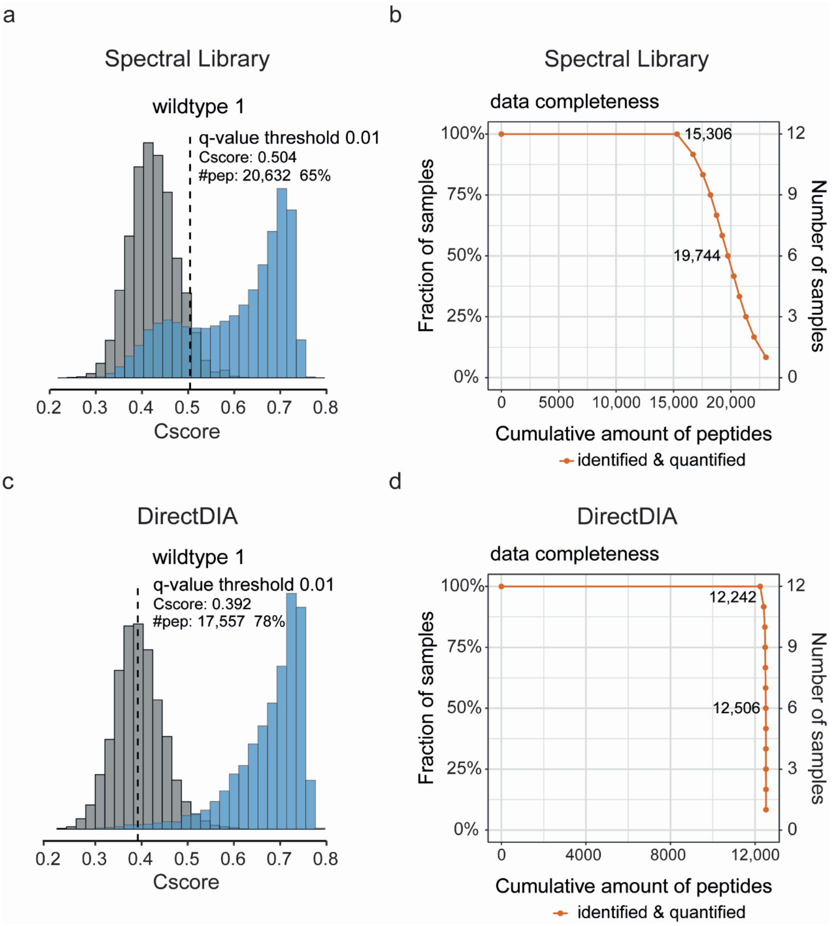

Figure 1. Comparison between the use of a Data Dependent Acquisition (DDA)-based spectral library or directDIA for protein identification and quantification. (**a**) Exemplary histogram of one sample (wildtype 1) showing both target (blue) and decoy (grey) confidence scores (cscores), indicating the level of confidence of peptide identification using the DDA-based spectral library. The q-value confidence threshold of 0.01 is shown as a dotted line, and the associated cscore and number of peptides quantified above this threshold are reported. (**b**) Cumulative distribution showing the number of peptides consistently identified across the range of samples, using the DDA-based spectral library. The exact number of peptides identified are shown at 100% or 50% of samples. (**c**) Analogous to panels a and b: an exemplary histogram of the same sample is shown to visualize target and decoy cscores obtained after identification of peptides in the raw SWATH data using directDIA. (**d**) A cumulative distribution showing the number of peptides consistently identified across the samples, using directDIA. Cscore histograms of all individual samples run against the DDA-based spectral library or directDIA library are reported in Figures S2 and S4, respectively.

To compare the effects of peptide identification using the DDA-based spectral library or directDIA on further downstream analysis, we first ran a differential expression analysis (DEA) on the 12-moa APP/PS1 experimental group and their wildtype controls searched against both types of libraries. For each search, DEA was performed using peptides detected with a q-value ≤ 0.01 in at least 75% of the samples in each experimental group. In addition, peptides shared between proteins were removed. DEA using the DDA-based spectral library and directDIA was performed on 17,153 peptides that mapped to 3039 proteins, and 12,441 peptides mapped to 2300 proteins, respectively (Figure 2a). Most proteins retained for DEA were observed in both dataset searches (74%) (Figure 2b). Those proteins observed only using the DDA-based spectral library were, for the largest part, based on one peptide (67%) (Figure 2c) and, as expected based on the earlier peptide analysis, of lower abundance (Figure S6).

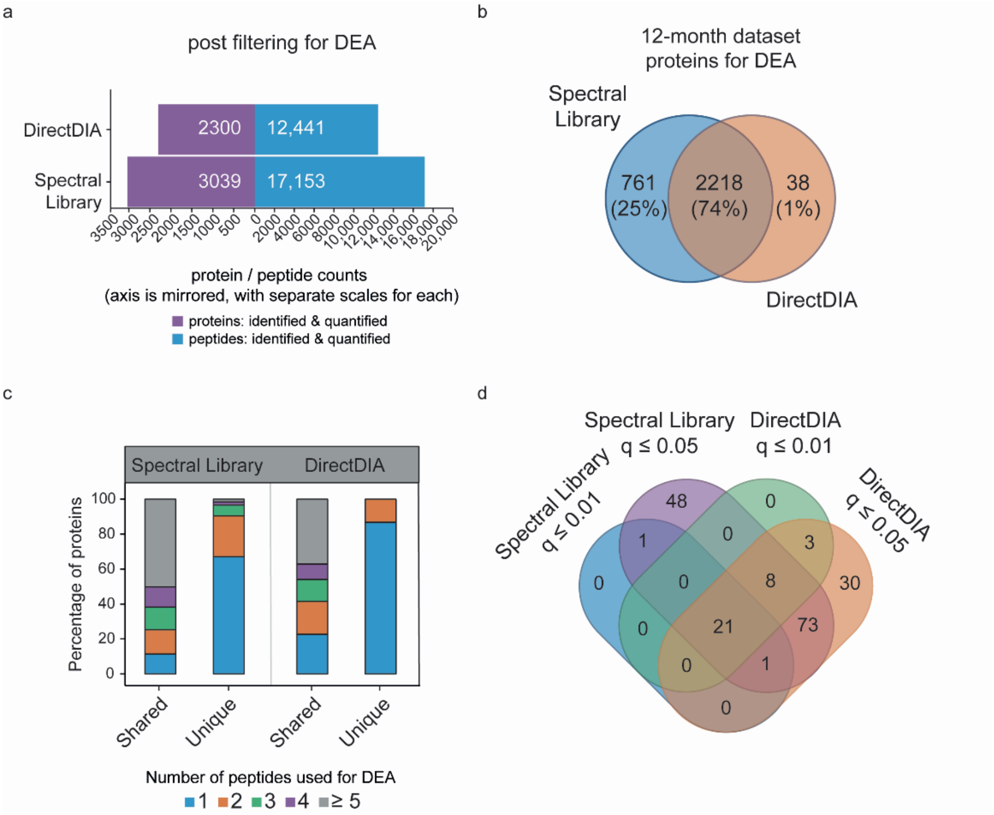

Figure 2. Characterization of proteins used for differential expression analysis in MS-DAP obtained by a DDA-based spectral library or directDIA. (**a**) Number of proteins and peptides that remain after filtering for differential expression analysis. (**b**) Number of unique and shared proteins used for downstream analysis identified by the DDA-based spectral library or directDIA. (**c**) The percentage of shared or uniquely identified proteins, using the spectral library or directDIA, that is represented by the specified number of peptides. (**d**) The number of regulated proteins identified using the different library searches and the specified empirical Bayes cut-offs for statistical significance.

Differential testing of protein expression levels revealed 23 and 32 regulated proteins with statistical significance (empirical Bayes corrected p-values, or q-values ≤ 0.01) in APP/PS1 mice versus their wildtype controls using the DDA-based spectral library search and directDIA, respectively (Figure 2d). Importantly, the majority of these proteins (21) were found significantly altered within both searches (Figure 2d). Of the two proteins detected as regulated uniquely in the DDA-based spectral library searched dataset, one showed significance with directDIA search when relaxing the criteria to a q-value ≤ 0.05 (Figure 2d). Relaxing the criteria to a q-value ≤ 0.05 revealed a substantial number of proteins reaching significance only in the DDA-based spectral library (49) or the directDIA library (33) (Figure 2d). Of the 49 significant proteins observed only using the DDA-based spectral library, 16 were not detected with directDIA, and the additional 33 revealed higher fold-changes than observed using directDIA (0.20 ± 0.11 versus 0.15 ± 0.1 log2 fold-change, respectively), which is therefore likely the cause of reaching significance at a q-value ≤ 0.05 using the DDA-based spectral library only. Variation in abundance for these proteins was the same between the two libraries (0.15 ± 0.08 versus 0.15 ± 0.1 SD, respectively). Of the 33 proteins only found significant using directDIA, two were not identified using the DDA-based spectral library. The additional 31 proteins revealed lower variation than observed with the DDA-based spectral library (0.15 ± 0.06 versus 0.27 ± 0.48 SD, respectively), while revealing the same log2 fold-changes (0.18 ± 0.16 and 0.18 ± 0.17, respectively). As directDIA gives high confident peptides, and showed a higher number of significant proteins at a q-value ≤ 0.01, we proceeded with directDIA for our 6-moa dataset in a subsequent analysis.

In the 6-moa dataset (n = 6/condition), quality control using MS-DAP showed a clear outlier in the wildtype group possibly due to a technical issue of the high-performance liquid chromatography run, and was removed from further analysis (Figure S7a-c). Like the 12- moa dataset run with directDIA, the 6-moa dataset showed high data completeness across samples (Figure S8a), and similar numbers of peptides and proteins were detected after filtering for DEA (12,010 and 2469 on average per sample, respectively) (sFigure 8b). Both 6- and 12-moa datasets showed low coefficients of variation, ranging between 8 and 12.3%, per experimental condition (Figure S8c), and the majority of proteins used for DEA were detected and tested in both age groups (78%) (Figure S8d).

In the 6-moa dataset, only a few proteins showed significant regulation with a q-value ≤ 0.01 (Figure 3a). These included NCSTN (one of the subunits of the gamma-secretase PS1 complex), DOCK9 and TXNRD1 that had higher levels in APP/PS1 mice, and GPC4 that showed a decrease in expression (Figure 3b). The level of APP itself was also increased, but at a higher p-value of 0.026 (Figure 3b). In contrast, the 12-moa dataset showed 30 proteins up and 2 down (MTMR1 and GAK) in the APP/PS1 group (Figure 3a). At 12-moa APP showed an increased level, and similar to the 6-moa dataset, a strong increase was observed for NCSTN and DOCK9 (Figure 3b). Besides APP and NCSTN, several of the additional most regulated proteins are known AD risk factors or proteins related to AD pathology, including APOE, CLU and C1QA-C (Figure 3b, Table S1). Indeed, Gene Ontology enrichment analysis in gProfiler using the mouse proteome as background revealed multiple significant terms associated with AD, including “regulation of amyloid fibril formation” (Biological Process) and “Alzheimer’s disease” (WikiPathways) (Figure 4a). Using our custom total list of proteins detected at 12-moa as background, Gene Ontology analysis showed enrichment of terms such as “Membrane proteolysis” (Biological Process) and “lysosome” (Cellular Component) (Figure 4b). Both terms were largely based on APP, APOE and NCSTN. In addition, the lysosomal term included VTI1B, ARL8B, EPDR1, HEXB, SYT11 and the AD-associated proteins PLD3 and LAMP2 (Table S1). An additional known AD-protein not annotated to Aβ, Alzheimer or lysosome-related terms, which was regulated here, was AQP4 (Figure 4b, Table S1).

To reveal possible specific subsynaptic compartments affected in APP/PS1 mice, we performed enrichment analysis with the Synaptic Gene Ontology (SynGO) knowledge base[13]. The list of 34 regulated proteins at 6- or 12-moa contained 11 proteins that were annotated to SynGO (Table S2). The additional proteins were not annotated in SynGO yet, or they came from non-synaptic impurities of the synaptosomal sample preparation with similar biochemical properties. The regulated synaptic proteins were equally annotated to the pre- and post-synapse (Figure S9), without significant enrichment towards a specific subsynaptic localization or function (Tables S3 and S4).

We then performed an Expression Weighted Cell-type Enrichment (EWCE) analysis[221] on the significantly upregulated proteins at 12-moa to distinguish the possible contributions of different cell types to the changed expression levels. This is based on the notion that these proteins will be non-equally expressed over all cell types. For EWCE analysis we used previously published single-cell RNAseq gene expression profiles obtained from mouse hippocampus[222]. We observed overrepresentation of microglial and, to a lesser extent, astrocytic proteins, albeit not significant (Figure 5a), which are therefore likely the major source of the observed increase in protein expression. Proteins with high microglial expression include C1QA-C and HEXB, and proteins showing high astrocytic expression include AQP4, GPC4, CLU and ATP1A2 (Figure S10).

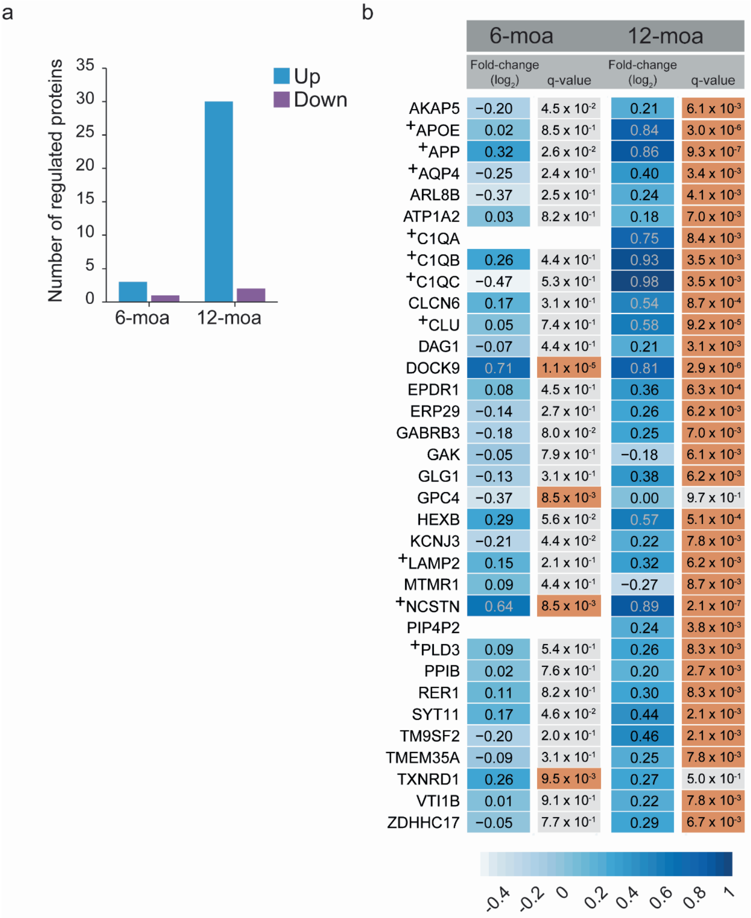

	6-moa		12-moa	
	Fold-change (log$_2$)	q-value	Fold-change (log$_2$)	q-value
AKAP5	−0.20	4.5×10^{-2}	0.21	6.1×10^{-3}
+APOE	0.02	8.5×10^{-1}	0.84	3.0×10^{-6}
+APP	0.32	2.6×10^{-2}	0.86	9.3×10^{-7}
+AQP4	−0.25	2.4×10^{-1}	0.40	3.4×10^{-3}
ARL8B	−0.37	2.5×10^{-1}	0.24	4.1×10^{-3}
ATP1A2	0.03	8.2×10^{-1}	0.18	7.0×10^{-3}
+C1QA			0.75	8.4×10^{-3}
+C1QB	0.26	4.4×10^{-1}	0.93	3.5×10^{-3}
+C1QC	−0.47	5.3×10^{-1}	0.98	3.5×10^{-3}
CLCN6	0.17	3.1×10^{-1}	0.54	8.7×10^{-4}
+CLU	0.05	7.4×10^{-1}	0.58	9.2×10^{-5}
DAG1	−0.07	4.4×10^{-1}	0.21	3.1×10^{-3}
DOCK9	0.71	1.1×10^{-5}	0.81	2.9×10^{-6}
EPDR1	0.08	4.5×10^{-1}	0.36	6.3×10^{-4}
ERP29	−0.14	2.7×10^{-1}	0.26	6.2×10^{-3}
GABRB3	−0.18	8.0×10^{-2}	0.25	7.0×10^{-3}
GAK	−0.05	7.9×10^{-1}	−0.18	6.1×10^{-3}
GLG1	−0.13	3.1×10^{-1}	0.38	6.2×10^{-3}
GPC4	−0.37	8.5×10^{-3}	0.00	9.7×10^{-1}
HEXB	0.29	5.6×10^{-2}	0.57	5.1×10^{-4}
KCNJ3	−0.21	4.4×10^{-2}	0.22	7.8×10^{-3}
+LAMP2	0.15	2.1×10^{-1}	0.32	6.2×10^{-3}
MTMR1	0.09	4.4×10^{-1}	−0.27	8.7×10^{-3}
+NCSTN	0.64	8.5×10^{-3}	0.89	2.1×10^{-7}
PIP4P2			0.24	3.8×10^{-3}
+PLD3	0.09	5.4×10^{-1}	0.26	8.3×10^{-3}
PPIB	0.02	7.6×10^{-1}	0.20	2.7×10^{-3}
RER1	0.11	8.2×10^{-1}	0.30	8.3×10^{-3}
SYT11	0.17	4.6×10^{-2}	0.44	2.1×10^{-3}
TM9SF2	−0.20	2.0×10^{-1}	0.46	2.1×10^{-3}
TMEM35A	−0.09	3.1×10^{-1}	0.25	7.8×10^{-3}
TXNRD1	0.26	9.5×10^{-3}	0.27	5.0×10^{-1}
VTI1B	0.01	9.1×10^{-1}	0.22	7.8×10^{-3}
ZDHHC17	−0.05	7.7×10^{-1}	0.29	6.7×10^{-3}

Figure 3. Differential expression analysis of 6- and 12-moa APP/PS1 mice. (a) Number of significantly higher and lower expressed proteins (empirical Bayes q-value ≤ 0.01) observed at 6- and 12-moa. (b) Fold-changes (log2) and q-values of regulated proteins in at least one of the two datasets. Fold changes are emphasized in color from most extreme decrease (light blue) to highest increase (dark blue). Q-values ≤ 0.01 are highlighted in orange. Proteins labeled with a+ have been implicated in human AD in previous reports, see Table S1.

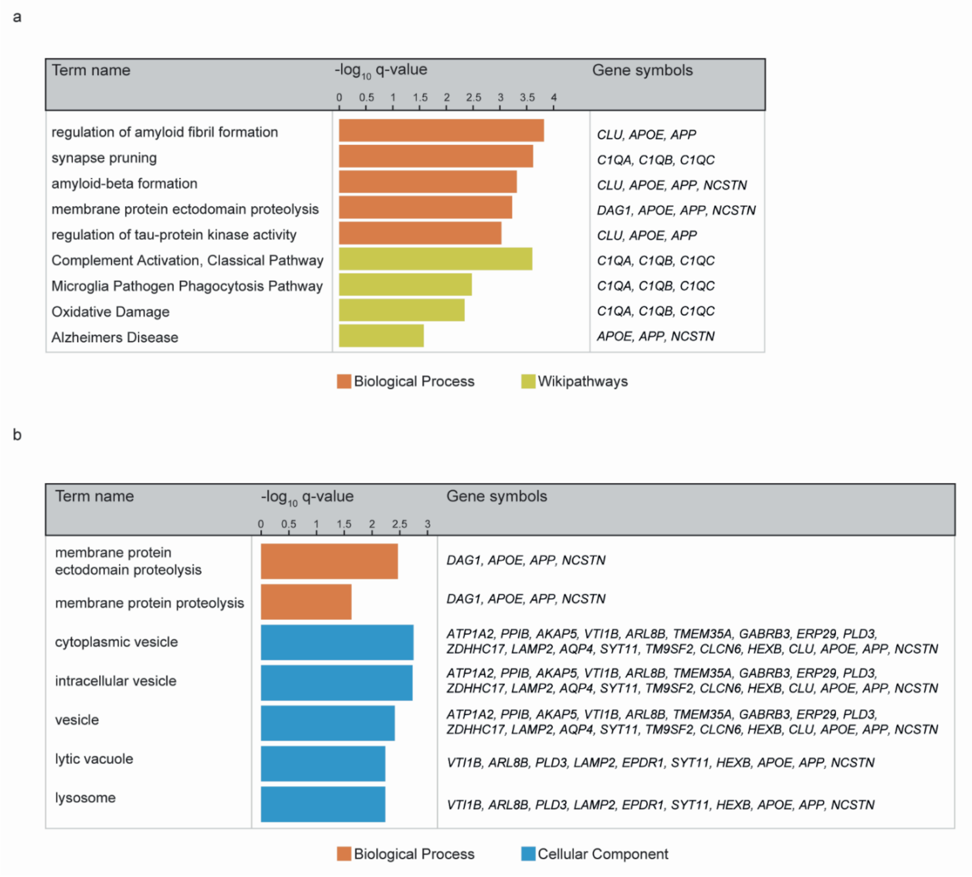

Figure 4. GO enrichment analysis on upregulated proteins in the 12-moa APP/PS1 dataset. (a) Enrichment analysis using the whole mouse genome as background results in terms related to Aβ and AD. (b) The use of the total list of proteins detected at 12-moa as background results in enrichment terms related to proteolysis and lysosome.

The level of APP expression showed an increase over time, and additional protein regulations were also stronger at 12-moa than at 6-moa (Figure 3b). To visualize the progressive temporal changes in expression of regulated proteins directly, we derived the fold change ratios of proteins significant in at least one of the two datasets (Figure 5b). Here we observed that the top 10 of proteins with the highest changing expression levels over time include APP, C1QB/C, APOE, CLU and AQP4 (Figure 5d).

Discussion

Toxicity and accumulation of Aβ is believed to play important roles in AD pathogenesis[138,139], starting in basal cortical areas spreading through the hippocampus and other areas of the cortex[2]. In addition, synapse loss has been indicated as early events in AD that correlate strongly with cognitive impairment[2,132]. Studies have shown that Aβ is important for synaptic failure[2]. As synapse loss especially affects the hippocampus[132], this structure was our brain area of interest.

Because aberrant molecular and cellular changes in and around the synapse are considered to play a part in the cause of AD progression, it is necessary to unravel their temporal changes in relation to the advancing Aβ challenge. To reveal changes in protein expression that may result from the overexpression and aberrant processing of APP into Aβ, we examined the hippocampal proteome of 6- and 12-moa APP/PS1 mice and their wildtype controls.

For our study we employed SWATH technology[216]. Current studies indicate that SWATH yields small variations and few missing values among samples that together enable the detection of subtle changes in expression, and may therefore be the preferred method of choice[183,207]. A typical SWATH experiment requires a project-specific spectral library for peptide identification during a database search. Building a spectral library requires extensive DDA analysis, preferably on the same or similar samples, and measured under comparable conditions to the measurements done on the samples of interest. This increases measurement time, and the conditions to generate the library are often not an exact copy of those while measuring the samples, leading to an increased chance of spectra mismatching. In contrast, directDIA assembles the precursor ions and fragment ions into pseudo–tandem Mass Spectrometry spectra, which can be built into a spectral library by the search against a conventional reference proteome database. The project-specific spectral library search in this study produced more peptides than did a directDIA library search. However, among the uniquely detected peptides, many of these were of lower intensity and quality compared to those identified by both workflows. These peptides are likely causing the reduced consistency observed in peptide detection across the sample replicates. Within the shared peptides generated from directDIA and the project-specific spectral library we revealed a high correlation in peptide intensity. This suggests these peptides are based on the same peaks and implicates that both approaches quantified peptides in similar ways. Importantly, downstream analysis showed that the directDIA protocol detected more significantly regulated proteins with high confidence, in addition to the shared proteins, demonstrating the usefulness of directDIA for database search.

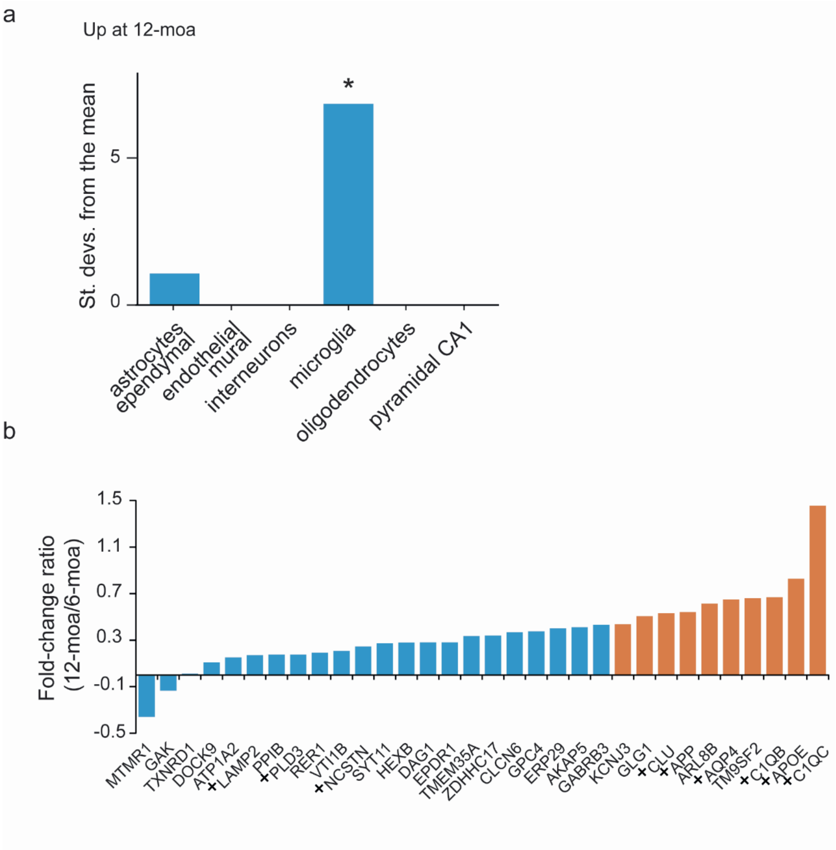

Figure 5. Cell-type enrichment and analysis of changing levels of protein expression over time. (a) Expression Weighted Cell-type Enrichment performed using single cell RNAseq level 1 cell-type data obtained from[222], on the upregulated proteins at 12-moa. * p-value < 0.01. (b) Fold-change ratios are shown for all proteins regulated in at least one of the two datasets demonstrating their level of regulation over time. Proteins labeled with a + have been implicated in human AD in earlier reports, see Table S1. The top 10 most regulated proteins over time are highlighted in orange.

We continued using directDIA for the analysis of protein changes in APP/PS1 mouse hippocampal synaptosomes of 6- and 12-moa. Synaptosomes were isolated with a standard protocol, which in the past has shown enrichment of synaptic proteins with high reproducibility[79,194,219,220]. Additionally, in the synaptosomal preparation under investigation, we observed enrichment of synaptic proteins, as revealed by GO-enrichment analysis. In addition, the synaptosomal fraction may contain structures with similar biochemical properties or structures of contacting non-neuronal cells. For instance, microglia have been implicated in the elimination of synapses during development and under pathological conditions such as exposure to Aβ oligomers[153]. Synapse engulfment and pruning by microglia occurs in a complement factor dependent manner[153,223]. Indeed, highest regulated proteins observed in our dataset are strongly expressed in microglia, as reflected in the cell-type enrichment analysis, and include the complement factors C1QA-C.

Despite enriching for synaptic proteins, surprisingly, only a few synaptic proteins are regulated in the APP/PS1 mice at 6- and 12-moa (e.g., SYT11 and GABRB3). SynGO-analysis revealed no enrichment of these proteins towards a specific subsynaptic compartment or biological process. In contrast, a recent proteomics study on the human (pre-clinical) AD cortex revealed changes in proteins related to the secretory pathway and synaptic vesicle endocytosis (e.g., SYT2 and SH3SGL2)[224], supporting the relevance of synaptic homeostasis in AD disease pathology. Proteins related to these pathways were among early responding, late responding and progressively changing protein groups[224]. In the APP/PS1 mouse model of AD, stronger changes in synaptic vesicle endocytosis proteins have been observed at 3-moa[209,225], suggesting the APP/PS1 model recapitulates especially early synaptic changes induced by Aβ. This is in line with a recent cross-species meta-analysis on human AD transcriptomics and mouse models of AD[226]. Among different human AD studies, the meta-analysis revealed consistent downregulation of gene groups enriched for neuronal genes[226]. The strongest overlap of regulated neuronal genes was observed in mice with a mild pathological burden[226].

In the current study, strongest (up-)regulation of proteins was observed in the 12-moa dataset and contained multiple microglial proteins. At 6-moa we observed no regulation of microglial proteins. In contrast, microglial activation has been observed in multiple amyloidosis mouse models of AD as one of the earliest phenotypes[227–229]. For example, a recent transcriptomics study on microglial cells enriched from AppNL-G-F mice[230] revealed upregulation of microglia in an activated state already at 3-moa[229]. This activated group of microglia was characterized by increased expression of Apoe[227–229], an apolipoprotein involved in lipoprotein homeostasis and clearance of Aβ[231,232]. Removal of Apoe resulted in suppression of microglial recruitment to Aβ-plaques, revealing a pivotal role for this transcript in Aβ-related microglial activity[229]. At 12-moa, we also observed increased levels of APOE and other proteins previously detected in activated microglia, including HEXB, EPDR1, ERP29, RER1, GLG1 and PLD3[227,229].

Lack of observed microglial protein regulation at 6-moa in the current study may be caused by several aspects. First, previous transcriptomics and proteomics studies isolated microglia before protein or transcript extraction[227–229]. As synaptosomes were used in the current study, there is reduced sensitivity towards changes that occur in this specific cell type. For example, APOE is expressed in both microglia and astrocytes, but Apoe mRNA was particularly shown to increase in microglia upon exposure to Aβ[229]. More subtle increases of microglial APOE at earlier timepoints may remain undetected due to dilution of protein changes. In addition, strong, early microglial effects were observed using amyloidosis mouse models, different from the APP/PS1 model used here[227–229]. Of interest, in AppNL-G-F mice[230] the relative number of reactive microglia increased over time from 6% at 3-moa, to 33% at 6-moa and 52% at 12-moa[229]. The same report also revealed an increase in reactive microglia in the APP/PS1 mouse model[209,229], the same model that was used in our current proteomics study[209]. This confirms activation of microglia as a consistent phenotype[229]. However, the APP/PS1 mouse only revealed a 15% increase at 18-moa[229], suggesting activation of microglia in different models follows distinct timelines or differences in severity.

A difference in microglia activation rate may be due to differences in Aβ pathophysiology between amyloidosis mouse models, as suggested in a previous report[227]. In a recent study, APP/PS1 mice (bearing the APPswe and PSEN1L166P mutations)[233] were shown to contain fibrillar Aβ plaque cores at 3-moa, along with protein abundancy alterations in isolated microglia[227]. In contrast, fibrillar Aβ was barely detectable in AppNL-G-F mice[230] of the same age with similar plaque load, and showed no microglia proteome alterations[227]. At higher age, both models expressed dense core fibrillar Aβ and an altered microglial proteome[227]. In line with this, the cross-species meta-analysis showed upregulation of human AD gene groups enriched for microglial genes, most strongly and consistently in mice with severe Aβ pathology[226].

Proteins regulated in the APP/PS1 datasets observed in the current study were over-represented by those involved in APP processing and Aβ formation. For example, NCSTN is an integral component of the γ-secretase complex comprising PS1-NCSTN-APH1-PSENEN, which cleaves APP to produce Aβ peptides[234]. Upregulation of NCSTN suggests increased levels of γ-secretase, likely due to overexpression of the PSEN1 gene in the APP/PS1 mouse model. PS1, APH1 and PSENEN were not detected in the proteomics dataset. The increased expression of APP is also most likely the direct consequence of the over-expression of the human APP gene.

RER1 also showed elevated levels in the APP/PS1 mice. This protein regulates the retrieval of endoplasmic reticulum membrane proteins from the early Golgi compartment[235]. Correspondingly, RER1 was revealed to affect γ-secretase assembly by regulating retention and retrieval of NCSTN and PSENEN[236–238]. Increased levels of RER1 expression cause reduced maturation of APP, negatively regulating the production of Aβ[238]. This suggests in the APP/PS1 mice, elevated levels of RER1 work to compensate for increased APP and NCSTN levels.

APOE and CLU (APOJ) were highly up-regulated in our dataset, and they are well-established genetic risk factors of late-onset AD[239]. Although these are two distinct proteins, they show many similarities. Both APOE and CLU are apolipoproteins mediating lipid transport between cells in the brain[231,240]. These proteins are mainly secreted by astrocytes, in healthy brains, and are associated with immune modulation including activation of microglia[241], and are possibly involved in microglia-associated phagocytosis of Aβ[232]. Thus, increased levels of APOE and CLU in the APP/PS1 dataset may reflect cellular responses towards increased Aβ clearance.

GO analysis revealed additional enriched terms including “Complement Activation, Classical Pathway” as well as “synapse pruning”. These are based on C1QA-C, three complement factors that initiate the classical complement immune response[242]. These proteins are highly expressed by microglia and, together with other complement factors, are found in human and mouse Aβ plaques[243,244]. Increasing evidence shows a detrimental role of C1Q in AD pathogenesis, as it can enhance Aβ fibrillogenesis[245–247], block Aβ uptake by microglia[248] and are involved in aberrant synaptic pruning[153]. Thus, C1Q upregulation observed here likely contributes to AD pathology.

In the APP/PS1 mouse we also observed GO enrichment of proteins expressed in the lysosome, for instance HEXB and LAMP2. Lamp2 revealed high expression in microglia in the single-cell RNAseq data[222]. In addition, Pld3 transcripts and HEXB revealed enriched expression in reactive microglia in AD mice[227,229]. Microglia may be the main source of increased lysosomal proteins observed in the APP/PS1 dataset. Of interest, an AD study on the microglial proteome revealed enrichment of phagocytic and lysosomal proteins alongside impaired microglial phagocytotic capabilities[227]. As the authors suggested, increased phagocytic and lysosomal protein expression in microglia may be part of a compensatory mechanism to enhance microglial phagocytosis of Aβ. This response eventually fails to improve capabilities for the removal of Aβ[227].

Taken together, regulation of proteins involved in APP and Aβ processing (NCSTN, APOE, CLU and RER1), microglial activity (C1QA-C, APOE, HEXB, PLD3, LAMP2, EPDR1, ERP29, RER1 and GLG1 and PLD3) and the endo-lysosome (PLD3, VTI1B, EPDR1, HEXB, ARL8B and LAMP2) in this APP/PS1 mouse model reflect multiple aspects of AD-related processes.

Regulation of these proteins in the APP/PS1 mouse model reinforces their importance in Aβ-induced pathology.

In addition, we observed proteins not linked to AD previously. Several of these have been associated with other neurodegenerative disorders (ZDHHC17 with Huntington's disease[249], SYT11 and GAK with Parkinson's disease[250] and GABRB3 with dementia with Lewy bodies[251]), and may be of special interest for future studies. We also detected dysregulated proteins with no reported relation to AD or neurodegeneration (e.g., AKAP or PIP4P2). Of special interest is DOCK9, which shows significant and high upregulation at both 6- and 12-moa. This suggests a role of DOCK9 as early responder to increased Aβ levels or participation of this protein in the production of Aβ. DOCK9 is a guanine nucleotide-exchange factor (GEF) that activates CDC42, a small effector protein involved in variety of cellular responses including cell migration[252]. Of interest, CDC42 activity has recently been shown to facilitate the microglial migration response to Aβ, downstream of TREM2[252]. TREM2 is a receptor expressed by microglia and is a risk factor for AD[253]. Although speculative, DOCK9 may be involved in similar migratory pathways. In addition, family members DOCK2 and 3 have shown involvement in the regulation of Aβ plaque load[254] and phosphorylation of tau[255], respectively, making DOCK9 an interesting candidate for future studies.

Materials and Methods

Mice. The use of APP/PS1 mice in this study was approved by the animal ethical care committee of the Vrije Universiteit Amsterdam. All wildtype and APP/PS1 mice of 12-moa were males. Both conditional groups at 6-moa were a mix of males and females (3 of each sex/condition).

Synaptosomal Enrichment. For all age and genotype conditions, synaptosomal fractions of 5 or 6 mice were individually prepared and analyzed. Samples were prepared as previously described[207,217]. Mouse hippocampi were dissected and stored at −80 °C until further use. Per mouse, the two hippocampi from both hemispheres were homogenized together in 6 mL of homogenization buffer (0.32 M sucrose (VWR, Radnor, PA, USA), 5 mM HEPES (Sigma-Aldrich, St. Louis, MO, USA) pH 7.4, Protease inhibitor cocktail (Roche, Basel, Switzerland)). Samples were homogenized using a potter and pestle (Sartorius, Göttingen, Germany; 12 strokes, 900 rpm) and centrifuged at 1000× g for 10 min at 4 °C. Subsequently, 4.5 mL of supernatant was loaded on top of a 0.85/1.2 M (6 mL each) sucrose gradient and centrifuged at 100,000× g for 2 h. Per sample, 1.5 mL synaptosomes were recovered between 0.85/1.2 M sucrose interface, mixed with 3.5 mL 5 mM HEPES, pH 7.4, and centrifuged at 20,000× g for 30 min to obtain the synaptosomal pellets. Synaptosomes were resuspended in 150 µL homogenization buffer, and protein concentration was determined with a Bradford assay (Protein Assay, Bio-rad, Hercules, CA, USA).

Filter-Aided Sample Preparation. Samples were digested following the filter-aided sample digestion protocol[256] with some modifications. In short, for each sample, 22 µg synaptosomes were solubilized in 100 µL 2% sodium dodecyl sulfate (Sigma-Aldrich, St. Louis, MO, USA) containing 1 µL 500 mM Tris (2-carboxyethyl) phosphine (Sigma-Aldrich, St. Louis, MO, USA) reducing reagent, at 55 °C for 1 h. Next, cysteine residues were blocked with 0.5 µL 500 mM methyl methanethiosulfonate (Fluka, Honeywell, Charlotte, NC, USA) for 15 min at room temperature. After addition of 200 µL 8M urea (Sigma-Aldrich, St. Louis, MO, USA) in tris buffer (Sigma-Aldrich, St. Louis, MO, USA), pH 8.8, the samples were transferred to YM-30 filters (Microcon®, Millipore, Burlington, MA, USA) and centrifuged at 14000× g for 15 min. The samples were washed with 8M urea solution four times by centrifugation at 13500 x g for 14 min each, followed by four washes with 50 mM ammonium bicarbonate (Sigma-Aldrich, St. Louis, MO, USA). Trypsin (Mass Spec Grade, Promega, Madison, WI, USA; 0.6-g trypsin in 100 µL 50 mM ammonium bicarbonate) was added to the proteins on filter and incubated overnight at 37 °C. The filters were centrifuged, and the digested peptides were collected in a clean centrifuge tube. The samples were dried in a speedvac (Savant, Thermo Scientific, Waltham, MA, USA) and stored at −20 °C until Liquid Chromatography–Tandem Mass Spectrometry (LC-MS/MS) analysis.

Micro-LC and SWATH Mass Spectrometry. Peptides were analyzed by micro-LC MS/MS using an Ultimate 3000 LC system (Dionex, Thermo Scientific, Waltham, MA, USA) coupled to the TripleTOF 5600 mass spectrometer (Sciex, Framingham, MA, USA) as described previously[183,207,257]. Peptides were trapped on a 5 mm Pepmap 100 C18 column (Dionex, Thermo Scientific, Waltham, MA, USA; 300 µm i.d., 5 µm particle size) and fractionated on a ChromXP C18 column (Eksigent, Sciex, Framingham, MA, USA; 3 µm particle size, 120A). The acetonitrile (VWR, Radnor, PA, USA) concentration in the mobile phase was increased from 5 to 18% in 88 min, to 25% at 98 min, 40% at 108 min and to 90% in 2 min, at a flow rate of 5 µL/min. The eluted peptides were electro-sprayed into the TripleTOF 5600 mass spectrometer, with a micro-spray needle voltage of 5500 V. SWATH experiments consisted of a parent ion scan of 150 ms followed by a SWATH window of 8 Da with scan time of 80 ms, that stepped through the mass range between 450 and 770 m/z. The collision energy for each window was determined based on the appropriate collision energy for a 2+ ion, centered upon the window with a spread of 15 eV.

SWATH Data Analysis. Spectronaut 14 (Biognosys, Schlieren, Switzerland) was used for data analysis of the raw files. All SWATH runs of the 12-moa experimental sample set were analyzed against both the spectral library and an internal spectral library using the directDIA function in Spectronaut 14. Analysis against the spectral library was done in the Analysis Perspective of Spectronaut by uploading all raw files, assigning the spectral library to each file and applying the Biognosys (BGS) Factory Settings. Analysis using the directDIA function in the Analysis Perspective of Spectronaut was performed by uploading raw files and assigning the mouse reference proteome files (the 2018_04 Uniprot release of UP000000589_10090.fasta and UP000000589_10090.additional.fasta). Additionally here, the Biognosys Factory Settings were applied. The 6-moa runs were analyzed only using directDIA, the same way as the 12-moa dataset. Before exporting data from Spectronaut, all filters were disabled. The dedicated spectral library was created with crude hippocampal synaptosomes containing spiked-in indexed Retention Time peptides (Biognosys, Schlieren, Switzerland), analyzed with the Triple TOF 5600 in DDA mode. The obtained library data were searched against the mouse proteome (the 2018_04 Uniprot release of UP000000589_10090.fasta and UP000000589_10090.additional.fasta) in Maxquant. Methyl methanethiosulfonate (C) was set as fixed modification. In the Library Perspective of Spectronaut, the dedicated spectral library was generated by uploading the Maxquant evidence.txt and modifications.xml files, the used fasta files, and assignment of the Shotgun Files (raw files).

The Mass Spectrometry Downstream Analysis Pipeline (MS-DAP) (available at https://github.com/ftwkoopmans/msdap; version beta 0.2.5.1) was used for quality control and candidate discovery. In MS-DAP, peptide intensities without normalization in Spectronaut were taken for downstream analysis. For differential expression analysis, the 6- and 12-moa datasets were analyzed separately. Peptides present in at least 75% of the wildtype or APP/PS1 groups were used for differential testing, with the limma emperical Bayes algorithm after rollup to proteins. Shared peptides were removed, and the Variation Within Mode Between and modebetween_protein algorithms were used for normalization. All proteomics data used here have been deposited to the ProteomeXchange Consortium via the PRIDE[258] partner repository with the dataset identifier PXD025777.

Author Contributions

Conceptualization, S.J.F.v.d.S., A.B.S. and K.W.L.; Methodology, S.J.F.v.d.S., and K.W.L.; Software, F.K.; Formal analysis, S.J.F.v.d.S., M.A.G.-L., S.S.M.M., F.K. and K.W.L.; Investigation, S.J.F.v.d.S., I.P. and K.W.L.; Writing—Original Draft Preparation, K.W.L.; Writing—Review and Editing, S.J.F.v.d.S., A.B.S. and K.W.L.; Visualization, S.J.F.v.d.S. and

F.K.; Supervision, K.W.L.; All authors have read and agreed to the published version of the manuscript.

Funding

S.J.F.v.d.S. was funded by ZonMW, grant no. 733050106, and S.S.M.M. by ZonMW, grant no. 733050811, that both are part of the dementia Research and Innovation Program "Memorabel". M.A.G-L. was funded by ZonMW, grant no. 733051076, part of the Joint Programming Initiative Neurodegenerative Diseases (JPND) program.

Institutional Review Board Statement

The use of APP/PS1 mice in this study was approved by the animal ethical care committee of the Vrije Universiteit Amsterdam.

Informed Consent Statement

Not applicable

Data Availability Statement

All proteomics data used here have been deposited to the ProteomeXchange Consortium via the PRIDE[258] partner repository with the dataset identifier PXD025777.

Acknowledgments

We thank R. V. Klaassen for providing the DDA-based spectral library of wildtype hippocampal crude synaptosomes, and M. Loos for providing the mice.

Conflicts of Interest

All authors declare that they have no conflict of interest.

Abbreviations

Abbreviation	Meaning:
AD	Alzheimer's disease
APP/PS1	Amyloid Precursor Protein swe/ Presenilin 1 dE9
Aβ	Amyloid-β
BP	Biological Process
CC	Cellular Component
Cscores	Confidence scores
DDA	Data-Dependent acquisition
DEA	Differential Expression Analysis
DIA	Data-independent acquisition
EWCE	Expression-Weighted Cell-type Enrichment
HPLC	High-Performance Liquid Chromatography
LC-MS/MS	Liquid Chromatography–Tandem Mass Spectrometry
Moa	Months of age
MS-DAP	Mass Spectrometry Downstream Analysis Pipeline
SWATH	Sequential Window Acquisition of all THeoretical fragment-ion
SynGO	Synaptic Gene Ontology
WP	WikiPathways

Supplementary Figures

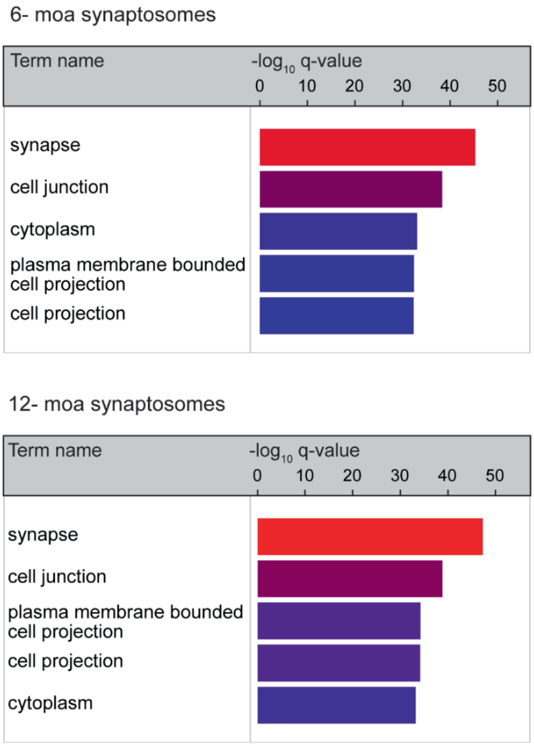

6- moa synaptosomes

12- moa synaptosomes

Figure S1. Enrichment of synaptic proteins in the synaptosomal sample preparation. GO-enrichment analysis of all proteins detected in the 6- and 12-moa synaptosomal datasets under investigation in the current study. Total brain expressed genes is used as background.

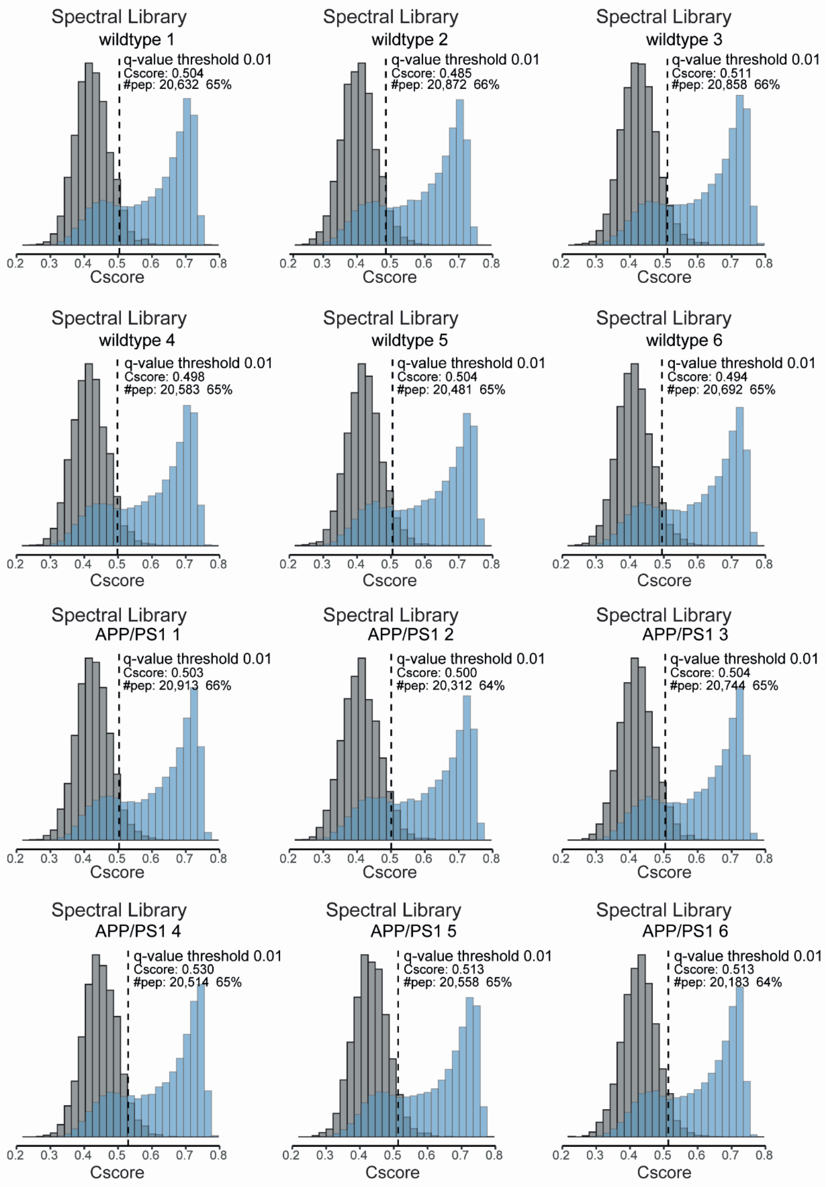

Figure S2. Target (blue) and decoy (grey) confidence score distributions of all 12-moa samples searched against the DDA-based spectral library. The confidence scores (cscores) indicate the level of confidence the software had in the identification of peptides in the raw SWATH data. The q-value confidence threshold of 0.01 is shown as a dotted line, and the associated cscore and number of peptides quantified above this threshold are reported.

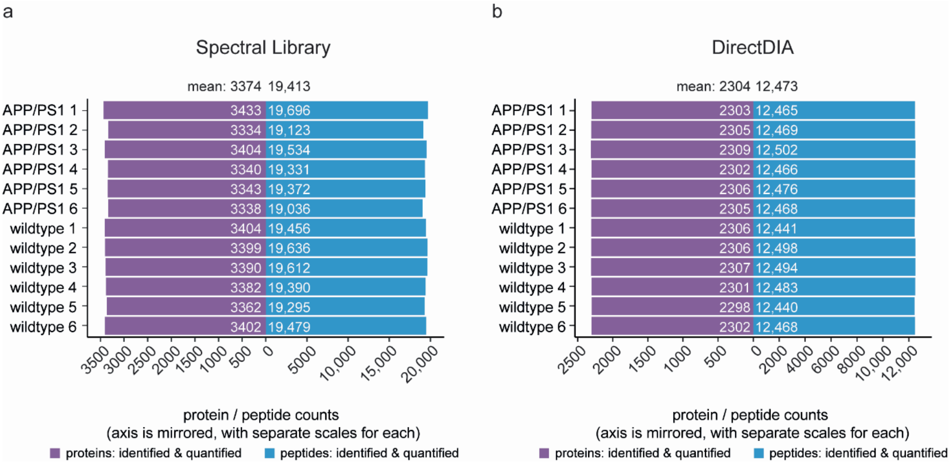

Figure S3. Number of identified and quantified proteins and peptides with a q- value ≤ 0.01 for identification. (**a**) Number of proteins and peptides identified using the DDA-based spectral library are shown on average and per individual sample; (**b**) Analogous to panel a, number of proteins and peptides are shown on average or per individual sample, identified using directDIA.

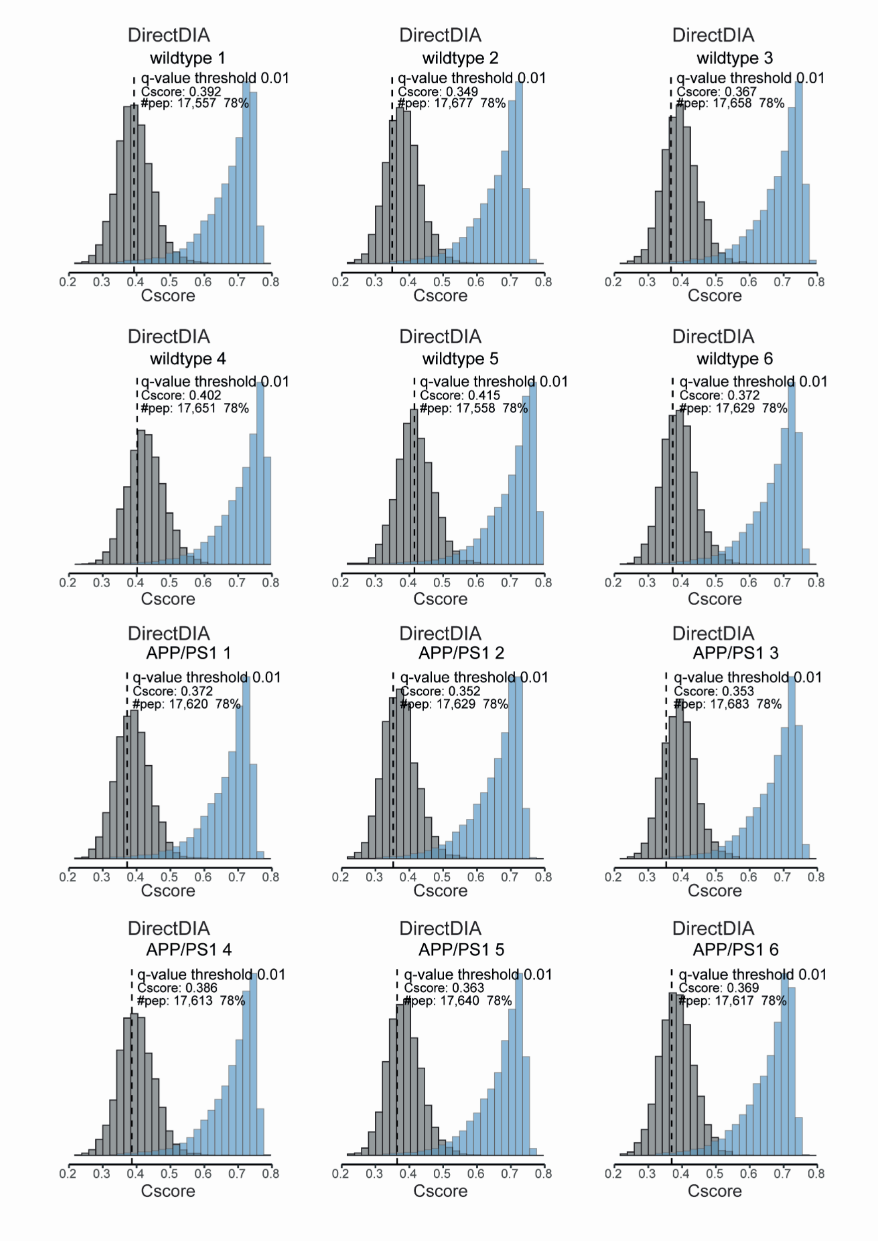

Figure S4. Target (blue) and decoy (grey) confidence score distributions of all 12-moa samples searched using directDIA. The confidence scores (cscores) indicate the level of confidence the software had in the identification of peptides in the raw SWATH data. The q-value confidence threshold of 0.01 is shown as a dotted line, and the associated cscore and number of peptides quantified above this threshold are reported.

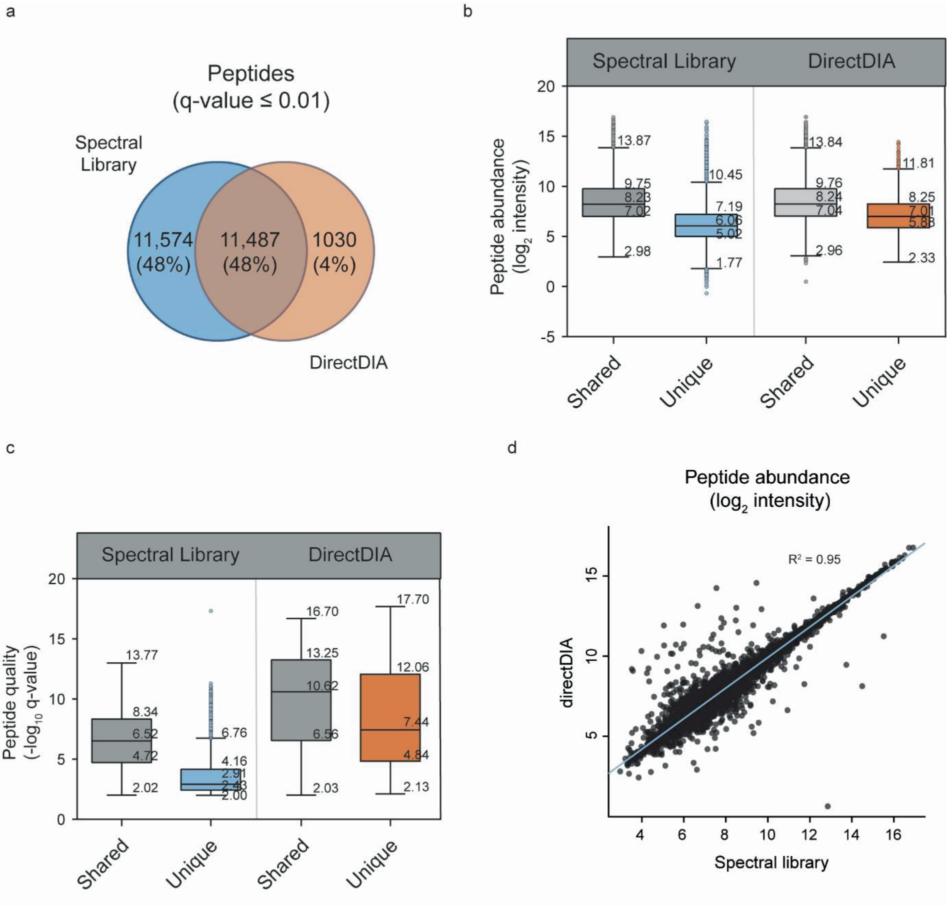

Figure S5. Characterization of unique and shared peptides identified using the spectral library or directDIA data searches. (**a**) Number of shared and unique identified peptides. (**b**) Abundance of shared and unique peptides identified using the spectral library. (**c**) Quality of shared and unique peptides identified using the spectral library. (**d**) Correlation in intensity between peptides identified using the spectral library or directDIA.

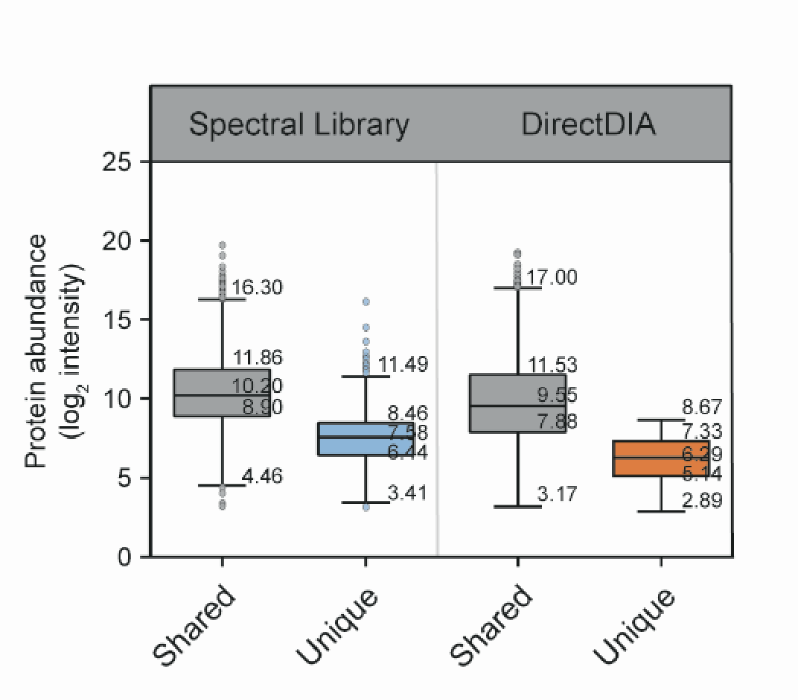

Figure S6. Abundance of shared and uniquely identified proteins using the spectral library or directDIA after filtering high quality peptides for differential expression analysis.

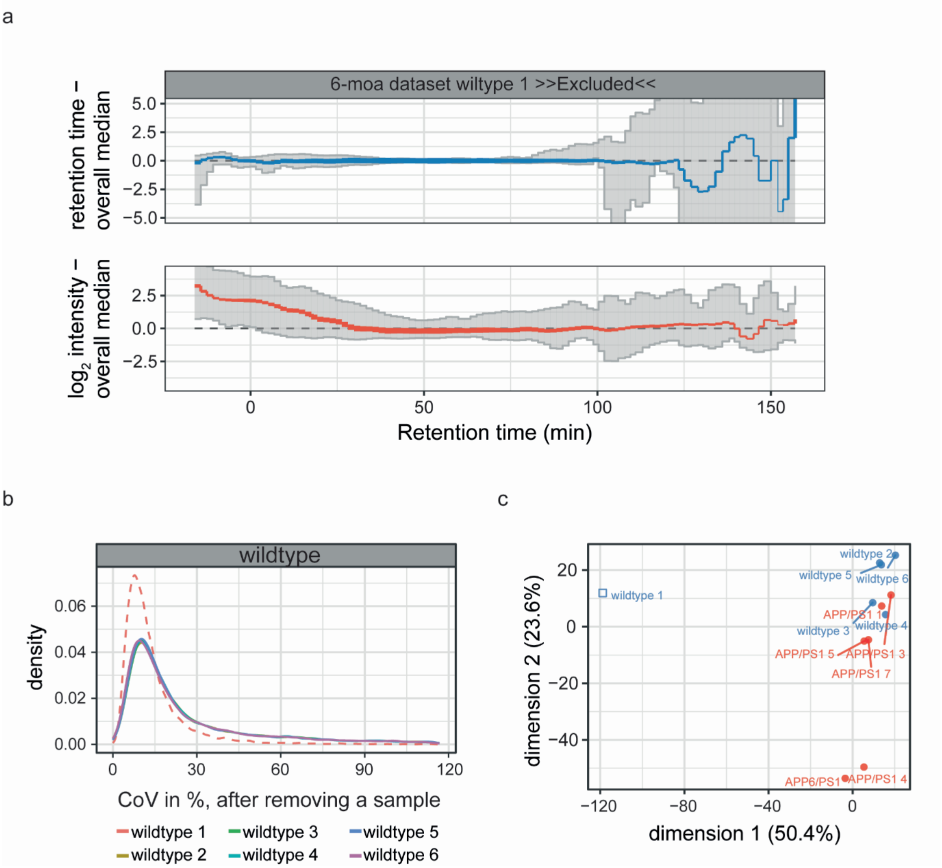

Figure S7. Quality control in MS-DAP of wildtype 1 in the 6-moa dataset. (**a**) Wildtype 1 showed large variation in retention time compared to the group median. Peptide retention time and abundance of wildype 1 are shown as a blue line (upper panel) and red line (lower panel), respectively, and are normalized to the median over all samples. Line widths correspond to the number of eluted peptides at that time point. The 5% and 95% quantiles are depicted in grey; (**b**) The effect of removing a sample prior to within-group Coefficient of Variation (CoV) computation is shown. The CoV is largely reduced after removal of wildtype 1; (**c**) A visualization of the first two Principal component analysis dimensions, showing that 50% of the variation explained by dimension 1 separates wildtype 1 from the other samples. Probabilistic Principal component analysis was performed on those peptides retained after filtering for differential expression analysis. The principal components and their respective percentage of variance explained are shown on the axis labels.

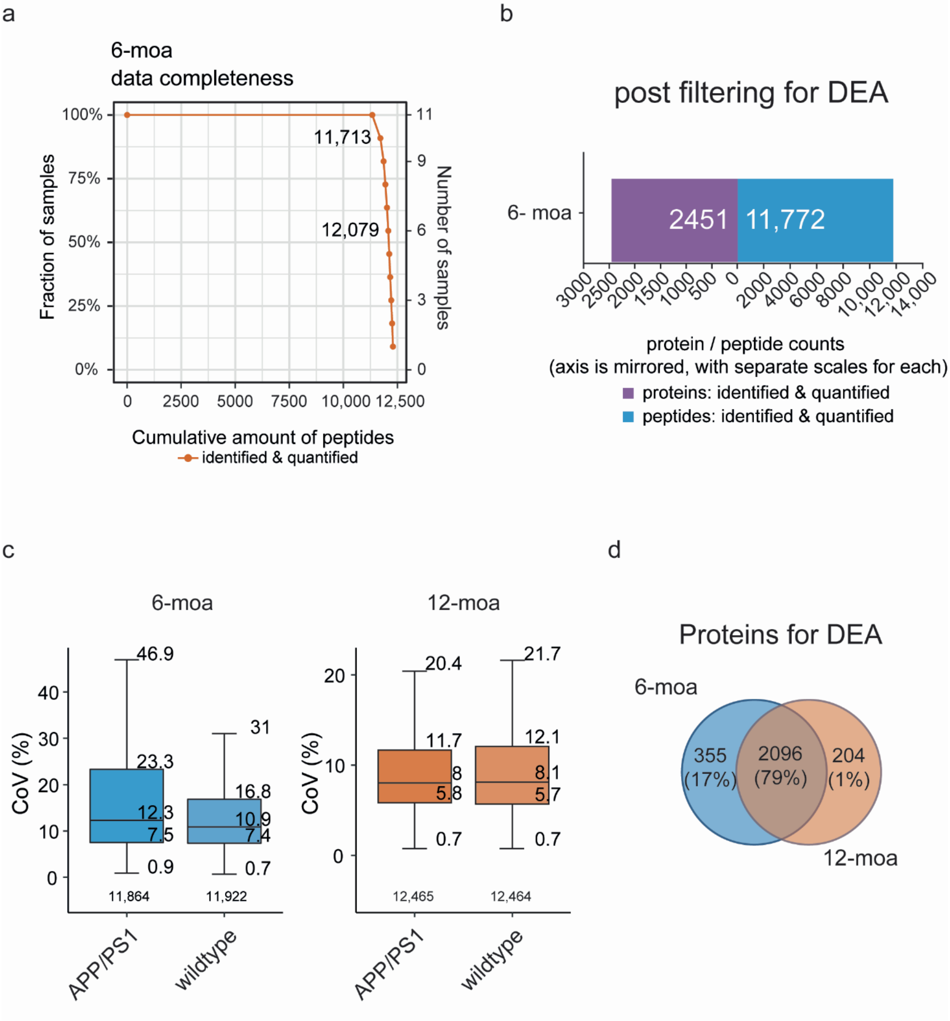

Figure S8. Quality control of the 6-moa dataset run against the directDIA library and comparison with the 12-moa dataset. (**a**) Cumulative distribution showing the number of peptides consistently identified across all samples; (**b**) Number of proteins and peptides that remain after filtering for differential expression analysis; (**c**) The Coefficient of Variation (CoV)s visualized as boxplots for the 6- and 12-moa datasets; (**d**) The number of proteins used for differential expression analysis observed in the 6- and 12-moa datasets.

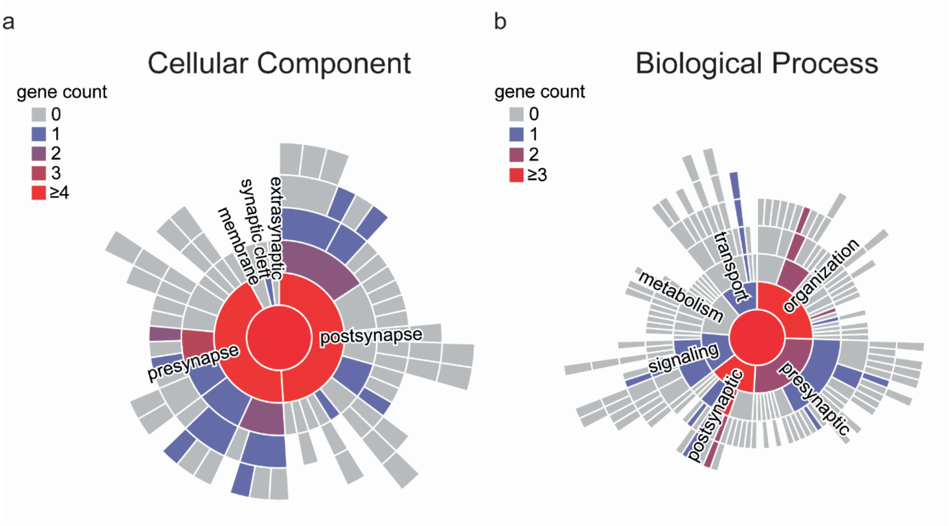

Figure S9. Sunburst plots of SynGO terms with highlighted gene counts of regulated 6- and 12-moa APP/PS1 mouse genes. The number of regulated genes annotated towards (**a**) location or (**b**) function terms are indicated per term.

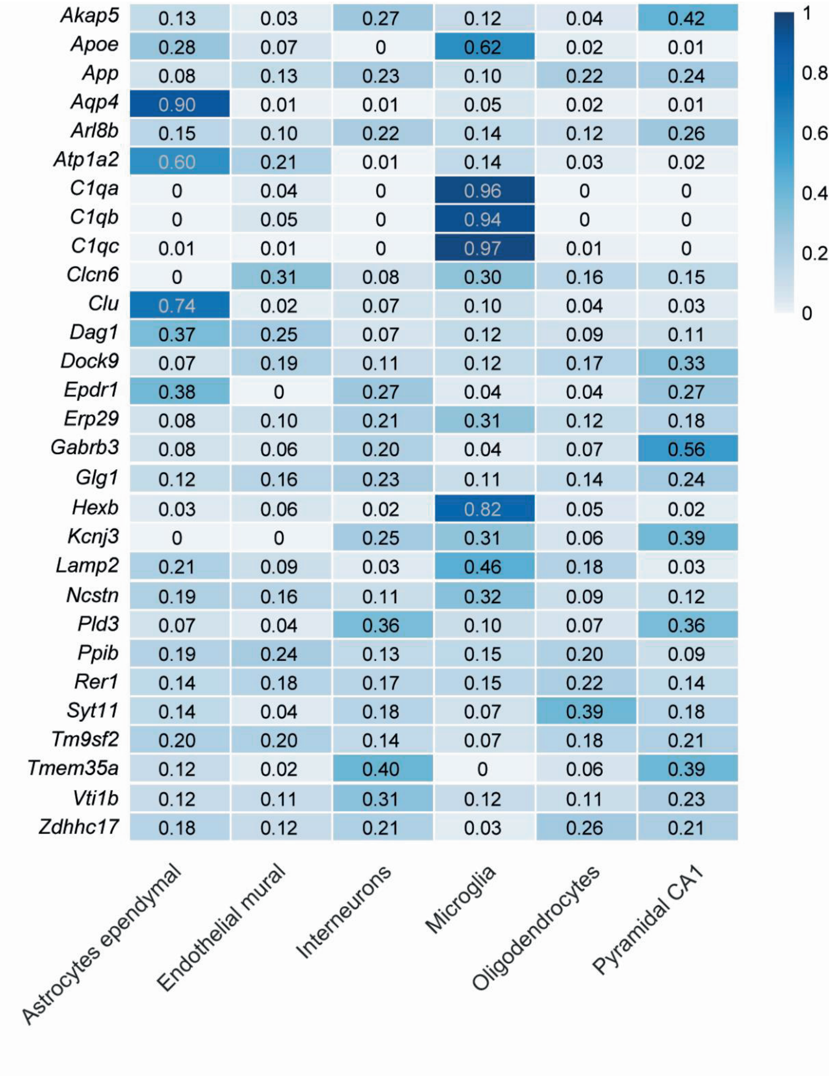

	Astrocytes ependymal	Endothelial mural	Interneurons	Microglia	Oligodendrocytes	Pyramidal CA1
Akap5	0.13	0.03	0.27	0.12	0.04	0.42
Apoe	0.28	0.07	0	0.62	0.02	0.01
App	0.08	0.13	0.23	0.10	0.22	0.24
Aqp4	0.90	0.01	0.01	0.05	0.02	0.01
Arl8b	0.15	0.10	0.22	0.14	0.12	0.26
Atp1a2	0.60	0.21	0.01	0.14	0.03	0.02
C1qa	0	0.04	0	0.96	0	0
C1qb	0	0.05	0	0.94	0	0
C1qc	0.01	0.01	0	0.97	0.01	0
Clcn6	0	0.31	0.08	0.30	0.16	0.15
Clu	0.74	0.02	0.07	0.10	0.04	0.03
Dag1	0.37	0.25	0.07	0.12	0.09	0.11
Dock9	0.07	0.19	0.11	0.12	0.17	0.33
Epdr1	0.38	0	0.27	0.04	0.04	0.27
Erp29	0.08	0.10	0.21	0.31	0.12	0.18
Gabrb3	0.08	0.06	0.20	0.04	0.07	0.56
Glg1	0.12	0.16	0.23	0.11	0.14	0.24
Hexb	0.03	0.06	0.02	0.82	0.05	0.02
Kcnj3	0	0	0.25	0.31	0.06	0.39
Lamp2	0.21	0.09	0.03	0.46	0.18	0.03
Ncstn	0.19	0.16	0.11	0.32	0.09	0.12
Pld3	0.07	0.04	0.36	0.10	0.07	0.36
Ppib	0.19	0.24	0.13	0.15	0.20	0.09
Rer1	0.14	0.18	0.17	0.15	0.22	0.14
Syt11	0.14	0.04	0.18	0.07	0.39	0.18
Tm9sf2	0.20	0.20	0.14	0.07	0.18	0.21
Tmem35a	0.12	0.02	0.40	0	0.06	0.39
Vti1b	0.12	0.11	0.31	0.12	0.11	0.23
Zdhhc17	0.18	0.12	0.21	0.03	0.26	0.21

Figure S10. Gene expression cell-type specificity matrix of upregulated proteins in synaptosomes of 12-moa APP/PS1 mice. For each gene the expression taken from[219] is normalized to the total level in all cell-types combined, highlighting the relative distribution. Low expression is shown in white and high expression in dark blue.

Table S1. Regulated proteins that have been associated with AD in previous human studies.

Protein symbol	Association to human AD	References
APOE	Genome wide association study shows association of APOE loci with disease status	Jansen et al. 2019
APP	Segregation of genetic variant with familial AD observed in a linkage study	Goate et al. 1991
AQP4	Targeted analysis shows association between genetic AQP4 variants and cognitive decline after diagnosis of AD	Burfeind et al. 2017
C1Q(A-C)	Astrocyte derived exosomes of AD patients show increased levels of C1Q Increased levels of C1Q(A-C) have been observed in CSF and blood of AD patients, albeit inconsistently	Goetzl et al. 2018 Krance et al. 2019
CLU	Genome wide association study shows association of CLU loci with disease status	Jansen et al. 2019
LAMP2	Increased levels in CSF of AD patients observed with mass spectrometry	Sjödin et al. 2016
NCSTN	Targeted analysis shows segregation of genetic variant in the promoter region of NCSTN with disease status	Zhong et al. 2009
PLD3	Segregation of genetic variants with disease status using whole exome sequencing	Cruchaga et al. 2014

Table S2. SynGO annotations of regulated proteins at 6- or 12-moa APP/PS1 mice.

Gene symbol	GO term name	GO domain
AKAP5	regulation of postsynaptic neurotransmitter receptor endocytosis (GO:0099149)	Biological Process
AKAP5	postsynaptic density, intracellular component (GO:0099092)	Cellular Component
APOE	regulation of synapse organization (GO:0050807)	Biological Process
APOE	synaptic cleft (GO:0043083)	Cellular Component
APP	regulation of presynapse assembly (GO:1905606)	Biological Process
APP	presynaptic active zone (GO:0048786)	Cellular Component
APP	neuronal dense core vesicle (GO:0098992)	Cellular Component
ARL8B	regulation of anterograde synaptic vesicle transport (GO:1903742)	Biological Process
CLU	synapse (GO:0045202)	Cellular Component
DAG1	regulation of synapse organization (GO:0050807)	Biological Process
DAG1	regulation of neurotransmitter receptor localization to postsynaptic specialization membrane (GO:0098696)	Biological Process
DAG1	retrograde trans-synaptic signaling by trans-synaptic protein complex (GO:0098942)	Biological Process
DAG1	postsynaptic cytosol (GO:0099524)	Cellular Component
GABRB3	transmitter-gated ion channel activity involved in regulation of postsynaptic membrane potential (GO:1904315)	Biological Process
GABRB3	integral component of postsynaptic membrane (GO:0099055)	Cellular Component
GABRB3	integral component of postsynaptic specialization membrane (GO:0099060)	Cellular Component
GPC4	regulation of neurotransmitter receptor localization to postsynaptic specialization membrane (GO:0098696)	Biological Process
GPC4	synapse adhesion between pre- and post-synapse (GO:0099560)	Biological Process
GPC4	regulation of presynapse assembly (GO:1905606)	Biological Process
GPC4	synapse (GO:0045202)	Cellular Component
GPC4	anchored component of presynaptic membrane (GO:0099026)	Cellular Component
KCNJ3	voltage-gated ion channel activity involved in regulation of presynaptic membrane potential (GO:0099508)	Biological Process
KCNJ3	integral component of presynaptic membrane (GO:0099056)	Cellular Component
NCSTN	integral component of presynaptic membrane (GO:0099056)	Cellular Component
SYT11	regulation of synaptic vesicle endocytosis (GO:1900242)	Biological Process
SYT11	integral component of synaptic vesicle membrane (GO:0030285)	Cellular Component
SYT11	postsynapse (GO:0098794)	Cellular Component
SYT11	integral component of presynaptic active zone membrane (GO:0099059)	Cellular Component

Table S3. SynGO enrichment analysis of synaptic proteins regulated in 6- or 12-moa APP/PS1 mice using location terms.

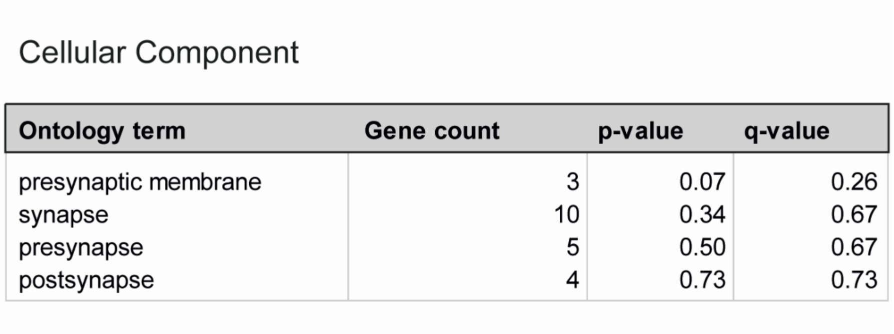

Cellular Component

Ontology term	Gene count	p-value	q-value
presynaptic membrane	3	0.07	0.26
synapse	10	0.34	0.67
presynapse	5	0.50	0.67
postsynapse	4	0.73	0.73

Table S4. SynGO enrichment analysis of synaptic proteins regulated in 6- or 12-moa APP/PS1 mice using function terms.

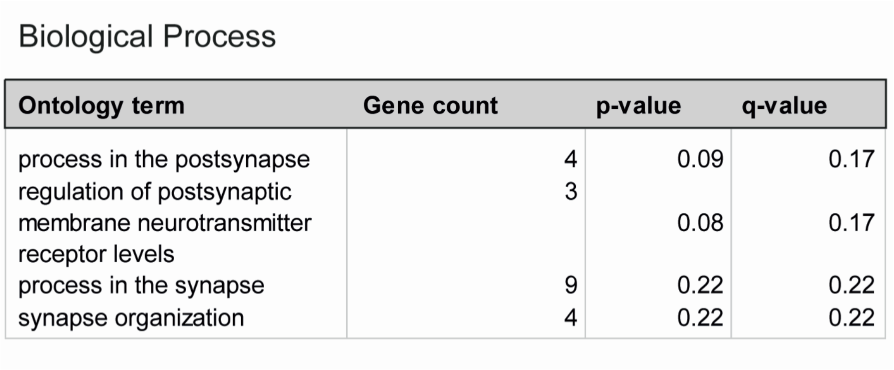

Biological Process

Ontology term	Gene count	p-value	q-value
process in the postsynapse	4	0.09	0.17
regulation of postsynaptic membrane neurotransmitter receptor levels	3	0.08	0.17
process in the synapse	9	0.22	0.22
synapse organization	4	0.22	0.22

Chapter 6: General discussion

Neurotransmission involves a diverse set of synaptic proteins that act in transient or stable protein complexes together forming an intricate molecular network[8]. Ligand-gated ion channels at the inhibitory and excitatory post-synaptic density play a central role in synaptic transmission, through binding of neurotransmitters and conductance of ions into the post-synapse. These receptors associate with a large variety of binding partners that regulate receptor localization and biophysical properties to ensure specificity and rate of signal transduction and thereby have a major impact on synaptic transmission[183]. In this thesis I made use of interaction proteomics approaches to determine protein complex compositions of major proteins of the glutamatergic excitatory, and glycinergic inhibitory synapse. By using a combination of IP-MS and IP-BN-PAGE/MS we further specified GlyR, Gephyrin and AMPAR interactomes, and provided a framework for further molecular and functional analyses. In addition, as part of my work on synaptic proteins, I studied the synapse proteome of a mouse model of Alzheimer's disease and revealed regulation of several synaptic and microglial proteins related to Aβ physiology and microglial-dependent processes. Here I elaborate on several findings from these studies and their biological implications, and discuss general technological considerations and advances for the study of synaptic (receptor) proteins and their assemblies by proteomics approaches.

Interaction proteomics of brainstem GlyRs

In **chapter 2**, I analyzed the interactome of the GlyR in brainstem. Protein-protein interactions can be identified by purification of a target protein, and the analysis of co-isolated constituents. Purification of GlyR complexes with multiple antibodies raised against the GlyR α1 and GlyR β GlyR subunits and the Gephyrin scaffold protein followed by mass spectrometry, resulted in the identification of IQSEC2 and IQSEC3 as novel GlyR complex interactors. Yeast-two-hybrid revealed direct interaction between amino acid 160-210 of the IQSEC3 N-terminal domain and the G-domain of Gephyrin, further specifying the N-terminal interaction site on IQSEC3 that was previously reported[117]. In addition, we revealed the GlyR-Gephyrin-IQSEC2/3 assembly as a distinct high molecular weight complex, in a combined approach of IP with BN-PAGE followed by mass spectrometry.

IQSEC2 and IQSEC3 in the glycinergic synapse

Our data revealed IQSEC2 as an interactor of GlyR complexes in the brainstem. IQSEC2 was originally identified in excitatory PSDs, where it binds NMDA-receptors, affects ARF6 functioning and AMPA-receptor membrane expression[255]. Mutations in the IQSEC2 gene give rise to intellectual disability (ID), which is often accompanied by various symptoms such as autistic features, seizures, stereotypic movements and delayed psychomotor development[256]. Underlying molecular mechanisms are considered in relation to the function of IQSEC2 in the excitatory synapse[255]. As our data reveal IQSEC2 as a GlyR complex interactor, mutations in IQSEC2 may also impact GlyR function, which may thus underlie part of the observed IQSEC2-related ID symptomatology. Further studies are required to determine the functional role of IQSEC2 in brainstem glycinergic synapses, and the potential relation to IQSEC2 associated disabilities. IQSEC2 especially reveals strong expression in the brainstem at embryonic age E14.5[257]. Future studies into IQSEC2 at glycinergic synapses during embryonic development may therefore be of special interest.

Previous research has indicated evidence that IQSEC3 may be part of inhibitory GABA$_A$R complexes[117,118,156,157]. The identification of IQSEC3 in our GlyR IP-MS experiments suggests that IQSEC3 additionally plays a role in glycinergic synaptic transmission. Removal of IQSEC3 in hippocampal neurons decreases Gephyrin clustering, reduces the number of postsynaptic GABA$_A$Rs and of GABAergic presynaptic terminals[117]. Involvement of IQSEC3 in GABA-ergic synapse maintenance and network activity was shown to depend on its ARF-GEF activity [117,258]. In line with this, ARF6 was shown to be important for GABA-ergic synapse development[259], and activation of ARF6 by IQSEC3 is required for correct pre- and post-synapse alignment[118]. The exact mechanisms by which IQSEC3 impact Gephyrin clustering, and GABAergic synapse physiology through its ARF-GEF remains unknown. Of interest, ARF6 is involved in regulation of the cytoskeleton and recycling of endosomes and proteins to and from the plasma membrane [260–262]. IQSEC3 may therefore impact on GABA-ergic synapse maintenance and network activity through regulating GABA$_A$-R endocytosis or recycling at the inhibitory PSD. As we showed associated of IQSEC3 with GlyR complexes, similar functions and regulatory mechanisms may apply to the GlyR and glycinergic synapses.

Considerations for the study of transient receptor interactors

Physical interactions between proteins are prerequisite for the execution of cellular processes. Immuno-purification of proteins from native tissues or homologous expression systems, and yeast two-hybrid methodologies are the most widely applied for detecting protein interactions[83,263–265]. By the use of IP-MS numerous binding partners of synaptic receptors like the AMPAR[46] and GABA$_B$-receptor[47] were revealed. In contrast, for the identification of high-confident novel GlyR interactors in our own study, this approach yielded limited success[172]. The glycinergic synapse has a relatively simple structure, containing multiple α1:β GlyRs clustered by Gephyrin, and is thought to have limited ability for plastic change[95]. Possibly the

GlyR truly has a limited number of interactors. Alternatively, potential weak interacting proteins of the GlyR may have been missed.

To isolate receptor complexes from their cellular environment, IP involves the lysis and solubilization of protein targets from the membrane. The efficiency of protein extraction on one hand, and strength of the protein interactions on the other hand are critical determinants for the successful recovery of intact target complexes[266]. In contrast to the traditional IP approach, new technologies have been developed to examine protein interactions in their physiological context and allow for the identification of less stable interacting partners[267]. For instance, chemical cross-linking makes use of small cross-linker reagents to capture proteins in close proximity in vivo[8,267]. Cross-linking of synaptic proteins prior to extraction has previously yielded the identification of 2362 connections within and between proteins[8]. Adding an enrichment step after cross-linking prior to MS detection, will assist the detection coverage of cross-links for a particular target protein of interest. Alternative approaches include proximity labeling methods which involve tagging of proteins located in the close vicinity of their potential interacting protein that is modified to contain a labeling enzyme (e.g. a biotin ligase, peroxidases or ascorbate peroxidase)[267]. Labeled proteins are subsequently enriched and identified by MS. Both methods allow the identification of even weak protein interactions in their physiological context and in a high-throughput manner. Further advances in these approaches hold the promise for providing a reliable and comprehensive picture of the protein interactomes in their native cellular environment. Reduction of false negatives and increase in coverage of the GlyR interactome may be ultimately improved by integration of such complementary techniques.

The study of protein subcomplex compositions

Synaptic receptor complexes are partly dynamic entities of which the molecular composition may depend on its subcellular localization. Interactomes of a target protein can differ across distinct subcellular compartments, for instance during its transport through the cell towards its final destination. Also it may change in correspondence to different functional states of the synapse[69,79]. Identification of receptor-interactor co-assembly, or inversely the preclusion of mutual co-assembly into receptor subcomplexes, provides the molecular framework for follow up on detailed receptor-related processes in synaptic physiology.

The identification of receptor subcomplexes can be achieved in several ways. For instance, IP-MS of a target protein followed by reverse IP-MS of interactors may provide evidence of protein co-occurrence or exclusion[79]. However, this approach may not be successful in case of sharing of interactors across different subcomplexes. An alternative approach is the biochemical fractionation of tissue lysates prior to MS detection, which is sometimes referred to as co-fractionation-MS[267,268]. Biochemical separation can be achieved with different strategies, such as size-exclusion chromatography (SEC)[269] or ion-exchange chromatography (IEX)[270]. Proteins contained in the same complex are expected to at least partially end up in the same biochemical fractions, resulting in similar quantitative protein profiles based on MS detection. Based on the highly correlating protein elution profiles, protein complex assembly can be predicted[269,270].

Co-fractionation-MS allows for the untargeted analysis of thousands of proteins and their protein complex compositions in a single assay[269,270]. However, complex samples and limited separation can result in co-elution of proteins that do not interact, resulting in reduced specificity[268]. To mitigate this problem, researchers extensively fractionate their samples by the application of multiple separation techniques consecutively on the same sample[270]. In addition, recently, researchers described a ‘complex-centric analysis’ workflow for the interpretation of co-fractionation-MS[269]. In this analysis strategy, prior information on protein interactions is used to analyze co-fractionation-MS data for evidence of protein complexes up to subcomplex resolution[269].

In chapter 2, we introduced a strategy that combines the specificity of IP with the resolution of blue-native PAGE to study the organization of native protein subcomplexes. After GlyR purification, native complexes were size separated on a blue-native PAGE gel followed by their analysis with mass spectrometry. Separation of GlyR complexes using IP/BN-PAGE/MS revealed IQSEC2/3 protein abundance at the high mass range of the GlyR-Gephyrin complexes. Revealing the GlyR-Gephyrin-IQSEC2/3 assembly as a distinct high molecular weight complex, next to lower molecular weight assemblies, exemplified how this strategy can be used to study subcomplex protein composition.

Interestingly, computational methods are being developed to detect subcomplexes from affinity purification data[271] and protein interaction databases[272,273]. Moreover, the elucidation of protein binding interfaces, for instance through cross-linking-MS, might allow the molecular understanding of subcomplexes by inferring the competitive binding of previously known interactors[8,274]. Advances in interaction proteomics, such as cross-linking-MS, that assist determining subcomplex compositions, hold the promise to improve the mechanistic understanding of protein interactions at the synapse.

Gephyrin splice-isoforms and their differential interactions

In **chapter 3**, we studied two major Gephyrin protein isoforms resulting from transcript splicing. Previous studies were done using mRNA-based approaches, in situ hybridization or overexpression of Gephyrin isoform constructs. We designed specific antibodies targeted against the major Gephyrin-C3 and C4A isoforms. Using these antibodies, we revealed expression of Gephyrin-C4A limited to neurons, and strong interaction with the GlyR, IQSEC3 and NOS1. Further dissection of the Gephyrin-C4A complexes revealed those containing the GlyR and/or IQSEC3 are separate from those containing NOS1. In contrast to Gephyrin-C4A, Gephryin-C3 revealed highest expression in astrocytes, only limited association with the GlyR and specific interaction with NLGN2.

Gephyrin-GlyR/Neuroligin assemblies in astrocytes

Gephyrin is the major scaffolding protein of the inhibitory synapse[163], and in addition, catalyzes Molybdenum Cofactor (MoCo) synthesis which is important for the functioning of a variety of enzymes[166]. Glia expressed Gephyrin-C3 was previously shown to be responsible for the main MoCo production in the brain[124]. Our IP-BN-PAGE/MS revealed interaction between a subset of Gephyrin-C3 proteins and the GlyR, and interaction between the majority of Gephyrin-C3 and NLGN2 and DYL2. The GlyR, NLGN2 and DYL2 are not involved in the catalyzation of MoCo synthesis[166]. The exact cellular location of these interactions has yet to be determined experimentally. However, as the majority of Gephyrin-C3 is expressed in astrocytes, these interactions likely occur in the astrocyte cell-type. Therefore, these data suggests that Gephyrin-C3 in astrocytes also operates beyond its enzymatic function.

Astrocytes are an abundant cell-type in the mammalian brain and are characterized by their elaborate morphology with numerous processes, among which those interacting with synapses[171]. Traditionally, astrocytes have been considered important for metabolic homeostasis and synaptic transmission through the regulation of extracellular concentrations of ions, neurotransmitters and molecules[275]. Recent evidence revealed astrocytes are intimately involved in local synapse formation and elimination[275,276]. In addition, dysfunctional synapse-astrocyte interactions are increasingly recognized as potential contributors to psychiatric and developmental disorders such as autism and schizophrenia[277].

Although astrocytes reveal an overall gene expression profile distinct from neurons[219,278], neurons and astrocytes reveal shared expression of certain proteins including Gephyrin, neurotransmitter receptors (e.g. AMPARs[279], GABARs[280] and GlyR[91]) and Neurologins[176,276].

The functions of these particular proteins in astrocytes are starting to be uncovered. Previous results revealed that by the expression of neurotransmitter receptors, astrocytes can sense neuronal activity. For instance, Bergmann glia in the cerebellum express Ca^{2+} permeable AMPA-receptors[279]. These receptors are activated upon glutamate release by neighboring neurons, resulting in increased Ca^{2+} levels in astrocytes[279]. Increased astrocytic Ca^{2+} levels in turn may affect neuronal activity, for instance, by insertion of neurotransmitter transporters in the astrocytic membrane or direct release of gliotransmitters[281]. Of interest, recent research revealed that activation of GlyRs on cortical astrocytes inhibits ATP-induced Ca^{2+} transients in these cells[177]. This inhibition likely involves changes in permeability to Cl^{-}, and the recruitment of GlyRs from the cytosol to the astrocytic plasma membrane through microtubule dependent transport[177]. In neurons, Gephyrin is involved in microtubule dependent transport and membrane accumulation of GlyRs[119], likely through binding DYL2, which may be similar in astrocytes. Further research would be required to determine the exact physiological conditions in which astrocytic GlyRs affect Ca^{2+} transients, how these GlyRs are regulated and the downstream effects of GlyR modulated Ca^{2+} transients.

Astrocyte conditioned media and neuron-astrocyte co-cultures are known to promote the formation and maturation of synapses[282]. Interestingly, recent research revealed high expression of NLGN2 in astrocytes, which upon removal impaired astrocyte morphogenesis and excitatory synapse formation and function in vivo[276]. Likewise, knock-down of neuronal neurexins, the trans-synaptic binding partners of neuroligins, prevented astrocytic morphogenesis[276]. This implies bidirectional signaling through the neuronal neurexins and astrocytic neuroligins plays a critical role in brain development[276]. The dependence of astrocytic neuroligins on Gephyrin and potential mechanisms of regulation remain unknown. Characterizing in depth the functionalities of 'typical' neuronal proteins in astrocytes is an exciting future direction that may reveal previously overlooked cellular mechanisms.

Potential role for Gephyrin isoforms in neurons

Whereas Gephyrin-C3 is preferentially expressed in astrocytes, its expression in neurons cannot be excluded. Recent applications of super-resolution imaging techniques have revealed the organization of synaptic proteins in nanocolumns[38,180,283]. In these nanocolumns, pre-synaptic active zone proteins and post-synaptic scaffolds each display subsynaptic distributions that are aligned by adhesion moleculesto ensure synaptic response efficiency[15]. Nanocolumns have been observed at both excitatory and inhibitory synapses and demonstrate the importance of spatial organization of proteins for proper functioning of the synapse[15,284]. The exact molecular mechanisms through which the nanocolumn subdomains are created are unknown, but under active investigation[285,286]. Differences between Gephyrin isoform clustering abilities may impact their subsynaptic location and that of their differentially associated proteins. To this end, future research determining presence of Gephyrin-C3 at the neuronal synapse, and its subsynaptic location compared to the Gephyrin-C4A isoform may be an interesting research direction.

AMPAR subtypes and their (sub)complex compositions

In **chapter 4** we analyzed protein complex compositions of the two most abundant AMPAR subtypes in the hippocampus, and provided a framework for molecular analysis of AMPAR subtypes and their functional diversity. Whereas TARP-γ8, PRRT1 and CNIH2 were the highest abundant interactors of GluA1/2 specifically, GluA2/3 receptors revealed strongest co-purification of CNIH2, TARP-γ2 and OLFM1. Further IP-MS, IP-BN-PAGE/MS and microscopy analysis revealed TARP-γ8 and PRRT1 to directly interact, and co-assemble into an AMPAR subcomplex, especially near synapses. Future research will be required to determine how both proteins coordinate the retention and/or insertion of AMPARs into the synapse.

Proteomics study of receptor assemblies at increasing (sub)cellular resolution

During the past decade a large variety of AMPAR interactors have been identified, and revealed critical for receptor assembly, trafficking and gating properties[69,183,186]. The functional examination of a large group of interactors has significantly contributed to the understanding of AMPAR regulation and synaptic plasticity mechanisms[69,183,186]. However, mapping the specific functions of the vast number of interactors alone or in combination has only started. Previous reports revealed brain regional diversity of AMPAR assemblies[82,83]. Moreover, recent single cell analyses reveal cell type differences in protein expression[219,278]. Differential expression of AMPAR subunits and interactors may result in unique combinations and/or stoichiometries that can have distinct functional effects[287] in different cell-types. Importantly, this diversity provides the opportunity of designing drug strategies to selectivity modulate specific receptor-interactor assemblies[288].

The identification and preferably also quantification of cell or synapse-type specific receptor assemblies would require the collection of large numbers of isolated cells or synapses of the same type and/or the detection of protein-protein interactions at (extreme) low abundance levels. Of interest in this respect, exciting recent innovations in mass spectrometry have shown strong improvements in sensitivity and quantification accuracy[289]. Novel acquisition strategies and computational data analysis have resulted in increased quantitative precision and deep proteome coverage, using decreasing amounts of sample[289]. In a recent study, high sensitivity proteomics using a timsTOF mass spectrometer was applied for IP-MS using down to $0.8x10^6$ Fluorescence- Activated Cell Sorting (FACS) sorted cells of starting material[290], a more than 10-fold reduction compared to previous reports[291,292]. Across a set of 1261 tagged target proteins, the number of identified interactors ranged between 1 and 798 with a median of 7 interactors per target[290]. Continuous improvements on automated cell isolation methods[293], small volume sample handling[294,295] and mass spec technologies[296] holds great promise for the future of interaction proteomics with increasing (sub)cellular resolution.

Proteome analysis of Alzheimer mouse model of AD synaptic fractions

In **chapter 5** we analyzed the proteome of a synapse enriched fraction obtained from the APP/PS1 mouse model of Alzheimer's disease. Hippocampi of 6- and 12-month-old mice were used for synapse enrichment, and proteomics analysis was done by data independent acquisition (DIA) mass spectrometry. We first assessed and subsequently applied an improved directDIA workflow for the analysis of our data, and revealed most regulation of proteins at 12-months in APP/PS1 mice. Especially proteins involved in Aβ homeostasis and microglial-dependent processes revealed increased expression.

Analysis of DIA mass spectrometry data by directDIA and MS-DAP

We first assessed the usefulness of a new improved directDIA library workflow for the analysis of proteomics data obtained in Data Independent Acquisition (DIA) mode. Typically, in proteomics mass spectrometry, proteins are enzymatically digested into tryptic peptides, fractionated by liquid chromatography (LC) and subsequently ionized and sprayed into the mass spectrometer for analysis. In the mass spectrometer, peptides (precursor ions) are fragmented, and the resulting ion fragment mass patterns are used for peptide identification. Along the last years DIA has emerged as the method of choice for data acquisition, as it allows for the identification and quantification of thousands of proteins with low variation[297].

Unlike the previous predominant data dependent acquisition (DDA) method, in DIA mode in principle *all* eluted peptides are fragmented and detected in the mass spectrometer within sequential windows of specified mass ranges[298]. This method creates highly complex fragment ion mass spectra, that are conventionally compared to a project-specific spectral library for peptide identification[298]. Such a library is typically based on extensively fractionated samples, of similar type and mass spec set-up as the experiment, which requires additional sample handling and running time. In addition, peptides absent in the spectral library cannot be analyzed in the experimental sample. The 'library free' analysis of DIA was developed as an alternative, which assembles precursor and fragment ions detected in the experimental runs in pseudo-tandem mass spectra[215]. These spectra are subsequently searched against a reference proteome database for identification and are built into a library for comparison with the original DIA data[215]. This strategy is used in the directDIA workflow provided by the popular commercial software Spectronaut.

By inclusion of a deep-learning strategy, directDIA was recently improved and now starts to reach comparable performance to classically generated spectral libraries[299]. With our study, we were one of the first to determine its applicability to an independent user dataset, and concluded that the analysis with the directDIA 2.0 workflow was of competitive quality with the conventional spectral library for downstream analysis. The more recently developed DIA analysis tool DIA-NN also incorporated deep-learning methods that can be used with or without a project-specific spectral library[300]. DIA-NN outperforms conventional analysis tools including Spectronaut, and reveals higher peptide identification and quantification precision[300]. DIA-NN particularly benefits high-throughput applications where data is acquired with short measurement times[300]. The combination of recent data analysis and technological advances that allow acquisition of high-quality data in ahigh-throughput manner holds great promise for future proteome research.

For our analysis we applied the recently released Mass Spectrometry Downstream Analysis Pipeline (MS-DAP) (https://github.com/ftwkoopmans/msdap). This pipeline combines extensive quality control with state-of-the-art algorithms, intuitive visualization and reporting, and facilitates reproducible proteomics analysis. The large variety of existing and newly created algorithms and analyses hampers comparisons between different studies and scientific progress. The use of tools like MS-DAP to facilitate analysis consistency across different laboratories should be encouraged.

Little detected regulation of synaptic proteins in APP/PS1 mice

The aim of our study was to detect regulation of synaptic proteins induced by the overexpression of Aβ. To this end we analyzed synapse enriched biochemical fractions obtained from hippocampus of wildtype and APP/PS1 mice. In our analysis we only observed modest effect of Aβ exposure on synaptic proteins at the age of 6- and 12 months. Few synaptic proteins were regulated without enrichment towards a specific (sub)synaptic compartment or molecular function. As we enriched for synapses, detection of synapse loss may be counteracted. Removal of a specific synapse type would still be possible to detect based on its specific protein repertoire. Lack of synaptic proteins regulated in our dataset, suggests removal of synapses at these ages is not selective towards a specific synapse type. Additionally, the relative number of synapses that are lost may be low. At 6- and 12 months, loss of 25% in synapse density has been reported in subregions of the hippocampus of APP/PS1 mice[185,301]. Isolation of hippocampal subregions may increase detection power.

A previous report revealed synaptic protein changes using the same APP/PS1 mouse model of a younger age[222]. Mega analysis of APP mouse models reveals most consistent synaptic protein changes across different studies at this earlier time point[223]. Perhaps this younger age falls within a time window of Aβ induced synaptic protein changes leading up to synaptic removal. If one wants to uncover the effects of Aβ oligomers on synaptic proteins and cascades prior to synapse loss, APP/PS1 mice of young age are likely more informative than those of 6- and 12 months. A previous study with an APP model revealed synapse tagging with C1Q prior to their removal by microglia as early as 3-months[147]. Analysis of C1Q tagged and untagged synapses after exposure to Aβ may be of special interest. Also, analysis of brain tissue exposed to Aβ oligomers acutely may be of interest to dissect the direct effects of Aβ oligomers on the synaptic proteome.

Role of microglia in Aβ pathophysiology

Several proteins that we observed regulated in our dataset are of microglial origin. In our study, we analyzed a biochemical enriched synaptic fraction. This fraction indeed revealed enrichment of synaptic proteins, but in addition may contain structures with similar biochemical properties or structures coming from contacting non-neuronal cells such as microglia. Microglia have been implicated in synapse engulfment and elimination under exposure to Aβ oligomers, in a complement factor dependent manner[147]. In our dataset, we observed regulated proteins that are strongly expressed in microglia, including the complement factors C1QA-C.

Increased expression of microglial proteins is the most consistent phenotype across various studies with different APP mouse models[223], and reactive gliosis is one of the hallmarks of Alzheimer's disease[2]. Where microglia-related mechanisms were long considered secondary events to neurodegeneration, in recent years microglia are increasingly considered active players in AD pathogenesis[130,146]. Multiple risk-genes associated with AD are expressed by microglia. Investigation of AD risk-genes in microglia, including APOE, CLU and HEXB observed in our study, revealed their regulation is particularly induced by exposure to Aβ and not Tau pathology[302]. This suggests that these microglial AD risk genes are downstream of the Aβ pathway, but upstream of Tau pathology[302].

Recent focus has been on TREM2, an AD risk factor expressed on the surface of microglia[303,304]. AD associated variants of the TREM2 gene cause a partial loss of function, which prevents microglia to respond to pathological changes[303,304]. The effect of TREM2 loss on Aβ and Tau pathology has been partially inconsistent[305]. A recent study addressed this by using a mouse model combining Aβ and Tau pathology[306]. Research revealed that loss of TREM2 worsens Tau pathology and brain atrophy, only in the presence of Aβ pathology, suggesting activated microglia prevent Aβ-driven Tau pathology[306]. The role of microglia in AD remains under intense study, and opens exciting avenues for novel therapeutic approaches[304].

Conclusion

Synaptic proteins and their interactors form crucial molecular machineries for brain functioning, and reveal high molecular and functional diversity. Understanding their diverse structural organization is essential to understand complex synaptic processes. In this thesis, I applied several (interaction) proteomics strategies to further specify the protein complex organization of major players in synaptic function. We identified novel interactors of GlyR complexes and introduced a strategy to interrogate protein sub-complex composition. We exposed the differential organization of Gephyrin splice isoform assemblies, and revealed the separate interactomes of two major AMPAR subtypes and an associated sub-complex. Together these data provide a framework for further molecular and functional analyses. In addition, we revealed regulation of synaptic proteins and proteins involved in microglial-dependent processes in a mouse model of Alzheimer’s disease. Rapid technological advances will allow for mapping of protein interactions in increasingly high resolution. Combined with high-throughput strategies, it is expected that the majority of the most stable synaptic protein complexes will be mapped within the next decade.

Summary

Synaptic transmission is the major form of communication between brain cells. Among many others, it enables complex cognitive processes like learning and memory. Ligand-gated ion channels at the inhibitory and excitatory post-synaptic density play a central role in synaptic transmission. They allow for neurotransmitters to alter functional properties of the receiving neuron by regulating ion fluxes across the synaptic membrane and modulation of intracellular signaling cascades. Synaptic receptors associate with a large variety of binding partners that tightly regulate receptor localization and properties to ensure specificity and rate of signal transduction. Due to their regulatory roles, these interacting proteins can majorly impact synaptic transmission. Together, synaptic proteins and their interactors form crucial molecular machineries for brain functioning, and reveal high molecular and functional diversity. Understanding their diverse structural organization is essential to understand complex synaptic processes in health and disease.

Mass spectrometry (MS)-based proteomics is a powerful tool for the unbiased identification and quantification of hundreds of proteins. In this thesis I made use of interaction proteomics approaches to determine protein complex compositions of major proteins of the inhibitory and excitatory synapse. We further specified the inhibitory synaptic Glycine receptor (GlyR) and Gephyrin scaffold, and excitatory α-amino-3-hydroxy-5-methyl-4-isoxazolepropionic acid receptor (AMPAR) interactomes. For this, we focused on their subcomplex compositions and the differential protein assemblies of AMPAR subtypes and Gephyrin isoforms and provided a framework for their molecular and functional analyses.

The GlyR mediates inhibitory neurotransmission, is involved with locomotion, respiration and nociception, and implicated in startle disease/hyperekplexia. In **chapter 2** I determined the GlyR interactome in the brainstem using an immuno-purification (IP)-MS strategy with multiple antibodies against the GlyR and its major interactor Gephyrin. I revealed IQSEC2 and IQSEC3 as novel components of GlyR complexes. Further yeast-two-hybrid revealed direct interaction between amino acid 160-210 of the IQSEC3 N-terminal domain and the G-domain of Gephyrin. Additionally, we introduced a strategy that combines the specificity of IP with the resolution of blue-native PAGE to study the organization of native protein complexes. Size separation of native GlyR complexes by IP-BN-PAGE/MS demonstrated that this novel GlyR-Gephyrin-IQSEC2/3 assembly forms a small and distinct high molecular weight population of GlyRs. These data exemplified how the IP-BN-PAGE/MS strategy can be used to study subcomplex composition which can be applied to additional target proteins.

Gephyrin is the major scaffold protein of the inhibitory synapse where it clusters GlyRs and $GABA_A$Rs at the post-synaptic density. Additionally, in the brain Gephyrin catalyzes Molybdenum Cofactor (MoCo) synthesis, an important cofactor for multiple enzymes, in glial cells. Interestingly, alternative splicing of Gephyrin results in multiple isoforms with different biochemical properties that may majorly impact Gephyrin functioning. In **chapter 3** I designed and validated specific antibodies against the major Gephyrin-C3 and -C4A splice isoforms. I then used these novel antibodies to determine the cellular expression, specific interaction profiles and subcomplex composition of Gephyrin-C3 and -C4A. The neuronally expressed Gephyrin-C4A revealed strong binding to the GlyR, IQSEC3 and Nitric oxide synthase 1 (NOS1), whereas Gephyrin-C3 revealed high expression in astrocytes, reduced binding to the GlyR and specific interaction with NLGN2. Strong expression of Gephyrin-C3 in astrocytes, and its interaction with the GlyR and NLGN2 suggests a non-enzymatic function of Gephyrin in this cell type and opens a new avenue for Gephyrin research.

The AMPAR is the major synaptic excitatory ionotropic receptor in the brain. The most abundant AMPAR subtypes in the hippocampus are GluA1/2 and GluA2/3 heterotetramers, which contribute differentially to mechanisms of synaptic plasticity. Their functional differences may be in part caused by regulation through specific associated proteins. In **chapter 4** we analyzed the protein complex compositions of the GluA1/2 and GluA2/3 AMPAR subtypes separately. By performing quantitative and interaction proteomics on wildtype and GluA1- and GluA3 knock-out mice, we revealed differences in the interactome of GluA1/2 and GluA2/3 receptors. Whereas GluA1/2 co-purified TARP-γ8, PRRT1 and CNIH2 with highest abundances, GluA2/3 receptors revealed strongest co-purification of CNIH2, TARP-γ2, and OLFM1. Additional IP-MS, IP-BN-PAGE/MS and microscopy analysis revealed a direct interaction between TARP-γ8 and PRRT1 and their co-assembly into an AMPAR subcomplex, especially near the synapse. Future research will be required to determine the exact mechanism of AMPAR regulation by PRRT1 and TARP-γ8, and the interplay between these two proteins.

As part of my work on synaptic proteins, I additionally studied the synapse proteome of a mouse model of Alzheimer's disease (AD). AD is one of the most well-known neurodegenerative brain disorders, and is characterized by early hippocampal memory deficits and dysfunctional synapses. The accumulation of Amyloid-beta (Aβ) is believed to play an important role in AD pathogenesis. Aβ peptides are products of the transmembrane Amyloid Precursor Protein (APP) that is cleaved by Presenilin 1 and 2 (PSEN1 and PSEN2) containing γ-secretases. Mutations in the APP and PSEN1/2 genes are causatives for cases of familial AD, and form the genetic basis of the APP/PS1 mouse model. In **chapter 5** I studied

the proteome of a synapse enriched fraction obtained from the hippocampus of the APP/PS1 mouse model of AD at 6 and 12 months of age using data independent acquisition (DIA) mass spectrometry. We first assessed the usefulness of a recently improved directDIA analysis workflow as an alternative to conventional DIA analysis using a project specific library. I concluded that the improved directDIA workflow was of competitive quality with the conventional spectral library for downstream analysis, and subsequently applied this workflow to our datasets. Most regulation was observed at 12-months, especially of proteins involved in Aβ homeostasis and microglial-dependent processes like Apolipoprotein, Clusterin and complement factors C1QA, C1QB and C1QC.

References

1. Selkoe, D. J. Alzheimer's disease is a synaptic failure. *Science* **298**, 789–791 (2002).
2. Raskin, J., Cummings, J., Hardy, J., Schuh, K. & Dean, R. A. Neurobiology of Alzheimer's Disease: Integrated Molecular, Physiological, Anatomical, Biomarker, and Cognitive Dimensions. *Curr. Alzheimer Res.* **12**, 712–722 (2015).
3. Scheltens, P. *et al.* Alzheimer's disease. *Lancet (London, England)* **388**, 505–517 (2016).
4. Signal Transmission at Chemical Synapses. in *Neuroscience* (eds. Purves, D. et al.) 88 (Sunderland (MA): Sinauer Associates, 2008).
5. Summation of Synaptic Potentials. in *Neuroscience* (eds. Purves, D. et al.) 114–115 (Sunderland (MA): Sinauer Associates, 2008).
6. Molecular Signaling within Neurons. in *Neuroscience* (eds. Purves, D. et al.) 153–176 (Sunderland (MA): Sinauer Associates, 2008).
7. Citri, A. & Malenka, R. C. Synaptic Plasticity: Multiple Forms, Functions, and Mechanisms. *Neuropsychopharmacology* **33**, 18–41 (2008).
8. Gonzalez-Lozano, M. A. *et al.* Stitching the synapse: Cross-linking mass spectrometry into resolving synaptic protein interactions. *Sci. Adv.* **6**, eaax5783 (2020).
9. Bourgeron, T. From the genetic architecture to synaptic plasticity in autism spectrum disorder. *Nat. Rev. Neurosci.* **16**, 551–563 (2015).
10. Fromer, M. *et al.* De novo mutations in schizophrenia implicate synaptic networks. *Nature* **506**, 179–184 (2014).
11. Grant, S. G. N. N. Synaptopathies: diseases of the synaptome. *Curr. Opin. Neurobiol.* **22**, 522–529 (2012).
12. Verhage, M. & Sørensen, J. B. SNAREopathies: Diversity in Mechanisms and Symptoms. *Neuron* **107**, 22–37 (2020).
13. Koopmans, F. *et al.* SynGO: An Evidence-Based, Expert-Curated Knowledge Base for the Synapse. *Neuron* **103**, 217-234.e4 (2019).
14. O'Rourke, N. A., Weiler, N. C., Micheva, K. D. & Smith, S. J. Deep molecular diversity of mammalian synapses: why it matters and how to measure it. *Nat. Rev. Neurosci.* **13**, 365–379 (2012).
15. Haas, K. T. *et al.* Pre-post synaptic alignment through neuroligin-1 tunes synaptic transmission efficiency. *Elife* **7**, (2018).
16. Sheng, M. & Kim, E. The postsynaptic organization of synapses. *Cold Spring Harb. Perspect. Biol.* **3**, (2011).
17. Tao, C.-L. *et al.* Differentiation and Characterization of Excitatory and Inhibitory Synapses by Cryo-electron Tomography and Correlative Microscopy. *J. Neurosci.* **38**, 1493–1510 (2018).
18. Takamori, S. *et al.* Molecular anatomy of a trafficking organelle. *Cell* **127**, 831–846 (2006).
19. Südhof, T. C. The presynaptic active zone. *Neuron* **75**, 11–25 (2012).
20. Rizo, J. & Südhof, T. C. Snares and Munc18 in synaptic vesicle fusion. *Nat. Rev. Neurosci.* **3**, 641–653 (2002).

21. Poirier, M. A. *et al.* The synaptic SNARE complex is a parallel four-stranded helical bundle. *Nat. Struct. Biol.* **5**, 765–769 (1998).

22. Watanabe, S. & Boucrot, E. Fast and ultrafast endocytosis. *Curr. Opin. Cell Biol.* **47**, 64–71 (2017).

23. Branco, T. & Staras, K. The probability of neurotransmitter release: variability and feedback control at single synapses. *Nature reviews. Neuroscience* vol. 10 373–383 (2009).

24. Hering, H. & Sheng, M. Dendritic spines: structure, dynamics and regulation. *Nat. Rev. Neurosci.* **2**, 880–888 (2001).

25. Harris, K. M. & Weinberg, R. J. Ultrastructure of synapses in the mammalian brain. *Cold Spring Harb. Perspect. Biol.* **4**, (2012).

26. LeVay, S. Synaptic patterns in the visual cortex of the cat and monkey. Electron microscopy of Golgi preparations. *J. Comp. Neurol.* **150**, 53–85 (1973).

27. Uchizono, K. Characteristics of excitatory and inhibitory synapses in the central nervous system of the cat. *Nature* **207**, 642–643 (1965).

28. Bosch, M. & Hayashi, Y. Structural plasticity of dendritic spines. *Curr. Opin. Neurobiol.* **22**, 383–388 (2012).

29. Noguchi, J. *et al.* In vivo two-photon uncaging of glutamate revealing the structure-function relationships of dendritic spines in the neocortex of adult mice. *J. Physiol.* **589**, 2447–2457 (2011).

30. Borczyk, M., Śliwińska, M. A., Caly, A., Bernas, T. & Radwanska, K. Neuronal plasticity affects correlation between the size of dendritic spine and its postsynaptic density. *Sci. Rep.* **9**, 1693 (2019).

31. Chen, X. *et al.* Organization of the core structure of the postsynaptic density. *Proc. Natl. Acad. Sci. U. S. A.* **105**, 4453–4458 (2008).

32. Choquet, D. & Triller, A. The dynamic synapse. *Neuron* **80**, 691–703 (2013).

33. Opazo, P. & Choquet, D. A three-step model for the synaptic recruitment of AMPA receptors. *Mol. Cell. Neurosci.* **46**, 1–8 (2011).

34. Lu, W. *et al.* Activation of synaptic NMDA receptors induces membrane insertion of new AMPA receptors and LTP in cultured hippocampal neurons. *Neuron* **29**, 243–254 (2001).

35. Rácz, B., Blanpied, T. A., Ehlers, M. D. & Weinberg, R. J. Lateral organization of endocytic machinery in dendritic spines. *Nat. Neurosci.* **7**, 917–918 (2004).

36. Borgdorff, A. J. & Choquet, D. Regulation of AMPA receptor lateral movements. *Nature* **417**, 649–653 (2002).

37. Penn, A. C. *et al.* Hippocampal LTP and contextual learning require surface diffusion of AMPA receptors. *Nature* **549**, 384–388 (2017).

38. Tang, A.-H. *et al.* A trans-synaptic nanocolumn aligns neurotransmitter release to receptors. *Nature* **536**, 210–214 (2016).

39. Nair, D. *et al.* Super-Resolution Imaging Reveals That AMPA Receptors Inside Synapses Are Dynamically Organized in Nanodomains Regulated by PSD95. *J. Neurosci.* **33**, 13204–13224 (2013).

40. Heine, M. & Holcman, D. Asymmetry Between Pre- and Postsynaptic Transient Nanodomains Shapes Neuronal Communication. *Trends Neurosci.* **43**, 182–196 (2020).

41. Specht, C. G. *et al.* Quantitative Nanoscopy of Inhibitory Synapses: Counting Gephyrin Molecules and Receptor Binding Sites. *Neuron* **79**, 308–321 (2013).

42. Rosenberg, M., Meier, J., Triller, A. & Vannier, C. Dynamics of glycine receptor insertion in the neuronal plasma membrane. *J. Neurosci.* **21**, 5036–5044 (2001).

43. Meier, J., Vannier, C., Sergé, A., Triller, A. & Choquet, D. Fast and reversible trapping of surface glycine receptors by gephyrin. *Nat. Neurosci.* **4**, 253–260 (2001).

44. Diering, G. H. & Huganir, R. L. The AMPA Receptor Code of Synaptic Plasticity. *Neuron* **100**, 314–329 (2018).

45. Sanz-Clemente, A., Nicoll, R. A. & Roche, K. W. Diversity in NMDA receptor composition: many regulators, many consequences. *Neurosci. a Rev. J. bringing Neurobiol. Neurol. psychiatry* **19**, 62–75 (2013).

46. Schwenk, J. *et al.* High-Resolution Proteomics Unravel Architecture and Molecular Diversity of Native AMPA Receptor Complexes. *Neuron* **74**, 621–633 (2012).

47. Schwenk, J. *et al.* Modular composition and dynamics of native GABAB receptors identified by high-resolution proteomics. *Nat. Neurosci.* **19**, 233–242 (2016).

48. Frank, R. A. W. *et al.* NMDA receptors are selectively partitioned into complexes and supercomplexes during synapse maturation. *Nat. Commun.* **7**, 11264 (2016).

49. Maher, M. P., Matta, J. A., Gu, S., Seierstad, M. & Bredt, D. S. Getting a Handle on Neuropharmacology by Targeting Receptor-Associated Proteins. *Neuron* **96**, 989–1001 (2017).

50. Traynelis, S. F. *et al.* Glutamate receptor ion channels: structure, regulation, and function. *Pharmacol. Rev.* **62**, 405–496 (2010).

51. Wenthold, R. J., Petralia, R. S., Blahos J, I. I. & Niedzielski, A. S. Evidence for multiple AMPA receptor complexes in hippocampal CA1/CA2 neurons. *J. Neurosci.* **16**, 1982–1989 (1996).

52. Zhao, Y., Chen, S., Swensen, A. C., Qian, W.-J. & Gouaux, E. Architecture and subunit arrangement of native AMPA receptors elucidated by cryo-EM. *Science* **364**, 355–362 (2019).

53. Lu, W. *et al.* Subunit composition of synaptic AMPA receptors revealed by a single-cell genetic approach. *Neuron* **62**, 254–268 (2009).

54. Burnashev, N., Monyer, H., Seeburg, P. H. & Sakmann, B. Divalent ion permeability of AMPA receptor channels is dominated by the edited form of a single subunit. *Neuron* **8**, 189–198 (1992).

55. Pelkey, K. A. *et al.* Pentraxins coordinate excitatory synapse maturation and circuit integration of parvalbumin interneurons. *Neuron* **85**, 1257–1272 (2015).

56. Choquet, D. & Hosy, E. AMPA receptor nanoscale dynamic organization and synaptic plasticities. *Curr. Opin. Neurobiol.* **63**, 137–145 (2020).

57. Andrásfalvy, B. K., Smith, M. A., Borchardt, T., Sprengel, R. & Magee, J. C. Impaired regulation of synaptic strength in hippocampal neurons from GluR1-deficient mice. *J. Physiol.* **552**, 35–45 (2003).

58. Kristensen, A. S. *et al.* Mechanism of Ca2+/calmodulin-dependent kinase II regulation of AMPA receptor gating. *Nat. Neurosci.* **14**, 727–735 (2011).

59. Shi, S., Hayashi, Y., Esteban, J. A. & Malinow, R. Subunit-specific rules governing AMPA receptor trafficking to synapses in hippocampal pyramidal neurons. *Cell* **105**, 331–343 (2001).

60. McCormack, S. G., Stornetta, R. L. & Zhu, J. J. Synaptic AMPA receptor exchange maintains bidirectional plasticity. *Neuron* **50**, 75–88 (2006).

61. Renner, M. C. *et al.* Synaptic plasticity through activation of GluA3-containing AMPA-receptors. *Elife* **6**, (2017).

62. Shepherd, J. D. & Huganir, R. L. The cell biology of synaptic plasticity: AMPA receptor trafficking. *Annu. Rev. Cell Dev. Biol.* **23**, 613–643 (2007).

63. Dong, H. *et al.* GRIP: a synaptic PDZ domain-containing protein that interacts with AMPA receptors. *Nature* **386**, 279–284 (1997).

64. Xia, J., Zhang, X., Staudinger, J. & Huganir, R. L. Clustering of AMPA receptors by the synaptic PDZ domain-containing protein PICK1. *Neuron* **22**, 179–187 (1999).

65. Seidenman, K. J., Steinberg, J. P., Huganir, R. & Malinow, R. Glutamate receptor subunit 2 Serine 880 phosphorylation modulates synaptic transmission and mediates plasticity in CA1 pyramidal cells. *J. Neurosci.* **23**, 9220–9228 (2003).

66. von Engelhardt, J. *et al.* CKAMP44: a brain-specific protein attenuating short-term synaptic plasticity in the dentate gyrus. *Science* **327**, 1518–1522 (2010).

67. Shanks, N. F. *et al.* Differences in AMPA and kainate receptor interactomes facilitate identification of AMPA receptor auxiliary subunit GSG1L. *Cell Rep.* **1**, 590–598 (2012).

68. Schwenk, J. *et al.* Functional proteomics identify cornichon proteins as auxiliary subunits of AMPA receptors. *Science* **323**, 1313 (2009).

69. Schwenk, J. & Fakler, B. Building of AMPA-type glutamate receptors in the endoplasmic reticulum and its implication for excitatory neurotransmission. *J. Physiol.* (2020) doi:10.1113/JP279025.

70. Chen, L. *et al.* Stargazin regulates synaptic targeting of AMPA receptors by two distinct mechanisms. *Nature* **408**, 936–943 (2000).

71. Letts, V. A. *et al.* The mouse stargazer gene encodes a neuronal Ca2+-channel gamma subunit. *Nat. Genet.* **19**, 340–347 (1998).

72. Tomita, S. *et al.* Functional studies and distribution define a family of transmembrane AMPA receptor regulatory proteins. *J. Cell Biol.* **161**, 805–816 (2003).

73. Bats, C., Groc, L. & Choquet, D. The Interaction between Stargazin and PSD-95 Regulates AMPA Receptor Surface Trafficking. *Neuron* **53**, 719–734 (2007).

74. Sumioka, A. *et al.* PDZ binding of TARPγ-8 controls synaptic transmission but not synaptic plasticity. *Nat. Neurosci.* **14**, 1410–1412 (2011).

75. Priel, A. *et al.* Stargazin reduces desensitization and slows deactivation of the AMPA-type glutamate receptors. *J. Neurosci.* **25**, 2682–2686 (2005).

76. Milstein, A. D., Zhou, W., Karimzadegan, S., Bredt, D. S. & Nicoll, R. A. TARP Subtypes Differentially and Dose-Dependently Control Synaptic AMPA Receptor Gating. *Neuron* **55**, 905–918 (2007).

77. Schwenk, J. *et al.* An ER Assembly Line of AMPA-Receptors Controls Excitatory Neurotransmission and Its Plasticity. *Neuron* **104**, 680-692.e9 (2019).

78. Harmel, N. *et al.* AMPA receptors commandeer an ancient cargo exporter for use as an auxiliary subunit for signaling. *PLoS One* **7**, e30681 (2012).

79. Pandya, N. J. *et al.* Correlation profiling of brain sub-cellular proteomes reveals co-assembly of synaptic proteins and subcellular distribution. *Sci. Rep.* **7**, 12107 (2017).

80. Brechet, A. *et al.* AMPA-receptor specific biogenesis complexes control synaptic transmission and intellectual ability. *Nat. Commun.* **8**, 15910 (2017).

81. Anggono, V. & Huganir, R. L. Regulation of AMPA receptor trafficking and synaptic plasticity. *Curr. Opin. Neurobiol.* **22**, 461–469 (2012).

82. Kirk, L. M. *et al.* Distribution of the SynDIG4/proline-rich transmembrane protein 1 in rat brain. *J. Comp. Neurol.* **524**, 2266–2280 (2016).

83. Schwenk, J. *et al.* Regional diversity and developmental dynamics of the AMPA-receptor proteome in the mammalian brain. *Neuron* **84**, 41–54 (2014).

84. Chen, N. *et al.* Interaction proteomics reveals brain region-specific AMPA receptor complexes. *J. Proteome Res.* **13**, 5695–5706 (2014).

85. Lynch, J. W. Native glycine receptor subtypes and their physiological roles. *Neuropharmacology* **56**, 303–309 (2009).

86. Hinckley, C., Seebach, B. & Ziskind-Conhaim, L. Distinct roles of glycinergic and GABAergic inhibition in coordinating locomotor-like rhythms in the neonatal mouse spinal cord. *Neuroscience* **131**, 745–758 (2005).

87. Schmid, K., Böhmer, G. & Gebauer, K. Glycine receptor-mediated fast synaptic inhibition in the brainstem respiratory system. *Respir. Physiol.* **84**, 351–361 (1991).

88. Harvey, R. J. *et al.* GlyR alpha3: an essential target for spinal PGE2-mediated inflammatory pain sensitization. *Science* **304**, 884–887 (2004).

89. Patrizio, A., Renner, M., Pizzarelli, R., Triller, A. & Specht, C. G. Alpha subunit-dependent glycine receptor clustering and regulation of synaptic receptor numbers. *Sci. Rep.* **7**, 10899 (2017).

90. Dutertre, S., Becker, C.-M. & Betz, H. Inhibitory glycine receptors: an update. *J. Biol. Chem.* **287**, 40216–40223 (2012).

91. Kim, E. Y. *et al.* Deciphering the structural framework of glycine receptor anchoring by gephyrin. *EMBO J.* **25**, 1385–1395 (2006).

92. Zhu, H. & Gouaux, E. Architecture and assembly mechanism of native glycine receptors. *Nature* **599**, 513–517 (2021).

93. Meyer, G., Kirsch, J., Betz, H. & Langosch, D. Identification of a gephyrin binding motif on the glycine receptor beta subunit. *Neuron* **15**, 563–572 (1995).

94. Shiang, R. *et al.* Mutations in the alpha 1 subunit of the inhibitory glycine receptor cause the dominant neurologic disorder, hyperekplexia. *Nat. Genet.* **5**, 351–358 (1993).

95. Bode, A. & Lynch, J. W. The impact of human hyperekplexia mutations on glycine receptor structure and function. *Mol. Brain* **7**, 2 (2014).

96. Avila, A. *et al.* Glycine receptor α2 subunit activation promotes cortical interneuron migration. *Cell Rep.* **4**, 738–750 (2013).

97. Zhang, Y., Ho, T. N. T., Harvey, R. J., Lynch, J. W. & Keramidas, A. Structure-Function Analysis of the GlyR α2 Subunit Autism Mutation p.R323L Reveals a Gain-of-Function. *Frontiers in Molecular Neuroscience* vol. 10 (2017).

98. Manzke, T. *et al.* Serotonin receptor 1A-modulated phosphorylation of glycine receptor α3 controls breathing in mice. *J. Clin. Invest.* **120**, 4118–4128 (2010).

99. Nishizono, H. *et al.* Glycine receptor α4 subunit facilitates the early embryonic development in mice. *Reproduction* **159**, 41 (2020).

100. Alvarez, F. J. Gephyrin and the regulation of synaptic strength and dynamics at glycinergic inhibitory synapses. *Brain Res. Bull.* **129**, 50–65 (2017).

101. Kirsch, J. *et al.* The 93-kDa glycine receptor-associated protein binds to tubulin. *J. Biol. Chem.* **266**, 22242–22245 (1991).

102. Del Pino, I. *et al.* Proteomic analysis of glycine receptor beta subunit (GlyRbeta)-interacting proteins: evidence for syndapin I regulating synaptic glycine receptors. *J. Biol. Chem.* **289**, 11396–11409 (2014).

103. Langlhofer, G. *et al.* A Novel Glycine Receptor Variant with Startle Disease Affects Syndapin I and Glycinergic Inhibition. *J. Neurosci.* **40**, 4954–4969 (2020).

104. del Pino, I., Paarmann, I., Karas, M., Kilimann, M. W. & Betz, H. The trafficking proteins Vacuolar Protein Sorting 35 and Neurobeachin interact with the glycine receptor beta-subunit. *Biochem. Biophys. Res. Commun.* **412**, 435–440 (2011).

105. Leite, J. F., Gribble, B., Randolph, N. & Cascio, M. In vitro interaction of the glycine receptor with the leptin receptor. *Physiol. Behav.* **77**, 565–569 (2002).

106. Melzer, N. *et al.* Multifunctional basic motif in the glycine receptor intracellular domain induces subunit-specific sorting. *J. Biol. Chem.* **285**, 3730–3739 (2010).

107. Gromova, K. V *et al.* Neurobeachin and the Kinesin KIF21B Are Critical for Endocytic Recycling of NMDA Receptors and Regulate Social Behavior. *Cell Rep.* **23**, 2705–2717 (2018).

108. Temkin, P. *et al.* The Retromer Supports AMPA Receptor Trafficking During LTP. *Neuron* **94**, 74-82.e5 (2017).

109. Tyagarajan, S. K. & Fritschy, J.-M. Gephyrin: a master regulator of neuronal function? *Nat. Rev. Neurosci.* **15**, 141–156 (2014).

110. Schwarz, G., Schrader, N., Mendel, R. R., Hecht, H. J. & Schindelin, H. Crystal structures of human gephyrin and plant Cnx1 G domains: comparative analysis and functional implications. *J. Mol. Biol.* **312**, 405–418 (2001).

111. Sola, M. *et al.* Structural basis of dynamic glycine receptor clustering by gephyrin. *EMBO J.* **23**, 2510–2519 (2004).

112. Schwarz, G., Mendel, R. R. & Ribbe, M. W. Molybdenum cofactors, enzymes and pathways. *Nature* **460**, 839–847 (2009).

113. Maric, H.-M., Mukherjee, J., Tretter, V., Moss, S. J. & Schindelin, H. Gephyrin-mediated γ-aminobutyric acid type A and glycine receptor clustering relies on a common binding site. *J. Biol. Chem.* **286**, 42105–42114 (2011).

114. Specht, C. G. *et al.* Regulation of glycine receptor diffusion properties and gephyrin interactions by protein kinase C. *EMBO J.* **30**, 3842–3853 (2011).

115. Mukherjee, J. *et al.* The residence time of GABA(A)Rs at inhibitory synapses is determined by direct binding of the receptor α1 subunit to gephyrin. *J. Neurosci.* **31**, 14677–14687 (2011).

116. Jonas, P., Bischofberger, J. & Sandkühler, J. Corelease of two fast neurotransmitters at a central synapse. *Science* **281**, 419–424 (1998).

117. Dugué, G. P., Dumoulin, A., Triller, A. & Dieudonné, S. Target-Dependent Use of Coreleased Inhibitory Transmitters at Central Synapses. *J. Neurosci.* **25**, 6490 LP – 6498 (2005).

118. Bedet, C. *et al.* Regulation of gephyrin assembly and glycine receptor synaptic stability. *J. Biol. Chem.* **281**, 30046–30056 (2006).

119. Studer, R. *et al.* Alteration of GABAergic synapses and gephyrin clusters in the thalamic reticular nucleus of GABAA receptor alpha3 subunit-null mice. *Eur. J. Neurosci.* **24**, 1307–1315 (2006).

120. Maas, C. *et al.* Neuronal cotransport of glycine receptor and the scaffold protein gephyrin. *J. Cell Biol.* **172**, 441–451 (2006).

121. Poulopoulos, A. *et al.* Neuroligin 2 drives postsynaptic assembly at perisomatic inhibitory synapses through gephyrin and collybistin. *Neuron* **63**, 628–642 (2009).

122. Um, J. W. *et al.* IQ Motif and SEC7 Domain-containing Protein 3 (IQSEC3) Interacts with Gephyrin to Promote Inhibitory Synapse Formation. *J. Biol. Chem.* **291**, 10119–10130 (2016).

123. Früh, S., Tyagarajan, S. K., Campbell, B., Bosshard, G. & Fritschy, J.-M. The catalytic function of the gephyrin-binding protein IQSEC3 regulates neurotransmitter-specific matching of pre- and post-synaptic structures in primary hippocampal cultures. *J. Neurochem.* **147**, 477–494 (2018).

124. Hanus, C., Vannier, C. & Triller, A. Intracellular Association of Glycine Receptor with Gephyrin Increases Its Plasma Membrane Accumulation Rate. *J. Neurosci.* **24**, 1119 LP – 1128 (2004).

125. Maas, C. *et al.* Synaptic activation modifies microtubules underlying transport of postsynaptic cargo. *Proc. Natl. Acad. Sci.* **106**, 8731 LP – 8736 (2009).

126. Prior, P. *et al.* Primary structure and alternative splice variants of gephyrin, a putative glycine receptor-tubulin linker protein. *Neuron* **8**, 1161–1170 (1992).

127. Meier, J., De Chaldée, M., Triller, A. & Vannier, C. Functional heterogeneity of gephyrins. *Mol. Cell. Neurosci.* **16**, 566–577 (2000).

128. Herweg, J. & Schwarz, G. Splice-specific glycine receptor binding, folding, and phosphorylation of the scaffolding protein gephyrin. *J. Biol. Chem.* **287**, 12645–12656 (2012).

129. Smolinsky, B., Eichler, S. A., Buchmeier, S., Meier, J. C. & Schwarz, G. Splice-specific functions of gephyrin in molybdenum cofactor biosynthesis. *J. Biol. Chem.* **283**, 17370–17379 (2008).

130. Fritschy, J.-M., Harvey, R. J. & Schwarz, G. Gephyrin: where do we stand, where do we go? *Trends Neurosci.* **31**, 257–264 (2008).

131. Meier, J. & Grantyn, R. A Gephyrin-Related Mechanism Restraining Glycine Receptor Anchoring at GABAergic Synapses. *J. Neurosci.* **24**, 1398 LP – 1405 (2004).

132. Arendt, T. Synaptic degeneration in Alzheimer's disease. *Acta Neuropathol.* **118**, 167–179 (2009).

133. 2020 Alzheimer's disease facts and figures. *Alzheimers. Dement.* (2020) doi:10.1002/alz.12068.

134. Long, J. M. & Holtzman, D. M. Alzheimer Disease: An Update on Pathobiology and Treatment Strategies. *Cell* **179**, 312–339 (2019).

135. Schindler, S. E. *et al.* High-precision plasma β-amyloid 42/40 predicts current and future brain amyloidosis. *Neurology* **93**, e1647–e1659 (2019).

136. Kunkle, B. W. *et al.* Genetic meta-analysis of diagnosed Alzheimer's disease identifies new risk loci and implicates Aβ, tau, immunity and lipid processing. *Nat. Genet.* **51**, 414–430 (2019).

137. Chen, W.-T. *et al.* Spatial Transcriptomics and In Situ Sequencing to Study Alzheimer's Disease. *Cell* **182**, 976-991.e19 (2020).

138. Hardy, J. A. & Higgins, G. A. Alzheimer's disease: the amyloid cascade hypothesis. *Science* **256**, 184–185 (1992).

139. Li, S. & Selkoe, D. J. A mechanistic hypothesis for the impairment of synaptic plasticity by soluble Aβ oligomers from Alzheimer's brain. *J. Neurochem.* **154**, 583–597 (2020).

140. Alzheimer's Disease Collaborative Group. The structure of the presenilin 1 (S182) gene and identification of six novel mutations in early onset AD families. *Nat. Genet.* **11**, 219–222 (1995).

141. Mullan, M. Familial Alzheimer's disease: second gene locus located. *BMJ (Clinical research ed.)* vol. 305 1108–1109 (1992).

142. Scheff, S. W. & Price, D. A. Synaptic pathology in Alzheimer's disease: a review of ultrastructural studies. *Neurobiol. Aging* **24**, 1029–1046 (2003).

143. Terry, R. D. *et al.* Physical basis of cognitive alterations in Alzheimer's disease: synapse loss is the major correlate of cognitive impairment. *Ann. Neurol.* **30**, 572–580 (1991).

144. Scheff, S. W., Price, D. A., Schmitt, F. A. & Mufson, E. J. Hippocampal synaptic loss in early Alzheimer's disease and mild cognitive impairment. *Neurobiol. Aging* **27**, 1372–1384 (2006).

145. Hsia, A. Y. *et al.* Plaque-independent disruption of neural circuits in Alzheimer's disease mouse models. *Proc. Natl. Acad. Sci.* **96**, 3228 LP – 3233 (1999).

146. Shankar, G. M. *et al.* Amyloid-beta protein dimers isolated directly from Alzheimer's brains impair synaptic plasticity and memory. *Nat. Med.* **14**, 837–842 (2008).

147. Götz, J., Chen, F., van Dorpe, J. & Nitsch, R. M. Formation of neurofibrillary tangles in P301l tau transgenic mice induced by Abeta 42 fibrils. *Science* **293**, 1491–1495 (2001).

148. Leroy, K. *et al.* Lack of tau proteins rescues neuronal cell death and decreases amyloidogenic processing of APP in APP/PS1 mice. *Am. J. Pathol.* **181**, 1928–1940 (2012).

149. Bloom, G. S. Amyloid-β and tau: the trigger and bullet in Alzheimer disease pathogenesis. *JAMA Neurol.* **71**, 505–508 (2014).

150. Benilova, I., Karran, E. & De Strooper, B. The toxic Aβ oligomer and Alzheimer's disease: an emperor in need of clothes. *Nat. Neurosci.* **15**, 349–357 (2012).

151. Palop, J. J. & Mucke, L. Amyloid-beta-induced neuronal dysfunction in Alzheimer's disease: from synapses toward neural networks. *Nat. Neurosci.* **13**, 812–818 (2010).

152. Heneka, M. T. *et al.* Neuroinflammation in Alzheimer's disease. *Lancet. Neurol.* **14**, 388–405 (2015).

153. Hong, S. *et al.* Complement and microglia mediate early synapse loss in Alzheimer mouse models. *Science* **352**, 712–716 (2016).

154. Lynch, J. W. Molecular structure and function of the glycine receptor chloride channel. *Physiol. Rev.* **84**, 1051–1095 (2004).

155. Ge, Y. *et al.* Clptm1 Limits Forward Trafficking of GABA(A) Receptors to Scale Inhibitory Synaptic Strength. *Neuron* **97**, 596-610.e8 (2018).

156. Pandya, N. J. *et al.* Group 1 metabotropic glutamate receptors 1 and 5 form a protein complex in mouse hippocampus and cortex. *Proteomics* **16**, 2698–2705 (2016).

157. Li, K. W. *et al.* Identifying true protein complex constituents in interaction proteomics: the example of the DMXL2 protein complex. *Proteomics* **12**, 2428–2432 (2012).

158. Gonzalez-Lozano, M. A., Koopmans, F., Paliukhovich, I., Smit, A. B. & Li, K. W. A Fast and Economical Sample Preparation Protocol for Interaction Proteomics Analysis. *Proteomics* **19**, e1900027 (2019).

159. Pfeiffer, F., Graham, D. & Betz, H. Purification by affinity chromatography of the glycine receptor of rat spinal cord. *J. Biol. Chem.* **257**, 9389–9393 (1982).

160. Rudashevskaya, E. L., Sickmann, A. & Markoutsa, S. Global profiling of protein complexes: current approaches and their perspective in biomedical research. *Expert Rev. Proteomics* **13**, 951–964 (2016).

161. Sakagami, H. *et al.* Distinct synaptic localization patterns of brefeldin A-resistant guanine nucleotide exchange factors BRAG2 and BRAG3 in the mouse retina. *J. Comp. Neurol.* **521**, 860–876 (2013).

162. Uezu, A. *et al.* Identification of an elaborate complex mediating postsynaptic inhibition. *Science* **353**, 1123–1129 (2016).

163. Nakamura, Y. *et al.* Proteomic Characterization of Inhibitory Synapses Using a Novel pHluorin-tagged γ-Aminobutyric Acid Receptor, Type A (GABAA), α2 Subunit Knock-in Mouse. *J. Biol. Chem.* **291**, 12394–12407 (2016).

164. Murphy, J. A., Jensen, O. N. & Walikonis, R. S. BRAG1, a Sec7 domain-containing protein, is a component of the postsynaptic density of excitatory synapses. *Brain Res.* **1120**, 35–45 (2006).

165. Chen, N. *et al.* Interaction proteomics of canonical Caspr2 (CNTNAP2) reveals the presence of two Caspr2 isoforms with overlapping interactomes. *Biochim. Biophys. Acta* **1854**, 827–833 (2015).

166. Tyanova, S., Temu, T. & Cox, J. The MaxQuant computational platform for mass spectrometry-based shotgun proteomics. *Nat. Protoc.* **11**, 2301–2319 (2016).

167. Pino, L. K. *et al.* The Skyline ecosystem: Informatics for quantitative mass spectrometry proteomics. *Mass Spectrom. Rev.* **39**, 229–244 (2020).

168. Harvey, K. *et al.* The GDP-GTP exchange factor collybistin: an essential determinant of neuronal gephyrin clustering. *J. Neurosci.* **24**, 5816–5826 (2004).

169. Krueger-Burg, D., Papadopoulos, T. & Brose, N. Organizers of inhibitory synapses come of age. *Curr. Opin. Neurobiol.* **45**, 66–77 (2017).

170. Sola, M., Kneussel, M., Heck, I. S., Betz, H. & Weissenhorn, W. X-ray Crystal Structure of the Trimeric N-terminal Domain of Gephyrin. *J. Biol. Chem.* **276**, 25294–25301 (2001).

171. Saiyed, T. *et al.* Molecular basis of gephyrin clustering at inhibitory synapses: role of G- and E-domain interactions. *J. Biol. Chem.* **282**, 5625–5632 (2007).

172. Stallmeyer, B., Nerlich, A., Schiemann, J., Brinkmann, H. & Mendel, R. R. Molybdenum co-factor biosynthesis: the Arabidopsis thaliana cDNA cnx1 encodes a multifunctional two-domain protein homologous to a mammalian neuroprotein, the insect protein Cinnamon and three Escherichia coli proteins. *Plant J.* **8**, 751–762 (1995).

173. Kirsch, J., Wolters, I., Triller, A. & Betz, H. Gephyrin antisense oligonucleotides prevent glycine receptor clustering in spinal neurons. *Nature* **366**, 745–748 (1993).

174. Ramming, M. *et al.* Diversity and phylogeny of gephyrin: tissue-specific splice variants, gene structure, and sequence similarities to molybdenum cofactor-synthesizing and cytoskeleton-associated proteins. *Proc. Natl. Acad. Sci. U. S. A.* **97**, 10266–10271 (2000).

175. Freeman, M. R. Specification and morphogenesis of astrocytes. *Science* **330**, 774–778 (2010).

176. van der Spek, S. J. F. *et al.* Glycine Receptor Complex Analysis Using Immunoprecipitation-Blue Native Gel Electrophoresis-Mass Spectrometry. *Proteomics* **20**, e1900403 (2020).

177. Machado, P. *et al.* Heat Shock Cognate Protein 70 Regulates Gephyrin Clustering. *J. Neurosci.* **31**, 3 LP – 14 (2011).

178. Fuhrmann, J. C. *et al.* Gephyrin interacts with Dynein light chains 1 and 2, components of motor protein complexes. *J. Neurosci.* **22**, 5393–5402 (2002).

179. Nawrotzki, R., Islinger, M., Vogel, I., Völkl, A. & Kirsch, J. Expression and subcellular distribution of gephyrin in non-neuronal tissues and cells. *Histochem. Cell Biol.* **137**, 471–482 (2012).

180. Sakers, K. & Eroglu, C. Control of neural development and function by glial neuroligins. *Curr. Opin. Neurobiol.* **57**, 163–170 (2019).

181. Morais, T. P., Coelho, D., Vaz, S. H., Sebastião, A. M. & Valente, C. A. Glycine Receptor Activation Impairs ATP-Induced Calcium Transients in Cultured Cortical Astrocytes. *Front. Mol. Neurosci.* **10**, 444 (2017).

182. Ule, J. *et al.* CLIP identifies Nova-regulated RNA networks in the brain. *Science* **302**, 1212–1215 (2003).

183. Rosato, M. *et al.* Combined cellomics and proteomics analysis reveals shared neuronal morphology and molecular pathway phenotypes for multiple schizophrenia risk genes. *Mol. Psychiatry* **26**, 784–799 (2021).

184. MacGillavry, H. D., Song, Y., Raghavachari, S. & Blanpied, T. A. Nanoscale scaffolding domains within the postsynaptic density concentrate synaptic AMPA receptors. *Neuron* **78**, 615–622 (2013).

185. Morise, J. *et al.* AMPA receptors in the synapse turnover by monomer diffusion. *Nat. Commun.* **10**, 5245 (2019).

186. Zhou, Z. *et al.* The C-terminal tails of endogenous GluA1 and GluA2 differentially contribute to hippocampal synaptic plasticity and learning. *Nat. Neurosci.* **21**, (2018).

187. Abdollahi Nejat, M., Klaassen, R. V, Spijker, S. & Smit, A. B. Auxiliary subunits of the AMPA receptor: The Shisa family of proteins. *Curr. Opin. Pharmacol.* **58**, 52–61 (2021).

188. Rao-Ruiz, P. *et al.* Retrieval-specific endocytosis of GluA2-AMPARs underlies adaptive reconsolidation of contextual fear. *Nat. Neurosci.* **14**, 1302–1308 (2011).

189. Reinders, N. R. *et al.* Amyloid-β effects on synapses and memory require AMPA receptor subunit GluA3. *Proc. Natl. Acad. Sci. U. S. A.* **113**, E6526–E6534 (2016).

190. Bissen, D., Foss, F. & Acker-Palmer, A. AMPA receptors and their minions: auxiliary proteins in AMPA receptor trafficking. *Cell. Mol. Life Sci.* **76**, 2133–2169 (2019).

191. Vandenberghe, W., Nicoll, R. a & Bredt, D. S. Stargazin is an AMPA receptor auxiliary subunit. *Proc. Natl. Acad. Sci. U. S. A.* **102**, 485–490 (2005).

192. Constals, A. *et al.* Glutamate-Induced AMPA Receptor Desensitization Increases Their Mobility and Modulates Short-Term Plasticity through Unbinding from Stargazin. *Neuron* **85**, 787–803 (2015).

193. Boudkkazi, S., Brechet, A., Schwenk, J. & Fakler, B. Cornichon2 Dictates the Time Course of Excitatory Transmission at Individual Hippocampal Synapses. *Neuron* **82**, 848–858 (2014).

194. Klaassen, R. V *et al.* Shisa6 traps AMPARs at postsynaptic sites and prevents their desensitization during high frequency synaptic stimulation. 1–12 (2016) doi:10.1038/ncomms10682.

195. Schmitz, L. J. M. *et al.* The AMPA receptor-associated protein Shisa7 regulates hippocampal synaptic function and contextual memory. *Elife* **6**, (2017).

196. Leonard, A. S., Davare, M. A., Horne, M. C., Garner, C. C. & Hell, J. W. SAP97 is associated with the alpha-amino-3-hydroxy-5-methylisoxazole-4-propionic acid receptor GluR1 subunit. *J. Biol. Chem.* **273**, 19518–19524 (1998).

197. Cai, C., Coleman, S. K., Niemi, K. & Keinänen, K. Selective binding of synapse-associated protein 97 to GluR-A alpha-amino-5-hydroxy-3-methyl-4-isoxazole propionate receptor subunit is determined by a novel sequence motif. *J. Biol. Chem.* **277**, 31484–31490 (2002).

198. Osten, P. *et al.* Mutagenesis reveals a role for ABP/GRIP binding to GluR2 in synaptic surface accumulation of the AMPA receptor. *Neuron* **27**, 313–325 (2000).

199. Setou, M. *et al.* Glutamate-receptor-interacting protein GRIP1 directly steers kinesin to dendrites. *Nature* **417**, 83–87 (2002).

200. Chung, H. J., Xia, J., Scannevin, R. H., Zhang, X. & Huganir, R. L. Phosphorylation of the AMPA receptor subunit GluR2 differentially regulates its interaction with PDZ domain-containing proteins. *J. Neurosci.* **20**, 7258–7267 (2000).

201. Matt, L. *et al.* SynDIG4/Prrt1 Is Required for Excitatory Synapse Development and Plasticity Underlying Cognitive Function. *Cell Rep.* **22**, 2246–2253 (2018).

202. Pandya, N. J. *et al.* Noelin1 Affects Lateral Mobility of Synaptic AMPA Receptors. *Cell Rep.* **24**, 1218–1230 (2018).

203. Kim, C.-H. *et al.* Persistent hippocampal CA1 LTP in mice lacking the C-terminal PDZ ligand of GluR1. *Nat. Neurosci.* **8**, 985–987 (2005).

204. Herguedas, B. *et al.* Architecture of the heteromeric GluA1/2 AMPA receptor in complex with the auxiliary subunit TARP γ8. *Science* **364**, (2019).

205. Herring, B. E. *et al.* Cornichon proteins determine the subunit composition of synaptic AMPA receptors. *Neuron* **77**, 1083–1096 (2013).

206. Specht, C. G. & Schoepfer, R. Deletion of the alpha-synuclein locus in a subpopulation of C57BL/6J inbred mice. *BMC Neurosci.* **2**, 11 (2001).

207. Koopmans, F. *et al.* Comparative Hippocampal Synaptic Proteomes of Rodents and Primates: Differences in Neuroplasticity-Related Proteins . *Frontiers in Molecular Neuroscience* vol. 11 364 (2018).

208. van der Spek, S. J. F. *et al.* Age-Dependent Hippocampal Proteomics in the APP/PS1 Alzheimer Mouse Model: A Comparative Analysis with Classical SWATH/DIA and directDIA Approaches. *Cells* **10**, (2021).

209. Borchelt, D. R. *et al.* Accelerated amyloid deposition in the brains of transgenic mice coexpressing mutant presenilin 1 and amyloid precursor proteins. *Neuron* **19**, 939–945 (1997).

210. Sasaguri, H. *et al.* APP mouse models for Alzheimer's disease preclinical studies. *EMBO J.* **36**, 2473–2487 (2017).

211. Huang, H. *et al.* Characterization of AD-like phenotype in aged APPSwe/PS1dE9 mice. *Age (Dordr).* **38**, 303–322 (2016).

212. Oyelami, T. *et al.* Age-dependent concomitant changes in synaptic dysfunction and GABAergic pathway in the APP/PS1 mouse model. *Acta Neurobiol. Exp. (Wars).* **76**, 282–293 (2016).

213. Abbink, M. R. *et al.* Characterization of astrocytes throughout life in wildtype and APP/PS1 mice after early-life stress exposure. *J. Neuroinflammation* **17**, 91 (2020).

214. Scheffler, K. *et al.* Determination of spatial and temporal distribution of microglia by 230nm-high-resolution, high-throughput automated analysis reveals different amyloid plaque populations in an APP/PS1 mouse model of Alzheimer's disease. *Curr. Alzheimer Res.* **8**, 781–788 (2011).

215. Remmelink, E., Smit, A. B., Verhage, M. & Loos, M. Measuring discrimination- and reversal learning in mouse models within 4 days and without prior food deprivation. *Learn. Mem.* **23**, 660–667 (2016).

216. Schubert, O. T. *et al.* Building high-quality assay libraries for targeted analysis of SWATH MS data. *Nat. Protoc.* **10**, 426–441 (2015).

217. Koopmans, F., Ho, J. T. C., Smit, A. B. & Li, K. W. Comparative Analyses of Data Independent Acquisition Mass Spectrometric Approaches: DIA, WiSIM-DIA, and Untargeted DIA. *Proteomics* **18**, (2018).

218. Tsou, C.-C. *et al.* DIA-Umpire: comprehensive computational framework for data-independent acquisition proteomics. *Nat. Methods* **12**, 258–64, 7 p following 264 (2015).

219. Gonzalez-Lozano, M. A. *et al.* Dynamics of the mouse brain cortical synaptic proteome during postnatal brain development. *Sci. Rep.* **6**, 35456 (2016).

220. Wilhelm, B. G. *et al.* Composition of isolated synaptic boutons reveals the amounts of vesicle trafficking proteins. *Science* **344**, 1023–1028 (2014).

221. Skene, N. G. & Grant, S. G. N. Identification of Vulnerable Cell Types in Major Brain Disorders Using Single Cell Transcriptomes and Expression Weighted Cell Type Enrichment. *Front. Neurosci.* **10**, 16 (2016).

222. Zeisel, A. *et al.* Brain structure. Cell types in the mouse cortex and hippocampus revealed by single-cell RNA-seq. *Science* **347**, 1138–1142 (2015).

223. Schafer, D. P. *et al.* Microglia sculpt postnatal neural circuits in an activity and complement-dependent manner. *Neuron* **74**, 691–705 (2012).

224. Li, X. *et al.* Sequence of proteome profiles in preclinical and symptomatic Alzheimer's disease. *Alzheimers. Dement.* (2021) doi:10.1002/alz.12345.

225. Végh, M. J. *et al.* Reducing hippocampal extracellular matrix reverses early memory deficits in a mouse model of Alzheimer's disease. *Acta Neuropathol. Commun.* **2**, 76 (2014).

226. Wan, Y.-W. *et al.* Meta-Analysis of the Alzheimer's Disease Human Brain Transcriptome and Functional Dissection in Mouse Models. *Cell Rep.* **32**, 107908 (2020).

227. Sebastian Monasor, L. *et al.* Fibrillar Aβ triggers microglial proteome alterations and dysfunction in Alzheimer mouse models. *Elife* **9**, (2020).

228. Parhizkar, S. *et al.* Loss of TREM2 function increases amyloid seeding but reduces plaque-associated ApoE. *Nat. Neurosci.* **22**, 191–204 (2019).

229. Sala Frigerio, C. *et al.* The Major Risk Factors for Alzheimer's Disease: Age, Sex, and Genes Modulate the Microglia Response to Aβ Plaques. *Cell Rep.* **27**, 1293-1306.e6 (2019).

230. Saito, T. *et al.* Single App knock-in mouse models of Alzheimer's disease. *Nat. Neurosci.* **17**, 661–663 (2014).

231. Holtzman, D. M., Herz, J. & Bu, G. Apolipoprotein E and apolipoprotein E receptors: normal biology and roles in Alzheimer disease. *Cold Spring Harb. Perspect. Med.* **2**, a006312 (2012).

232. Yeh, F. L., Wang, Y., Tom, I., Gonzalez, L. C. & Sheng, M. TREM2 Binds to Apolipoproteins, Including APOE and CLU/APOJ, and Thereby Facilitates Uptake of Amyloid-Beta by Microglia. *Neuron* **91**, 328–340 (2016).

233. Radde, R. *et al.* Abeta42-driven cerebral amyloidosis in transgenic mice reveals early and robust pathology. *EMBO Rep.* **7**, 940–946 (2006).

234. De Strooper, B. Aph-1, Pen-2, and Nicastrin with Presenilin generate an active gamma-Secretase complex. *Neuron* **38**, 9–12 (2003).

235. Annaert, W. & Kaether, C. Bring it back, bring it back, don't take it away from me - the sorting receptor RER1. *J. Cell Sci.* **133**, (2020).

236. Kaether, C. *et al.* Endoplasmic reticulum retention of the gamma-secretase complex component Pen2 by Rer1. *EMBO Rep.* **8**, 743–748 (2007).

237. Spasic, D. *et al.* Rer1p competes with APH-1 for binding to nicastrin and regulates gamma-secretase complex assembly in the early secretory pathway. *J. Cell Biol.* **176**, 629–640 (2007).

238. Park, H.-J. *et al.* Retention in endoplasmic reticulum 1 (RER1) modulates amyloid-β (Aβ) production by altering trafficking of γ-secretase and amyloid precursor protein (APP). *J. Biol. Chem.* **287**, 40629–40640 (2012).

239. Jansen, I. E. *et al.* Genome-wide meta-analysis identifies new loci and functional pathways influencing Alzheimer's disease risk. *Nat. Genet.* **51**, 404–413 (2019).

240. de Silva, H. V *et al.* A 70-kDa apolipoprotein designated ApoJ is a marker for subclasses of human plasma high density lipoproteins. *J. Biol. Chem.* **265**, 13240–13247 (1990).

241. Xie, Z. *et al.* Apolipoprotein J (clusterin) activates rodent microglia in vivo and in vitro. *J. Neurochem.* **93**, 1038–1046 (2005).

242. Kishore, U. & Reid, K. B. C1q: structure, function, and receptors. *Immunopharmacology* **49**, 159–170 (2000).

243. Afagh, A., Cummings, B. J., Cribbs, D. H., Cotman, C. W. & Tenner, A. J. Localization and cell association of C1q in Alzheimer's disease brain. *Exp. Neurol.* **138**, 22–32 (1996).

244. Reichwald, J., Danner, S., Wiederhold, K.-H. & Staufenbiel, M. Expression of complement system components during aging and amyloid deposition in APP transgenic mice. *J. Neuroinflammation* **6**, 35 (2009).

245. Webster, S., Glabe, C. & Rogers, J. Multivalent binding of complement protein C1Q to the amyloid beta-peptide (A beta) promotes the nucleation phase of A beta aggregation. *Biochem. Biophys. Res. Commun.* **217**, 869–875 (1995).

246. Webster, S., O'Barr, S. & Rogers, J. Enhanced aggregation and beta structure of amyloid beta peptide after coincubation with C1q. *J. Neurosci. Res.* **39**, 448–456 (1994).

247. Boyett, K. W. *et al.* Increased fibrillar beta-amyloid in response to human clq injections into hippocampus and cortex of APP+PS1 transgenic mice. *Neurochem. Res.* **28**, 83–93 (2003).

248. Webster, S. D. *et al.* Complement component C1q modulates the phagocytosis of Abeta by microglia. *Exp. Neurol.* **161**, 127–138 (2000).

249. Sanders, S. S. *et al.* Huntingtin interacting proteins 14 and 14-like are required for chorioallantoic fusion during early placental development. *Dev. Biol.* **397**, 257–266 (2015).

250. Nalls, M. A. *et al.* Imputation of sequence variants for identification of genetic risks for Parkinson's disease: a meta-analysis of genome-wide association studies. *Lancet (London, England)* **377**, 641–649 (2011).

251. Sanghvi, H., Singh, R., Morrin, H. & Rajkumar, A. P. Systematic review of genetic association studies in people with Lewy body dementia. *Int. J. Geriatr. Psychiatry* **35**, 436–448 (2020).

252. Rong, Z. *et al.* Activation of FAK/Rac1/Cdc42-GTPase signaling ameliorates impaired microglial migration response to Aβ(42) in triggering receptor expressed on myeloid cells 2 loss-of-function murine models. *FASEB J. Off. Publ. Fed. Am. Soc. Exp. Biol.* **34**, 10984–10997 (2020).

253. Guerreiro, R. *et al.* TREM2 variants in Alzheimer's disease. *N. Engl. J. Med.* **368**, 117–127 (2013).

254. Cimino, P. J. *et al.* Ablation of the microglial protein DOCK2 reduces amyloid burden in a mouse model of Alzheimer's disease. *Exp. Mol. Pathol.* **94**, 366–371 (2013).

255. Chen, Q. *et al.* Loss of modifier of cell adhesion reveals a pathway leading to axonal degeneration. *J. Neurosci.* **29**, 118–130 (2009).

256. Wisniewski, J. R., Zougman, A., Nagaraj, N. & Mann, M. Universal sample preparation method for proteome analysis. *Nat. Methods* **6**, 359–362 (2009).

257. He, E. *et al.* MIR137 schizophrenia-associated locus controls synaptic function by regulating synaptogenesis, synapse maturation and synaptic transmission. *Hum. Mol. Genet.* **27**, 1879–1891 (2018).

258. Perez-Riverol, Y. *et al.* The PRIDE database and related tools and resources in 2019: improving support for quantification data. *Nucleic Acids Res.* **47**, D442–D450 (2019).

259. Levy, N. S. *et al.* IQSEC2-Associated Intellectual Disability and Autism. *Int. J. Mol. Sci.* **20**, (2019).

260. Lopergolo, D. *et al.* IQSEC2 disorder: A new disease entity or a Rett spectrum continuum? *Clin. Genet.* **99**, 462–474 (2021).

261. Morleo, M. *et al.* Disruption of the IQSEC2 transcript in a female with X;autosome translocation t(X;20)(p11.2;q11.2) and a phenotype resembling X-linked infantile spasms (ISSX) syndrome. *Mol. Med. Rep.* **1**, 33–39 (2008).

262. Kim, S. *et al.* Loss of IQSEC3 Disrupts GABAergic Synapse Maintenance and Decreases Somatostatin Expression in the Hippocampus. *Cell Rep.* **30**, 1995-2005.e5 (2020).

263. Kim, H. *et al.* The small GTPase ARF6 regulates GABAergic synapse development. *Mol. Brain* **13**, 2 (2020).

264. Rankovic, M. *et al.* ADP-ribosylation factor 6 regulates mu-opioid receptor trafficking and signaling via activation of phospholipase D2. *Cell. Signal.* **21**, 1784–1793 (2009).

265. Cho, D. I. *et al.* ARF6 and GASP-1 are post-endocytic sorting proteins selectively involved in the intracellular trafficking of dopamine D_2 receptors mediated by GRK and PKC in transfected cells. *Br. J. Pharmacol.* **168**, 1355–1374 (2013).

266. D'Souza-Schorey, C. & Chavrier, P. ARF proteins: roles in membrane traffic and beyond. *Nat. Rev. Mol. Cell Biol.* **7**, 347–358 (2006).

267. Huttlin, E. L. *et al.* The BioPlex Network: A Systematic Exploration of the Human Interactome. *Cell* **162**, 425–440 (2015).

268. Michaelis, A. C. *et al.* The social architecture of an in-depth cellular protein interactome. *bioRxiv* 2021.10.24.465633 (2021) doi:10.1101/2021.10.24.465633.

269. Luck, K. *et al.* A reference map of the human binary protein interactome. *Nature* **580**, 402–408 (2020).

270. Schulte, U., Müller, C. S. & Fakler, B. Ion channels and their molecular environments--glimpses and insights from functional proteomics. *Semin. Cell Dev. Biol.* **22**, 132–144 (2011).

271. Basu, A., Ash, P. E., Wolozin, B. & Emili, A. Protein Interaction Network Biology in Neuroscience. *Proteomics* **21**, e1900311 (2021).

272. Bludau, I. & Aebersold, R. Proteomic and interactomic insights into the molecular basis of cell functional diversity. *Nat. Rev. Mol. Cell Biol.* **21**, 327–340 (2020).

273. Heusel, M. *et al.* Complex-centric proteome profiling by SEC-SWATH-MS. *Mol. Syst. Biol.* **15**, e8438 (2019).

274. Pourhaghighi, R. *et al.* BraInMap Elucidates the Macromolecular Connectivity Landscape of Mammalian Brain. *Cell Syst.* **10**, 333-350.e14 (2020).

275. Zaki, N. & Mora, A. A comparative analysis of computational approaches and algorithms for protein subcomplex identification. *Sci. Rep.* **4**, 4262 (2014).

276. Zaki, N., Mohamed, E. A. & Mora, A. Characterization of protein complexes and subcomplexes in protein-protein interaction databases. *Biochem. Res. Int.* **2015**, 245075 (2015).

277. Glatigny, A., Gambette, P., Bourand-Plantefol, A., Dujardin, G. & Mucchielli-Giorgi, M.-H. Development of an in silico method for the identification of subcomplexes involved in the biogenesis of multiprotein complexes in Saccharomyces cerevisiae. *BMC Syst. Biol.* **11**, 67 (2017).

278. Evans, R. *et al.* Protein complex prediction with AlphaFold-Multimer. *bioRxiv* 2021.10.04.463034 (2021) doi:10.1101/2021.10.04.463034.

279. Takano, T. *et al.* Chemico-genetic discovery of astrocytic control of inhibition in vivo. *Nature* **588**, 296–302 (2020).

280. Stogsdill, J. A. *et al.* Astrocytic neuroligins control astrocyte morphogenesis and synaptogenesis. *Nature* **551**, 192–197 (2017).

281. Blanco-Suárez, E., Caldwell, A. L. M. & Allen, N. J. Role of astrocyte-synapse interactions in CNS disorders. *J. Physiol.* **595**, 1903–1916 (2017).

282. Tasic, B. Single cell transcriptomics in neuroscience: cell classification and beyond. *Curr. Opin. Neurobiol.* **50**, 242–249 (2018).

283. Piet, R. & Jahr, C. E. Glutamatergic and purinergic receptor-mediated calcium transients in Bergmann glial cells. *J. Neurosci.* **27**, 4027–4035 (2007).

284. Kowalczyk, S. *et al.* Direct binding of GABAA receptor β2 and β3 subunits to gephyrin. *Eur. J. Neurosci.* **37**, 544–554 (2013).

285. Bazargani, N. & Attwell, D. Astrocyte calcium signaling: the third wave. *Nat. Neurosci.* **19**, 182–189 (2016).

286. Ullian, E. M., Sapperstein, S. K., Christopherson, K. S. & Barres, B. A. Control of synapse number by glia. *Science* **291**, 657–661 (2001).

287. Pennacchietti, F. *et al.* Nanoscale Molecular Reorganization of the Inhibitory Postsynaptic Density Is a Determinant of GABAergic Synaptic Potentiation. *J. Neurosci.* **37**, 1747 LP – 1756 (2017).

288. Crosby, K. C. *et al.* Nanoscale Subsynaptic Domains Underlie the Organization of the Inhibitory Synapse. *Cell Rep.* **26**, 3284-3297.e3 (2019).

289. Liu, P.-W., Hosokawa, T. & Hayashi, Y. Regulation of synaptic nanodomain by liquid-liquid phase separation: A novel mechanism of synaptic plasticity. *Curr. Opin. Neurobiol.* **69**, 84–92 (2021).

290. Yang, X., Le Corronc, H., Legendre, P., Triller, A. & Specht, C. G. Differential regulation of glycinergic and GABAergic nanocolumns at mixed inhibitory synapses. *EMBO Rep.* **22**, e52154 (2021).

291. Khodosevich, K. *et al.* Coexpressed auxiliary subunits exhibit distinct modulatory profiles on AMPA receptor function. *Neuron* **83**, 601–615 (2014).

292. Kato, A. S. & Witkin, J. M. Auxiliary subunits of AMPA receptors: The discovery of a forebrain-selective antagonist, LY3130481/CERC-611. *Biochem. Pharmacol.* **147**, 191–200 (2018).

293. Meier, F. *et al.* diaPASEF: parallel accumulation-serial fragmentation combined with data-independent acquisition. *Nat. Methods* **17**, 1229–1236 (2020).

294. Cho, N. H. *et al.* OpenCell: proteome-scale endogenous tagging enables the cartography of human cellular organization. *bioRxiv* 2021.03.29.437450 (2021) doi:10.1101/2021.03.29.437450.

295. Hein, M. Y. *et al.* A human interactome in three quantitative dimensions organized by stoichiometries and abundances. *Cell* **163**, 712–723 (2015).

296. Huttlin, E. L. *et al.* Architecture of the human interactome defines protein communities and disease networks. *Nature* **545**, 505–509 (2017).

297. Mund, A. *et al.* AI-driven Deep Visual Proteomics defines cell identity and heterogeneity. *bioRxiv* 2021.01.25.427969 (2021) doi:10.1101/2021.01.25.427969.

298. Zhu, Y. *et al.* Nanodroplet processing platform for deep and quantitative proteome profiling of 10–100 mammalian cells. *Nat. Commun.* **9**, 882 (2018).

299. Hartlmayr, D. *et al.* An automated workflow for label-free and multiplexed single cell proteomics sample preparation at unprecedented sensitivity. *bioRxiv* 2021.04.14.439828 (2021) doi:10.1101/2021.04.14.439828.

300. Meier, F., Park, M. A. & Mann, M. Trapped Ion Mobility Spectrometry and Parallel Accumulation-Serial Fragmentation in Proteomics. *Mol. Cell. Proteomics* **20**, 100138 (2021).

301. Bruderer, R. *et al.* Extending the limits of quantitative proteome profiling with data-independent acquisition and application to acetaminophen-treated three-dimensional liver microtissues. *Mol. Cell. Proteomics* **14**, 1400–1410 (2015).

302. Gillet, L. C. *et al.* Targeted data extraction of the MS/MS spectra generated by data-independent acquisition: a new concept for consistent and accurate proteome analysis. *Mol. Cell. Proteomics* **11**, O111.016717 (2012).

303. Gessulat, S. *et al.* Prosit: proteome-wide prediction of peptide tandem mass spectra by deep learning. *Nat. Methods* **16**, 509–518 (2019).

304. Demichev, V., Messner, C. B., Vernardis, S. I., Lilley, K. S. & Ralser, M. DIA-NN: neural networks and interference correction enable deep proteome coverage in high throughput. *Nat. Methods* **17**, 41–44 (2020).

305. Spires-Jones, T. L. & Hyman, B. T. The intersection of amyloid beta and tau at synapses in Alzheimer’s disease. *Neuron* **82**, 756–771 (2014).

306. Sierksma, A. *et al.* Novel Alzheimer risk genes determine the microglia response to amyloid-β but not to TAU pathology. *EMBO Mol. Med.* **12**, e10606 (2020).

307. Deczkowska, A., Weiner, A. & Amit, I. The Physiology, Pathology, and Potential Therapeutic Applications of the TREM2 Signaling Pathway. *Cell* **181**, 1207–1217 (2020).

308. Lewcock, J. W. *et al.* Emerging Microglia Biology Defines Novel Therapeutic Approaches for Alzheimer’s Disease. *Neuron* **108**, 801–821 (2020).

309. Haass, C. Loss of TREM2 facilitates tau accumulation, spreading, and brain atrophy, but only in the presence of amyloid pathology. *Neuron* **109**, 1243–1245 (2021).

310. Lee, S.-H. *et al.* Trem2 restrains the enhancement of tau accumulation and neurodegeneration by β-amyloid pathology. *Neuron* **109**, 1283-1301.e6 (2021).

List of publications

van der Spek SJF, Gonzalez-Lozano MA, Koopmans F, Miedema SSM, Paliukhovich I, Smit AB, Li KW (**2021**) Age-Dependent Hippocampal Proteomics in the APP/PS1 Alzheimer Mouse Model: A Comparative Analysis with Classical SWATH/DIA and directDIA Approaches. Cells, 10, 1588.

van der Spek SJF, Koopmans F, Paliukhovich I, Ramsden SL, Harvey K, Harvey RJ, Smit AB, Li KW (**2020**) Glycine Receptor Complex Analysis Using Immunopurification-Blue Native Gel Electrophoresis- Mass Spectrometry. Proteomics, 20, 1900403.

van der Spek SJF, AB Smit, NJ Pandya (**2019**) Integrated Immunoprecipitation: Blue native gel electrophoresis-mass spectrometry for the identification of protein subcomplexes. Neuromethods, Vol. 146, pp. 85-94.

Uyaniker S, van der Spek SJF, Reinders NR, Xiong H, Li KW, Bossers K, Smit AB, Verhaagen J, Kessels HW (**2019**) The Effects of Sindbis Viral Vectors on Neuronal Function. Front Cell Neurosci, 13:362.

Janssen SF, van der Spek SJF, Ten Brink JB, Essing AH, Gorgels TG, van der Spek PJ, Jansonius NM, Bergen AA (**2013**) Gene expression and functional annotation of the human and mouse choroid plexus epithelium. PLoS ONE 8(12): e83345.

In preparation:

Koopmans F, van der Spek SJF, Sahasrabudhe DA, Bakali C, The SynGO Consortium, Verhage M, Bayés Puig A and Smit AB. Extending the synaptic parts list- a SynGO meta-analysis of existing proteomics data.

van der Spek SJF, Pandya NJ, Koopmans F, Paliukhovich I, Smit AB and Li KW. Interactomes of GluA1 and GluA3 subunit containing AMPARs reveal distinct protein composition.

Reinders NR, van der Spek SJF, Klaassen RV, Koymans KJ, Li KW, Smit AB and Kesssels HW. Aβ-mediated synaptic depression requires PDZ protein interactions at AMPA-receptor subunit GluA3. *bioRxiv* 2021.10.03.462970 (2021).

Acknowledgements

“I come as one, but I stand as 10,000”- Maya Angelou

I would like to express my gratitude towards all the people around who gave me support and inspiration, I am very thankful for all you have taught me.

Guus, you were the one who took me as PhD student and gave me the opportunity to work in your group and I would like to thank you for that. Thank you for introducing me to the fascinating world of molecular neurobiology, protein-protein interactions and mass spectrometry during lectures at the VU preceding my PhD appointment, and for taking me in 7 years ago. Thank you for giving me the freedom to explore and develop myself as a researcher with the trust that things will work out. Your genuine care for science, your positive attitude, and the way you convey your ideas on paper and in spoken word are inspiring. **Ka Wan,** without you my PhD trajectory would not have been possible. You have been absolutely essential for my work and achievements. Because of your ability to put ideas in perspective and to clearly separate main from detail your input always improved my work. Thank you for the occasional push, for being so approachable and having your door always open. This allowed me and my projects to land on our feet. I will always remember the care you show for your students, our recurrent proteomics dinners, and of course our trips to China and the US.

I would like to thank the **doctorate board** for their time reading my dissertation. **Helmut**, thank you for our meetings and discussions on the AMPAR and its involvement in Alzheimer’s disease and having me on the memorabel team. **Nikhil,** you introduced me to the lab and the world of AMPAR interactors. Thank you for your patience, guidance and sharing your knowledge. These first extensive lab experiences are unforgettable and invaluable to me. **Robert**, the contribution of your lab on my first first-author paper felt like a nice present and added the extra touch that made the story complete. **Connie,** thank you for our shared proteomics meetings at the medical center and the Annual Meetings of the Netherlands Proteomics Platform that have expanded my knowledge on proteomics outside of neuroscience. **Ronald,** thank you for contributing to the nice environment at the MCN and your always sharp insights during our weekly Thursday morning meetings.

I would like to thank all the people of the **MCN** who make the lab a great and exciting environment to work in. **Sabine** and **Priyanka**, experiencing you as (becoming) female PIs from up-close has been empowering, thank you for doing great and fulfilling this essential role. **Sabine**, I will never forget the sound of your running heels and your cheerful energy. Thank you for your joyfulness, scientific inputs and advices. **Priyanka**, thank you for being so knowledgeable, accessible, and for your unforgettable wit. **Mark**, thank you for contributing to a constructive atmosphere in the lab with your calm and friendly attitude. And of course, thanks for teaching me how to recognize the Macula Densa, Kuppfer cells and the tunica intima, media and externa. **Michel,** thank you for your critical eye, your persistent efforts to improve the quality of the MCN output, and exemplifying the successful development of a young scientist. **Rolinka,** thank you for enabling many of my experiments, for all the time we spent dissecting animals and teaching me how to isolate the hippocampus. I really enjoyed our talks during our work together. Your contributions to the lab are big and much appreciated. **Yvonne** and **Brigitte,** thank you for keeping everything in- and outside the lab running like an oiled machine, and for organizing the many borrels and lab outings, which have been unforgettable. **Marion, Titia, Mylene** and **Chaimaa,** thank you for all the cells you've cultured for me. Without your efforts, I would not have been able to learn (super resolution) microscopy and answer our questions with pretty pictures taken of pretty cells. **Brendan**, your staining's were perfect! Thanks again for stepping in when hands were needed.

I would like to thank the **proteomics team** for all the fun we had, sharing our love (and frustrations) for proteins and mass spectrometry, our conversations, travels and dinners. **Frank**, our data genius. Thank you for your optimism, your deep understanding of mass spec data and your unwavering willingness to help wherever you can. I will always remember our trips, regular dinners and conversations on work and life. **Roel,** thank you for teaching me the basics of mass spectrometry, your enthusiasm for science and all the stories you shared. **Iryna**, thank you for our conversations between experiments, our laughs and of course your care for all our samples (there have been a lot). **Remco,** thank you for your thoughtful answers to all my questions and your detailed observations and remarks. Every lab would wish to have someone like you on their team. **Pim,** the joy you radiate is unforgettable. Thank you for your laughs and big smiles. **Ning,** I've met you in China and during my bachelor studies**.** You have left nothing but good impressions, and you will continue to do great. Thank you for paving our ways in the proteomics lab. **Andrea,** thinking back on our shared experiences far from home always makes me smile. Thank you for being my China and US travel buddy, our conversations and adventures. **Suzanne,** thank you for your joyful attitude, your eagerness to help out and of course for your scientific contribution to my work. **Miao,** I am so happy I met you. Coming from the other side of the world to Amsterdam to become a PhD is admirable. You are doing great, and I'm certain you'll continue to do great in the future wherever you decide to go. Thank you for always being available to help out, your camaraderie is invaluable. **Evangelia** and **Debora,** thank you for bringing a fresh joyful spirit to our lab, I wish you all the best on your own PhD adventures.

To all **PhD students and postdocs** that I met along the years (including those already mentioned): I'm so happy I got to know you and that we were able to share our experiences, our lunch breaks, dinners and meet-ups. Thinking of you gives me the biggest smile. **Demir**, the lab has been so empty without you! Thank you for all our talks about tattoos and fashion, our shared laughs and frustrations, and our skating expeditions. These I will always remember. **Martina,** I love your calm energy. Thank you for always being up to participate in any event, for stepping-in when help was needed, and for being such a great and reliable friend. **Maija,** thank you for being the first to welcome me into our office, your peaceful attitude made me feel directly at home. **Mariana**, so competent, knowledgeable and kind. Thank you for the stories you shared, our laughs and for taking us all under your wings. **Sonya,** the things you have achieved are very impressive, coming to Amsterdam, learning Dutch, the work you have done and continue to do in China. Thank you for sharing your experiences and for being so kind. **Elena,** thank you for all the stories you shared with great enthusiasm, our dinners and the fun times we spent together. **Sara,** I still remember you were the first inviting me for lunch, thank you for being so laid-back, happy and welcoming. **Aina**, you immediately were a great addition to the group, thank you for bringing your outgoing and friendly enthusiasm. **Esther,** thank you for exemplifying such extraordinary energy, discipline and joy. Your (pro)active approach is very impressive, and will get you far in work and life. **Christina**, thank you for all the conversations we had between experiments, about the big and small things in life. I appreciated them a lot. **Mandy,** thank you for being so easygoing and for always being up to participate or help out with a big smile. **Leonidas,** thanks again for cheering for me when I was on stage. I really enjoyed our talks and time we spent together. **Azra!!** I'm so happy we met; you have taught me so much. I am still amazed by how similar we are and yet so different. Thank you for the great times we have spent together, and will continue to do so in the future (no no, I'm not going to forget about Malaysia!). **Fran,** thank you for being my paranymph!! I'm so happy we became office mates and we got to know each other better. Thank you for all our conversations, the times we met up at work and outside of the lab, and the fun things we've done. **Mio,** thank you for bringing your laid-back vibes to the lab and complementing the department so nicely. **Marieke,** I really enjoyed our walks and conversations in- and outside the lab. Thank you for your down-to-earth perspectives and, of course, for letting me cuddle your cute cats! **Niels** and **Seçil**, it was always nice to catch up with you wherever we met. Thank you for our conversations and sharing experiences in science.

Dnyanada, Mazyar, Biswajit, Agnieszka, Aline, Julia, Femke, Annetrude, Payam, the newest additions to the department. I wish you all the best in- and outside the lab, and that you may enjoy the MCN and learn there as much as I have. **Dnyanada** and **Mazyar,** thank you for the many talks we shared in the office, our lunches and dinners. I will never forget our time together leading up to the lock-downs, and of course I wish we could have seen each other more.

To PhD students of previous generations: **Leanne, Céline, Danai, Anne-Lieke, Sigrid, Mariette, Esther, Bart, Loek, Joerg, Ioannis, Karen, Natasha** and **Anya**, thank you for welcoming me into the lab when I met you during my internship or PhD at the MCN.

To members of the **Microscopy and Cytometry Core Facility at the Amsterdam UMC**, **Marko, Nanne and Evelien**, thank you for helping me set up, perform and analyze my work with super-resolution imaging. To my students **Ruben** and **Nila**, thank you for your help in the lab.

Aan mijn **familie** en **vrienden** thuis, met jullie sta ik nooit alleen. Papa, mama en Felix, bedankt voor jullie onvoorwaardelijke steun. **Mama**, zoals jij mij en anderen altijd met raad en daad bijstaat is van onschatbare waarde, dankjewel daarvoor. **Papa,** bedankt voor jouw positiviteit en enthousiasme voor het leven, en jouw inzet voor ons geluk. **Felix,** bedankt voor jouw open deur, onze gesprekken en gedeelde pret. **Arnold, Brigitte, Maarten, Helen, Marije** en **Jean Paul**, bedankt voor jullie hartelijke aanmoedigingen en belangstelling vanaf de zijlijn. **A mi familia española**, **Ana, Gustavo, Gus** y **Eva**, muchas gracias por acogerme, por ser un equipo en las buenas y en las malas, y por apoyar a Miguel y a mí en nuestros viajes. Aan **Myka, Mexx en Nana**, we kennen elkaar nu al zo lang, dat vind ik super leuk! Bedankt voor alle gezellige uitjes, gesprekken, feestjes en afleiding van werk, onze vriendschap is goud waard. **Opa, Oma, Marlies en Karen**, bedankt voor alles wat jullie me hebben geleerd.

Migueliii, mi persona favorita, muchas gracias por todo. Gracias por tu paciencia, tu apoyo sin fin, y tu oído atento. Me encanta como nosotros reímos juntos, y como afrontamos los buenos y los malos momentos. Creo que juntos podemos mover montañas, y estoy muy emocionada por ver lo que los años que vienen nos traerán.

“My life extends far beyond the limitations of me”- David Mitchell, Cloud Atlas. Een passende uitspraak voor degene aan wie ik graag mijn laatste dank wil betuigen en niet onbenoemd wil laten: **Sibbeltje Verdam-Okma**, mijn overgroot moeder, initiatiefnemer spaaractie VU-plan en president organisatie Vrouwen VU-hulp (VU-busjes). Mede dankzij jouw initiatief heeft de universiteit in de jaren 1932-1970 kunnen uitbreiden met faculteiten in de medische en exacte wetenschappen, waaraan ik mijn studies en deze promotie heb kunnen volbrengen. Bedankt voor jouw inzet.